

SYNOPTIC-SCALE DEFORMATION

AND

TROPICAL CLOUD BANDS

by

HOWARD BRUCE BLUESTEIN

S.B., Massachusetts Institute of Technology, 1971

S.M., Massachusetts Institute of Technology
Department of Electrical Engineering, 1972
Department of Meteorology, 1972

SUBMITTED IN PARTIAL FULFILLMENT OF THE
REQUIREMENTS FOR THE DEGREE OF DOCTOR OF PHILOSOPHY

at the

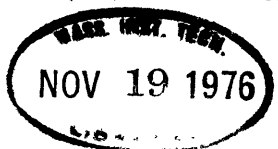
MASSACHUSETTS INSTITUTE OF TECHNOLOGY

May, 1976

Signature of Author Department of Meteorology, 30 April 1976

Certified by Thesis Supervisor

Accepted by Chairman, Departmental Committee



SYNOPTIC-SCALE DEFORMATION AND TROPICAL CLOUD BANDS

by

Howard B. Bluestein

Submitted to the Department of Meteorology
on 30 April 1976 in partial fulfillment of
the requirements for the degree of Doctor
of Philosophy

ABSTRACT

It was hypothesized that synoptic-scale deformation plays a role in the formation and structure of tropical cloud bands.

The orientations of climatological bands of cloudiness in the North Pacific, North Atlantic, South Indian, and South Pacific were found to be well-correlated with the respective climatological gradient-level axis-of-dilatation orientations. The wind field was objectively analyzed for BOMEX Phase IV at 950, 850, 700, and 450 mb from vertically averaged rawinsonde data. The statistics of synchronous and asynchronous data were used to determine the interpolating function. Significant correlations were found between cloud-band orientation and the orientation of the respective axes of dilatation of the nondivergent wind at 950, 850, and 700 mb. The significance decreased with height. On days when cloud bands were zonally oriented, the average axis-of-dilatation orientation was zonal; when cloud bands were nonzonally oriented, the average axis-of-dilatation orientation was nonzonal. The orientation of a spectacular cloud band during GATE was well-correlated with the axis of dilatation of the 850-mb wind. It was therefore concluded that tropical cloud-band orientation is related to synoptic-scale deformation at low levels.

A simple quasigeostrophic analytic model of a frontal zone in the tropics indicated that the horizontal virtual-temperature gradients in the BOMEX and GATE areas were too small for thermal forcing to be dynamically significant in the absence of latent heat release. Since latent heat release drove the BOMEX cloud bands, and some necessary conditions for CISK were observed, it is possible that deformation at the gradient level produces bands of cyclonic vorticity along which cumulus convection occurs.

Thesis Supervisor: Frederick Sanders
Title: Professor of Meteorology

To

Ma

and

Pa

ACKNOWLEDGEMENTS

I am deeply grateful to Frederick Sanders, my advisor, for his advice, patience, and stimulation for the past six years. Many other people at M.I.T. were also quite helpful. My financial support came from an M.I.T. teaching assistantship and from research assistantships supported by NOAA grant 04-5-022-9 and NSF grant DES 74-24405. Computations were done at the M.I.T. Information Processing Center. The BOMEX data were generously supplied by CEDDA, and the GATE data were obtained from NCC. In addition, some satellite data were given to me by NESS.

Harry Hawkins at NHRL (now NHEML) gave me the opportunity to observe tropical weather for two exciting summers. I was also lucky enough to have flown with RFF into Hurricane Dawn (1972), into turbulent cumulus towers which were being seeded, and around a waterspout. I thank also Bob Burpee of NHEML for his gentle prodding, and other people at NHEML and NHC for stimulating discussions.

Pauline Austin and Speed Geotis made it possible for me to participate in GATE. Aboard the rolling R.V. Gilliss, I visually and by radar observed many of the fascinating features of the ITCZ.

The typing was expertly done by Ms. Kathy Madison. Ms. Isabel Kole ably drafted the figures. Ms. Wendy Gottesman and Ms. Virginia Mills also assisted with the typing.

I thank Janet Cutler for her love and patience during the course of this research.

Finally, I thank nature for having captured my imagination.

Let's close our eyes
and talk about the weather

from The Pirates of Penzance
W.S. Gilbert and
Arthur S. Sullivan

TABLE OF CONTENTS

ABSTRACT.	2
DEDICATION.	3
ACKNOWLEDGEMENTS.	4
TABLE OF CONTENTS.	5
1. INTRODUCTION.	7
2. DEFORMATION AND SYNOPTIC-SCALE CLOUD BANDS.	12
2.1 Properties of deformation.	12
2.2 Deformation and baroclinic frontal structures.	15
3. CLIMATOLOGY OF DEFORMATION AND CLOUD BANDS OVER THE TROPICAL OCEANS.	28
3.1 Data processing.	28
3.2 Discussion of climatology.	30
3.3 Summary.	34
4. CLOUD BANDS OF BOMEX PHASE IV.	35
4.1 Discussion of the data.	35
4.1.1 Fixed-ship observations.	35
4.1.2 Land observations.	42
4.1.3 Satellite observations.	43
4.1.4 Aircraft observations.	44
4.2 Objective analysis of the wind field.	45
4.2.1 The objective analysis method.	46
4.2.2 Analysis of parameters derived from the wind. field.	64
4.3 Statistical analysis of nondivergent deformation. and cloud-band orientation.	68
4.4 Compositing analyses.	72
4.4.1 The compositing analyses and their implications.	73
4.4.2 The cross-sectional analyses and their implications.	79
4.4.3 Heat and water-vapor budget analyses and their implications.	84
4.5 Summary and discussion.	94

5.	CASE STUDY OF THE CLOUD BAND OF 12 AUGUST 1974 (GATE)	99
6.	CONCLUSIONS AND SUGGESTIONS FOR FUTURE RESEARCH.	102
6.1	Summary and conclusions.	102
6.2	Suggestions for future research.	103
	APPENDICES.	105
A	Determination of the axis-of-dilatation orientation and the resultant deformation.	105
B	Computation of water vapor mixing ratio from relative humidity, pressure, and temperature.	108
C	Computation of relative humidity from wet-bulb temperature, pressure, and dry-bulb temperature.	109
D	Format of coded card wind data from BOMEX Phase IV.	110
E	Hanning filter.	111
F	The discrete Fourier transform of the auto- covariance function: the power spectrum	112
G	The discrete inverse Fourier transform of the power spectrum: the autocovariance function	113
H	The discrete Fourier transform of the cross- covariance function: the cross-spectral density function.	114
I	Relaxation formulas.	115
J	Estimation of the accuracy of the measurements of the orientation of the axis of dilatation.	116
K	Designations of all objective analyses for BOMEX Phase IV.	118
L	Computation of vertical velocity (ω).	120
M	Derivation of heat and moisture-budget equations	121
N	Computation of $E_0 - P_0$	125
	FIGURES.	126
	TABLES	197
	BIBLIOGRAPHY.	202
	BIOGRAPHICAL NOTE	208

1. INTRODUCTION

Geophysical fluids often have a marked streaky, banded appearance. Photographs of Venus from Mariner 10 and of Jupiter from Pioneer II, for example, show distinct elongated bright and dark zones; photographs of the Earth from space also show banded structures, most of which are elongated cloudy regions.

The organization of clouds into long, narrow zones occurs on many scales in the Earth's troposphere: Synoptic-scale cloud bands are frequently found along midlatitude frontal zones. They may be longer than 1000 km and last for more than a day. The mesoscale squall-line cloud band persists for less than a day, and small-scale cumulus cloud streets persist for only an hour or less. Synoptic-scale cloud bands will henceforth be referred to as cloud bands, and structures of smaller scale will be ignored, since they are often obscured. In any case, adequate data for the study of smaller scale structures are not available.

About the time satellites were first sent into orbit about the Earth, Malkus and Riehl (1964) made visual observations from aircraft of tropical oceanic cumulus clouds that were organized into mesoscale patterns. Later satellite observations confirmed this phenomenon (Anderson et al., 1969). Cloud bands, for example, frequently appear in the intertropical convergence zone (ITCZ).

There is observational and numerical evidence that the physical mechanism by which midlatitude frontal vertical circulations are

organized depends upon the deformation of the geostrophic wind field (Bergeron, 1928; Sawyer, 1956; Hoskins and Bretherton, 1972). Since the satellite-observed appearance of tropical cloud bands is often curiously similar to that of midlatitude frontal cloud bands, the following hypothesis is proposed: Synoptic-scale deformation plays a significant role in the life-cycle of tropical cloud bands.

This notion is supported by some observational studies. The streamfunction $\psi = K e^{-ay^2} \cos (bx - cy)$, for example, represents a tilted wave train embedded in a basic current with horizontal shear; the accompanying pattern (Fig. 1.1) of the orientation of axes of dilatation (see section 2.1) is also wavelike, and lags the wavelike flow pattern by about one-quarter of a wavelength. If the cloud bands that define the "inverted-V" pattern of the tropical Atlantic (Frank, 1969) are oriented along the axes of dilatation, then the crest of the cloud band-"V" would lie east of the trough in the wind field. Such a relationship has been found in wind analyses of easterly waves based on satellite-derived winds (Fett, 1973). Furthermore, front-like features which in midlatitudes are related to deformation (see sec. 2.2), have also been found in the tropics (Riehl, 1954). Among these are sharp wind shifts, surface temperature falls and low-level cyclonic relative vorticity.

Can deformation explain why tropical cloud patterns are sometimes banded and at other times are not? What physical processes in the tropics may depend on deformation? The main objectives of this study

are presenting evidence for the hypothesis and answering the preceding questions.

The problem of why tropical cloud patterns frequently are banded has probably never been comprehensively examined, since the literature contains little mention of it. Furthermore, deformation seems to have been ignored as a mechanism that may be important in the tropics.

The approach taken in this study was statistical analysis of observational data, in order to determine whether or not synoptic-scale deformation is related to cloud band organization. The data were then more thoroughly analyzed to ascertain what role deformation might play. Only oceanic tropical cloud bands were considered, in order to avoid complicating factors such as varying topography and diurnal surface heating. Perhaps that is why tropical cloud bands are most prominent over the oceans.

Barbados Oceanographic and Meteorological Experiment (BOMEX) Phase IV rawinsonde data were chosen as the primary data source because they were gathered in a region where cloud bands commonly occur, because they were plentiful, and because the observation network was laid out so that estimates of zonal and meridional gradients were possible.

Data from the earlier phases of BOMEX were not used because most cloud bands were outside the observation network. Western Pacific island data compiled in the Northern Hemisphere Data Tabulations (NHDT) are not adequate for analysis because the islands are clustered about the same latitude. Meridional gradients are therefore difficult to measure adequately. Marshall Islands (1956) data were not used because there

were no satellite data then. Although the Line Islands Experiment of 1967 provided many oceanic ITCZ data, only three islands and a roving ship made rawinsonde observations. Finally, satellite-derived winds alone were not used for the following reasons: (1) It is difficult to determine the height for which the wind estimates are most accurate. (2) There is some ambiguity between cloud-element movement and cloud-element formation and decay, causing some doubt about the accuracy of the inferred wind observation. (3) Errors in the gridding of satellite photographs result in further wind-estimate uncertainty.

Preliminary GARP Atlantic Tropical Experiment (GATE) data were used as a secondary data-source. Although the coverage of GATE was superior to that of BOMEX, preliminary GATE data have become available only recently (Ruttenberg, 1975). Since many difficulties were experienced with some of the GATE upper-level wind-measuring systems, it is likely that some of the presently available wind data are of poor quality.

In chapter 2 the physical effects of deformation on fluid motion are discussed in order to lay a proper theoretical framework. The role deformation plays in the dynamics of midlatitude fronts is examined in the light of observation and theory. A global climatology of oceanic tropical cloud bands and of deformation is presented in chapter 3. In chapter 4 the focus is on cloud bands in the BOMEX area. A crude analysis of the life-cycle of a spectacular cloud band from GATE Phase II is presented in chapter 5. The presentation of this study, then, proceeds from a global climatology to a detailed regional climatology,

and finally on to a particular case. The conclusions based on the results of this study are summarized in chapter 6. Future courses of investigation are also suggested.

2. DEFORMATION AND SYNOPTIC-SCALE CLOUD BANDS

2.1 Properties of deformation

Horizontal deformation (hereafter referred to simply as deformation) is the fractional rate at which an area element of a fluid with a material boundary is being lengthened along one axis and foreshortened along the orthogonal axis (Sanders, 1975a). According to this definition a rectangular area element having dimensions of δx and δy is being deformed (Pettersen, 1956) at the rate

$$\text{deformation} = \frac{d}{dt} \left[\frac{\delta x}{\delta y} \right] \quad (2.1)$$

The two orthogonal axes along with the fluid element are being only lengthened and only foreshortened are called the axes of dilatation and contraction, respectively. The angle, θ_d , measured counterclockwise from the axis oriented along the flow, specifies the orientation of the axis of dilatation when the resultant deformation (D) is positive, but specifies the orientation of the axis of contraction when D is negative.

$$\theta_d = \frac{1}{2} \tan^{-1} \left[\frac{R}{S} \right] \quad (2.2)$$

$$D = S \sec \left[2\theta_d \right] \quad (2.3)$$

$$|D| = [R^2 + S^2]^{1/2} \quad (2.4)$$

where S is the stretching deformation and R is the shearing deformation (see Appendix A). The resultant deformation, D , may be interpreted simply as the deformation via (2.1), if δx and δy are the dimensions of the hypothetical rectangular area element, one side being

aligned along the axis of dilatation (or contraction). When δx is oriented along the axis of dilatation (contraction), δy is along the axis of contraction (dilatation), and the resultant deformation is positive (negative). (The fluid element was chosen to be a rectangle for simplicity. A circular fluid element could have been used, for example, in which case it would have been deformed into an ellipse, the axis of dilatation being along the major axis, and the axis of contraction being along the minor axis.)

Both stretching and shearing deformation contribute toward the net elongation (foreshortening) of a material fluid element. Stretching deformation acts to elongate (foreshorten) the material fluid element along the flow, while shearing deformation acts to elongate (foreshorten) the fluid element at an angle of 45° from the flow. Their combined effect is specified by θ_d and D .

The physical importance of deformation is its tendency to change the gradients of scalar fields (whose isopleths are oriented within 45° of the axis of dilatation or axis of contraction. Otherwise nothing happens.) The individual rate at which the magnitude of the horizontal gradient of a scalar field a changes is given by the following (Sommers, 1967):

$$\frac{d}{dt} |\nabla_h a| = \nabla_h \left[\frac{da}{dt} \right] \cdot \frac{\nabla_h a}{|\nabla_h a|} + \frac{|\nabla_h a|}{2} D \cos 2\gamma - \frac{|\nabla_h a|}{2} \delta \quad (2.5)$$

where γ is the angle between the axis of dilatation and the orientation of the isopleths of a . The magnitude of the horizontal gradient of a is changed by the horizontal variation of individual changes, by deformation, and by convergence (divergence).

If a is a conservative field, and if the wind field is nondivergent,

$$\frac{d}{dt} |\nabla_h a| = K |\nabla_h a| \quad (2.6)$$

where $K = \frac{D \cos 2\gamma}{2}$. If D and γ are constant,

$$|\nabla_h a| = |\nabla_h a|_0 e^{Kt} \quad (2.7)$$

where $|\nabla_h a|_0$ is the initial $|\nabla_h a|$. That is, the horizontal gradient of a changes exponentially with an e-folding time of K^{-1} . For a K of 10^{-5} sec^{-1} , a typical synoptic-scale value, the e-folding time is about two and a half days. Stretching deformation is a more efficient mechanism than shearing deformation for making stationary narrow zones of sharp horizontal a -gradients: shearing deformation tends to rotate the isopleths of a until γ approaches 45° . Therefore exponential growth exists only for a limited time because K approaches zero.

Three-dimensional deformation could be analyzed as it was in two dimensions, and three orthogonal axes could be found along which a material volume element would be deformed. In addition to the spatial variation of individual changes, to horizontal deformation, and to convergence, twisting, vertical deformation, and divergence could also contribute to changes in $|\nabla a|$.

The implications of the properties of deformation for the dynamics of cloud band systems are examined in the following section.

2.2 Deformation and baroclinic frontal structures

Large quasi-horizontal synoptic-scale temperature gradients are frequently found in the midlatitude troposphere. Most are an indirect result of the global meridional imbalance of net solar energy input. Differential surface heating on smaller scales also results in horizontal temperature gradients. In the tropical troposphere, however, large horizontal temperature gradients, which are due mostly to differential surface-heating (e.g., Carlson, 1969) and concentrated latent heat release from cumulus convection (e.g., Hawkins and Rubsam, 1968), are not as common as in midlatitudes. Geostrophic deformation, as a consequence of the distribution of synoptic-scale disturbances, distorts the horizontal temperature field in both midlatitudes and the tropics.

Surface fronts in midlatitudes are characterized by intense horizontal temperature gradients which often approach infinity even on the mesoscale (Sanders and Plotkin, 1966). In 1918 J. Bjerknes on the basis of surface observations first suggested that the front is a sloping boundary between two air masses of different temperature. Bergeron in 1928 suggested that frontal formation is related to deformation, because pre-existing horizontal temperature gradients can be concentrated along the axis of dilatation of the wind field (Pettersen, 1956). Pettersen in 1935 further developed this kinematic theory of frontogenesis. According to (2.7), though, typical geostrophic deformation can

increase horizontal temperature gradients at a rate that is much slower than the frequently observed frontogenesis rate (Eliassen, 1959). Furthermore, the kinematical increase in horizontal temperature gradient cannot account for the rapid increase in vorticity which is observed along the frontal zone unless there is convergence (Pettersen and Austin, 1942). The convergence can be produced by a mechanism which was first proposed to explain the jet stream (Namias and Clapp, 1949): As the average horizontal temperature gradient within an atmospheric layer is increased by geostrophic deformation, the thickness of the relatively cold side of the layer decreases and the thickness of the relatively warm side of the layer increases in order that hydrostatic balance be maintained. The flows at the top and bottom of the layer become sub-geostrophic due to an increase of the horizontal pressure gradient. The ensuing cross-isobar ageostrophic flow is from the warm side to the cold side above, and in the reverse sense below. If the horizontal temperature gradient outside of a slab normal to the incipient frontal zone is relatively small, then convergence and divergence are produced above and below respectively in the warm region, whereas the opposite happens in the cold region. Thus, a thermally direct circulation is produced, which results in adiabatic cooling of the warm air and warming of the cold air in opposition to the effects of deformation.

The strength of the direct circulation as a function of geostrophic deformation, horizontal temperature gradient, and static stability can be determined quantitatively by finding an analytical solution to the

quasigeostrophic ω -equation in Cartesian coordinates (2.8) with appropriate boundary conditions and a realistic forcing function, i.e., the right-hand side of (2.8).

$$\left[\nabla^2 + \frac{f_0 \eta_0}{\sigma} \frac{\partial^2}{\partial p^2} \right] \omega = \frac{f_0}{\sigma} \frac{\partial}{\partial p} \left[\mathbf{v} \cdot \nabla \eta \right] - \frac{1}{\sigma} \nabla^2 \left[\mathbf{v} \cdot \nabla \frac{\partial \Phi}{\partial p} \right] \quad (2.8)$$

where $f = 2\Omega \sin \phi$, the Coriolis parameter, ϕ is the latitude, $\eta = \xi + f$, the absolute vorticity, $\sigma = \frac{\kappa}{p} - \frac{d \ln T}{dp} \frac{RT}{p}$, the stability parameter, $\gamma = \kappa - p \frac{d \ln T}{dp}$, $\kappa = R/C_p$, and $\Phi(x, y, p) = gz$, the geopotential. The x and y -coordinates are measured to the east and north respectively. The subscript "0" refers to the latitude of the center of the domain of the forcing function. The forcing function is determined from a prescribed geostrophic wind field at the lower boundary and a prescribed three-dimensional temperature field. The approach used here is identical to that of a study of disturbances in midlatitudes (Sanders, 1971).

The streamfunction $\psi = -\alpha xy$ was prescribed at 1000 mb, the bottom of the model atmosphere. It depicts a nondivergent wind field whose axis of dilatation is zonally oriented. The 1000-mb height field is therefore

$$\Phi(x, y, 1000) = -\frac{D_{1000} f_0}{2} xy \quad (2.9)$$

where D_{1000} is the resultant deformation at 1000 mb. The 1000-mb geostrophic wind field is similar to that at the gradient level over the North Atlantic during July (see chapter 3). The model, however, has no

vorticity at 1000 mb, whereas the real atmosphere has substantial amounts of vorticity, especially in the Western North Atlantic.

The choice of a model temperature field required special care. The temperature field was to be zonally symmetric, nearly uniform at some distance away from the origin, and varying monotonically near the origin. Not all these requirements are met by the simple linear (constant meridional temperature gradient) function used by Sanders (1971). A hyperbolic tangent function, which meets all the aforementioned conditions, requires that the solution to the ω -equation be nonseparable. A sinusoidal function of y was chosen, since it has vanishing gradients away from the origin, and requires the solution to the ω -equation be separable. Furthermore, it is possible to simulate warm-core perturbations by changing the phase of the sinusoid. The sinusoidal function, however, yields an unrealistic temperature field more than a quarter-wavelength on either side of the origin. A function which describes the variation of horizontal temperature gradient with pressure was required to reverse sign at the tropopause, so that ω would also change sign there. Thus, ω is dynamically required to vanish near the tropopause. A realistic simple analytic function is a sinusoid. Unfortunately, a sinusoidal variation with pressure led to an untractable integral during the process of solving (2.8). The logarithmic function used by Sanders (1971) was chosen because of its simplicity. Its main deficiency is its failure to damp the horizontal temperature gradient near the lower boundary. Since the layer of air near an ocean surface is approximately homogeneous, the logarithmic function does not correctly

simulate the temperature field at such a lower boundary. Furthermore, the model does not include boundary-layer friction. Since the purpose of this simple analytical model is only to estimate the strength of the vertical flow due to quasigeostrophic forcing, and not to simulate boundary-layer phenomena, this deficiency is overlooked. The effect of the logarithmic function is a distortion of the vertical circulation. (It would have been possible to use a parabolic function which has a maximum in the mid-troposphere and which vanishes at the lower and upper boundaries. However, the additional mathematical complication was deemed unjustified.) The logarithmic function is also responsible for enormous horizontal temperature gradients in the stratosphere. Since motions between the stratosphere and troposphere are probably mainly uncoupled, unrealistic stratospheric motions probably do not induce unrealistic tropospheric motions. The temperature field is therefore described as

$$T(y,p) = T_m(p) + T'(y,p) \quad (2.10)$$

where $T'(y,p) = (1 - \alpha \ln \frac{1000}{p}) \hat{T} \cos \frac{2\pi}{L} (y + \lambda)$. $T_m(p)$ is the mean vertical temperature profile, $T'(y,p)$ is the temperature perturbation, α is chosen so $1 - \alpha \ln \frac{1000}{p} = 0$ at the tropopause, and \hat{T} , L , and λ are the amplitude, horizontal wavelength, and phase of the temperature perturbation. In the tropics, where the water vapor mixing ratio (q) is often large, virtual temperature (T_v) is substituted for temperature.

The stability factor, σ , is given by

$$\sigma(p) = \frac{R\bar{T}\gamma_0}{p^2} \quad (2.11)$$

where \bar{T} is the average temperature in the atmospheric column, and is assumed to be independent of x and y , and γ is assumed to be independent of p . Sanders (1975b) has discussed in some detail the restrictive effects of these assumptions, which were later supported by observations.

The geopotential, Φ , above 1000 mb was computed by hydrostatically integrating the height field upwards from 1000 mb, given $T(y)$. Thus

$$\Phi(x,y,p) = \Phi_m(p) - \left[\frac{D_{1000} f_0}{2} \right]_{xy} + B(p) \hat{T} \cos \frac{2\pi}{L} (y + \lambda) \quad (2.12)$$

where $\Phi_m(p)$ is the mean height of p , and $B(p) = R \ln \frac{1000}{p} - \frac{R\alpha}{2} \left(\ln \frac{1000}{p} \right)^2$. Figure 2.1 shows schematically the height fields at 1000 mb and at some pressure aloft. So

$$\begin{aligned} U_g(x,y,p) &= \frac{D_{1000}}{2} x + \frac{B(p)}{f_0} \left[\frac{2\pi}{L} \right] \hat{T} \sin \frac{2\pi}{L} (y + \lambda) \\ V_g(x,y,p) &= -\frac{D_{1000}}{2} y \end{aligned} \quad (2.13)$$

where the subscript "g" means geostrophic.

$$\xi(x,y,p) = \frac{-B(p)}{f_0} \left[\frac{2\pi}{L} \right]^2 \hat{T} \cos \frac{2\pi}{L} (y + \lambda) \quad (2.14)$$

$$D(x,y,p) = D_{1000} \left[\sec \left(2\theta_d(x,y,p) \right) \right] \quad (2.15)$$

where $\theta_d(x, y, p) = \frac{1}{2} \tan^{-1} \left[-\xi(x, y, p)/D_{1000} \right]$. Because $\xi \sim D_{1000}$ in the upper portion of the troposphere, $\theta_d \sim 0$ only in the lower and middle portions of the troposphere. That is, the axis of dilatation is zonally oriented only in the lower and middle portions of the troposphere.

Substituting the solution $\omega = \hat{\omega}(p) \cos \frac{2\pi}{L}(y + \lambda)$ and the forcing function into (2.8) yields the following:

$$\left[\frac{f_0 \eta_0}{R T_0 \gamma_0 (2\pi/L)^2} \right] p^2 \frac{\partial^2 \hat{\omega}}{\partial p^2} - \hat{\omega}(p) = \left[\frac{D_{1000} \hat{T}}{\gamma_0 T_0} \right] A(p) \quad (2.16)$$

where $A(p) = p(1 - \alpha \ln \frac{1000}{p})$. Equation (2.16) was solved by using the method of variation of parameters to get the particular solution and a mathematical table (Rektorys, 1969) to get the homogenous solution.

The following simple boundary conditions

$$\hat{\omega}(0) = 0, \quad \hat{\omega}(1000) = 0 \quad (2.17)$$

were used to arrive at the final solution,

$$\omega(y, p) = -KP \cos \frac{2\pi}{L}(y + \lambda) \quad (2.18)$$

$$\text{where } K = \frac{D_{1000} \hat{T}}{\gamma_0 T_0}, \quad P = (\alpha k + 1) p \left[1 - \frac{p}{1000} \right]^{\hat{h}} - \alpha p \left[\ln \frac{1000}{p} \right],$$

$$k = \frac{f_0 \eta_0}{R T_0 \gamma_0 (2\pi/L)^2}, \quad \text{and } \hat{h} = \frac{1}{2} \left(1 + \frac{4}{k} \right)^{1/2} - \frac{1}{2}. \quad \text{The vertical motion}$$

field is thus proportional to the resultant deformation at the lower boundary, the meridional temperature gradient as represented by \hat{T} ; it is inversely proportional to the static stability.

Since a β -plane approximation for f was used, (2.18) is most accurate near ϕ_0 , slightly incorrect north of ϕ_0 , and more incorrect south of ϕ_0 , especially at very low latitudes.

The parameter α was chosen so that the model tropopause was at 150 mb ($\alpha = .527$). γ_0 was determined from average temperature soundings. \bar{T} , whose exact value is not crucial, was chosen to be 250° K. D_{1000} was a typical synoptic-scale value. L and \hat{T} were chosen so that the maximum temperature variation over a distance of $L/2$ is $2\hat{T}$.

Figure 2.2 qualitatively depicts the temperature and vertical-motion fields for $\lambda = 0$ and $L \approx 2000$ km, a warm core at y_0 ; and also for $\lambda = L/4$ and $L \approx 4000$ km, a reverse baroclinic zone at y_0 . The maximum vertical motions are found in the lower and middle portions of the troposphere because the tightening of the meridional temperature gradient by deformation is a maximum there. Because the vorticity in the warm core case is so strongly anticyclonic aloft, the absolute vorticity at low latitudes becomes negative. The model is therefore unable to simulate the low-latitude vertical motions in the upper half of the troposphere for the warm core case. This is due mainly to the low value of f_0 at low latitude and the β -plane approximation, and in part to the unrealistic variation of the horizontal temperature gradient with height.

For $\phi_0 = 10^\circ$ N, the latitude of the summer Atlantic ITCZ,

$$\left| \frac{\xi}{f_0} \right| < \frac{B(p)}{f_0^2} \left[\frac{2\pi}{L} \right]^2 \hat{T} \quad \text{from (2.14)}$$

Table 2.1 shows the maximum magnitude of ξ/f_0 at five pressure-levels for $L = 2000$ km and $\hat{T} = 0.5^\circ$ C, 1.0° C; and for $L = 4000$ km and $\hat{T} = 1^\circ$ C, 4° C. Unfortunately, at 10° N $\xi_{\max} \ll f_0$ for all x and y only at or below 850 mb. Above 850 mb $\xi_{\max} \sim f_0$, and therefore

quasigeostrophic theory is not appropriate for a quantitative diagnosis of the vertical motions. Therefore, the implied vertical motions at 850 mb and below will be regarded as quantitatively accurate, while the vertical motions above 850 mb will be regarded as only qualitatively accurate. (If the model had more accurately simulated the wind field, ξ would not be zero at low levels, and would be of order f_0 or greater at all levels; quasigeostrophic theory could therefore only qualitatively describe the vertical circulation at low levels. A model wind field with little or no relative vorticity at low levels was therefore indeed a good choice, since it yields a more quantitatively accurate low-level vertical motion field. Furthermore, there are sometimes cloud bands present in regions of small vorticity (see chapter 3).

The quasigeostrophic frontal mechanism will be regarded as significant if the analytical model, whose parameters had been chosen on the basis of observations, simulates rising motions strong enough to induce deep cumulus convection in a conditionally unstable atmosphere. It is not clear just how strong vertical motions should be, given an average vertical temperature and water vapor distribution. Over the South Florida peninsula on undisturbed summer days (i.e., when there is little synoptic-scale vertical motion), double sea-breeze convergence results in upward motion that triggers thunderstorm activity (Pielke, 1973). Since the sea-breeze is usually about 7.5 msec^{-1} , and since South Florida is about 150 km wide, the low-level (i.e., at 1 km) convergence $\frac{-\partial u}{\partial x}$ is about 10^{-4} sec^{-1} . Kinematically, upwards motions of about 10 cm sec^{-1}

occur. This may be considered an upper limit on what the minimum magnitude of vertical motion is needed to trigger deep convection for average conditions. To get an estimate of the minimum vertical velocities needed, neglect vertical mixing. Then ascent of 2 cm sec^{-1} for about one day raises air parcels about 1.5 km, the average distance in the tropics between the surface and the lifting-condensation level for air near the surface. The ascent may also result in deepening the low-level moist layer by at least 1.5 km. Thus, cumulus towers could grow taller. Therefore, in the absence of adequate theoretical guidance vertical motions of at least $1\text{-}10 \text{ cmsec}^{-1}$ will be considered significant.

For $\gamma_0 = 0.128$, $D_{1000} \sim 10^{-5} \text{ sec}^{-1}$, and $L = 2000 \text{ km}$, \hat{T} must be $\gtrsim 5^\circ\text{C}$, i.e., $\frac{\partial \bar{T}}{\partial y} \sim 10^\circ\text{C}/1000 \text{ km}$, (see table 2.1), in order that $w_{\max} \gtrsim 1 \text{ cmsec}^{-1}$. For $L = 4000 \text{ km}$, \hat{T} must be $\gtrsim 7.4^\circ\text{C}$, i.e., $\frac{\partial \bar{T}}{\partial y} \sim 7.4^\circ\text{C}/1000 \text{ km}$, in order that $w_{\max} \gtrsim 1 \text{ cmsec}^{-1}$. With some reservations, then, we find that the analytical model requires synoptic-scale horizontal (virtual) temperature gradients of at least $10^\circ\text{C}/1000 \text{ km}$ to initiate deep cumulus convection at 10° N latitude by the quasigeostrophic frontal mechanism.

Once deep cumulus activity has begun, latent heat release can significantly affect the synoptic-scale vertical motions. Since the quasigeostrophic ω -equation is linear, the qualitative effects of latent heat release can be ascertained by solving (2.8) with an additional heating term in the forcing function. The quasigeostrophic ω -equation with only the heating forcing is (Phillips, 1971)

$$\left(\nabla^2 + \frac{f_0 \eta_0}{\sigma} \frac{\partial^2}{\partial p^2}\right) \omega_L = -\frac{1}{\sigma} \nabla^2 H \quad (2.19)$$

where $H = \frac{R}{pC_p} \frac{dQ}{dt} = \frac{R}{p} Q_1$, Q is the heat energy added to system per unit mass, and Q_1 is the rate of temperature change for a given mass of air.

The heating function is most simply parameterized in terms of the vertical velocity (2.18), so that

$$Q_1 = Q^* \left(1 - \alpha \ln \frac{1000}{p}\right) \cos \frac{2\pi}{L} (y + \lambda) \quad (2.20)$$

where Q^* is the amplitude of the heating function in $^{\circ}\text{C sec}^{-1}$.

It is thereby assumed that ascending motion is associated with deep cumulus convection and latent heat release, whereas subsidence is associated with shallow convection and cooling. The most unrealistic feature of this model is that cooling, when it occurs, occurs throughout the troposphere, whereas studies of the effects of small-scale cumulus convection on the large-scale suggest that cooling takes place only in layers where there is evaporation of liquid water (Nitta and Esbensen, 1974). Also, the vertical variation of heating is unrealistic in that the maximum is at the ground, not in the middle portion of the troposphere as is observed. Finally, radiative effects are not included. However, much more mathematical complexity would be required to derive and use a more realistic heating function.

The additional solution due to latent release is

$$\omega_L = -\left[\frac{Q^*}{T_0 \gamma_0}\right] P \cos \frac{2\pi}{L} (y + \lambda) \quad (2.21)$$

where the subscript "L" indicates latent heat release. To estimate Q^* , assume that a net amount of one inch (~ 2.5 cm) of liquid water (Δq) is condensed in one day in a vertical column of air of 1 cm^2 cross-sectional area, which extends throughout the depth of the troposphere. This is a realistic daily precipitation total in a disturbed tropical area. Furthermore, assume that all of the latent heat release is absorbed uniformly in the column. Then the rate of temperature change of the column due to latent heat release alone is $\frac{L}{mC_p} \frac{\Delta q}{\Delta t}$ $= + 7.1^\circ\text{C day}^{-1}$, where Δq is 2.5×10^{-6} tons, Δt is 1 day, and m is 8.7×10^{-4} tons, the total mass of air in the column. This estimate agrees qualitatively with some diagnostic studies (Yanal *et al.*, 1973). So, if $Q^* = 7.1^\circ\text{C day}^{-1}$, the maximum value of w implied by (2.21) is $1.7 \text{ cm}\cdot\text{sec}^{-1}$. Therefore latent heat release can significantly increase the strength of vertical motions.

Since front-like structures have been produced in rotating tanks (Faller, 1956), latent heat release, not present in the tank, is probably of secondary concern in midlatitude fronts. Results from Williams's (1972) model with an Ekman boundary layer, moisture, and latent heat release parameterized by convective adjustment, suggest that frontal structure is intensified only aloft by deep cumulus convection (Cornelius, 1974). However, in the tropics where horizontal virtual temperature gradients are relatively weak, it is likely that latent heat release is ultimately the primary driver of vertical motions of front-like structures (Hoskins, 1972), and that thermodynamic forcing by temperature advection is not effective.

Low-level convergence (see (2.5)) further increases the low-level horizontal temperature gradient. This effect, (Eliassen, 1966) numerically simulated by Edelmann in 1963, may be responsible for the rapid formation of frontal zones. Results from more sophisticated models (Mudrick, 1973; Hoskins and Bretherton, 1972) have also suggested that the nonlinear effects of convergence induced by geostrophic deformation of the horizontal temperature field are responsible for rapid frontogenesis. Thus, geostrophic deformation can be regarded as initiating frontogenesis (Eliassen, 1959), whereas nongeostrophic effects are responsible for development of truly intense gradients.

3. CLIMATOLOGY OF DEFORMATION AND CLOUD BANDS OVER THE TROPICAL OCEANS

The relationship between climatological deformation (and vorticity, sea-surface temperature, and cross-equatorial flow) and bands of cloudiness is now discussed.

3.1 Data processing

Wind data were obtained from subjective gradient-level streamline analyses (Atkinson and Sadler, 1970) for the months of January, April, July, and October. The streamline analyses are based on data from USAF Environmental Technical Applications Center (ETAC), Environmental Data Service (EDS), and other more esoteric sources (Atkinson, 1970). Gradient level was assumed to be 3,000 ft, 1 km, or 900 mb, depending upon what units were used in the raw data source. Monthly resultant surface-wind summaries (based on ship reports and atoll-station observations) from Crutcher and Davis in Vol. VIII of the Marine Climatic Atlas of the World were used to estimate the resultant gradient-level winds over selected open oceanic areas. The turning with height of the surface wind was assumed to be 10 degrees, the surface wind speed was assumed to be about 75% of the gradient-level wind speed, and the wind speed at each atoll was assumed to be some function of the gradient-level wind speed. The function had been determined from recent data. The period of record was five to ten years for most observation stations, although a few stations had fewer than five years of data (Atkinson, 1975). Objective analyses of 850-mb rawinsonde data from seven years of observations (Newell et al.,

1972) were occasionally used for comparison. Although Newell's data coverage over the open ocean was nil, the plotted rawinsonde data at island sites, included with the analyses, were helpful.

The zonal and meridional wind components (within 25 degrees of latitude from the equator) for January, April, July, and October were estimated by linear interpolation of the analyses at staggered grid points, separated by 10 degrees of latitude and longitude. (Although it was easy to measure wind direction on smaller scales, it was difficult to estimate the wind speed on smaller scales.) Resultant deformation, orientation of axis of dilatation, and vorticity were computed in Cartesian coordinates. The former two quantities are represented (in Figs. 3.1a, 3.3a, 3.5a, 3.7a, 3.9a, 3.11a, 3.13a, and 3.15a) by tick marks: the length of each tick mark is proportional to the magnitude of the resultant deformation, and the orientation is that of the axis of dilatation. The tick marks are superposed on the streamline analyses. The sign of the vorticity is plotted in Figs. 3.1b, 3.3b, 3.5b, 3.7b, 3.9b, 3.11b, 3.13b, and 3.15b.

Monthly mean cloud-brightness charts from 1 January 1967 through 31 December 1970 (Miller and Feddes, 1971) were used to locate prominent bands of cloudiness. The charts for January, April, July, and October (at 1400-1600 local suntime) are shown in Figs. 3.2a, 3.4a, 3.6a, 3.8a, 3.10a, 3.12a, 3.14a, and 3.16a. The whitest areas are those with the most reflectance. The numbers on the gray scale represent the mean occurrence of cloudiness in octas. The resolution of the photographs is

40 km. The raw data, originally quantized into 64 brightness levels, were compressed into 16 brightness levels. The process of converting the brightness values to octas from a set of empirically derived weights is described by Miller and Feddes. There are many difficulties in normalizing the brightness levels of each satellite photograph (Hubert, 1975). Among other less serious problems discussed by Miller and Feddes is the failure of the satellite's camera system to "see" thin cirrus. (The objective cloud-brightness data were supplemented by mean cloud-cover charts from February, 1965 through January, 1968, based on operational nephanalyses (Sadler, 1970). In all, 7 years of cloud-brightness data were available.)

Regions of cloudiness were classified as banded or nonbanded on the basis of their dimensions: If the average length along the most elongated region was more than twice the average length across it, then the region was classified as a band. For the most part, regions of 4-5 octas or more of cloudiness had well-defined banded structures. Thus, cloudiness in the banded regions ranged from 50-65%.

Mean monthly sea-surface temperature charts (Newell et al, 1972), shown in Figs. 3.2b, 3.4b, 3.6b, 3.8b, 3.10b, 3.12b, 3.14b, and 3.16b, were used to identify regions of relatively warm and cool water.

3.2 Discussion of climatology

The features of the most prominent bands of cloudiness are now described.

The most spectacular band of cloudiness is located between 5 and 10° N latitude in the North Pacific Ocean, mostly in the eastern portion.

The band (of 4 or more octas) extends as far west as approximately 155° W longitude in January and in April; it extends farther west to 165° E longitude in July (when it is 11500 km long), and to 170–180° E longitude in October. In January, April, and October the westernmost areas of cloudiness of 6 octas coincide with the end of zonally acting nondivergent stretching deformation (and an end to cross-equatorial flow into the band). West of the band, the axis of dilatation is not zonally oriented, since there is a downstream decrease in wind speed (and, in January and April, some anticyclonic shear). In July, however, the region of zonally acting nondivergent stretching deformation (and the region of cross-equatorial flow into the band) ends at about 160° W longitude, whereas the band of cloudiness extends farther westward to 165° E longitude. (In January and April there is a fair correlation between vorticity and the cloudiness band. In July, however, the zonal band of cyclonic vorticity is broken at about 150–170° W longitude. In October the band of cyclonic vorticity extends across the entire Pacific Ocean, whereas the cloudiness band extends westward only to 170–180° E longitude. Thus, deformation is better correlated with the band of cloudiness than vorticity is. There is little correlation between relative sea-surface temperatures and the cloudiness band.)

A zonal band of cloudiness between 3 and 10° N latitude extends across the North Atlantic Ocean from about 45° W longitude to 15–20° W longitude in January, and to Africa in the other three months. It coincides with a region of zonally acting nondivergent stretching deformation (and cross-equatorial flow into the band). (A zonal to west-

southwest to east-northeast oriented band of cyclonic vorticity coincides with the cloudiness band. Therefore deformation and vorticity correlate equally well with the cloudiness band. The band coincides with a band of relative sea-surface temperature maximum in January, July, and October. In April, however, the band of sea-surface temperature maximum extends almost to 10° S latitude across the Atlantic, whereas there is no cloudiness band south of the equator.)

There is a north-northwest to south-southeast oriented band of cloudiness, most spectacular in October, in the South Pacific from about New Guinea east-southeastward into midlatitudes. The axis of dilatation of the wind field is also oriented northwest-southeast; deformation is due mainly to a downstream decrease in wind speed (i.e., the deformation is mostly divergent) although in October there is a zone of confluence south of 20° S latitude. There is a weak northwest-southeast oriented trough west of the cloudiness band. (Vorticity does not appear to be well-correlated with the cloudiness band. There is also little correlation between the sea-surface temperature and the position of the band.) Since in October the southern region of the band lies along a zone of confluence, which probably separates the poleward flow of warmer air from the equatorward flow of cooler air, frontogenesis may be the cause of the cloudiness. Furthermore, in October, the Southern Hemisphere spring, the troposphere is highly baroclinic, as evidenced by strong gradient-level to 200-mb shear (Atkinson, 1970) It is most interesting that the band extends from midlatitudes to within 5° of latitude from the equator; it therefore has both baroclinic and

barotropic sections.

In January there is a wide band of cloudiness oriented west-southwest to east-northeast between 5 and 10° S latitude from 50 to 90° E longitude. It lies along and slightly north of a zone of confluence. Deformation is due mainly to the divergent part of the wind. (There is anticyclonic vorticity along the band, and cross-equatorial flow into the band. Sea-surface temperatures are a maximum in the area of the band.)

Interpreting the climatological data is difficult for the following reasons: (1) Some cloudiness bands may actually represent the average of propagating cloud clusters. (2) Different bands or different sections of a given band may be produced by different mechanisms. (3) Since very few gradient-level wind observations are available over the tropical oceans, Atkinson and Sadler used a model to estimate them based on surface ship reports. Janota (1971) has found that at low latitudes the turning with height can be complex. Therefore, near the equator the actual amount of turning with height of the wind was probably different from that in the model. Then, the wind analyses of Atkinson and Sadler may be inaccurate over some low latitude oceanic areas. (4) The satellite brightness-photographs are subject to brightness normalization and to brightness-to-relative cloudiness conversion errors, and therefore the relative cloudiness cutoff level may actually vary from place to place and from month to month. Therefore the exact location of banded cloudiness maxima may be in some doubt because of quantization noise. A comparison of the two sources of satellite brightness data, however, shows fair qualitative

agreement.

3.3 Summary

The regions of zonally acting nondivergent stretching deformation (at the gradient-level) in the tropical North Pacific and tropical North Atlantic are locations of zonally oriented bands of relatively high cloudiness.

The northwest-southeast oriented band of cloudiness in the South Pacific, which may be the average cloudiness from midlatitude frontal bands which extend into the tropics, lies along the axis of dilatation of the wind field. Most of the deformation, however, is due to the divergent part of the wind. The west-southwest to east-northeast oriented band of cloudiness in the South Indian Ocean in January is also along the axis of dilatation of the wind field, and most of the deformation is due to the divergent part of the wind.

(Cross-equatorial flow into the band, vorticity, and sea-surface temperature are not as well-correlated with the bands of cloudiness as deformation is.)

The July climatology of the western area of the North Atlantic is examined in the next chapter.

4. CLOUD BANDS OF BOMEX PHASE IV

4.1 Discussion of data

BOMEX Phase IV (11-28 July 1969) was intended for the study of tropical convective systems (BOMAP, 1971) in the Western North Atlantic. The principal sources of data were five research vessels at which rawinsonde observations were made at intervals of three to six hours.

4.1.1 Fixed ship observations

Temperature and relative humidity were measured on the sondes by standard National Weather Service (NWS) thermistors and hygrometers, respectively. Two types of balloon-tracking systems were used to estimate the horizontal wind speed and direction. (Details on the procedures of raw data reduction are found in EDS 12 (CEDDA, 1975).) The data were available in the following three forms: teletype messages, microfilm, and digital magnetic tape.

The teletype messages were standard coded reports of wind speed and direction, temperature, and dewpoint depression at mandatory and significant levels (BOMAP, 1971) every three to six hours.

The microfilm data set consisted of sampled wind, temperature, and humidity data from NASA's Mississippi Test Facility (MTF) Signal Conditioning and Recording Device (SCARD) averaged over five-second intervals. These data are called the "A₀" intermediate data set.

Digital magnetic tapes were supplied by Tom Carpenter at the Center for Experiment Design and Data Analysis (CEDDA). The data on the tapes are the final processed product; all feasible corrections to known

errors were presumed to have been made.

In addition to commonly experienced calibration errors, instrumentation failure, thermistor thermal lag, hygistor humidity lag, and inaccuracy of the hygistor at relative humidities of less than 10% and at temperatures less than -40° C, there were the following problems, none of which were corrected in the teletype and "A₀" data sets (and some of which were not correct on tape, either):

- (1) diurnal relative humidity bias (Teweles, 1970) due to the reflection of solar radiation into the ventilation duct; empirical daylight corrections have been worked out by Ostapoff (Janota, 1971).
- (2) frequency doubling of the relative humidity signal sometimes, which resulted in relative humidities of 5-50% too low; corrective procedures were developed to solve most of these errors (Janota, 1971).
- (3) radiometersonde interference which resulted in some unusable temperature and relative humidity data on the Discoverer, Rainier, and Rockaway; these bad data points appeared as spikes and could be easily spotted (Janota, 1971).
- (4) missing data during the first thirty seconds of the balloon flight due to radar tracking problems, especially on the Rockaway; wind data were interpolated between the surface wind and the wind centered at one minute after launch (CEDDA, 1975).
- (5) sea anchor failure (BOMAP, 1971) early in BOMEX which resulted in wind measurements with ship-motion bias; although the

observers aboard the ships were supposed to have corrected the upper air wind measurements for ship motion before transmitting their teletype reports, adequate ship-motion data were not available for correction of the final processed data; the ship motion was assumed to have been small, anyway (Janota, 1971).

- (6) loss of 0 degree azimuth reference on the Rainier: true north was 220 degrees from 1200 GMT, Julian day 192, to 0600 GMT, Julian day 196; true north was 140 degrees from 0000 GMT, Julian day 198, to 2130 GMT, Julian day 209 (Williams, 1973); these corrections had to be made even on the final processed tapes.
- (7) scarcity of data above 400 mb; because balloon launches were so frequent (CEDDA, 1975), no time, supposedly, was available for processing data from higher levels.

In addition, the following special problems were encountered:

- (8) incorrect dates on Rainier microfilm and tape data, because balloon launches often began only minutes before the beginning of the following day; 7/n/69 0000 GMT was often recorded as 7/n-1/69 0000 GMT; this error could be easily found.
- (9) no teletype data were available from the Mt. Mitchell.
- (10) bad "A₀" and tape wind data from the Rockaway; Janota recommended using the teletype data only from the Rockaway because of serious analysis problems he had encountered.
- (11) tape format errors: most of the tapes had bad file marks; after a month of intensive debugging, Joe Bergstein and

Dick Steinberg of the M.I.T. Information Processing Center decided to give up, and simply copy the seven-track CDC 6600 tapes onto nine-track IBM 370 tapes, and put on new file marks; record number 904 of the Discoverer tape has a length of 410 bytes, not 1300 bytes as indicated on the tape; on the Oceanographer tape for Julian day 209, ID = 1, MHR = 0, NO = 595, MAX = 61, not 60 as specified on the tape (see the tape headers for a description of how to read the tapes).

The wind data set was a combination of teletype, microfilm, and tape data. Tape data were considered the best wind-data source; the microfilm data were used when tape data were unavailable; the teletype data were used when neither tape nor microfilm data were available. Exceptions to these guidelines were necessary at the Rockaway, where only teletype data were used.

The wind data, expressed as zonal and meridional components in meters per second, were extracted from the tapes from 1000-400 mb at 50-mb increments. Representative "A₀" wind data (i.e., data which were subjectively similar to data taken within 30 seconds of the time the balloon was at the specified pressure level) were extracted from the microfilm when needed. When wind data from the mandatory teletype levels (in wind direction and speed in knots converted to zonal and meridional components in meters per second) were needed, but were not available, data from significant ("winds aloft") levels were used if they were obtained within 25 mb of the specified mandatory pressure level. Data from the tapes and microfilm were cross-checked with the teletype

data whenever possible. If they compared poorly, the teletype data were used, since they were subject to less processing, and therefore should contain fewer handling errors; furthermore, the teletype data should have been corrected for ship motion by the observer.

In spite of all the precaution, some subjective pruning was necessary when absurd observational data were found. At some observation times teletype or microfilm data were available, whereas tape data were not. It is not known whether the tape data were missing by mistake or intentionally; the former was assumed. In addition, there were some times when the data inventory (BOMAP, 1971) indicates that data were available, although they were not found on teletype, microfilm, or tape.

Since the corrections needed for the raw relative humidity and temperature data were quite complicated, the temperature and derived water vapor mixing ratios were extracted at 50-mb increments from 1000 mb to 400 mb from the processed tapes only. CEDDA had corrected soundings which had doubtful superadiabatic lapse-rates. Since this data set was rather extensive, an exhaustive cross-check with the teletype and microfilm data was not deemed worthwhile. Random spot checks, however, indicated that the temperature and relative humidity data on tape had been corrected for problems 1-3.

Data from the ships' boom (at about ten meters above the sea surface) were recorded on microfilm by SCARD at thirty-second intervals on all five ships. Details about the instrumentation and corrections needed are given in EDS-12. Although five and ten-minute averages were available, they were not used because they were sometimes computed

through spikes, thereby producing some unrepresentative averages. Instead, representative data, subject to judicious pruning, were extracted at three-hourly intervals.

Air temperature (T), air wet-bulb temperature (T_w), and sea-surface temperature (T_o) in degrees Celsius, wind speed relative to ship motion (V) in meters per second, relative humidity (RH) in percent, and atmospheric pressure (p) in millibars were independently measured. The RH, p , and T observations were used to compute the water vapor mixing ratio (q) as described (Phillips, 1970) in Appendix B.

The T measurements were assumed to have no unusual errors, since EDS-12 mentions no special problems. The T_w and RH sensors, however, suffered problems, some correctable, others not; e.g., T_w measurements from intervals over which the wick had dried out were erroneous. T_o readings recorded by the boom were compared with manual Nansen bottle measurements: Since the two sensors were mounted on different platforms and may have been submerged at different depths, significant differences were found. The extent to which the measurements were representative of the sea surface is not known. The wind speed was not corrected for ship motion. It is assumed (as before) that the ships' motion was too small to significantly affect the surface wind data. A good correlation was found on all ships between the surface wind speed recorded on the boom and that recorded by the surface synoptic observer. Many problems were encountered with the p measurements; their corrections are given in EDS-12.

The following remarks reflect problems experienced on specific ships:

- (1) The pressures recorded on the Discoverer were too high. A comparison of the pressures with those from the surface synoptic observations and with those of other ships, suggested that they were probably 5-6 mb too high.
- (2) The wind data from the Rockaway were recorded in knots and had to be converted into meters per second (BOMAP, 1971).
- (3) The Rockaway's relative-humidity sensor seems to have stopped functioning after Julian day 199. Wet-bulb and dry-bulb temperatures were then used to compute the relative humidity, via the method described in Appendix C. When the wet-bulb temperatures were recorded as being greater than the dry air temperature data, the relative humidity was not computed. Since this occasionally happened, the accuracy of other wet-bulb temperature data which were physically possible is somewhat suspect.

Ship surface synoptic data were available as teletype messages (BOMAP, 1971) in the standard synoptic code at six-hourly intervals. They were assumed to be of varying quality (CEDDA, 1975) and no corrections were made, even though CEDDA had found some discrepancies. Sea-surface temperature measurements made manually from bucket samples were available at two-hourly intervals on teletype messages (BOMAP, 1971).

A digital magnetic tape of "BOMEX marine meteorological observations and surface pressure" contained detailed surface synoptic

observations at 3-6 hourly intervals. Precipitation data were also available; precipitation amounts in millimeters were recorded along with the times of the precipitation events, trace quantities of precipitation having been recorded as 1 mm. Problems were encountered with data from the Rockaway, where precipitation events but not amounts were recorded. The Oceanographer's data were similar to Rockaway's data, except that sometimes precipitation amounts were recorded.

4.1.2 Land observations

Caribbean island rawinsonde data were obtained on microfilm from NHDT. It was assumed that no corrections were needed. Wind data (speed and direction) only were extracted at 50-mb increments from 1000 mb to 400 mb. Most islands made soundings both at 0000 GMT and 1200 GMT, although a few took only 1200 GMT soundings. The wind data were converted into zonal and meridional components. In addition, teletype messages of rawinsonde data (wind speed and direction) for Kourou, French Guiana were obtained from ETAC for some days at 0000 GMT and 1200 GMT. Rawinsonde data were also available from Barbados at an Air Force Air Weather Service (AWS) station near BOMEX Field Headquarters for 0600 GMT, 1800 GMT, and sometimes for 1500 GMT and 2100 GMT; these data supplemented the 0000 GMT and 1200 GMT data from soundings taken at Seawall Airport. Unfortunately, the AWS wind data correlated miserably with the Seawall data and other adjacent island data because the compass headings of the radar were misoriented (Rasmussen, G., 1974). Since no corrections or documentation of the error were available, these data were disregarded.

The complete wind data set for BOMEX Phase IV were punched on cards according to the format described in Appendix D. The nine island stations along with the five ships used are listed in Table 4.1. The locations of all stations are shown in Fig. 4.1.

4.1.3 Satellite observations

Photographs in the visible part of the spectrum were taken of the BOMEX area during the daylight hours by the spin-scan cloud camera aboard the ATS-III geosynchronous satellite, which was stationed 35,800 km above the earth at 46° W longitude, 10° N latitude. Although global pictures were available about every 25 minutes, only selected gridded regional images were used (BOMAP, 1971). Usually a local morning, noon, and late afternoon picture were available. The resolution was 2.5 miles at the sub-satellite point and less elsewhere. Gridding procedures are described in the BOMEX Atlas of Satellite Cloud Photographs (BOMAP, 1971).

The ATS-III photographs were used only for nephanalyses. Brightness normalization problems made distinguishing among low, middle, and high clouds difficult. Pinpointing regions of very active convection was difficult, since bright areas might not always be indicative of deep cumulus convection; viz., bright cloud cover is probably a necessary but not sufficient sign of deep cumulus convection.

Photographs from the ESSA-9 operational polar-orbiting satellites supplemented the ATS-III photographs; they were available for the BOMEX region once a day (during the local early afternoon). The resolution of these photographs was one mile at nadir. The images were pieced together

into hemispheric pictures and displayed in a catalog (NOAA, 1971). Some of the original negatives were available on microfilm for the period 16-31 July 1969; prints for selected days were made on a microfilm printer, and were used only for nephanalyses.

Crude infrared (IR) photographs were taken by the experimental polar-orbiting Nimbus-III satellite near local midnight. Images were obtained in five spectral regions. Those from the 6.5-7.0 μ band and the 20-23 μ band provided information about the water-vapor distributions in the upper and lower regions of the troposphere. Unfortunately, visible clouds, when present, dominated the image. The IR data, being small strips of photographs (Allied Research Associates, 1969), were used infrequently.

4.1.4 Aircraft observations

Airborne wind, temperature, and relative-humidity data were available on some days at certain levels. The Research Flight Facility (RFF) of NOAA operated three planes, each of which used Doppler radar navigation to estimate the wind. The Woods Hole Oceanographic Institute (WHOI) also operated an aircraft which had a Doppler radar. The RFF and WHOI data were extensively processed and amenable to analysis. Other aircraft data (from the Navy, Air Force, and NASA), which required further processing (Janota, 1971), were not used.

The APN-82 Doppler systems were considered the primary source of wind data on the RFF "A" and "B" planes, because their data had less noise in them and correlated better with nearby fixed-ship data than did

the data from the APN-153 (Janota, 1971). The APN-82 system was intended to be the major instrument, although the APN-153 was supposed to have better response below 1000 feet (CEDDA, 1975). The RFF "E" plane used only the APN-153 system. Processing of the RFF data is fully described in EDS-12.

Data from computer printouts were first subjectively pruned. The RFF wind data, in the form of zonal and meridional wind components, were averaged over a minute (i.e., 7 measurements 10 seconds apart). The WHOI one-minute raw data were noisier than the RFF one-minute averaged data; the WHOI data were therefore averaged over three one-minute intervals. Since there were differences in the characteristics of the wind measuring devices, no attempt was made to compare them rigorously.

4.2 Objective analysis of the wind field

Estimates of the zonal and meridional wind components at all points of a Cartesian grid were needed so that finite-difference approximations of deformation, vorticity, and divergence could be easily computed by machine. The estimates were to be based on irregularly spaced data via an interpolating function. Since there were few BOMEX data at each observation time, it was necessary also to use asynchronous data.

Curve-fitting is a simple objective-analysis procedure. The polynomial curve-fitting (Panofsky and Brier, 1958) technique using the least-square error criterion is not suitable for BOMEX data, since

instabilities tend to develop over areas with scant data (Cressman, 1957). Cubic spline interpolating functions have been used for analysis of a BOMEX Phase IV case (Smith et al, 1975). Since the spline function passes through each data point, however, data which are many standard deviations away from the mean are weighted as much as data which are close to the mean. Spline interpolation is therefore also not suitable.

The application of corrections to a first-guess field, using a somewhat arbitrary spatial weighting function (Cressman, 1959) is another analysis method. This method, in a slightly modified form, has been used for analysis in the tropics (Yanai, 1964); it makes no use of the statistical properties of the data in determining the weighting function, and the analysis is somewhat dependent on the first-guess field.

The variational analysis method (Sasaki, 1970) was developed to make the analysis consistent with the dynamical conditions implied in numerical models; it therefore requires a knowledge of dynamical constraints. Some subjectivity is added to the analysis, since only certain types of motions are allowed. Worst of all, the technique is very complicated.

4.2.1 The objective analysis method

The technique used for analysis of the BOMEX data is based on those of Gandin (1963) and Eddy (1967). It is one in which the statistics of the data themselves prescribe the interpolating function. The predictand (\hat{y}), the analysis value at a grid point, is based on the predictors, the data $\{x\}$ (where $\{ \}$ denotes "the set of").

Since the conditional probability density function of y given x ($f(y|x)$) was unknown, $\hat{y} \approx E[f(y|x)]$ (where $E[A] = \frac{1}{n} \sum_{i=1}^n A_i$, the "expected value of A ", and n is the number of A_i 's being averaged), the predictand, was expressed as a linear function of the predictors.

$$\hat{y} = \sum_{i=1}^n a_i x_i + b \quad (4.1)$$

where $\{a\}$ are the regression coefficients, and n is the number of data. This estimation method is called multiple linear regression. It is linear because the a_i 's are linear, and was chosen because it is simple yet not totally arbitrary. If \hat{y} is the estimate of the eddy value of y , the deviation of y from $E[y]$, then $b = 0$. (It will be assumed hereafter that \hat{y} is the predictand eddy value, y is the actual eddy value, and x is the predictor eddy value.)

The loss function $L(\hat{y}, y)$ is an expression for the weight of seriousness of incorrectly estimating y : if \hat{y} is equal to y then $L(\hat{y}, y)$ should be zero; if $|y - \hat{y}|$ is large, then $L(\hat{y}, y)$ should be large. The mean squared error (MSE) (or quadratic loss) was convenient to use and had the properties just mentioned (Hoel, et al, 1971).

$$L(\hat{y}, y)_{\text{MSE}} = E[(\hat{y} - y)^2] \quad (4.2)$$

substituting (4.1) (with $b = 0$) into (4.2), the loss function is expressed as follows:

$$L(\hat{y}, y)_{\text{MSE}} = E[y^2] - 2 \sum_{i=1}^n a_i E[y x_i] + \sum_{i=1}^n \sum_{j=1}^n a_i a_j E[x_i x_j] \quad (4.3)$$

A minimum in $L(\hat{y}, y)_{\text{MSE}}$ (obtained by differentiating $L(\hat{y}, y)_{\text{MSE}}$ with respect to a_i and then setting the expression to zero) requires the following n equations in n unknowns, the normal equations, to be satisfied:

$$\sum_{j=1}^n a_j E[x_i x_j] = E[y x_i] \quad (4.4)$$

These simultaneous linear equations of a_j can be solved if the determinant of the matrix $E[x_i x_j]$ is nonzero. In order that the loss function is a minimum, $E[x_i x_j]$ must be positive, i.e., all the eddy data must be positively correlated with each other. (When the loss function is quadratic, the linear regression technique is also called mean-square estimation or optimum interpolation.)

Once $\{a\}$ has been determined, the MSE according to (4.3) is as follows:

$$L(\hat{y}, y)_{\text{MSE}} = E[y^2] (1 - Q) \quad (4.5)$$

where $Q = \frac{\sum_{i=1}^n a_i E[y x_i]}{E[y^2]}$. The quantity $L(\hat{y}, y)_{\text{MSE}}$ is also called the error, noise, or unexplained variance, and Q is sometimes called the reduction in variance, where $0 \leq Q \leq 1$. The reduction in variance, Q , is also equivalent to ρ_{yx_i} , the covariance coefficient of y with x_i . Since $E[yx_i]$ was not known, some further assumptions had to be made in order that (4.4) could be solved.

Gandin (1963) suggested two hypotheses which make the computation of $E[yx_i]$ possible, and simplify the computation of both $E[yx_i]$ and

$E[x_i x_j]$:

- (1) The fields of $\{x\}$ and $\{y\}$ are isotropic; therefore $E[x_i x_j]$ is a function only of the separation (or lag) distance (r) between the observation stations at points i and j .
- (2) The fields of $\{x\}$ and $\{y\}$ are homogeneous; i.e., the statistics of $\{x\}$ are the same everywhere, and are equivalent to those of $\{y\}$.

So if r is the same distance from the analysis point y to point j , as from i to j , $E[x_i x_j] = E[yx_j]$; the r at which $E[x_i x_j]$ (and $E[yx_j]$) first go to zero is called the influence radius, since only data that lie within the influence radius are used as predictors. Thus, the coefficients of the normal equations are functions of the cross-products of data from all pairs of observation stations. Gandin's hypotheses were assumed to be valid and are discussed in detail later.

The covariance function ($m(r) = E[x_i x_j] = E[yx_j]$) was computed as Eddy (1967) has done in the midlatitudes and Sanders et al (1975) have done in the tropics and the subtropics. Since the procedure followed was actually slightly different from Eddy's, it is now briefly described.

The zonal and meridional wind components were treated separately, as Eddy had. After their respective means had been subtracted, the remaining eddy components were used to compute cross-products between

all pairs of data points. (Eddy also subtracted the latitudinal trends; it was not necessary to do this in this study, for the observational network spanned a small area.) The cross-products were stratified according to the separation distance of the observation points, as Eddy had. The sum of the products within each group were then divided by the number of products within each group. The raw covariance function ($\hat{m}(r)$) was completed at r 's smaller than the distance between the closest pair of stations by fitting a parabola having a maximum at the origin (to insure that $\hat{m}(r)$ is a smooth, even function) to $\hat{m}(r)$ at small lag. The values of the parabola at $r=0$ and at nearby r 's at which more than ten pairs of points had been used to compute $\hat{m}(r)$, were used for $\hat{m}(r)$. Although a cutoff of ten pairs of points is somewhat arbitrary, the smoothing process about to be discussed should render this procedure relatively unimportant. Eddy, also, considered ten cross-products to be an adequate sample. Linear interpolation and extrapolation were used elsewhere, where fewer than ten pairs of points had been used to compute $\hat{m}(r)$.

The function $\hat{m}(r)$ was usually noisy because of sampling error. Some smoothing was therefore necessary to minimize the possibility of instabilities in the regression process. The following was subjectively chosen to be the necessary condition for smoothness: $\hat{m}(r)$ must be a monotonic function of lag in the region adjacent to the origin and within the influence radius. Since $\hat{m}(r)$ was truncated at some lag, a hanning filter (synthesized through trial and error by Julius von Hann,

an Austrian meteorologist) was applied to $\hat{m}(r)$ in order to smooth and concentrate the side lobes of the spectrum of $\hat{m}(r)$ (Blackman and Tukey, 1958); see Appendix E). The discrete Fourier transform of $\hat{m}(r)$, the power density spectrum, was then computed (Appendix F), and a uniform low-pass filter was applied in order to remove some of the high frequency noise. A 720 km horizontal-wavelength cutoff was large enough so that in most cases $\hat{m}(r)$ had been smoothed satisfactorily. This filtering process differed from Eddy's process, in which the data were used to specify the cutoff wavelength (Eddy assumed that the fraction of the variance which is noise, $E[(y-\bar{y})^2]/E[y^2]$, was at worst spread out uniformly over all wavelengths; the cutoff wavelength was the one up to which the ratio of the integrated power spectrum to the total variance was equal to $m(0)/E[x^2]$). The discrete inverse Fourier transform was then taken of the power spectrum (Appendix G) to obtain the smoothed covariance function ($m(r)$).

If the ratio of the smoothed covariance function at $r=0$ to the total variance, the autocovariance coefficient, $(m(0)/E[x^2])$ was less than 0.2, the data were considered too noisy to analyze, and climatology was considered the best analysis. Because of the Schwarz inequality (Hoel et al, 1971), the magnitude of the autocovariance coefficient was forced to be less than unity by keeping $m(0)$ sufficiently small.

The regression coefficients at each grid point were calculated by solving the normal equations with data points only within the influence radius. The coefficients of the normal equations were obtained by

linearly interpolating $m(r)$ at the required r 's. The nearest data point to each analysis point was used as the first predictor and the estimated error variance was computed. More data points were added until the error-variance estimate converged to within 1% of the preceding error-variance estimate. If the error variance became negative, the regression process was terminated. This happened in a few rare instances, when the error variance was near zero and truncation errors were relatively large. A maximum of nine predictors were used in the screening process, because the machine time needed for solving systems of more than nine equations was too high. Fewer than nine were necessary most of the time, anyway.

At each grid point $E[x]$ was added to \hat{y} to obtain the final predictand, and $E[(\hat{y} - y)^2]$ was computed from the regression coefficients. If there were no data points within the influence radius, the predictand was set to $E[x]$.

If \hat{y} is normally distributed about y , then \hat{y} is known to within approximately two standard deviations of y with 95% confidence. The error-variance estimates, however, are somewhat dependent upon Gandin's isotropy and homogeneity assumptions, since they are computed from the regression coefficients. The accuracy of the error-variance estimate could have been quantitatively determined in the following way: Each synchronous data point could be considered a predictand, and the regression process could be carried out using the remaining synchronous data points as predictors. The error variance of the predictand is now known exactly, since both the estimate and the real data are known.

Since this procedure was not thought of early enough, and since the programming complexity involved in making such a calculation was extraordinary, it was not carried out.

The objective analysis method of Gandin and Eddy, therefore, has the following virtues:

- (1) The interpolating function is dependent upon the statistics of the data.
- (2) Estimates of the accuracy of the analysis are also obtained.
- (3) Data which are many standard deviations from the mean are weighted less than data which are near the mean.
- (4) Some predictands may be greater than or less than all their predictors. (Eddy demonstrated that a ridge in the pressure field can be analyzed even if the surrounding pressure data have relatively low values), because the sum of the regression coefficients can be greater than one.

This objective analysis scheme also has some weaknesses. The isotropy hypothesis is invalid for linearly symmetric data fields, i.e., when the covariance function is not symmetric with respect to rotation. The lines of constant $E[x_i x_j]$ (as a function of direction) for anisotropic data are elliptical rather than circular. If the ratio of the length of the major axis to the length of the minor axis and the orientations of the axes are known, then a simple coordinate transformation will make the data appear isotropic. Unfortunately, not enough data were available to do this properly. Furthermore, the type and degree of anisotropy of the field might vary from analysis to analysis (and from

place to place) and computations could be very time-consuming.

Although Gandin's homogeneity hypothesis is probably valid over the BOMEX domain because the domain is small, the statistics of the data in the regions equatorward and poleward of the ITCZ might be different from the statistics of data from ITCZ region itself. Not enough data were available, though, to gather separate statistics for each region.

The procedure for obtaining $\hat{m}(r)$ required some arbitrary operations. For example, $\hat{m}(r)$ was estimated at increments of 50 km lag so that it would have the highest resolution possible under the constraint that at least ten pairs of data points were needed for $\hat{m}(r)$ at most r 's. The maximum lag number (i.e., the maximum lag divided by the lag increment) should be less than 10% of the sample size (Bendat and Piersol, 1966) in order to avoid instabilities that could occur because the number of cross-products used to estimate $\hat{m}(r)$ was nonuniform. The maximum lag for the data was chosen to be 3600 km on the basis of size of the data domain. Although the maximum lag number (72) was actually close to the sample size, the maximum lag number after $m(r)$ had been filtered was effectively smaller, and instabilities rarely occurred.

The arbitrary smoothing and parabola-fitting procedures were necessary because the sample size was small and because the smallest distance between pairs of observations was about 300 km. The final analysis was probably not very sensitive to these operations. They affected $\hat{m}(r)$ most for $r \sim 0$ and $r \gg 0$, where the number of cross-products were small. When values of $m(r)$ at $r \sim 0$ are required for the

regression process, the predictand is most likely embedded in predictors, and the regression process itself is probably not as important as are the predictors; when values of $m(r)$ at $r \gg 0$ are required for the regression process, the predictors may be beyond the influence radius, and are therefore not used.

During the regression procedure the values of some predictands suddenly changed significantly when they weren't converging rapidly enough. No attempt was made to remedy this, because it did not affect the analyses much. In regions of few data, e.g., near the borders of the analysis grid, the regression process on rare occasions became unstable, because the regression coefficients were large. For this reason, all the objective analyses were subjectively inspected. When instabilities were found, former iterations in the regression process were screened for stable predictand values. If no stable value had ever been attained, the predictand was set to zero, and the analysis was given the value $E[x]$; otherwise, a stable value was used.

Because an insufficient number of synchronous data were available, asynchronous data were also incorporated into the objective analysis. This was accomplished by extending Gandin's hypotheses to three-dimensional (x,y,t') -space, where t' is a scaled time-coordinate; viz., the $\{x\}$ and $\{y\}$ were assumed to be homogeneous and isotropic with respect to horizontal space and to time. (Homogeneous temporal statistics are the same as stationary statistics.) Over small time spans the statistics of large-scale meteorological variables are stationary. Since wind observations more than six hours from analysis time

were almost never needed, the time spanned by the data was at most twelve-hours, probably a small enough time interval for stationarity to be valid. If the data are isotropic in both horizontal space, and in time, the shapes of the covariance functions in space and time should be the same. If the scaled time coordinate is expressed as

$$t' = T t \quad (4.6)$$

where T is the scale factor in units of velocity, then T can be estimated by r_{inf}/t_{inf} , where r_{inf} is the influence radius of the spatial covariance function, and t_{inf} is the time of first the zero of the temporal covariance function. Since the shapes of spatial and temporal covariance functions from wind data were qualitatively similar, the isotropy hypothesis was accepted.

There is evidence from cloud-cluster motions and from spectral analyses of wind data (Wallace, 1971) that propagating disturbances are common in the tropical troposphere. Disturbances, then, can be crudely represented for brief time-intervals as statistically stationary events having constant phase speeds. The time-compositing analysis technique (Fig. 4.2), which is based on this model, has been successfully applied to subjective analyses in the tropics when the synchronous data supply was inadequate (Leary, 1972; Janota, 1971; Zipser, 1969). If a composited asynchronous data point is adjacent to a synchronous data point, the synchronous data point is given more weight, unless it is many standard deviations from the mean.

The time-compositing and multiple linear-regression procedures, subject to Gandin's hypotheses in (x,y,t') -space, were therefore combined so that asynchronous data could be objectively weighted along with the synchronous data. This new technique is illustrated in Fig. 4.3. The function $m(r)$ was computed from cross-products of data in (x,y,t') -space, the separation distance (r) between pairs of points at (x_1, y_1, t_1') and (x_2, y_2, t_2') being

$$r = \left[(x_2 - x_1)^2 + (y_2 - y_1)^2 + (t_2' - t_1')^2 \right]^{1/2} \quad (4.7)$$

The phase speed of disturbances in the wind field were estimated from spectral analysis and by inspection of satellite-observed cloud clusters. It was assumed that the time series of wind were stationary. Cross-spectral analysis of the component of the wind normal to the direction of propagation, from pairs of time series at observation stations that are situated along the direction of propagation, is the more rigorous method, since the measurements are based on the wind field itself. Phase speeds of waves whose periods are on the synoptic time-scale are estimated from the curve which fits the phase difference between versus the separation distance of pairs of observing stations. This method has been used by others (Wallace, 1971).

Since the wind data were very noisy, they were vertically averaged (from three data separated by 50 mb). The $m(r)$'s that had been estimated from unaveraged data had influence radii on the order of only a few grid spacings. (Vertical averaging was used, rather than resorting to (x,y,z,t') -space, because not enough data were available to compute a

covariance function in z .) The following 150-mb layer-averaged zonal and meridional wind components were computed:

- (1) the 950-mb average, representing the boundary layer
- (2) the 850-mb average representing the gradient level
- (3) the 700-mb average representing the wind at the level of large wave amplitude (Burpee, 1971)
- (4) the 450-mb average representing the wind at the highest level for which data were available.

When data from one or two of the levels which were part of a layer average was missing, the average of the two data points was used, or one was used, respectively. Surface wind observations alone were not used because they could have biased the analysis, since there is, on the average, a directional and speed shear between the surface winds and the 950-mb winds (Janota, 1971).

The propagation of disturbances was assumed to be zonal on the average. Therefore time series of the meridional component of the wind were compiled at the four levels, the time interval between observations ranging from 3 to 24 hours. The autocovariance function $(R(t))$ (Bendat and Piersol, 1966) was estimated in the same way that $m(r)$ was.

$$\hat{R}(r, \Delta t) = \frac{1}{N-r} \sum_{n=1}^{N-r} x_n x_{n+r} \quad (4.8)$$

where Δt is the lag interval, N is the number of observations in the time series $\{x\}$, r is the lag number ($r=0,1,2,\dots,m$), m is the maximum lag number and x_n is the value of the eddy data on the n 'th

observation of the time series. More than 30 observations were available for stations other than 78861, 78866, 81403, and the Rockaway (at 950 mb only); m was chosen to be 5 so that it would be much less than N , as suggested by Bendat and Piersol; Δt was chosen to be 12 hours, the maximum time interval between observations (most of the time). The cross-covariance function $R_{xy}(t)$ (Bendat and Piersol, 1966) was estimated in the same way, except that a parabola was not fit to the curve near zero lag.

$$\hat{R}_{xy}(r \Delta t) = \frac{1}{N-r} \sum_{n=1}^{N-r} x_n y_{n+r} \quad (4.9)$$

for

$r = -m, -m+1, \dots, 0, 1, \dots, m-1, m$, where Δt , N , r , and m have the same meanings as in (4.8), and x_n , y_n are values of eddy data at the n 'th observation of the $\{x\}$ and $\{y\}$ time series, respectively.

The power spectral density function ($S(f)$, where f is frequency) of each time series was estimated by computing the discrete Fourier transform of $R(r \Delta t)$ according to the formula in Appendix F. The cross-spectral density function for the time-series $\{x\}$ and $\{y\}$, ($S_{xy}(f)$) was estimated by computing the discrete Fourier transform of $R_{xy}(r \Delta t)$ (Appendix H). Unlike $S(f)$, $S_{xy}(f)$ is usually complex, because $R_{xy}(r \Delta t)$ is not usually even like $R(r \Delta t)$. $\text{Re}[S_{xy}(f)] = C_{xy}(f)$, the cospectrum; $-\text{Im}[S_{xy}(f)] = Z_{xy}(f)$, the quadrature; $\theta_{xy}(f) = \tan^{-1}[Q_{xy}(f)/C_{xy}(f)]$, the phase angle of $\{y\}$ relative to $\{x\}$. Coherence, the analogue to the correlation coefficient, is defined as follows:

$$CH(f) = [S_{xy}^2(f)/(S_x(f) S_y(f))]^{1/2} \quad (4.10)$$

Goodman has demonstrated that if the probability of finding a $CH^2(f)$ equal to or greater than β when $CH^2(f)$ is really zero (Panofsky and Brier, 1958), is p , then

$$\beta = 1 - p^{1/(df - 1)^{1/2}} \quad (4.11)$$

where df is the number of degrees of freedom, $\frac{2N - m/2}{m}$.

There has recently been some disagreement about how to interpret β and df (Yanai, 1975; Julian; 1975). In addition, the time series were of neither uniform length (N) nor density. Therefore, the significance of the coherence of pairs of time series could not be rigorously tested.

Figs. 4.4 - 4.7 show the phase differences ($\Delta\theta$) of the time series of the meridional wind component between nine pairs of observation stations as a function of longitudinal separation ($\Delta\lambda$) at 950, 850, 700, and 450 mb for the 2.5 to 5 day period. The coherence-squared is also plotted. For $p = .05$, $m = 5$, and $N = 32$ (16 days at 2 day^{-1}), $\beta = 0.48$. Therefore, only some of the coherences were significant according to Goodman's criterion. Each pair of stations were within 1.5° of latitude of each other. A line, subjectively fit to the data, was extrapolated to 180° phase difference, and the estimated horizontal half-wavelength of 2.5 - 5 day (average period of $3 \frac{1}{3}$ days) waves was the longitudinal separation at 180° phase difference ($\Delta\lambda_{180}$). The zonal phase speed measured toward the west (C) ($2 \Delta\lambda_{180} / 3 \frac{1}{3} \text{ days}$) was 12.8 m sec^{-1} at 950, 850, and 700 mb; at 450 mb it was a little faster.

If satellite-observed cloud clusters are associated with disturbances in the wind field, then estimates of cloud-cluster motion should be reasonable estimates of disturbance motion. Measurements of westward cloud-cluster motion ranged from 2 - 15 m sec⁻¹; the average was 6 - 7 m sec⁻¹, substantially below the estimate based on spectral analysis.

Several reasons are possible for this apparent contradiction.

- (1) Disturbance activity was intermittent (Burpee, 1971).
- (2) There were nontilted disturbances that propagated in a nonzonal direction.
- (3) Disturbances in the wind field moved faster than cloud clusters.

The scale factor (T) was estimated (Table 4.2) to be 25 km hr⁻¹ (about 7 m sec⁻¹), based on the influence radii of the $m(r)$'s for the zonal and meridional wind components at 950, 850, 700, and 450 mb on 25 July 1969 at 1200GMT, a time when all fixed rawinsonde observing stations had reported. The $R(r \Delta t)$'s (of the meridional wind component) went to zero on the average at about one day. The zonal wind component was assumed to have behaved similarly.

If there were waves of only one wavelength and frequency, then $C = \text{wavelength/frequency} = 2r_{\text{inf}}/2t_{\text{inf}} = T \sim 7 \text{ m sec}^{-1}$. The spectral analyses were therefore weighted lightly, and a zonal phase speed of 8 m sec⁻¹ was used.

The entire objective-analysis routine was programmed in FORTRAN IV and was run on the M.I.T. Information Processing Center's IBM 370

computer. The grid (Fig. 4.1) was converted from spherical coordinates to Cartesian coordinates, and then was transformed back to polar coordinates after the data had been analyzed. The analysis grid extended from 50 - 65° W longitude and from 5 - 20° N latitude. Grid spacing was 1 degree between the adjoining 256 (16 × 16) grid points. An ultra-high precision method was required to solve the normal equations when they were of order 7 or greater, especially when the coefficients of the equations were similar (i.e., when the coefficient matrix was nearly singular). The standard IBM Scientific Subroutine Package routines SIMQ and DSIMQ were discovered to be inadequate. The double precision versions of the routines DMFG and DMRG from IBM's SLMATH subroutine library, which used iterative refinement and other advanced matrix inversion techniques to solve systems of simultaneous linear equations, were able to solve the higher-order normal equations, and even gave a measure of the accuracy of their solutions. The subroutine TRESRT from the MATHLIB subroutine library was slightly modified to sort efficiently the predictors used in the regression process in ascending order of distance from the predictand. No other exotic algorithms were used. Because the discrete Fourier transform and inverse transform operations were computed only on relatively short sets of data, the fast Fourier transform algorithm was not needed.

The computer program was compiled in FORTRAN H so execution time would be low (and compilation time was high), and was stored on disc as a load module. The analysis routine was run quickly and efficiently, the average computing time for analysis of both wind components being only

about thirty seconds, at least half of which was for the regression process. At least half the cost of objective analysis was for printing. Therefore different regression coefficients were computed for each station for each analysis because the process was relatively inexpensive. Furthermore, it was desirable to isolate the statistics of each analysis from each other as much as possible, so that statistical tests could be performed on a sample of analyses. The stationarity hypothesis was therefore assumed to be true for periods of only a day (Sanders had assumed stationarity when he used the same regression coefficients for all SANBAR analyses (Sanders, et al, 1975). Also, days of inadequate data could be objectively pruned.

The covariance function $m(r)$ for each analysis was based upon observations made within twelve hours of analysis time (Fig. 4.8). Thus, the $m(r)$'s for analyses more than one day apart were independent. Fixed rawinsonde stations provided 70-100 raw data points for each analysis.

The addition of aircraft data sometimes drastically changed $m(r)$ and resulted in some numerical problems, probably because the statistics of the aircraft data were much different from those of the rawinsonde data. It had been hoped that the $m(r)$ measurements (based on aircraft data) at $r \sim 0$ would confirm the values inferred from the rawinsondes. Sampling aircraft data at high rate caused $m(r)$ at $r \sim 0$ to be over-weighted by the aircraft data which had measured small-scale motions, whereas sampling at a low rate resulted in only a few new pieces of data on the large scale. In addition, much of the rawinsonde data were vertically averaged, whereas none of the aircraft

data were, so the aircraft data were probably relatively noisy. Since the number of rawinsonde data was usually at least marginally sufficient, most aircraft data were not used. A posteriori some random spot-checks indicated that the aircraft data usually fit the objective analyses fairly well. The problem of how to combine aircraft and rawinsonde data into objective analyses is an interesting topic for future research.

4.2.2 Analysis of parameters derived from the wind field

Vorticity (ξ) and divergence (δ) were computed at each of the 196 (14×14) grid points enclosed within the area between $6 - 19^\circ$ N latitude and $51 - 64^\circ$ W longitude by centered finite-difference approximations.

The wind field was separated into its nondivergent (rotational) and divergent (irrotational) parts according to Helmholtz's theorem (Haltiner, 1970), in order that the effects of geostrophic deformation could be examined separately from the effects of divergent deformation. Furthermore, the nondivergent wind field is a filtered wind field, and is therefore less noisy than the observed wind field. The nondivergent wind component is a good estimate of the geostrophic wind if the ageostrophic and divergent winds are similar, or if both are small in magnitude compared to the magnitude of the geostrophic wind. Height data could not be used to estimate the geostrophic wind accurately, because small errors in the temperature and water-vapor mixing-ratio data would result in errors in the hydrostatically-integrated height field that are on the order of horizontal variations in the height field itself. The stream-function (ψ) and velocity potential (χ) are defined by the following

Poisson equations:

$$\nabla^2 \psi = \xi \quad (4.12)$$

$$\nabla^2 \chi = \delta \quad (4.13)$$

where $V_{nd} = \hat{k} \times \nabla \psi$ ($\hat{k} \equiv$ unit vector pointing upward) and $V_d = \nabla \chi$. The fields of ψ and χ were obtained by extrapolated Liebmann relaxation (Phillips, 1970), i.e., sequential estimates of $\psi(\chi)$ and were made by forcing the difference between $\nabla^2 \psi$ ($\nabla^2 \chi$) and $\xi(\delta)$ to vanish. The relaxation formulas and parameters that were used were selected for rapid convergence for a grid of size 14×14 (Appendix I). The convergence criterion was a change (for a new iteration) of less than 0.1% at each grid point. The ψ -field, on the average, converged within 100 iterations, and the χ -field converged within fewer than 50 iterations.

The Neumann and Dirichlet boundary conditions were imposed on the ψ and χ -fields, respectively, in order to minimize the kinetic energy of the divergent part of the wind (Eliassen, 1955), since the divergent part of the wind cannot be as well estimated as the nondivergent part of the wind (because for typical synoptic-scale motions, ξ can be measured with more precision than δ). Shukla and Saha (1974) have found that use of these boundary conditions results in a relatively small difference between the observed wind field and the sum of the derived nondivergent and divergent components. The following constraints were therefore imposed along the edges of the grid:

$$\chi = 0 \quad (4.14)$$

$$\frac{\partial \psi}{\partial n} = V_s \quad (4.15)$$

where n is the direction normally outward from the grid boundary, V_s is the wind component tangential to the grid boundary; the tangential direction is along the curve in a counterclockwise manner. The difference between the observed zonal wind component and the sum of the zonal components of the nondivergent and divergent parts of the wind was small most of the time compared to the observed zonal wind component. The corresponding difference for the meridional wind component, however, was sometimes relatively large, probably partly because (the meridional gradient of) the meridional wind component was a significant part of the poorly estimated divergence, and also because the meridional wind component was much less than the zonal wind component.

The resultant deformation (D) and orientation of the axis of dilatation (θ_d) of both the nondivergent and divergent wind were computed at each of the 144 (12×12) grid points enclosed within the area between $7 - 18^\circ$ N latitude and $52 - 63^\circ$ W longitude by centered finite-difference approximations.

The observed wind field was depicted by vectors, and deformation was depicted by tick marks whose orientation and length represented the orientation of the axis of dilatation and magnitude, respectively. The vectors and tick marks were drawn by the CALCOMP plotter at the MIT IPC. The nondivergent wind field was depicted by a streamfunction and isotachs.

Although the wind analyses, etc., were plotted on a mesoscale grid, the features represented were larger than mesoscale because the covariance function had been low-pass filtered, and also the spacing of the observations was more than the grid spacing of the analysis.

The accuracy of the vorticity, divergence, resultant deformation, and orientation of axis of dilatation can be estimated from the accuracy of the zonal and meridional wind components. All except the latter are simple to compute; the accuracy of the latter could be estimated from the linear terms of a Taylor series expansion of θ_d in terms of R and S (Chernoff, 1976). Details for this computation are presented for reference in Appendix J. The preceding error estimates were not actually made because the accuracy of the estimates of the wind error variances had not been quantitatively verified.

The sensitivity of the axis-of-dilatation orientation (θ_d) to the scale factor (T) and zonal phase velocity (C) was tested as follows: The 24 July 1969, 1200 GMT, 850-mb wind data, chosen for their striking character, were objectively analyzed for five different sets of the parameters C and T. The average θ_d at 20 grid points within the cloud-band area was computed for each analysis (Table 4.3). Since the difference between the largest and smallest θ_d -measurements was only 9 degrees (out of a possible 180 degrees), the objective analysis was fairly insensitive to the manner with which asynchronous data were used. The predictand, on the average, was a function of only 5-6 nearby predictors, of which fewer than half were asynchronous. Therefore, synchronous data contributed most to the predictand's reduction in variance, and asynchronous

data "fine-tuned" the analysis.

4.3 Statistical analysis of nondivergent deformation and cloud band orientation

The wind fields at 950, 850, 700, and 450 mb were objectively analyzed for each of twelve days on which satellite-observed cloud bands were within the analysis grid. The analysis time was 1200 GMT for nine of these days and 1800 GMT (near local noon) for the other three. Analysis times were selected on the basis of availability of wind data and clarity of the corresponding satellite photograph. The 48 analyses spanned the entire period except for July 16, when no rawinsonde observations were made and few clouds were visible, July 17, when the clouds did not appear to be organized, and July 26, when the clouds were clustered. (In Appendix K there is a list of all the analyses which were made, along with their designations.)

The synchronous and asynchronous (within six hours of analysis time) wind observations were also plotted so they could be compared with the objective analysis. The asynchronous observations were time-composited, assuming an 8 m sec^{-1} westward phase speed. The 950, 850, and 700 mb objective analyses fit the respective synchronous and asynchronous observations well. At 450 mb, however, the fit was poor in some places where the data were very noisy.

Error variances near the edges of the grid, where few observations were available, were relatively high. Reductions in variance were near zero in the southwestern portion of the grid, which included data-void

South America. The objective analyses in these regions were disregarded.

Subjective cloud-band nephanalyses were prepared from satellite photographs taken nearest the time for which the wind field had been objectively analyzed. The nephanalyses were made by Prof. F. Sanders in ignorance of the wind analyses. The nephanalyses consisted of traced cloud outlines, and no attempt was made to distinguish between regions of deep convection from regions of inactive stratiform cloud. Only the brightest regions, however, were outlined. Tick marks were drawn at wind-analysis grid points within the cloud-band area, thereby marking the approximate orientation of the band. This was also done independent of the wind-field analyses. Each tick mark's orientation, i.e., azimuth (θ_b) was measured with a protractor.

The difference between the orientation of the axes of dilatation of the nondivergent wind (θ_d) and the orientation of the cloud band (θ_b) was computed at each grid point, where $\Delta\theta = \theta_b - \theta_d$, $0^\circ < \theta_b < 180^\circ$, and $0^\circ \leq \theta_d \leq 180^\circ$. If $\Delta\theta$ were greater than 90 degrees, $\Delta\theta$ was replaced by the supplementary angle. The average of the absolute magnitude of the difference ($|\overline{\Delta\theta}|$) where $0^\circ \leq |\overline{\Delta\theta}| \leq 90^\circ$, was computed for each analysis, even though at some analysis times more than one cloud band was present.

The $|\overline{\Delta\theta}|$ measurements were treated as independent samples (at each analysis level), since each $|\overline{\Delta\theta}|$ was computed from a unique set of wind data and a unique satellite photograph.

The following experiment was performed at each analysis level in order to test the significance of the $|\overline{\Delta\theta}|$ measurements: $|\overline{\Delta\theta}|$

measurements were considered to be trials, and if $|\overline{\Delta\theta}|$ were less than some critical value (θ_c) the trial was a success; if $|\overline{\Delta\theta}|$ were greater than or equal to θ_c , the trial was a failure. If the $|\overline{\Delta\theta}|$ measurements were random, then the probability of a successful trial (p) would be $\theta_c/90$. The probability of getting k successes in n independent trials ($P(k)$) is given by the binomial probability distribution function (Drake, 1967).

$$P(k) = \binom{n}{k} p^k (1-p)^{n-k} \quad \text{for } k = 0, 1, 2, \dots, n \quad (4.16)$$

where $\binom{n}{k} = \frac{n!}{(n-k)! k!}$. The probability of getting greater than or equal to k successes in n trials is given by the cumulative binomial distribution function,

$$P(k \geq k_0) = \sum_{k=k_0}^n \binom{n}{k} p^k (1-p)^{n-k} \quad (4.17)$$

This function was tabulated for $p = 5/90$ to $45/90$ in increments of $5/90$. Thus, the probability of getting greater than or equal to k successes in n trials if the $|\overline{\Delta\theta}|$ measurements are random is known for $\theta_c = 5^\circ, 10^\circ, \dots, 45^\circ$. An experiment is therefore valid at the $P\%$ significance level if $P(k) = 1 - \frac{P}{100}$ or less.

The results of these experiments are given in Table 4.4, where $|\overline{\Delta\theta}|$ for each analysis is given by level. The number of successful trials for $\theta_c = 25, 30, 35, 40,$ and 45 degrees are tabulated along with the corresponding significance level. The axis-of-dilatation orientation

was within 35 degrees of the cloud-band orientation with 95% confidence at 950 mb, and within 40 degrees at 850 mb. It was within 35 degrees with 90% confidence at 700 mb, and within 45 degrees with only 61% confidence at 450 mb. Axis-of-dilatation and cloud-band orientations were considered to be significantly correlated if there were less than a 5% chance that random data could have produced a result as good for $\theta_c \leq 45^\circ$. Since the axis of dilatation of the nondivergent wind was significantly correlated with the orientation of the cloud bands in the low regions of the troposphere, slightly less well-correlated in the middle region of troposphere, and not at all well-correlated in the upper region of the troposphere, any possible physical link between deformation and tropical cloud bands must be at low levels.

There was no significant correlation between the magnitude of the resultant nondivergent deformation and cloud bands, as large values of resultant nondivergent deformation were found both within and outside of cloud-band areas.

A scatter diagram of the average orientation of each cloud band versus the corresponding average orientation of the axis of dilatation at 850 mb is shown in Fig. 4.9. (The process of determining the average orientations by averaging the orientations at grid points was slightly tricky; e.g., the average of a 10° azimuth and a 170° azimuth is a 0° (or 180°) azimuth, whereas simple averaging yields an average azimuth of 90° .) The scatter diagram shows that the orientations of the axes of dilatation were within 45 degrees of the respective orientations of the meridionally oriented cloud bands as well as those of the zonally

oriented cloud bands.

Cloud bands had been selected subjectively and their orientations had been specified subjectively, because consistent, high quality, normalized satellite photographs were not available. If they had been available, objective procedures for selecting bands and for measuring band orientations could have been used. The two-dimensional auto-correlation function of the satellite-observed brightness field, for example, could have been used to determine if there were a preferred direction to the cloudiness pattern (Leese, et al, 1970). This pattern recognition problem is an interesting topic for further investigation.

I prepared subjective nephanalyses, in ignorance of those made by Prof. Sanders, and in ignorance of the wind-field analyses. The results of the statistical tests based on my $|\overline{\Delta\theta}|$ measurements were virtually identical to the former ones. Therefore, the subjective nephanalyses are probably not biased. Then, the results of the statistical tests can be accepted with confidence, and there was probably no need for an objective band selection scheme, anyway.

4.4 Composited analysis

In order to determine the physical processes responsible for cloud-band formation, and to determine what role deformation may play, composited analyses were prepared for zonally oriented cloud bands ($068^\circ \leq \bar{\theta}_b \leq 112^\circ$, where $\bar{\theta}_b$ is the average cloud band orientation for each analysis) and for nonzonally oriented cloud bands ($0^\circ \leq \bar{\theta}_b \leq 67^\circ$ and $113^\circ \leq \bar{\theta}_b < 180^\circ$): The zonal cloud-band composite (hereafter

referred to as the zonal composite) was the average of the 13, 15, 19, 20, 21, and 24 July analyses, and the nonzonal cloud-band composite (hereafter referred to as the nonzonal composite) was the average of the 14, 18, 22, 25, 27, and 28 July 1969 analyses. (A composite at 850 mb of the 14, 17, 18, 22, 23, 25, 26, 27, and 28 July 1969 analyses was nearly identical to the nonzonal composite. Because the addition of three analyses for which there were no cloud bands did not significantly alter the nonzonal composite, the nonzonal composite may also represent the composite for nonbanded cloud structures.)

Compositing increases one's confidence in the analysis. For example, the standard deviations of the zonal and meridional wind component estimates were estimated to be approximately 1 m sec^{-1} and $0.5 - 1 \text{ m sec}^{-1}$ respectively (away from the borders and away from South America). Therefore they are known with about 95% confidence to be within 2 m sec^{-1} and $1 - 2 \text{ m sec}^{-1}$ of their "true" values, whereas the composited zonal and meridional wind components are known within 0.8 m sec^{-1} and $0.4 - 0.8 \text{ m sec}^{-1}$ of their "true" values.

4.4.1 The composited analyses and their implications

There is a zone of maximum cloudiness (Fig. 4.10) from $9 - 10^\circ \text{ N}$ latitude, eastward from about 55° W longitude in the zonal composite. The regions north of 12° N latitude and south of 8° N latitude are either clear, or are covered by clouds of small albedo. The nonzonal composite nephanalysis (Fig. 4.11) is comparatively ill-defined; there is an amorphous cloudiness maximum near 11° N latitude 57° W longitude,

and a zone of moderate cloudiness from 10 - 11° N latitude eastward of about 56° W longitude. Elsewhere there is little cloudiness.

In the discussions which follow, wind speeds less than 10 knots, from 10 - 20 knots, and in excess of 20 knots, are classified as weak, moderate, and strong, respectively.

There is a zone of confluence at 950 mb in the zonal composite (Fig. 4.12) at 10.5° N latitude, extending eastward from 55° W longitude. The southeasterly flow equatorward of the confluent zone is weak, and the east-northeasterly flow poleward of the confluent zone is moderate.

The axes of dilatation of the nondivergent wind (Fig. 4.13) are aligned zonally and west-northwest to east-southeasterly in the vicinity of and equatorward of the confluence zone and cloudiness maximum. The nondivergent resultant deformation, due mostly to confluence and partly to shear, is about $1 - 2 \times 10^{-5} \text{ sec}^{-1}$, the axes of dilatation elsewhere are mostly meridionally oriented, and resultant deformation is, on the average, weaker. (The axes of dilatation of the divergent wind are zonally oriented in the vicinity of the confluent zone, and divergent deformation is about $5 \times 10^{-6} \text{ sec}^{-1}$. Elsewhere, the divergent deformation is very weak.)

The 950-mb wind in the nonzonal composite (Fig. 4.14) is weak easterly, increasing polewards to moderate. There are no well-defined zonally oriented features.

The axes of dilatation of the nondivergent wind (Fig. 4.15) are aligned north-northwest to south-southeasterly between 10 and 12° N

latitude eastward from 55° W longitude, and the resultant deformation, which is due mostly to shear, is about 10^{-5} sec^{-1} . (The orientations of the axes of dilatation of the divergent wind are too noisy to be significant.)

The salient features of the wind field at 850 mb (Figs. 4.16 and 4.18) are similar to those at 950 mb. The axes of dilatation in the zonal composite (Fig. 4.17) are slightly more zonally oriented near the zone of confluence at 850 mb than at 950 mb. The resultant deformation at 850 mb is about the same as its 950 mb counterpart. The nondivergent deformation (Fig. 4.19) in the 850 mb nonzonal composite is also similar to that of its 950 mb counterpart.

In the region of maximum cloudiness in the zonal composite, the e-folding time of the meridional gradient of any conservative quantity from nondivergent deformation, is less than 1.5 days. Zonal gradients of conservative quantities may be rapidly increased near 10° N latitude and eastward of 55° W longitude in the nonzonal composite as a consequence of nondivergent deformation.

In the zonal composite, a band of maximum vorticity (Fig. 4.20) of about $2 \times 10^{-5} \text{ sec}^{-1}$ coincides with the zone of confluence eastward of 54° W longitude, but slopes southwestward west of 54° W longitude. The maximum eastward of 54° W is due mainly to cyclonic shear, whereas the southwestward sloping area, however, is due to primarily the cyclonic curvature of southeasterlies back to the climatological easterlies and east-southwesterlies over data-void South America, and is therefore not realistic. The July gradient-level climatological

analyses (see Chapter 3) indicate that the winds are in fact more southerly west of 54° W longitude than Fig. 4.16 indicates. A minimum zone of about $-1.0 \times 10^{-5} \text{ sec}^{-1}$, due mainly to anticyclonic shear, is near $13-14^\circ$ N latitude. A kinematically computed zone of maximum rising motion of $1-2 \mu\text{b sec}^{-1}$ (i.e., $\sim 1-2 \text{ cm sec}^{-1}$) correlates well with the band of cyclonic vorticity and the cloudiness maximum (Fig. 4.10), east of 54° W longitude; a zone of subsidence of less than $1 \mu\text{b sec}^{-1}$ near $15-16^\circ$ N latitude correlates fairly well with a region of weak anticyclonic vorticity and minimum cloudiness. The region of large anticyclonic vorticity near $13-14^\circ$ N latitude $55-59^\circ$ W longitude, however, is not accompanied by strong subsidence

In the nonzonal composite, the vorticity maximum of $1-2 \times 10^{-5} \text{ sec}^{-1}$ near 12° N latitude, 55° W longitude correlates fairly well with the region of rising motion of greater than $1 \mu\text{b sec}^{-1}$ (Fig. 4.21) and is $1-2^\circ$ of latitude east of the cloudiness maximum. The patterns of vorticity and vertical motion elsewhere are not well correlated.

Therefore if 850 mb can be considered to be the top of the Ekman layer, the CISK hypothesis (Charney and Eliassen, 1964) is weakly supported.

The zonal composite wind field at 700 mb (Fig. 4.22) is similar to those at 850 and 950 mb, except that the wind speeds are moderate to strong, and a weak ridge is centered near 58° W longitude northward of 16° N latitude. The nondivergent deformation acts zonally and is about 10^{-5} sec^{-1} (Fig. 4.23) in the equatorward sector of the zone of confluence. The nonzonal composite wind (Fig. 4.24) is moderate to strong

from the southeast, north of 12° N latitude, as a result of strong jets associated with travelling waves. The axes of dilatation of the nondivergent wind (Fig. 4.25) are meridionally oriented.

The zonal composite wind field at 450 mb (Fig. 4.26) is similar to that at 700 mb, except that the wind speeds at 450 mb are mostly weaker. The nonzonal composite wind field (Fig. 4.27) is similar to the zonal composite, except that the low-latitude flow is slightly northerly.

Since the radiosonde virtual-temperature data were too noisy to analyze objectively or otherwise, the wind analyses were used to infer the average thermal structure for roughly the lower half of the troposphere. If the nondivergent part of the wind is approximately equal to the geostrophic wind, then the thermal-wind relation can be used to obtain estimates of the vertically averaged horizontal virtual-temperature gradients as follows:

$$\frac{\partial \hat{T}_v}{\partial y} = \frac{f \bar{p}}{R_d} \frac{\partial U_{nd}}{\partial p} \quad (4.18)$$

$$\frac{\partial \hat{T}_v}{\partial x} = \frac{-f \bar{p}}{R_d} \frac{\partial V_{nd}}{\partial p} \quad (4.19)$$

where " $\hat{}$ " denotes "estimate" and the other symbols have been defined earlier. The accuracy of these estimates is therefore

$$\left| \delta \left(\frac{\partial \hat{T}_v}{\partial y} \right) \right| = \frac{f \bar{p} \left| \delta \left(\frac{\Delta U_g}{\Delta p} \right) \right|}{R_d} \quad (4.20)$$

$$\left| \delta \left(\frac{\partial \hat{T}_v}{\partial x} \right) \right| = \frac{f \bar{p} \left| \delta \left(\frac{\Delta v}{\Delta p} \right) \right|}{R_d} \quad (4.21)$$

where \bar{p} is the average pressure of the layer, which is Δp thick, and $\delta()$ denotes "error of". Therefore as deep a layer as possible was used, i.e., 950 - 450 mb.

For horizontal virtual-temperature gradients of about $1^\circ\text{C}/1000$ km, geostrophic wind measurements are needed within 0.4, 0.6, 0.8, and 1.6 m sec^{-1} of the true values at 20° , 15° , 10° , and 5° N latitude respectively, in order to obtain horizontal virtual-temperature gradient estimates with 10% or less uncertainty. Since the objectively analyzed wind data are known with 95% confidence to within $1 - 2 \text{ m sec}^{-1}$ of their "true" values, the thermal-wind analyses are at least qualitatively accurate.

There is a zonally oriented warm core (Fig. 4.28) along the low-level zone of confluence in the zonal composite. The magnitude of the horizontal virtual-temperature gradient is about $0.5^\circ \text{C}/1000$ km equatorward of the warm core, and $0.5 - 1^\circ\text{C}/1000$ km poleward of the warm core. The warm core correlates well with the cloudiness maximum and 850-mb rising motion.

The nearly circular warm core of the nonzonal composite (Fig. 4.29) is centered within a few degrees of the cloudiness maximum. The magnitude of the horizontal virtual-temperature gradient is about $0.4^\circ\text{C}/1000$ km equatorward of 10° N latitude, and $0.5 - 0.8^\circ\text{C}/1000$ km poleward of the warm core.

The vertical motions implied by the simple quasigeostrophic analytical model of section 2.2 are only on the order of 0.1 cm sec^{-1} with

the aforementioned nondivergent (i.e., approximately geostrophic) deformation, horizontal virtual-temperature gradients, and an average static-stability parameter. Therefore the midlatitude frontogenetical mechanism is probably not significant. The vertical circulation associated with the cloud bands are more likely driven by latent heat release from deep cumulus convection, which is also probably responsible for the warm cores.

4.4.2 The cross-sectional analyses and their implications

Subjective cross-sectional analyses in the meridional plane were drawn in order to examine the vertical structure of the zonal and non-zonal composites in more detail. Cross-sectional meridional wind component, vorticity, and divergence composites were prepared for the longitudes nearest the ships and at which cloud bands were most prominent, 53 - 55° W (i.e., each grid point value was the average of the 53, 54, and 55° W values). The cross-sectional composites were made at 50-mb increments from temperature and water-vapor mixing-ratio data from 1000 - 450 mb. The thermodynamic fields were assumed to be zonally symmetric, and only thermodynamic data available within six hours of the analysis time of the individual objective analyses were used. Tape data alone were used, since only they had been corrected for the errors discussed in section 4.1.

The vertical velocity (ω) was estimated kinematically from the composited divergences (see Appendix L). Boom surface-pressure measurements were reduced to sea level and averaged over all the analysis times.

These data were not crucial to the vertical motion analysis, since errors of several millibars affect the estimate of ω very little. Diurnal surface pressure changes affected ω little also (see Nitta and Esbensen, 1974). (Surface pressures dropped monotonically about 3 mb from the Rainier at 17.5° N latitude to the Oceanographer at 7.5° N latitude. The rate of drop increased with latitude. The surface geostrophic zonal-wind component was therefore about 7.5 m sec⁻¹ at 12.5° N latitude. The 950-mb zonal wind at 12.5° N latitude for the average of both composites was also about 7.5 m sec⁻¹. Unless there was a large shear between the surface and 950-mb zonal-wind components, the magnitudes of the surface zonal wind and zonal geostrophic wind were similar. In addition, the zonal divergent wind components were much less than the zonal nondivergent wind components. Therefore the estimates of the zonal geostrophic wind in terms of the zonal nondivergent wind should be good.)

With $\omega = 0$ as a lower boundary condition, the vertical motion estimates were suspect at 450 mb, because strong upward motions were present near 15° N latitude, where few clouds were visible. Since wind data up to the tropopause were not available, it was impossible to use the upper boundary condition $\omega = 0$ to prevent unrealistic vertical motion estimates in the upper regions of the troposphere as some have (e.g., Yanai et al, 1973). Therefore, vertical motion estimates only up to 700 mb were plotted.

The meridional circulation is depicted by vectors, the vertical component of which is proportional to $-\omega$, and the horizontal component of which is proportional to the meridional wind component. (It was not

possible to define accurately a meridional streamfunction because $\frac{\partial U}{\partial x}$ was significantly different from zero.) The vorticity cross-sections are superposed on the meridional circulation along with the average cloudiness for 53 - 55° W longitude.

The vertical motion for the zonal composite (Fig. 4.30) is upward at the northern edge of the cloudiness maximum and the 950 and 850-mb vorticity maxima. There is downward motion in the clear region, where the 950 and 850-mb vorticity is mostly anticyclonic. This qualitatively good correlation among cloudiness, vorticity, and vertical motion is evidence in support of the CISK hypothesis. There are, however, significant amounts of cloudiness at 8 and 9° N latitude, where the composite indicates weak subsidence. Therefore the estimates of vertical motion there either were based on poor divergence estimates, or the cloudiness amounts were poorly estimated, or high level cirrus produced by deep cumulus activity at 11° N latitude were advected equatorwards by the upper flow. Since the low-level flow into the area of the cloudiness maximum is cross-equatorial, the boundary layer is probably nonEkman-like (Janota, 1971), and therefore the poor correlation between 950 and 850-mb vorticity and vertical motion equatorward of 10° N latitude is not surprising.

The nonzonal composite vertical motion (Fig. 4.31) is upward equatorward of 12° N latitude and downward poleward of 12° N latitude (at 950 and 850 mb only). Although the region of maximum rising motion corresponds to the region of maximum cloudiness and low-level vorticity, the correlation between low-level vorticity, vertical motion, and

cloudiness is qualitatively poor elsewhere. The rising motions at 700 mb, near 15° N latitude, probably are due to processes associated with waves and are responsible for mid-level cloudiness. This composite, then, does not offer strong evidence for CISK. The boundary layer is probably not very accelerated, since above 900 mb the flow is not cross-equatorial, and below 900 mb the flow is only weakly cross-equatorial.

The water vapor mixing ratio generally decreases with latitude in the zonal composite (Fig. 4.32). The maximum meridional q -gradient ($9\text{gkg}^{-1}/1000\text{ km}$) between 750 and 800 mb coincides with the boundary between the regions of subsidence over the trade inversion and ascent in the ITCZ. Since there are relatively large amounts of water vapor at 7.5° N latitude, and there are large cloudiness amounts at 8 - 9° N latitude, but there is kinematically implied subsidence south of 9° N latitude, the meridional flow pattern south of 9° N latitude is suspect. The meridional q -gradients in the nonzonal composite (Fig. 4.33) are relatively weak, and the q -pattern is noisy.

Virtual-temperature cross-sectional analyses were prepared from the water-vapor mixing-ratio and temperature data via the approximate formula, $T_v = T(1 + 0.609 q)$ (Phillips, 1970). The virtual temperatures in the zonal composite (Fig. 4.34) generally decrease with latitude, except at 750 and 800 mb, where the relatively warm trade inversion results in a meridional T_v -gradient in the reverse sense, even though the q -gradient is acting to produce the opposite effect. The vertically averaged meridional T_v -gradient of about $-0.9^\circ\text{ C}/1000\text{ km}$ (-0.5° C to -1.3° C) north of 12° N latitude is in qualitative agreement with the

thermal-wind calculations. The vertically averaged gradient between the Oceanographer and the Mt. Mitchell (south of 10° N latitude) is less than 0.1°C/1000 km, i.e., much less than the 0.5°C/1000 km implied by the thermal wind. This may be due to the inaccuracy of the thermal wind relation at low latitudes.

The nonzonal virtual-temperature cross-sectional composite (Fig. 4.35) is unrepresentative, because, as suggested by the thermal-wind analysis, the vertically averaged virtual-temperature field is not zonally symmetric. For example, the relatively warm vertically averaged virtual temperatures at the Rockaway (15.2° N) and the Mt. Mitchell (10.3° N) are probably due to their proximity to the warm core at 55.5° W implied by the thermal-wind field).

Cross-sections of equivalent-potential temperature (θ_e) were prepared from the temperature and water-vapor mixing-ratio data via the simple Rossby formula (Phillips, 1970),

$$\theta_e = \theta_e^{Lq/C_p T} ,$$

where $\theta = T(1000/p)^{R/C_p}$. The θ 's and θ_e 's were computed from the averaged temperatures and averaged water vapor mixing ratios.

In the zonal composite (Fig. 4.36) θ_e is a minimum between 550 and 600 mb equatorward of 10° N latitude, and a lesser minimum from 600 to 700 mb poleward of 12° N latitude. Therefore the lower portion of the troposphere in these two regions is convectively unstable. Between 10 and 12° N latitude, the region of maximum rising motion, the θ_e -profile above 850 mb is approximately neutrally stable, and the region below

850 mb is convectively unstable. The θ_e -profile poleward of 12° N latitude and equatorward of 10° N latitude qualitatively typifies an "undisturbed" tropical atmosphere, whereas the profile between 10 and 12° N typifies a "disturbed" tropical atmosphere (Betts, 1974). There is therefore qualitative evidence from the independent thermodynamic data that the estimated meridional circulation is, for the most part, reasonable. The nonzonal composite θ_e -cross-section (Fig. 4.37) is similar to that of the zonal composite. The features of the former, however, are less prominent than the features of the latter.

4.4.3 Heat and water-vapor budget analyses and their implications

Heat and water-vapor budgets were calculated in order to check the wind, temperature, and water-vapor analyses with independent surface ship data, and to infer the effects of cumulus convection.

The apparent heat source (Yanai et al, 1973) (Q_1) is defined as the rate at which heat is added to an air parcel per unit mass, following the grid-scale motions. From the first law of thermodynamics and from scale analysis (Appendix M)

$$Q_1 = c_p \left(\bar{u} \frac{\partial \bar{T}}{\partial x} + \bar{v} \frac{\partial \bar{T}}{\partial y} \right) + \bar{\omega} \bar{s} \quad (4.22)$$

where "-" indicates an average over the grid-scale (i.e., about 100 km) of the composited cross-sectional data, and the static stability parameter $\bar{s} = c_p \frac{\partial \bar{T}}{\partial p} - \frac{R}{p} \bar{T}$. The flow has been assumed to be steady-state. The apparent heat source is therefore due to large-scale horizontal

sensible-heat advection and large-scale adiabatic cooling or heating. Since the horizontal temperature gradients in the zonal and nonzonal cross-sections are small, the apparent heat source should be a result mostly of vertical motions. The apparent heat source is also equivalent to the net condensational heating, net radiational heating, and heating due to the turbulent sensible-heat fluxes. So,

$$Q_1 = L(c - e) + Q_R - C_p \frac{\partial \overline{\omega' T'}}{\partial p} \quad (4.23)$$

where c is the condensation rate, e is the evaporation rate, Q_R is the radiational heating rate, and the prime ($'$) indicates the deviation from the average. The integrated $Q_1 - Q_R$ over a unit column of air up to the tropopause is the net rate of heating in the column due to latent heat of condensation (as evidenced by the rate at which precipitation hits the ground) and the turbulent flux of sensible heat from the ocean surface to the atmosphere. That is,

$$\frac{1}{g} \int_{p_T}^{p_0} (Q_1 - Q_R) dp = \frac{-C_p}{g} \overline{\omega' T'} \Big|_{p_0} + \frac{L}{g} \int_{p_T}^{p_0} (c - e) dp \quad (4.24)$$

where p_0 is the surface pressure and p_T is the pressure at the tropopause. All net condensation is assumed to fall out vertically as rain. The turbulent (subgrid-scale) flux of sensible heat across the tropopause is assumed to be negligible since the tropopause is a region of large static stability. Furthermore, radar observations in the ITCZ region off the African coast during GATE suggest that few cumulonimbus towers penetrate the tropopause (Geotis, 1974). Since $\omega \approx -w \rho g$, (4.24)

can be rewritten as

$$\frac{1}{g} \int_{P_T}^{P_0} (Q_1 - Q_R) dp = C_p \rho \overline{w_0' T_0'} + LP_0 = S_0 + LP_0 \quad (4.25)$$

where S_0 is the rate at which heat is being transferred by eddies from the ocean surface to the atmosphere, and P_0 is the surface precipitation rate.

The apparent moisture source (Q_2) is the rate at which water vapor is added to an air parcel following the grid-scale motions. From the continuity equation and scale analysis (Appendix M),

$$Q_2 = \bar{u} \frac{\partial \bar{q}}{\partial x} + \bar{v} \frac{\partial \bar{q}}{\partial y} + \bar{\omega} \frac{\partial \bar{q}}{\partial p} \quad (4.26)$$

Again, the flow is assumed to be steady state. The apparent moisture source is therefore due to large-scale horizontal and vertical advection. It is also equivalent to condensation, evaporation, and the turbulent flux of water vapor. So,

$$Q_2 = e - c - \frac{\partial \overline{\omega' q'}}{\partial p} \quad (4.27)$$

The integrated Q_2 over a unit column of air up to the tropopause is the net rate at which water vapor is accumulating in the column from sea-surface evaporation less condensation loss due to precipitation falling onto the sea-surface.

$$\frac{1}{g} \int_{P_T}^P Q_2 dp = \left. \frac{-\overline{\omega'q'}}{g} \right|_{P_0} + \frac{1}{g} \int_{P_T}^P (e - c) dp \quad (4.28)$$

The flux of water vapor across the tropopause is assumed to be negligible. Equation (4.28) can be rewritten as,

$$\frac{1}{g} \int_{P_T}^P Q_2 dp = -\rho \overline{w_0'q_0'} - P_0 = E_0 - P_0 \quad (4.29)$$

where E_0 is the evaporation rate from the sea surface.

The quantities Q_1 and Q_2 were estimated for the zonal and non-zonal composites by centered finite-difference approximations. The quantities T_v and q were estimated at 950, 850, 700, and 450 mb at each degree of latitude by linear interpolation, except poleward of the Rainier and equatorward of the Oceanographer, where T_v and q were assumed to have the values at each ship, respectively. It was assumed that $\frac{\partial q}{\partial x}$ and $\frac{\partial T_v}{\partial x}$ were zero. The satellite nephanalyses and thermal-wind analyses support this assumption for the zonal composite, but not for the nonzonal composite. If horizontal advections are small relative to vertical advections, then this assumption is not important anyway. The $\bar{\omega}$ and \bar{v} data were obtained from the cross-sectional analyses.

The radiative heating rates were obtained from the results of a numerical model (Dopplick, 1970). The data taken from the model were valid for 0, 10, and 20° N latitude at 925, 775, 600, and 400 mb.

The radiative heating rate (Q_R) was determined at each grid point by linear interpolation. Dopplnick's temperature data were July mean (6 years of record) zonally averaged values. He used a July zonal-mean cloudiness of about 20%, which had been obtained from a combination of TIROS VII and TIROS VIII cloudiness averages at 10° squares, neph-analyses from ETAC, and digitized data from the 1968 ESSA satellite. The percentages of high, middle, and low clouds were estimated from satellite-observed brightness and from surface observations. This was necessary because different types of clouds have different thermal spectral properties, and different transmissivities and reflectivities for visible solar radiation. Low and middle clouds were assumed to have thicknesses of 150 and 100 mb, respectively; high cirrus were assumed to be 50-mb thick. The water-vapor distribution was obtained in the form of a July zonal mean from the Geophysical Fluid Dynamics Laboratory (GFDL) based on the MIT general circulation data library. Other details such as surface albedo and the gas models are found in Dopplnick's report. The major mechanisms responsible for Q_R in the model tropical troposphere were longwave radiative cooling (about 2°C day^{-1}) from water vapor and solar near-infrared heating (about $0.5 - 1^\circ\text{C day}^{-1}$) from water vapor, carbon dioxide, and monatomic oxygen. Some weaknesses of Dopplnick's model are as follows:

- (1) The percentages of high clouds is probably underestimated, since the gray range of the satellite's optical sensor was too small to "see" thin high clouds.
- (2) Surface albedoes are probably underestimated.

(3) Clouds are highly parameterized.

The cooling rates at 950, 850, 700, and 450 mb were 1.8, 1.6, 0.9, and $1.1^{\circ}\text{C day}^{-1}$ respectively. Albrecht and Cox (1975) recently found that within deep cirrostratus and altostratus, heating of about $0.5^{\circ}\text{C day}^{-1}$ occurred, and intense cooling occurred above (cooling rates of $4.5^{\circ}\text{C day}^{-1}$ were found). Therefore Dopplnick's model underestimates the meridional Q_R -gradient, since the model does not have as sharp meridional cloudiness gradients as the composited nephanalyses.

The apparent heat source (Q_1) in the zonal composite (Fig. 4.38) is a maximum ($8^{\circ}\text{C day}^{-1}$) at 700 mb at 11° N latitude, and a minimum ($-6^{\circ}\text{C day}^{-1}$) at 850 mb around $16-17^{\circ}$ N latitude. Since the temperature-advection terms are relatively small (see (4.22)), Q_1 is roughly proportional to $\bar{\omega}$. The apparent moisture source (Q_2) (Fig. 4.39) looks qualitatively like Q_1 . Since the horizontal advection terms are relatively small (see (4.26)), Q_2 is roughly proportional to $\bar{\omega}$. The patterns of Q_1 and of Q_2 form a doublet, i.e., heating due to latent heat of condensation in the ascending air at $10-12^{\circ}$ N latitude and cooling due to evaporation near the trade inversion north of 12° N latitude. The meridional Q_1 -gradients from radiative effects are smaller than the Q_1 -gradients from latent heat release. The magnitude of the heating-cooling doublet, Q^* , (see (2.20)) was about $7^{\circ}\text{C day}^{-1}$. Since (2.21) with $L \approx 1000$ km and $Q^* \approx 7^{\circ}\text{C day}^{-1}$ implies w 's on the order of centimeters per second, it is likely that the condensation-evaporation

doublet drives the meridional flow (compare Fig. 2.2 with Fig. 4.30).

The nonzonal composite of Q_1 (Fig. 4.40) has a relatively small meridional gradient, and therefore the implied (from (2.2)) meridional flow is weak. The apparent heat source (Q_1) south of 12° N latitude is a bit more than half that of the zonal composite; there is little if any negative Q_1 north of 12° N latitude. The apparent moisture source (Q_2) (Fig. 4.41) indicates condensation everywhere except below 850 mb, north of 12° N latitude. The condensation at midlevels of the troposphere north of 12° N latitude is probably associated with wave activity, since African waves have been shown to be most prominent at midlevels (Burpee, 1971) in these latitudes.

The excess of surface evaporation over precipitation was estimated by (4.28). When the boundary conditions, $\omega = 0$ at the surface and tropopause are used, the computations in (4.28) are independent of $\bar{\omega}$.

$$\begin{aligned}
 -\frac{1}{g} \int_{P_T}^{P_0} Q_2 dp &= P_0 - E_0 = -\frac{1}{g} \int_{P_T}^{P_0} \left[\bar{u} \frac{\partial \bar{q}}{\partial x} + \bar{v} \frac{\partial \bar{q}}{\partial y} + \bar{\omega} \frac{\partial \bar{q}}{\partial p} \right] dp \\
 &= -\frac{1}{g} \int_{P_T}^{P_0} \left[\frac{\partial \bar{u} \bar{q}}{\partial x} + \frac{\partial \bar{v} \bar{q}}{\partial y} + \frac{\partial \bar{\omega} \bar{q}}{\partial p} \right] dp \\
 &= -\frac{1}{g} \int_{P_T}^{P_0} \left[\bar{u} \frac{\partial \bar{q}}{\partial x} + \bar{v} \frac{\partial \bar{q}}{\partial y} + \bar{q} \left(\frac{\partial \bar{u}}{\partial x} + \frac{\partial \bar{v}}{\partial y} \right) \right] dp - \bar{\omega} \bar{q} \Big|_{P_T}^{P_0} \\
 &= -\frac{1}{g} \int_{P_T}^{P_0} \left[\bar{u} \frac{\partial \bar{q}}{\partial x} + \bar{v} \frac{\partial \bar{q}}{\partial y} + \bar{q} \delta \right] dp \tag{4.30}
 \end{aligned}$$

Then, Q_2 may be replaced by $Q_2' = \bar{u} \frac{\partial \bar{q}}{\partial x} + \bar{v} \frac{\partial \bar{q}}{\partial y} + \bar{q} \delta$. Since the contributions of the 700 and 450-mb Q_2' to the integral were very

small because q was very small, and since q should be even smaller above 450 mb, the integrand of (4.30) was assumed to decrease linearly from its 450-mb value to zero at the tropopause, 150 mb (Appendix N). Calculations made by others with data above 450 mb (e.g., Yanai et al, 1973) support this assumption. The estimates of $E_0 - E_0$ for the zonal and nonzonal composites are shown in Fig. 4.39 and Fig. 4.41.

In the absence of direct evaporation measurements, the surface evaporation rate was estimated via the bulk aerodynamic method at each ship (for both composites) from the boom data. The following formula was used (Garstang, 1967):

$$E_0 = \rho C_D (q_0 - q_a) V \quad (4.31)$$

where ρ is the air density, q_0 is the saturation water vapor mixing ratio at the sea-surface temperature, q_a is the water vapor mixing ratio at anemometer level (5-10 m), V is the wind speed at anemometer level in m sec^{-1} , and C_D is the drag coefficient. The drag coefficient depends on the stability and the wind speed as follows:

$$C_D(6 \text{ meters}) = [1.46 + 0.07 V - 4.2 R_B] \times 10^{-3} \quad (4.32)$$

where $R_B = \frac{g}{T} 60 \frac{\theta_a - \theta_0}{V^2}$, and θ_a and θ_0 are the potential temperatures at anemometer level and at the surface. The estimates of E_0 and the implied daily precipitation amounts (\hat{P}_0) are also shown in Fig. 4.39 and Fig. 4.41.

The implied surface-precipitation rates (\hat{P}_0) for the zonal composite at the Oceanographer, Discoverer, and Rockaway were very small, in qualitative agreement with the nephanalysis which showed little cloudiness at these ships. At the Discoverer, however, 0.9 cm day^{-1} on the average actually fell; this amount is unrepresentative, since most of the precipitation at the Discoverer (5.12 cm) fell on one day (24 July). The \hat{P}_0 of 2.9 cm at the Mt. Mitchell is less than the actual recorded average precipitation rate (P_0), which was only 1.1 cm day^{-1} , and on no days did more than 2.3 cm of precipitation actually fall. The discrepancy is probably due to either unrepresentative precipitation measurements or divergence error. The \hat{P}_0 at the Rainier was significantly less than zero, whereas P_0 was very small and positive. The estimate of E_0 at the Rainier was similar to those of other ships, and is therefore not suspect. Either the cross-sectional analysis poleward of 16° N latitude is poor, or there was "negative" precipitation, possibly in the form of airborne ocean spray evaporating into the air (Blanchard and Woodcock, 1957). In this process, the latent heat of vaporization is supplied by the air, not the ocean. The surface wind speeds at the Rainier of 15 knots or greater were probably sufficient to generate foam on the sea surface. There was not much evidence of "negative" precipitation at 15° N latitude, however, where the surface wind was probably also sufficiently strong enough to generate foam. Now, the sensible heat flux from the ocean to the air (S_0) on the average, was positive everywhere, since the sea-surface temperature was generally warmer than the overlying air temperature (see the BOOM data). Then if

$S_0 + LP_0$ from (4.24) and (4.25) were significantly less than zero, then P_0 was also probably less than zero. The integral of $Q_1 - Q_R$ with pressure, upon which the estimate of $S_0 + LP_0$ is made, is dependent on ω , and therefore cannot be evaluated above 700 mb. Qualitatively, if $Q_1 - Q_R > 0$ at all analysis levels, and if $Q_1 - Q_R$ decreases to zero at 150 mb from its value at 700 mb, then "negative" precipitation probably does not occur. If $Q_1 - Q_R < 0$ at all analysis levels and if $Q_1 - Q_R$ increases to zero at 150 mb, then there is possibly "negative" precipitation. The quantity $Q_1 - Q_R$ for the zonal composite is positive at all analysis levels in the region from 10 to 12° N latitude, where significant precipitation occurred. Poleward of 12° N latitude, $Q_1 - Q_R$ is near zero at the 700 mb and 950-mb levels, and less than zero at the 850-mb level. If the cloud tops of trade-wind cumulus are near 850 mb, then Q_R may really be $-4^\circ\text{C day}^{-1}$ to $-5^\circ\text{C day}^{-1}$ (not $-1.6^\circ\text{C day}^{-1}$), and therefore $Q_1 - Q_R$ is close to zero at 850 mb also. Therefore, the evidence for the occurrence of "negative" precipitation is weak.

The \hat{P}_0 's for the nonzonal composite at all ships except the Rainier (Fig. 4.41) are $1-2 \text{ cm day}^{-1}$, in qualitative agreement with the nephanalysis, which shows significant cloud cover near every ship except the Rainier. There is no evidence anywhere of "negative" precipitation. The P_0 's are qualitatively similar to the \hat{P}_0 's. The nonzonal composite cross-sectional analyses are therefore probably also qualitatively sound.

4.5 Summary and discussion

The BOMEX Phase IV rawinsonde data were objectively analyzed by a method in which the interpolating function is determined by the statistics of the synchronous and asynchronous data. At low levels significant correlations were found between the orientations of cloud bands and the orientations of the respective axes of dilatation of the nondivergent wind field. Composited analyses of the nondivergent wind for days on which cloud bands were zonally oriented and nonzonally oriented had the following features: At low levels, the axes of dilatation near the cloud bands were zonally oriented on the former days, and meridionally oriented on the latter days. Therefore there is a relationship between nondivergent deformation and tropical cloud-band orientation.

The horizontal virtual-temperature gradients were probably too small for the frontogenetical mechanism to be of dynamical importance in the absence of latent heat release. Heat and water-vapor budget analyses suggested that the analyses of the meridional flow were qualitatively reasonable, and that latent heat release from deep cumulus convection drove the cloud bands. Regions of maximum cloudiness were warmer than the surroundings.

The mechanism by which geostrophic deformation controls the orientation of tropical cloud bands is therefore one which operates in a barotropic atmosphere at low-levels, and one in which latent heat release is important.

Hoskins (1972) has suggested that latent heat release along a band of gradient-level cyclonic vorticity, which had been produced by vertical

motions due to thermal forcing, can lead to significant vertical motions in the absence of frontogenesis. Since 850-mb vertical motion and vorticity were to some extent correlated, it is possible that bands of gradient-level cyclonic vorticity lead to frictionally induced upward motions at low levels which trigger bands of deep cumulus convection. Charney (1968) has shown numerically that the CISK mechanism may be responsible for the formation of the ITCZ in a barotropic low-latitude atmosphere. The CISK mechanism depends upon a monotonic functional relationship among boundary-layer pumping, gradient-level vorticity, and latent heat release above the boundary layer. Although Williams and Gray (1973) have found such a relationship between the first and the second, and Cho and Ogura (1974) have implicitly found such a relationship between the last and the first, it is not known which of the three initially cause the other two. Synoptic-scale deformation may be responsible for producing bands of vorticity. Sanders (1975c) has noted that a barotropic model applied at low latitudes tends to produce banded regions of absolute and relative vorticity. It is difficult to determine, without the aid of a numerical model, how deformation in a barotropic atmosphere may distort the absolute-vorticity field so that bands of relative vorticity might be produced, because distortions of the absolute vorticity field lead to changes in the deformation itself.

Lindzen (1974) has suggested that in shallow disturbances convergence due to internal Rossby-gravity waves may result in deep cumulus convection. It is not known how deformation affects the pattern of low-

level convergence due to internal Rossby-gravity waves. Furthermore, there have not recently been any observational studies on the relationship between convergence due to internal Rossby-gravity waves and latent heat release.

Since there were sharp meridional water-vapor mixing-ratio gradients and meridional temperature gradients at the trade inversion-ITCZ interface, it is possible that nonlinear biconstituent diffusion (Schaefer, 1975) is responsible for triggering cumulus convection even if the virtual-temperature field is initially quasi-horizontally uniform. This mechanism, which is thought to trigger cumulus convection along the dry-lines of West Texas and Oklahoma (Schaefer, 1973), can produce a small-scale virtual-temperature perturbation. In the BOMEX area, however, the nonlinear biconstituent mechanism could not be important near the sea surface, where the temperature and water-vapor fields are nearly homogeneous. It is not clear what effects synoptic-scale deformation has on the production of a small-scale virtual-temperature perturbation aloft. Synoptic-scale deformation alone cannot produce sharp enough water-vapor gradients (if the horizontal virtual-temperature gradient is initially zero) in a reasonable length of time to lead to large virtual-temperature perturbations.

There is observational and numerical evidence (Janota, 1971; Mahrt, 1972) that a boundary-layer transition between Ekman-like flow poleward of the ITCZ and accelerated flow equatorward of the ITCZ, is responsible for low-level convergence. If the boundary-layer adjustment

time is more than a day, then cross-equatorial flow might retain the characteristic vertical wind profile of the opposite hemisphere (if the atmosphere is barotropic) for 5 degrees of latitude or more away from the equator. The axis of dilatation of the boundary-layer wind at low latitudes is a zone along which there might be a boundary-layer transition if the character of the boundary layer is a function of the time since the air has crossed the equator. The relationships among deformation, low-latitude boundary-layer transitions, and low-level convergence have never been studied.

Although Pike (1968) has demonstrated numerically that the sea-surface temperature controls the position of the ITCZ, the BOMEX data do not support this idea. Therefore the indirect effects of deformation of the surface wind on the sea-surface temperatures via upwelling and downwelling are probably not important for cloud-band orientation.

Radiative effects on tropical cloud-band orientation are secondary, since typical heating and cooling rates (Albrecht and Cox, 1975) are less than those due to latent heat release in deep cumulus convection. Furthermore, cloud bands are generated on time scales too small for radiation to be important.

The kinematical generation of banded cumulus elements by synoptic-scale deformation is insignificant, since the lifetime of cumulus clouds is much less than the time it would take synoptic-scale deformation to gather cumulus clouds into a band.

The most likely mechanisms responsible for cloud-band orientation are the production of bands of cyclonic vorticity by synoptic-scale

deformation, along which CISK occurs, and the production of zones of low-latitude boundary-layer transitions in regions of cross-equatorial flow, along which low-level convergence occurs. Since tropical cloud bands are often found at significant distances from the equator (e.g., the South Pacific band; see chapter 3), the former is the more probable mechanism.

5. CASE STUDY OF THE CLOUD BAND OF 12 AUGUST, 1974 (GATE)

The most spectacular cloud band of GATE began between 2100 GMT, 11 August 1974 (Fig. 5.1a) and 0000 GMT, 12 August 1974 (Fig. 5.1b). At 0000 GMT a broken line of cloud elements oriented east-northeast to west-southwest suddenly appeared on the SMS IR satellite photograph between $4-8^{\circ}$ N, from about 22° W to 35° W. The Oceanographer's radar at this time showed a few cells oriented east-northeast to west-southwest 75 to 100 n mi to the south-southeast, and the Quadra's radar showed lines of very small cells to the east and north (Fig. 5.3). By 0600 GMT, the broken line of cloud elements appeared as a solid cloud line oriented 063° , roughly 1500 km long, and 250 km wide (Fig. 5.1c). Cirrus were evident, streaming off toward the west-northwest. At this time, the composite radar picture from the Oceanographer and the Quadra showed a well-defined band of cells less than 50 n mi wide oriented about 063° (Fig. 5.4). The cloud band had become wider at 1200 GMT (Fig. 5.2a), although the band of radar echoes remained less than 50 n mi wide (Fig. 5.5). Evidently the cirrus-anvil blowoff was making the band appear much wider than the band of precipitation. Also, at this time the radar echoes appeared to be less cellular, and more stratiform. The sequences of the 0000, 0600, and 1200 GMT radar composites indicated a component of band motion toward the north-northwest at a little more than 5 nautical mph. The band at 1800 GMT was nearly 700 km wide (Fig. 5.2b), and the band of echoes was no longer visible (Fig. 5.6).

The 0000 GMT, 13 August satellite photograph shows only a broad zone of cloud elements (Fig. 5.2c). The sequences of satellite photographs from 0000 GMT, 12 August through 0000 GMT, 13 August indicated that the banded cloud area moved westward at more than 10 degrees of longitude day⁻¹ (25 mph).

At 850 mb, a cyclonic circulation (from subjective analysis of preliminary data) centered near 12.5° N latitude, 20.5° W longitude at 1800 GMT, 11 August 1974 (Fig. 5.7), moved westward to about 29° W longitude about one day later (Fig. 5.10). Since its westward speed was only slightly less than that of the cloud band, i.e., 8.5 degrees longitude day⁻¹, it is likely that the cloud band was related to the cyclonic circulation in some way. At 1800 GMT, 11 August a cyclonic windshift from moderate southwesterly to weak southeasterly was found in region where the cloud band formed (Fig. 5.7). The axis of dilatation was oriented approximately the same as the cloud band was 6-12 hours later. When radar echoes and satellite-observed cloud elements appeared at 0000 GMT, 12 August, the cyclonic wind shift line had moved westward, and the wind field was noisier, probably as a result of the convective activity (Fig. 5.8). The orientation of the axis of dilatation was therefore difficult to determine. At 0600 GMT the region of northeast-southwest deformation was near 25-30° W longitude, and a sharp convergent zone was found near 9° N latitude (Fig. 5.9). The 1200 GMT (Fig. 5.10) analysis showed a well-defined northeast-southwest oriented axis of dilatation in the region of the cloud band. At 1800 GMT, 12 August and 0000 GMT, 13 August, the cyclonic circulation was so far west that the deformation

field could not be adequately analyzed.

The temperatures at 850 mb south of 13° N latitude ranged from about $15-19^{\circ}$ C, and were noisy. North of 13° N the temperatures were generally in excess of 22° C. Therefore, although there was a baroclinic zone, with relatively cool maritime air equatorward of the cyclonic circulation, and warm continental air poleward of the cyclonic circulation, the zone of maximum horizontal temperature gradient was far north of the cloud band, so the frontogenetical mechanism of section 2.2 was probably unimportant for the formation of the cloud band.

In conclusion, 850-mb deformation was related to the orientation of the cloud band. The 850-mb flow field at 1200 GMT, 12 August 1974 (Fig. 5.10) resembled that of an occluded midlatitude cyclone with a front trailing off to the southwest. The cloud band at this time was located along the axis of dilatation. The temperature structure was dissimilar, though.

6. CONCLUSIONS AND SUGGESTIONS FOR FUTURE RESEARCH

6.1 Summary and conclusions

The similar satellite-observed appearance of midlatitude frontal cloud bands and tropical cloud bands led to the following hypothesis: Synoptic-scale deformation, which plays a significant role in the formation and structure of the former, is related in some way to the latter.

A simple quasigeostrophic analytical model of a frontal zone in the tropical troposphere was used to determine quantitatively what values of geostrophic deformation, meridional virtual-temperature gradient, and static stability are needed to produce thermally-forced vertical motions that are strong enough to trigger deep cumulus convection (if the troposphere is conditionally unstable). For a precipitation rate of 1 inch day⁻¹, latent heat release induced vertical motions on the order of 1-2 cm sec⁻¹.

The orientations of climatological bands of cloudiness in the North Pacific, North Atlantic, South Indian, and South Pacific were well-correlated with the orientations of the respective axes of dilatation of the climatological gradient-level wind.

An objective-analysis method in which the interpolating function is determined by the statistics of synchronous and asynchronous data was used to estimate the 950, 850, 700, and 450-mb wind fields during BOMEX Phase IV from vertically averaged rawinsonde data. At the lower three levels significant correlations were found between the orientations of cloud bands and the orientations of the respective axes of dilatation

of the nondivergent wind. The significance of the correlations decreased with height. The average axis of dilatation was zonally oriented on days when similarly oriented cloud bands were present, and was meridional on days when cloud bands were nonzonally oriented or were absent.

There is some evidence that the orientation of a spectacular cloud band during GATE was qualitatively similar to that of the 850-mb axis-of-dilatation orientation. It was therefore concluded that tropical cloud-band orientation is related to the deformation of the nondivergent wind at low levels.

According to the simple quasigeostrophic analytical model, horizontal virtual-temperature gradients in the BOMEX area were too small for thermal forcing, in the absence of latent heat release, to be of dynamical importance. The latent heat release inferred from heat and moisture-budget analyses, according to the model, could produce significant vertical motions.

Several mechanisms by which synoptic-scale deformation in a barotropic atmosphere may be responsible for cloud-band orientation were considered. The formation of bands of gradient-level cyclonic vorticity by synoptic-scale deformation, along which CISK occurs, is the most likely mechanism.

6.2 Suggestions for future research

There are many possibilities for future observational and numerical research. When the final GATE data are available, detailed case studies of cloud-band formation and decay will yield more evidence about what role synoptic-scale deformation plays. New South Pacific island

rawinsonde data may be used to study the relationship between synoptic-scale deformation and the spectacular northwest-southeast oriented South Pacific cloud band. Techniques should be developed to incorporate aircraft data and satellite data into the objective analysis scheme along with rawinsonde data.

The effects of deformation on the vorticity field can be studied with a simple barotropic numerical model. The effects of synoptic-scale deformation on low-latitude boundary-layer flow and on dry-line formation should be studied numerically, also.

Appendix A

Determination of the axis-of-dilatation
orientation and the resultant deformation

If higher order nonlinear terms are neglected, a Taylor series expansion of the horizontal wind components in natural coordinates about point "0" is as follows:

$$\begin{bmatrix} U \\ V \end{bmatrix} = \begin{bmatrix} U_0 \\ V_0 \end{bmatrix} + \frac{1}{2} \begin{bmatrix} \delta & 0 \\ 0 & \delta \end{bmatrix} \begin{bmatrix} s \\ n \end{bmatrix} + \frac{1}{2} \begin{bmatrix} 0 & -\xi \\ \xi & 0 \end{bmatrix} \begin{bmatrix} s \\ n \end{bmatrix} \\ + \frac{1}{2} \begin{bmatrix} S & R \\ R & -S \end{bmatrix} \begin{bmatrix} s \\ n \end{bmatrix}$$

where,

$$\delta = \frac{\partial U}{\partial s} + U \frac{\partial \beta}{\partial n} \quad (\text{divergence})$$

$$\xi = U \frac{\partial \beta}{\partial s} - \frac{\partial U}{\partial n} \quad (\text{vorticity})$$

$$S = \frac{\partial U}{\partial s} - U \frac{\partial \beta}{\partial n} \quad (\text{stretching deformation})$$

$$R = U \frac{\partial \beta}{\partial s} + \frac{\partial U}{\partial n} \quad (\text{shearing deformation})$$

and, U is the wind component along the direction of the flow, V is the wind component perpendicular and to the left of the flow, s is the coordinate along the flow, n is the coordinate perpendicular and to the

left of the flow, and β is the direction of the wind vector measured counterclockwise from due east. The first three terms on the right-hand side of the above expression represent uniform translation, expansion (contraction) about point O , and rotation about point O ; the fourth (and last) term represents contraction and elongation about the principal axes with no change in volume.

To find the orientation of the principal axes let $A = \frac{1}{2} \begin{bmatrix} S & R \\ R & -S \end{bmatrix}$

and $\tilde{r} = \begin{bmatrix} s \\ n \end{bmatrix}$. Then $A \tilde{r} = \lambda \tilde{r}$ for some constant λ and some vector \tilde{r} if A is a nonsingular matrix. So,

$$A \tilde{r} = \frac{1}{2} \begin{bmatrix} S & R \\ R & -S \end{bmatrix} \begin{bmatrix} s \\ n \end{bmatrix} = \lambda \begin{bmatrix} s \\ n \end{bmatrix}$$

For a nontrivial solution to exist, $A \tilde{r} - \lambda \tilde{r} = 0 = \tilde{r} (A - \lambda I)$, where I is the identity matrix. Then,

$$\lambda = \pm \frac{1}{2} (S^2 + R^2)^{1/2} = \pm \frac{D}{2}$$

It follows that $\frac{r_2}{r_1} = \tan \theta_d = \frac{D-S}{R}$, where the subscript "d" means deformation. Since $\tan \frac{\gamma}{2} = \frac{1 - \cos \gamma}{\sin \gamma} = \tan \theta_d$ when $\tan \gamma = R/S$,

$$\tan \theta_d = \frac{R}{S} \quad \text{and} \quad \frac{S}{D} = \cos 2\theta_d$$

Then, $A \tilde{r} = A' \tilde{r}'$, where $A' = \frac{1}{2} \begin{bmatrix} D & 0 \\ 0 & -D \end{bmatrix}$

$$\text{and} \quad \tilde{r}' = \begin{bmatrix} s' \\ n' \end{bmatrix} = \begin{bmatrix} \cos \theta_d & \sin \theta_d \\ -\sin \theta_d & \cos \theta_d \end{bmatrix} \begin{bmatrix} s \\ n \end{bmatrix}$$

In other words, if the coordinate axes are rotated by angle θ_d and $D > 0$, then a fluid element is being stretched only along the s' -axis and foreshortened only along the n' -axis; if $D < 0$, the reverse is true.

Appendix B

Computation of water vapor mixing ratio from
relative humidity, pressure, and temperature

The relative humidity, $RH = q/q_s$, where q is the water vapor mixing

ratio, and $q_s(T) = 0.622 \frac{e_s(T)}{p - e_s(T)}$. The saturation vapor pressure,

$$e_s(T) \approx e_3 \left(\frac{T_3}{T} \right)^a e^{[(a-b)(1 - \frac{T_3}{T})]}, \text{ where}$$

$$a = 5.00650,$$

$$b = 19.83923,$$

$$T_3 = 273.16^\circ \text{ K, and}$$

$$e_3 = 0.611 \text{ cb,}$$

$$\text{So, } q = (RH)[q_s(T,p)]$$

Appendix C

Computation of relative humidity from wet-bulb temperature, pressure, and dry-bulb temperature

The relation between T_w , T , and q is

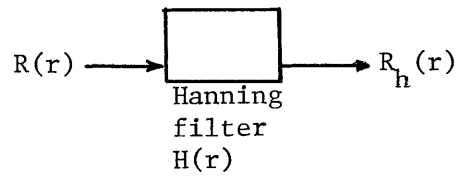
$$(T - T_w)(C_{pd} + q C_{pv}) = (q_w - q) L_v(T_w)$$

where $L_v(T_w) = L_{v_3} + (C_{pv} - C_l)(T - T_3)$ and

$$\begin{aligned} C_{pv} &= 1876.5 \text{ kJ ton}^{-1} \text{ deg}^{-1}, \\ C_l &= 4187 \text{ kJ ton}^{-1} \text{ deg}^{-1}, \text{ and} \\ L_{v_3} &= 2501 \text{ kJ ton}^{-1}. \end{aligned}$$

The quantities $e_s(T_w)$, $q_s(T_w) = q_w$, $e_s(T)$, and $q_s(T)$ were obtained from the equations in Appendix B. The water-vapor mixing-ratio q was obtained from the above relation. The relative humidity (RH) was easily obtained from $RH = q/q_s$.

Appendix E
Hanning filter



$$R_h(r) = H(r) R(r)$$

$$H(n \Delta r) = \frac{1}{2} \left(1 + \cos \frac{\pi n}{m} \right) \quad \begin{array}{l} r = 0, 1, 2, \dots, m \\ r > m \end{array}$$

$$= 0$$

where n is the lag number,
 m is the maximum lag number,
and Δr is the lag increment

Appendix F

The discrete Fourier transform of the autocovariance function: the power spectrum

The following is valid for a discrete spatial autocovariance function $R(n \Delta r)$:

The power spectral density function

$$S\left(\frac{kf_c}{m}\right) = 2 \Delta r \left[R(0) + 2 \sum_{n=1}^{m-1} R(n \Delta r) \cos\left(\frac{\pi n k}{m}\right) + (-1)^k R(m) \right]$$

where k is the harmonic number, $f_c = \frac{1}{2\Delta r}$, the Nyquist sampling rate, Δr is the spatial lag increment, n is the lag number, and m is the maximum lag number.

For a discrete temporal autocovariance function $R(n \Delta t)$, Δr is replaced by Δt , the time lag increment.

Appendix G

The discrete inverse Fourier transform of a power spectrum: the autocovariance function

The following is valid for a discrete spatial autocovariance function

$R(n \Delta r)$:

The autocovariance function

$$R(n \Delta r) = \frac{\Delta f}{2} \left[S(0) + 2 \sum_{k=1}^{m-1} S\left(\frac{kf_c}{m}\right) \cos\left(\frac{\pi kn}{m}\right) + (-1)^n S(f_c) \right]$$

where, $\Delta f = f_c/m$, the frequency increment, and the other symbols are defined in Appendix F.

For a discrete temporal autocovariance function $R(n \Delta t)$, Δr is replaced by Δt , the time lag increment.

Appendix H

The discrete Fourier transform of a
cross-covariance function: the cross-spectral
density function

The cospectral density function,

$$C_{xy} \left(\frac{kf}{m} \right) = 2 \Delta t [A(0) + 2 \sum_{n=1}^{m-1} A(n \Delta t) \cos \left(\frac{\pi nk}{m} \right) + (-1)^k A(k \Delta t)]$$

and the quadrature,

$$Q_{xy} \left(\frac{kf}{m} \right) = 4 \Delta t \sum_{n=1}^{m-1} B(n \Delta t) \sin \left(\frac{\pi nk}{m} \right)$$

$$\begin{aligned} \text{where } A(n \Delta t) &= \frac{1}{2} [R_{xy}(n \Delta t) + R_{yx}(n \Delta t)] \\ &= \frac{1}{2} [R_{xy}(n \Delta t) + R_{xy}(-n \Delta t)] \\ B(n \Delta t) &= \frac{1}{2} [R_{xy}(n \Delta t) - R_{yx}(n \Delta t)] \\ &= \frac{1}{2} [R_{xy}(n \Delta t) - R_{xy}(-n \Delta t)] \end{aligned}$$

and the symbols were defined in Appendix F and in the text; Δt is used in place of Δr , and $R(n \Delta t)$ is used in place of $m(n \Delta r)$.

Appendix I

Relaxation formulas

$$\psi_{\nu+1} = \psi_{\nu} + a[\sum_4 \psi_{\nu,\nu+1} - 4\psi_{\nu} - \xi]$$

$$\chi_{\nu+1} = \chi_{\nu} + a[\sum_4 \chi_{\nu,\nu+1} - 4\chi_{\nu} - \delta]$$

where ν is the iteration number, \sum_4 is the sum of the 4 values surrounding the point and a is chosen (for rapid convergence) as follows:

$$a = \frac{1 + \gamma_{\text{OPT}}}{4}, \text{ where } \gamma_{\text{OPT}} = \frac{1 - \sin \beta}{1 + \sin \beta},$$

$\beta = \cos^{-1}[1/2(\cos \pi/N + \cos \pi/M)]$, where N is the number of grid points in the x-direction, and M is the number of grid points in the y-direction.

Appendix J

Estimation of the accuracy of the measurements of the
the orientation of the axis of dilatation(θ_d)

Near point Q ,

$$\theta_d \approx \theta_d(R_0, S_0) + \left. \frac{\partial \theta_d}{\partial R} \right|_{R_0, S_0} (R - R_0) + \left. \frac{\partial \theta_d}{\partial S} \right|_{R_0, S_0} (S - S_0) ,$$

where R and S are defined in Appendix A.

$$\left. \frac{\partial \theta_d}{\partial R} \right|_{R_0, S_0} = \frac{1}{2} \frac{1}{S_0} \frac{1}{1 + (R_0/S_0)^2} = b_1$$

$$\left. \frac{\partial \theta_d}{\partial S} \right|_{R_0, S_0} = - \frac{R}{2S_0^2} \frac{1}{1 + (R_0/S_0)^2} = b_2$$

$$\text{so, } \sigma_{\theta_d}^2 \approx b_1^2 \sigma_R^2 + b_2^2 \sigma_S^2 + 2b_1 b_2 \sigma_{RS}$$

If the grid spacing is Δ ,

$$R = [(V_{i+1j} - V_{i-1j}) + (U_{ij+1} - U_{ij-1})]/2\Delta$$

$$S = [(U_{i+1j} - U_{i-1j}) - (V_{ij+1} - V_{ij-1})]/2\Delta$$

If the wind field is isotropic and homogeneous,

Appendix J (continued)

$$\begin{aligned} \sigma_{\theta}^2 &\approx 2b_1^2(1/2\Delta) [\sigma_V^2 + \sigma_U^2 - m_U(2\Delta) - m_V(2\Delta) + \sigma_{ab}] \\ &+ 2b_2^2(1/2\Delta)^2 [\sigma_V^2 + \sigma_U^2 - m_U(2\Delta) - m_V(2\Delta) + \sigma_{cd}] \\ &+ 2b_1 b_2 \sigma_{RS} \end{aligned}$$

where

$$\begin{aligned} a &= V_{i+j} - V_{i-1j} , \\ b &= U_{ij+1} - U_{ij-1} , \\ c &= U_{i+1j} - U_{i-1j} , \\ d &= V_{ij+1} - V_{ij-1} , \end{aligned}$$

and $m(r)$ is the covariance function.

Appendix K

Designations of all objective analyses for
BOMEX Phase IV

<u>Date</u>	<u>Time</u>	<u>Julian day</u>	<u>Band Case</u>	<u>950 mb</u>	<u>850 mb</u>	<u>700 mb</u>	<u>450 mb</u>
7/11/69	--	192	n.d.	--	--	--	--
12	--	193	n.d.	--	--	--	--
13	12	194	yes	L1567 M0506	J1025 J1047	S1026 U0241	S1037 G0821
14	12	195	yes	M0514 M1143	P1560 Q0030	W0557 W1499	U0950, H1135 H1223
15	12	196	yes	M0649 M1148	K0271 K0277 K0308	T0145 W1501	T0154 G0824
16	--	197	n.d.	--	--	--	--
17	18	198	no	Q00471 Q10599 Q1465	Q0047 Q0599 Q1465	Q0047 Q1091	Z0480 Z0292 Z0497
18	18	199	yes	M0652 S0469(A)	S0298 S0469	S0298 S0469(A)	A0203 A0412(A)
19	12	200	yes	M1155 L1569 M0508	J1020 J1064	S1029 W1502	S1042 G0825
20	12	201	yes	M0516 M1158	K0269 K0309	T0147 W1503	T0157 G0826
21	12	202	yes	M0653 M1159	K0650 K0898	U0939 W1504	U0944 G0827
22	12	203	yes	L1571 M0509	K1215 XNF0395	S1031 W1505	S1048 G0829
23	12	204	not in ana- lysis area	--	N1353 N1408	--	--
24	12	205	yes	H0456 H01435	H0457 I0256	H0458 I0256	H0459 I1171

Appendix K (continued)

<u>Date</u>	<u>Time</u>	<u>Julian day</u>	<u>Band Case</u>	<u>950 mb</u>	<u>850 mb</u>	<u>700 mb</u>	<u>450 mb</u>
7/25/69	12	206	yes	L1572 M0512	J0689 J0780	S1033 W1506	S1051 G0830
26	12	207	no	--	00116 00133	--	--
27	18	208	yes	M0517 M1160	I0736 I1172	T0150 W1507	T0162 G0835
28	18	209	yes	L1575 M0513	J0688 J0782	V0721 W1508(A)	S1053 G0831
29	--	210	n.d.	--	--	--	--

The upper designation is for the objective analysis and the lower designation is for the plot and the analysis of parameters derived from the wind field; the designation refers the job number assigned by the computer.

(A) indicates that some aircraft data were used.

Appendix L

Computation of vertical velocity (ω)

$$\omega_{950} = (p_0 - 95) \delta_{950}$$

$$\omega_{850} = (p_0 - 90) \delta_{950} + 5 \delta_{850}$$

$$\omega_{700} = (p_0 - 90) \delta_{950} + 12.5 \delta_{850} + 7.5 \delta_{700}$$

$$\omega_{450} = (p_0 - 90) \delta_{950} + 12.5 \delta_{850} + 20 \delta_{700} + 12.5 \delta_{450}$$

where δ is in units of sec^{-1} , and ω is in units of cb sec^{-1} , and p_0 is the surface pressure in cb

Appendix M

Derivation of heat and moisture-budget equations

$$\Delta q = \Delta E + \Delta w \text{ (first law of thermodynamics (per unit mass))}$$

$$= C_v \Delta T + p \Delta v$$

$$Q = C_p \frac{dT}{dt} - v \omega \text{ (by dividing by } \Delta t \text{, taking the limit as } \Delta t \rightarrow 0)$$

$$L(c - e) + Q_R = C_p \frac{dT}{dt} - \frac{R_d \omega T}{p} \text{ (assuming that the addition of heat is due to radiation and latent heat release only)}$$

$$= C_p \left[\frac{\partial T}{\partial t} + \nabla \cdot \mathbf{V} T - T \nabla \cdot \mathbf{V} \right] - \frac{R_d \omega T}{p} \text{ (by assuming a steady-state)}$$

$$= C_p \left[\frac{\partial \overline{UT}}{\partial x} + \frac{\partial \overline{VT}}{\partial y} + \frac{\partial \overline{\omega T}}{\partial p} \right] - \frac{R_d \omega T}{p}$$

Let $() = (\overline{\quad}) + ()'$, where the former term indicates the grid-scale average, and the latter term indicates the sub-grid (eddy) scale, i.e., the scale of cumulus convection (only two scales are assumed).

Expanding each variable into its grid-scale average and eddy component, and averaging over the grid-scale,

$$\begin{aligned} L(c - e) + Q_R &= C_p \left[\frac{\partial \overline{UT}}{\partial x} + \frac{\partial \overline{VT}}{\partial y} + \frac{\partial \overline{\omega T}}{\partial p} \right] - \frac{R_d \overline{\omega T}}{p} + C_p \left[\frac{\partial \overline{U'T'}}{\partial x} + \frac{\partial \overline{V'T'}}{\partial y} + \frac{\partial \overline{\omega'T'}}{\partial p} \right] \\ &\quad - \frac{R_d}{p} \overline{\omega'T'} \\ &= C_p \left[\overline{U} \frac{\partial \overline{T}}{\partial x} + \overline{V} \frac{\partial \overline{T}}{\partial y} \right] + \overline{\omega} \left[C_p \frac{\partial \overline{T}}{\partial p} - \frac{R_d \overline{T}}{p} \right] + C_p \left[\frac{\partial \overline{U'T'}}{\partial x} + \frac{\partial \overline{V'T'}}{\partial y} \right] \end{aligned}$$

$$+ \frac{\partial \overline{\omega' T'}}{\partial p}] - \frac{R_d}{p} \overline{\omega' T'}$$

$$\text{and } S = C_p \frac{\partial \bar{T}}{p \partial p} - \frac{R_d \bar{T}}{p}$$

$$\text{Let } \left| \frac{\partial \bar{T}}{\partial x} \right|, \left| \frac{\partial \bar{T}}{\partial y} \right| \sim 1^\circ \text{C}/1000 \text{ km} = 10^{-6} \text{ }^\circ \text{C m}^{-1} \quad \frac{\partial T}{\partial p} \quad 30^\circ/50 \text{ cb} = .6 \text{ }^\circ \text{C cb}^{-1}$$

$$|\bar{U}|, |\bar{V}| \sim 10 \text{ m sec}^{-1}$$

$$x, y \sim 100 \text{ km} = 10^5 \text{ m}$$

$$|\bar{\omega}| \sim 10^{-4} \text{ cb sec}^{-1}$$

$$\bar{T} \sim 250^\circ \text{ K}$$

$$|\overline{U' T'}|, |\overline{V' T'}| \lesssim \sigma |U'| |T'|$$

where σ = fraction of area covered by deep cumulus convection $\sim 10^{-2}$

$$|U'| \sim 5 \text{ m sec}^{-1}$$

$$|T'| \sim 1^\circ \text{ K}$$

$$|\overline{\omega' T'}| \lesssim \sigma |\omega'| |T'| \quad \text{where } |\omega'| \lesssim 10^{-1} \text{ cb sec}^{-1} \text{ (10 m sec}^{-1}\text{)}$$

$$\text{Then, } \left| C_p \bar{U} \frac{\partial \bar{T}}{\partial x} \right|, \left| C_p \bar{V} \frac{\partial \bar{T}}{\partial y} \right| \sim 10^3 \cdot 10 \cdot 10^{-6} = 10^{-2} \quad \text{kJ ton}^{-1} \text{ sec}^{-2} \quad (1)$$

$$\left| \bar{\omega} C_p \frac{\partial T}{\partial p} \right| \sim 10^{-4} \cdot 10^3 \cdot (.6) = 6 \times 10^{-2} \quad (2)$$

$$\left| \frac{\bar{\omega} R_d \bar{T}}{p} \right| \sim \frac{10^{-4} (300) (250)}{(50)} = 1.5 \times 10^{-1} \quad (3)$$

$$\left| C_p \frac{\partial \overline{U' T'}}{\partial x} \right|, \left| C_p \frac{\partial \overline{V' T'}}{\partial y} \right| \lesssim 10^3 \frac{(5)(1)}{10^5} 10^{-2} \sim (5) 10^{-4} \quad (4)$$

$$\left| c_p \frac{\overline{\partial \omega' T'}}{\partial p} \right| \lesssim 10^3 \frac{10^{-1}(1)}{10} 10^{-2} \sim 10^{-1} \quad (5)$$

$$\left| \frac{R_d \overline{\omega' T'}}{p} \right| \lesssim \frac{(300) 10^{-1}(1)}{(50)} 10^{-2} \sim 6 \times 10^{-3} \quad (6)$$

Then (4) and (6) can be neglected relative to (1), (2), (3), and (5)

So,

$$L(c - e) + Q_R = c_p [\bar{u} \frac{\partial \bar{T}}{\partial x} + \bar{v} \frac{\partial \bar{T}}{\partial y}] + \bar{\omega} s + c_p \frac{\overline{\partial \omega' T'}}{\partial p}$$

$$\text{where } Q_1 = c_p [\bar{u} \frac{\partial \bar{T}}{\partial x} + \bar{v} \frac{\partial \bar{T}}{\partial y}]$$

Now, $e - c = \frac{dq}{dt}$ (continuity equation for water vapor)

$$= \frac{\partial q}{\partial t} + \nabla \cdot qV - q \nabla \cdot V \quad (\text{from steady-state assumption})$$

$$= \frac{\partial qU}{\partial x} + \frac{\partial qV}{\partial y} + \frac{\partial q\omega}{\partial p}$$

$$= \frac{\partial \bar{q}\bar{u}}{\partial x} + \frac{\partial \bar{q}\bar{v}}{\partial y} + \frac{\partial \bar{q}\bar{\omega}}{\partial p} + \frac{\partial \overline{q'u'}}{\partial x} + \frac{\partial \overline{q'v'}}{\partial y} + \frac{\partial \overline{q'\omega'}}{\partial p}$$

(by expanding variables into grid-scale average and eddy terms)

$$= \bar{u} \frac{\partial \bar{q}}{\partial x} + \bar{v} \frac{\partial \bar{q}}{\partial y} + \bar{\omega} \frac{\partial \bar{q}}{\partial p} + \frac{\overline{q'u'}}{\partial x} + \frac{\overline{q'v'}}{\partial y} + \frac{\overline{q'\omega'}}{\partial p}$$

$$\text{Let } \bar{q} \sim 10 \text{ g/kg} \sim 10^{-2} \quad \frac{\partial \bar{q}}{\partial p} \sim 3 \text{ g/kg/10 cb} \sim 3 \times 10^{-4}$$

$$|\overline{q'u'}| \sim |\overline{q'v'}| \lesssim \sigma |q'| |v'|$$

$$\text{where } |q'| \sim 5 \text{ g/kg} = 5 \times 10^{-3}$$

$$\text{Then, } \left| \bar{u} \frac{\partial \bar{q}}{\partial x} \right|, \left| \bar{v} \frac{\partial \bar{q}}{\partial y} \right| \sim \frac{10 \cdot 10^{-2}}{10^5} \sim 10^{-6} \text{ sec}^{-1} \quad (1)$$

$$\left| \bar{\omega} \frac{\partial \bar{q}}{\partial p} \right| \sim 10^{-4} (3) 10^{-4} = 3 \times 10^{-8} \quad (2)$$

$$\left| \frac{\partial \overline{q'u'}}{\partial x} \right|, \left| \frac{\partial \overline{q'v'}}{\partial y} \right| \lesssim \frac{5 \times 10^{-3} \cdot 5 \cdot 10^{-2}}{10^5} = 2.5 \times 10^{-9} \quad (3)$$

$$\left| \frac{\partial \overline{q'\omega'}}{\partial p} \right| \lesssim \frac{5 \times 10^{-3} \cdot 10^{-1} \cdot 10^{-2}}{10} = 5 \times 10^{-7} \quad (4)$$

Then (3) can be neglected relative to (1), (2), and (4)

$$\text{So, } e - c = \bar{u} \frac{\partial \bar{q}}{\partial x} + \bar{v} \frac{\partial \bar{q}}{\partial y} + \bar{\omega} \frac{\partial \bar{q}}{\partial p} + \frac{\partial \overline{q'\omega'}}{\partial p}$$

Appendix N

Computation of $E_0 - P_0$

$$P_0 - E_0 \approx \frac{1}{g} [(90 - p_0) Q'_{2950} - 12.5 Q'_{2850} - 20.0 Q'_{2700} - 30.0 Q'_{2450}]$$

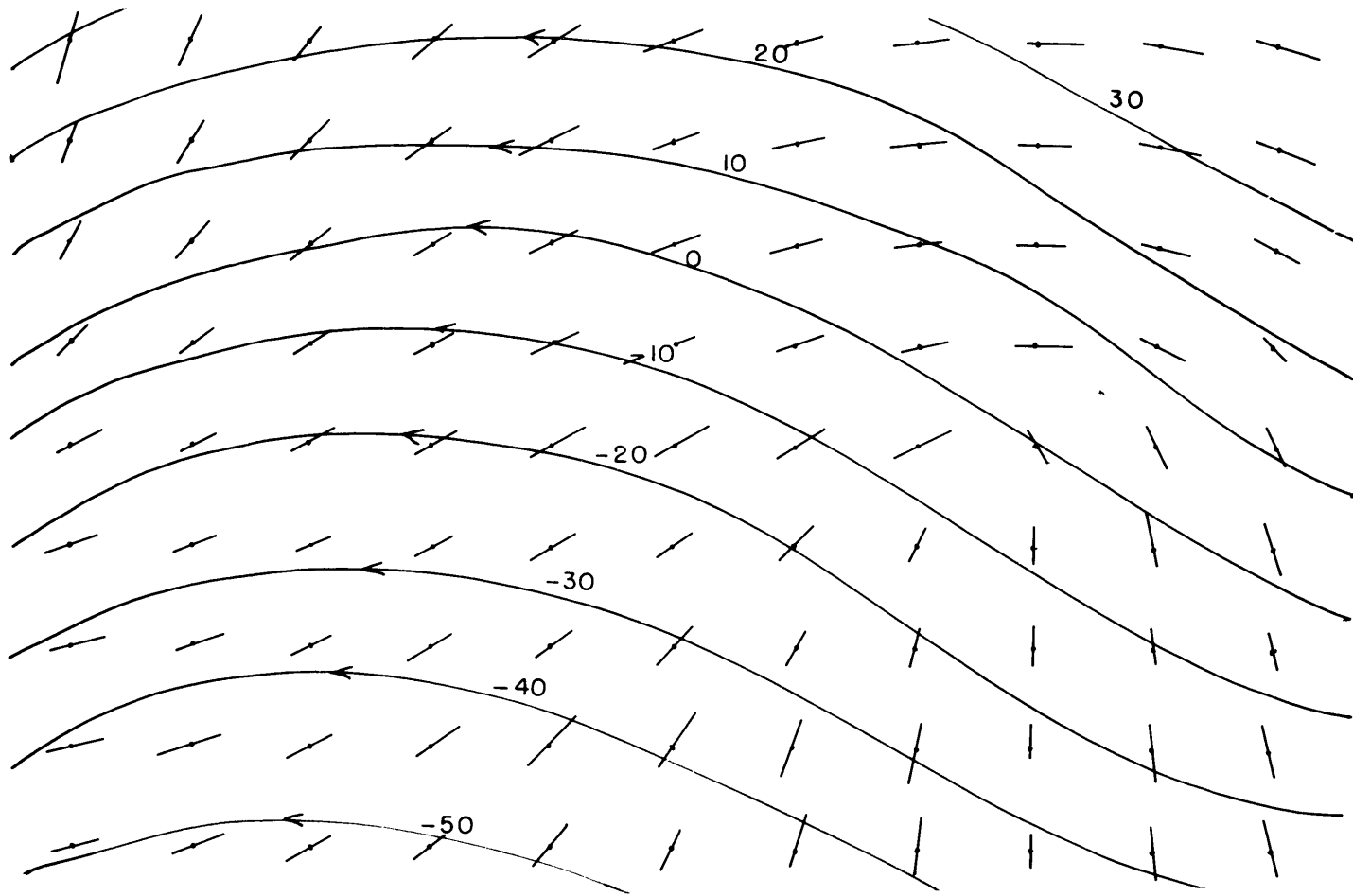


Fig. 1.1 Streamlines and axes of dilatation of an idealized kinematic model of a wave in the easterlies: The streamfunction $\psi = Ke^{-ay^2} \cos 2\pi(bx - cy)$ is depicted by the solid lines in units of $10^5 \text{ m}^2 \text{ sec}^{-1}$ ($k=2 \times 10^6$, $a=2 \times 10^{-12}$, $b=5 \times 10^{-7}$, $c=10^{-7}$). The orientations of the dashed lines represent the relative magnitudes of the resultant deformation. Grid spacing is 100 km.

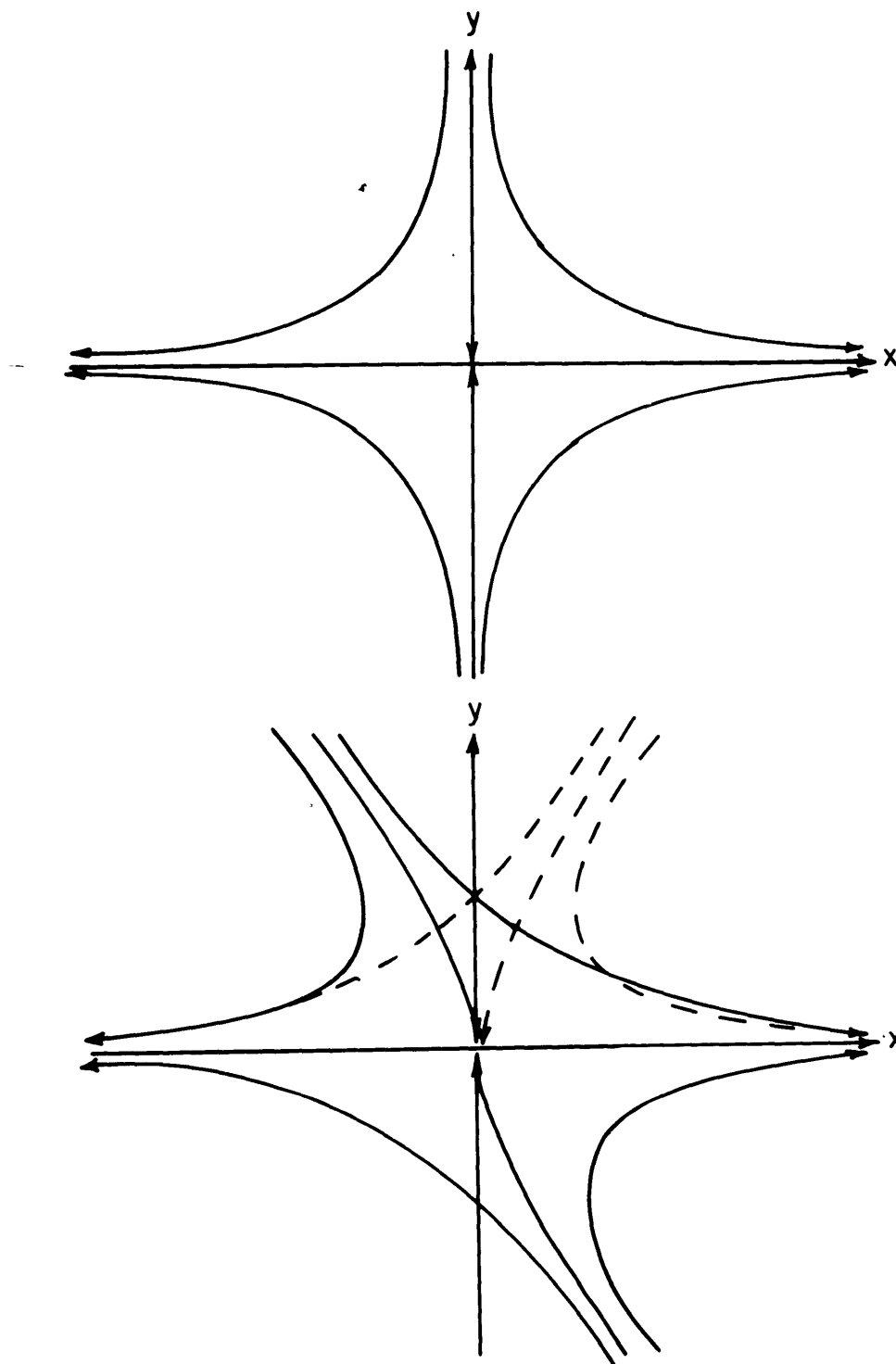


Fig. 2.1 Streamlines for the quasigeostrophic analytic model:
 (Above) The streamlines at 1000 mb are depicted by solid lines.
 (Below) The streamlines aloft are depicted by solid lines for $y < 0$;
 for $y > 0$, the streamlines are depicted by solid lines for a warm core
 at $v=0$, and by dashed lines for a monotonically increasing temperature
 with y .

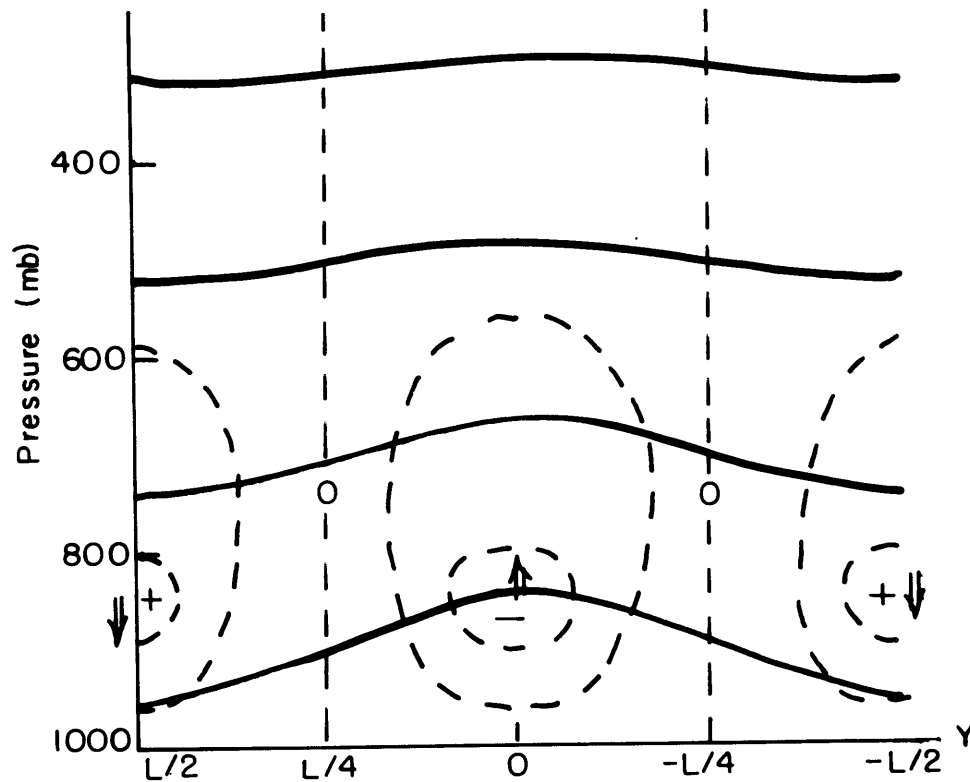


Fig. 2.2a Temperature (T) and vertical-velocity (ω) distributions in the meridional plane for the quasigeostrophic analytic model (warm core at $y=0$); Isopleths of ω are given by dashed lines. Arrows indicate the direction of vertical mass flux. The solid lines represent the meridional temperature distribution as a function of height.

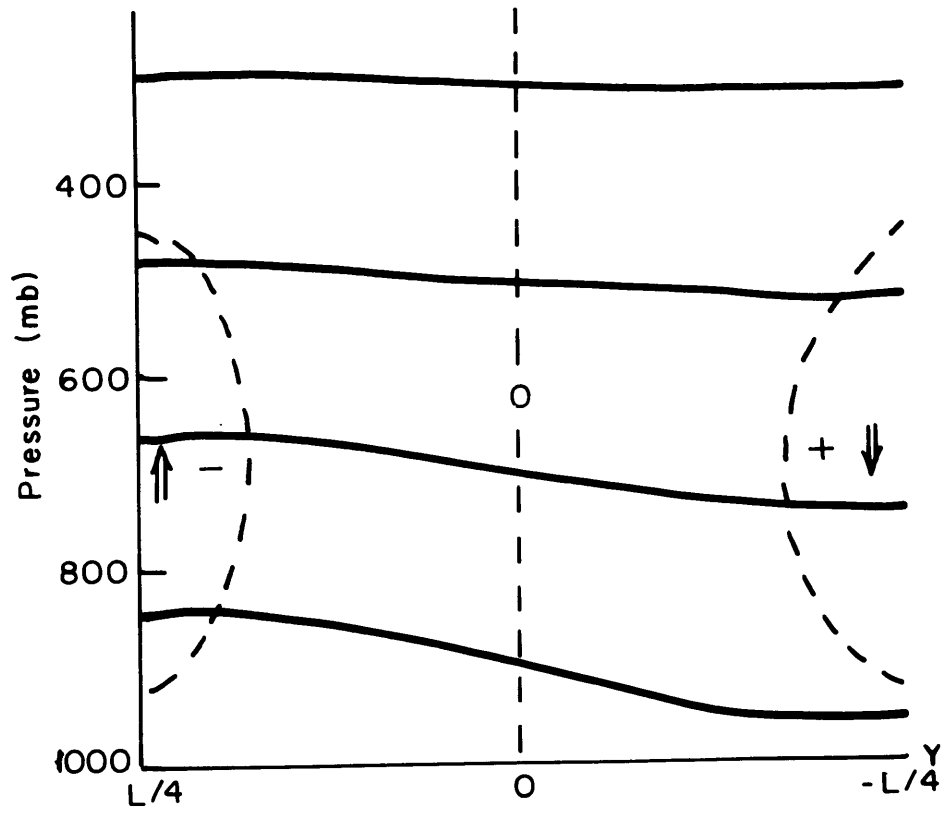


Fig. 2.2b. Same as 2.2a, but for monotonically increasing temperature with y .

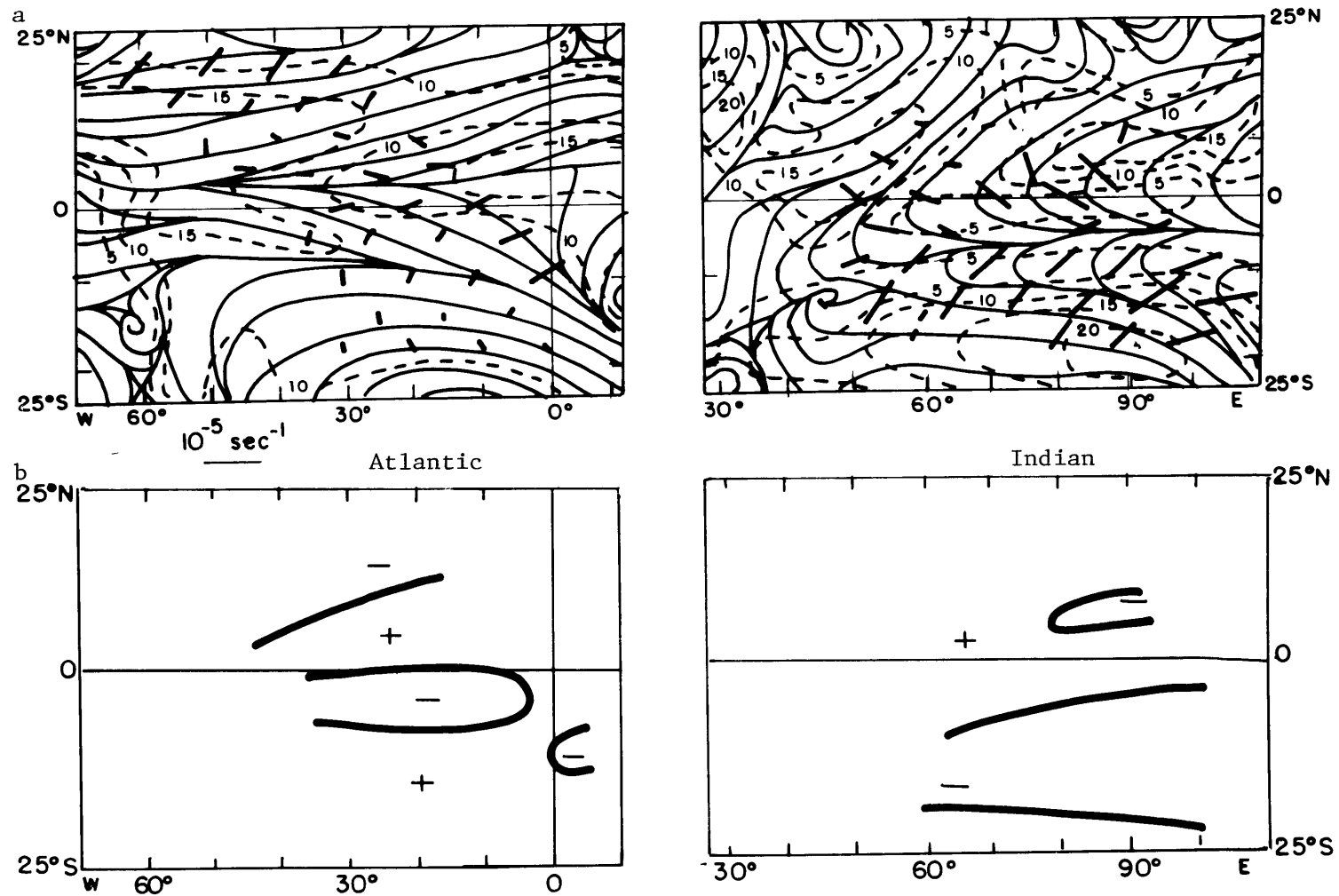


Fig. 3.1 (Above) January resultant gradient-level wind (streamlines and isotachs) after Atkinson (1970). The orientation of the axis of dilatation is the orientation of the thick dashed lines; the magnitude of the resultant deformation is depicted by the length of the thick dashed lines. (Below) Sign of the vorticity.

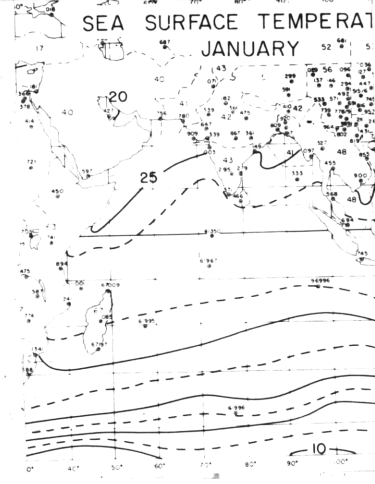
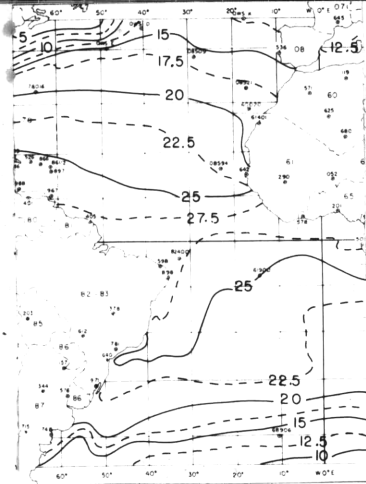
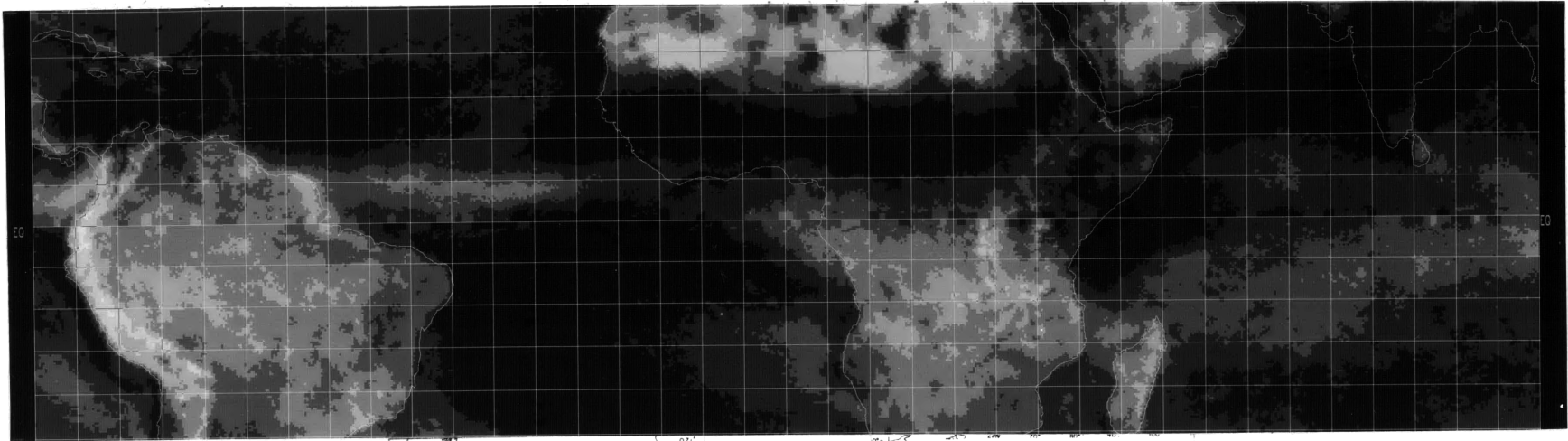


Fig. 3.2 (Above) Mean cloud-brightness chart for January for 1400-1600 local time (after Miller and Feddes). (Below) Sea-surface temperatures (after Newell et al).

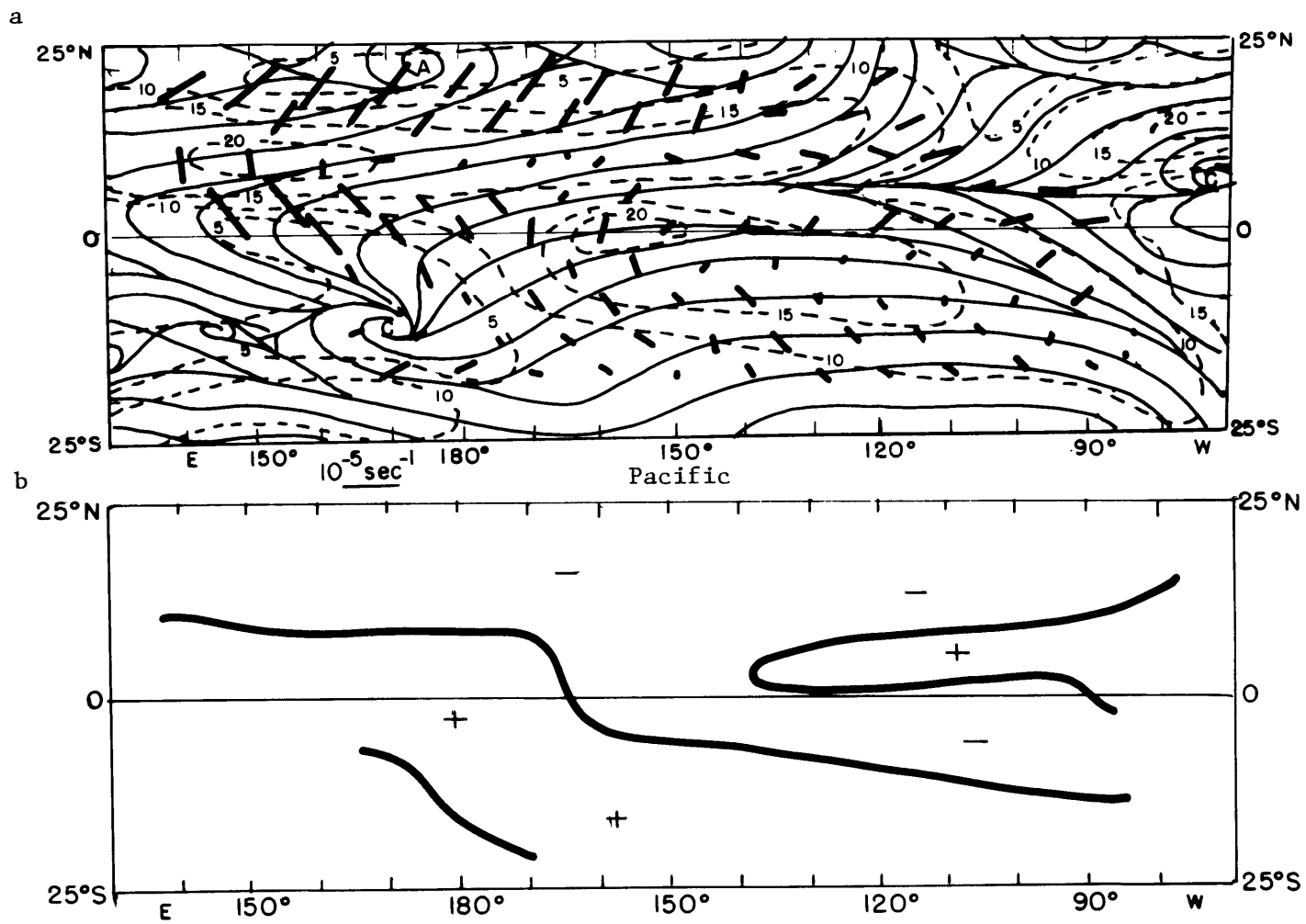


Fig. 3.3 Same as Fig. 3.1.

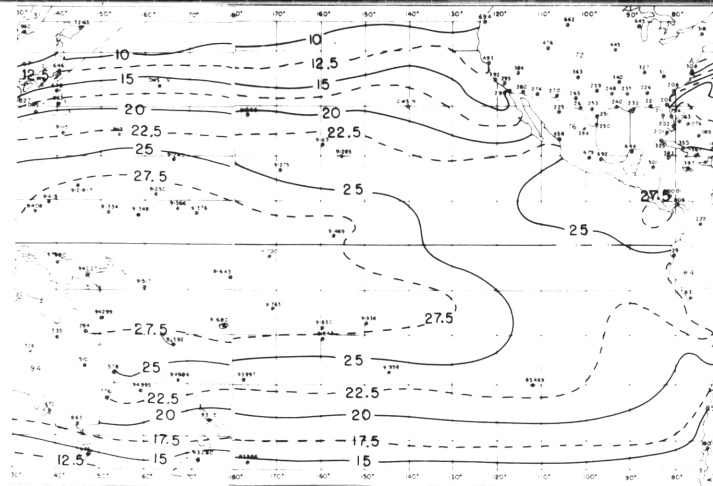
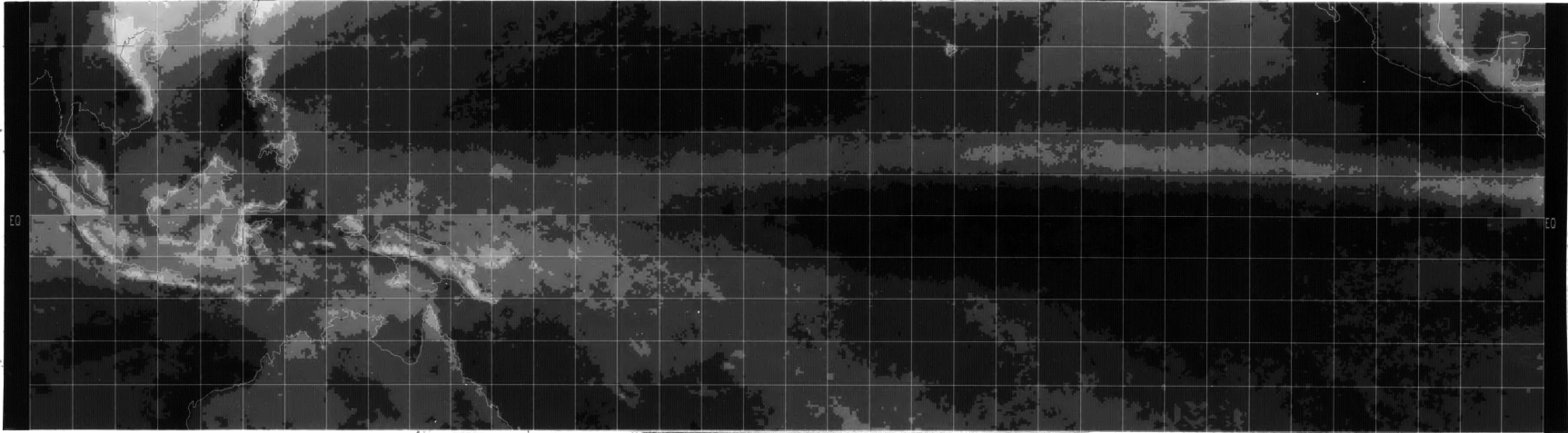


Fig. 3.4 same as Fig. 3.2.

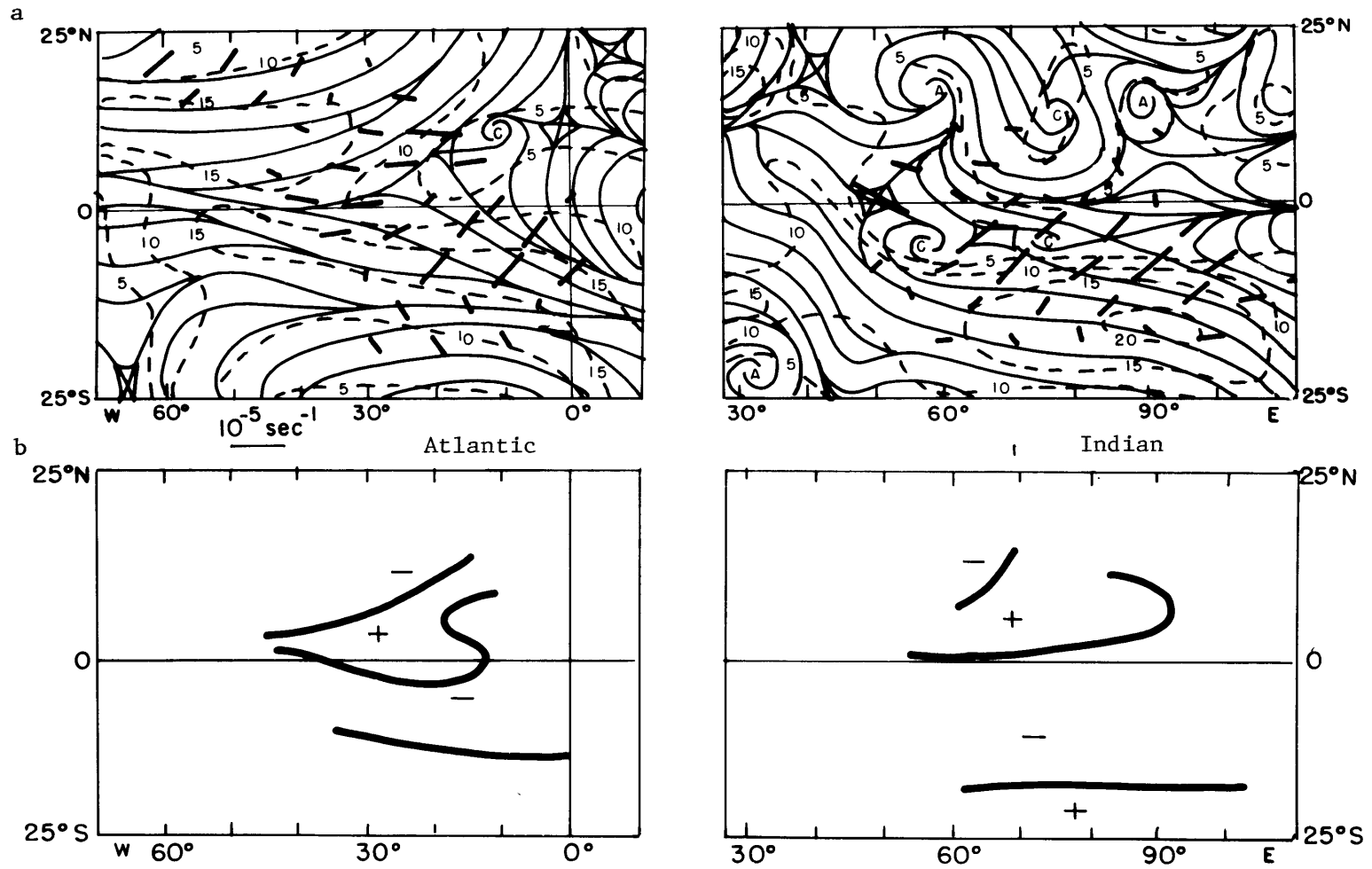


Fig. 3.5 Same as Fig. 3.1, but for April.

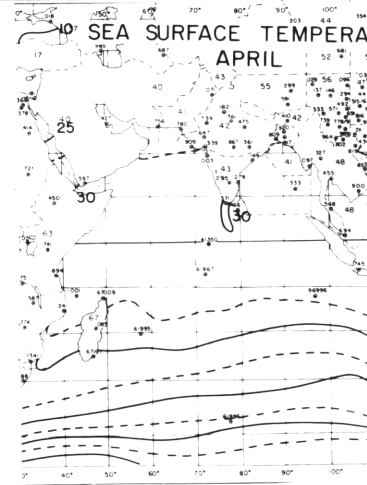
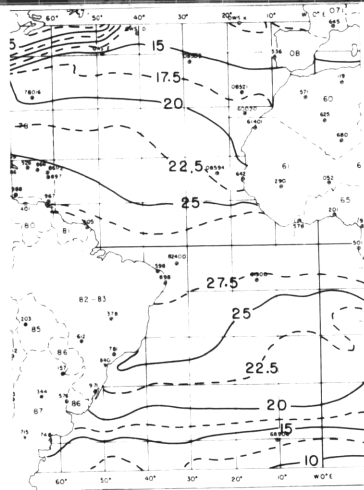
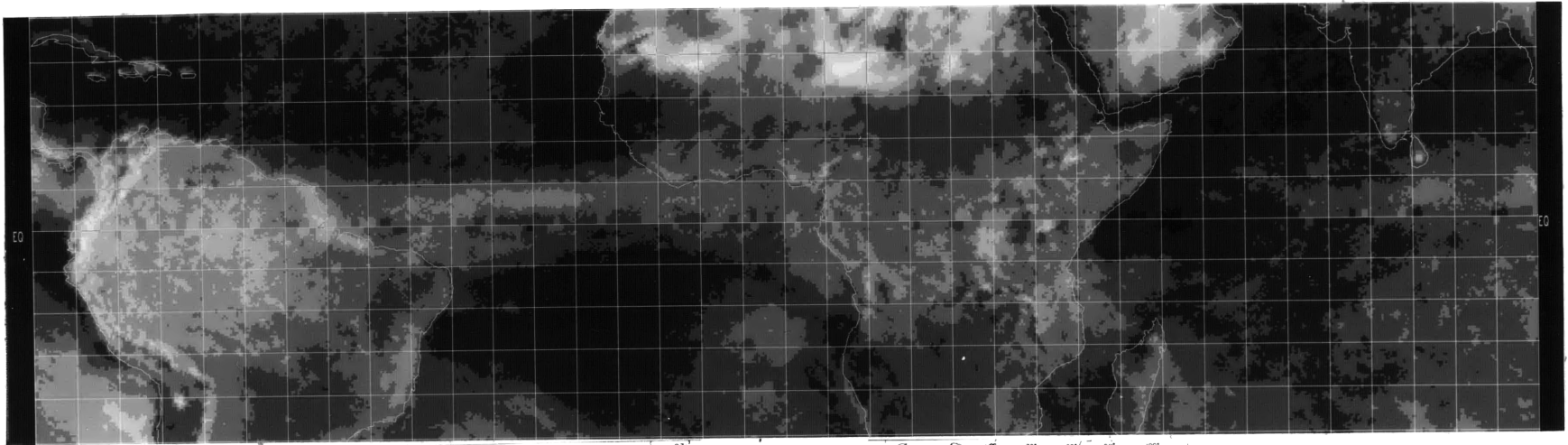


Fig. 3.6 same as Fig. 3.2 , but for April.

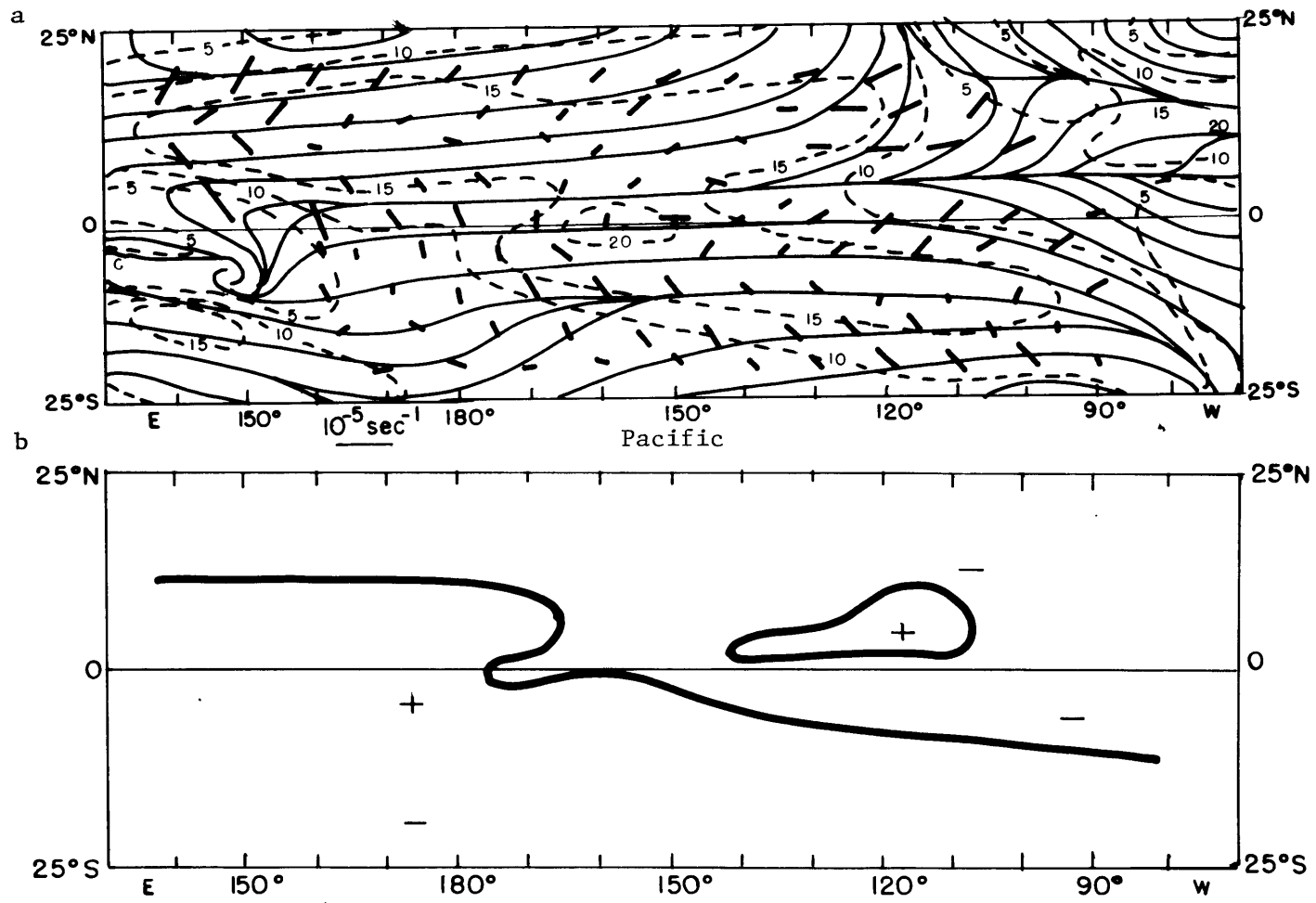


Fig. 3.7 Same as Fig. 3.1, but for April.

0 1 2 3 4 5 6 7 8

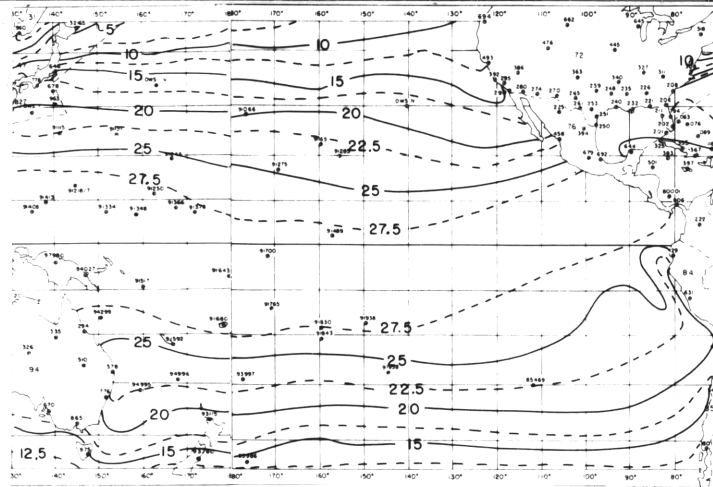
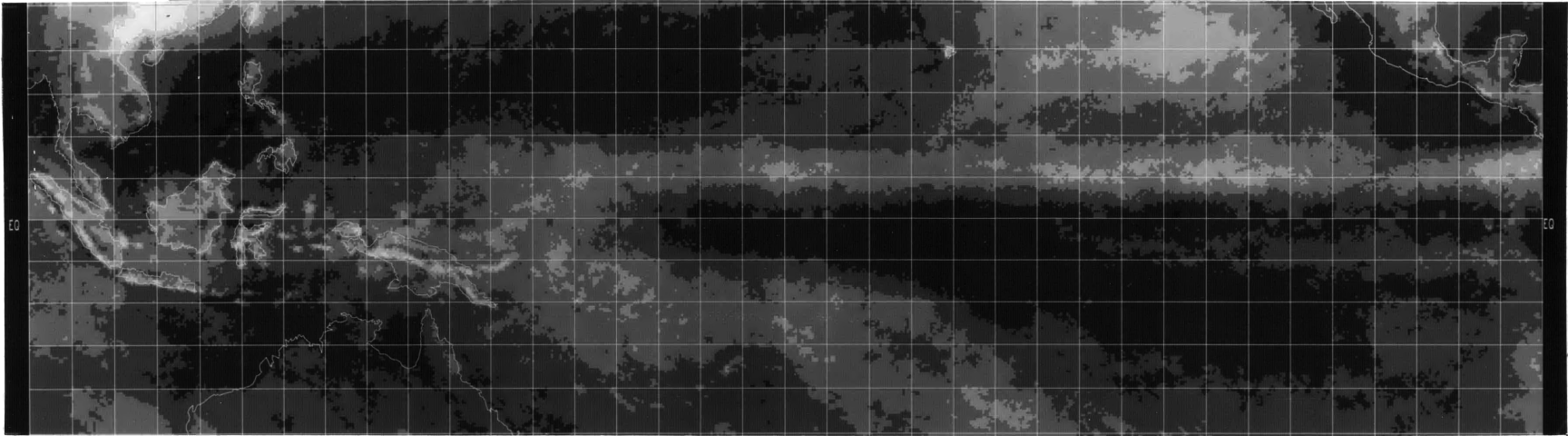


Fig. 3.8 same as Fig. 3.2, but for April

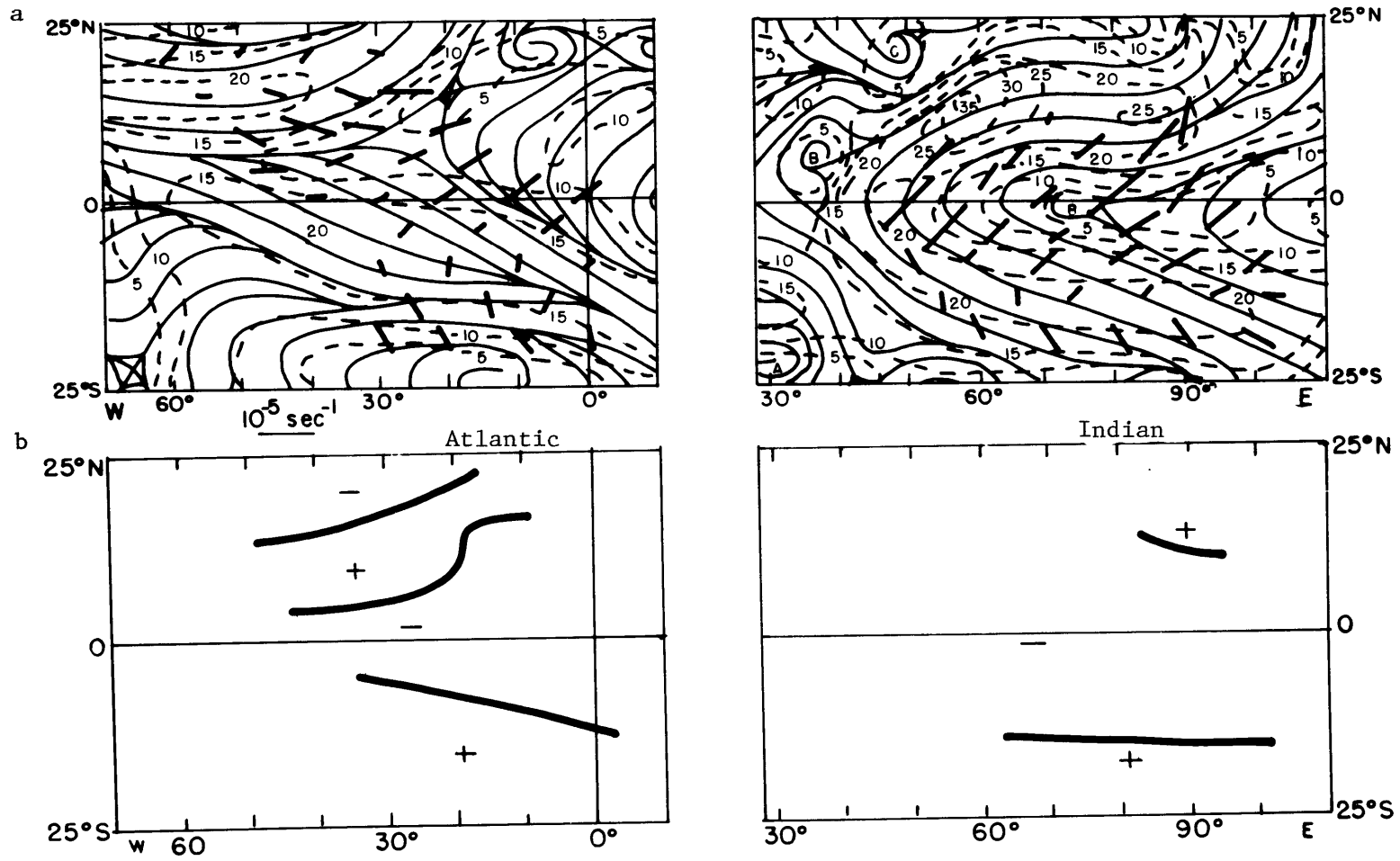


Fig. 3.9 Same as Fig. 3.1, but for July.

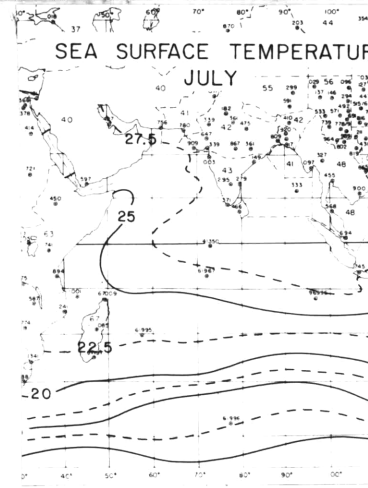
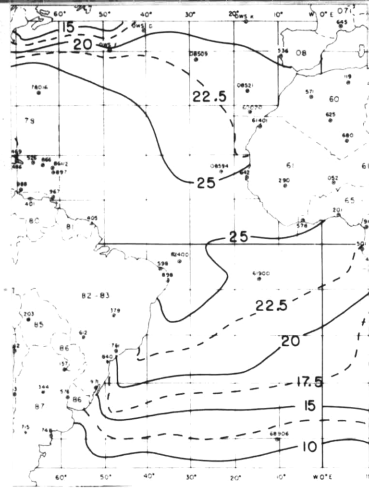
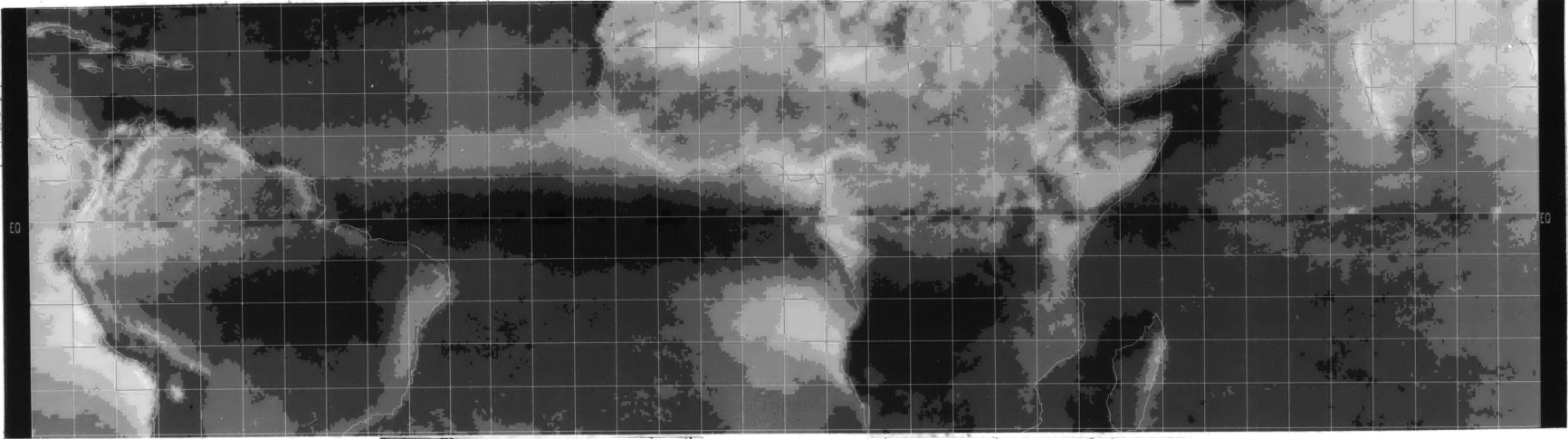


Fig. 3.10 same as Fig. 3.2, but for July

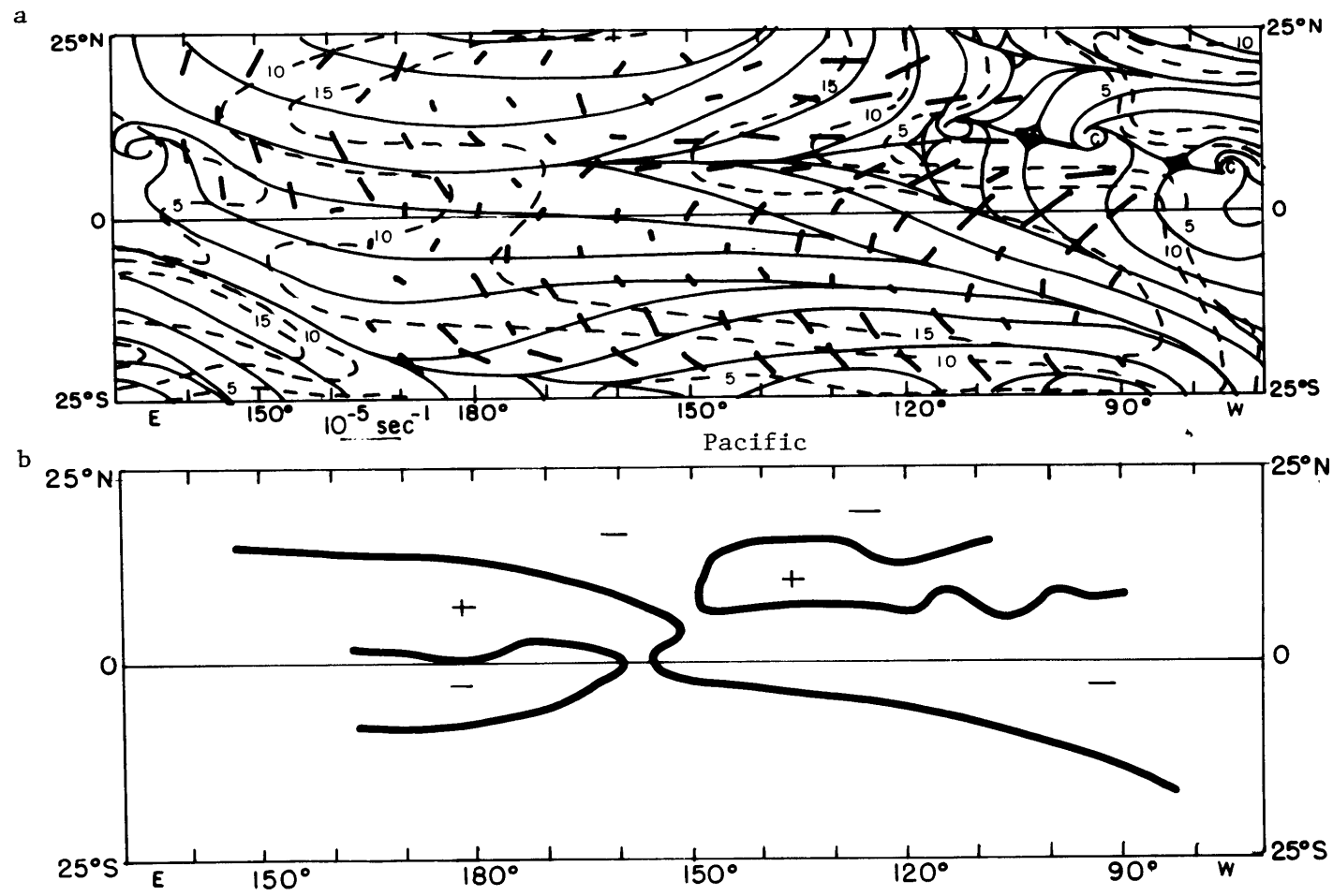


Fig. 3.11 Same as Fig. 3.1, but for July.

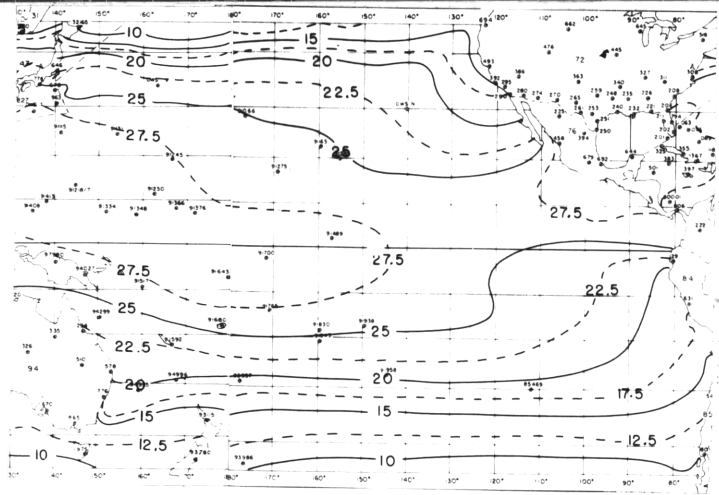
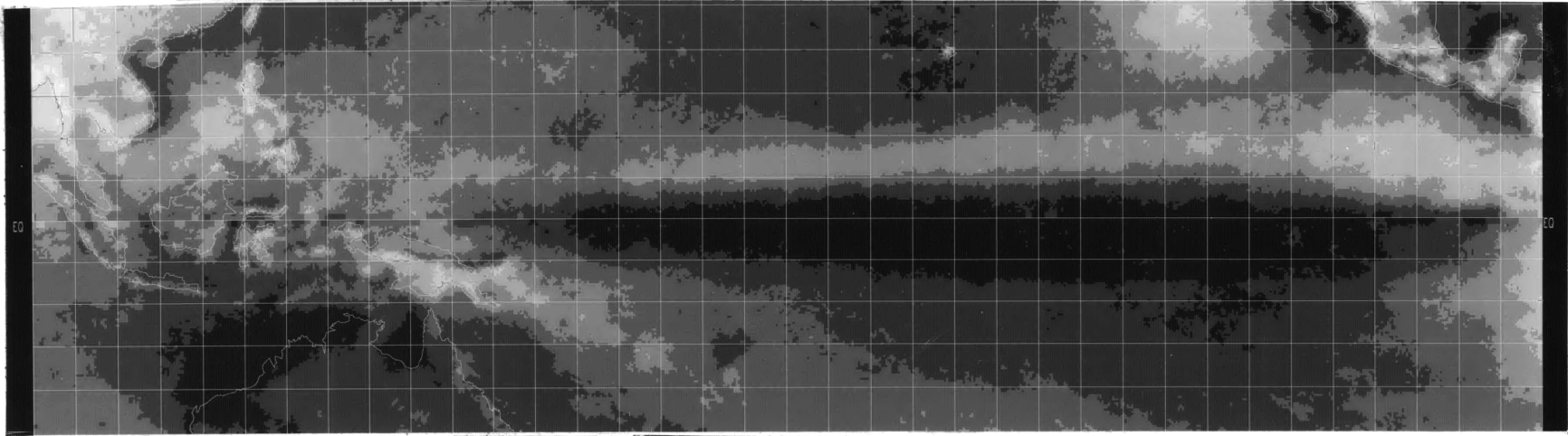


Fig. 3.12 same as Fig. 3.2, but for July

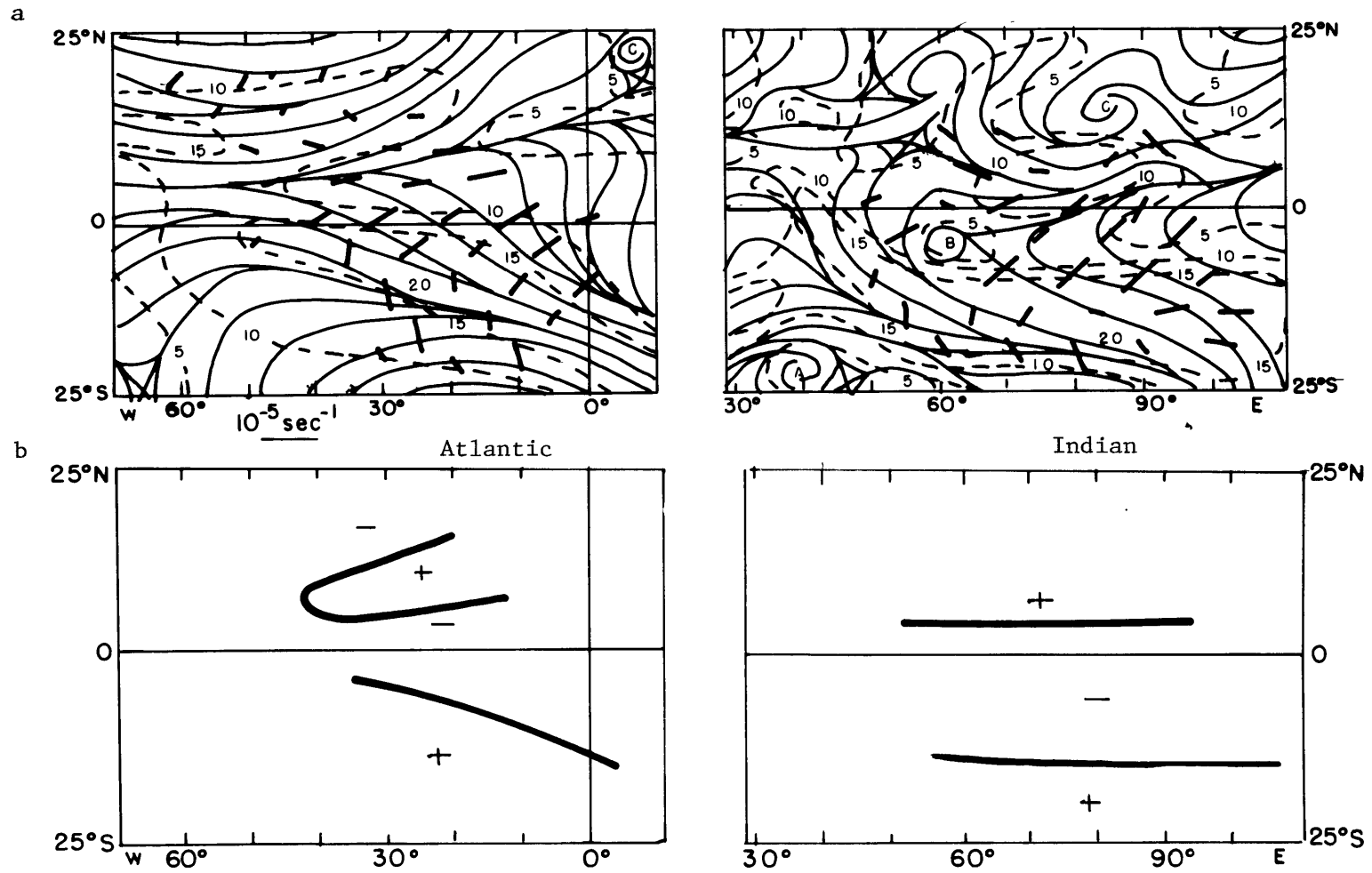


Fig. 3.13 Same as Fig. 3.1, but for October.

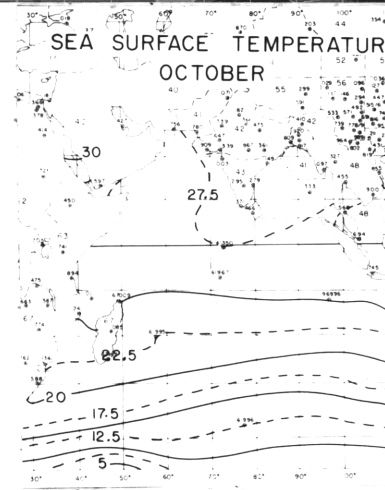
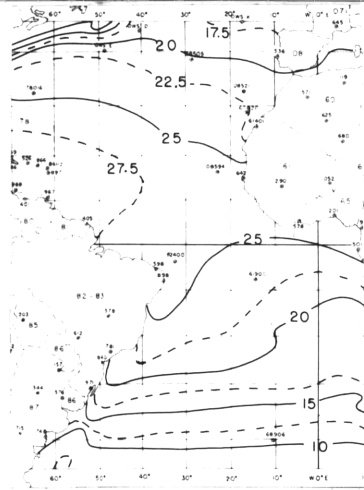
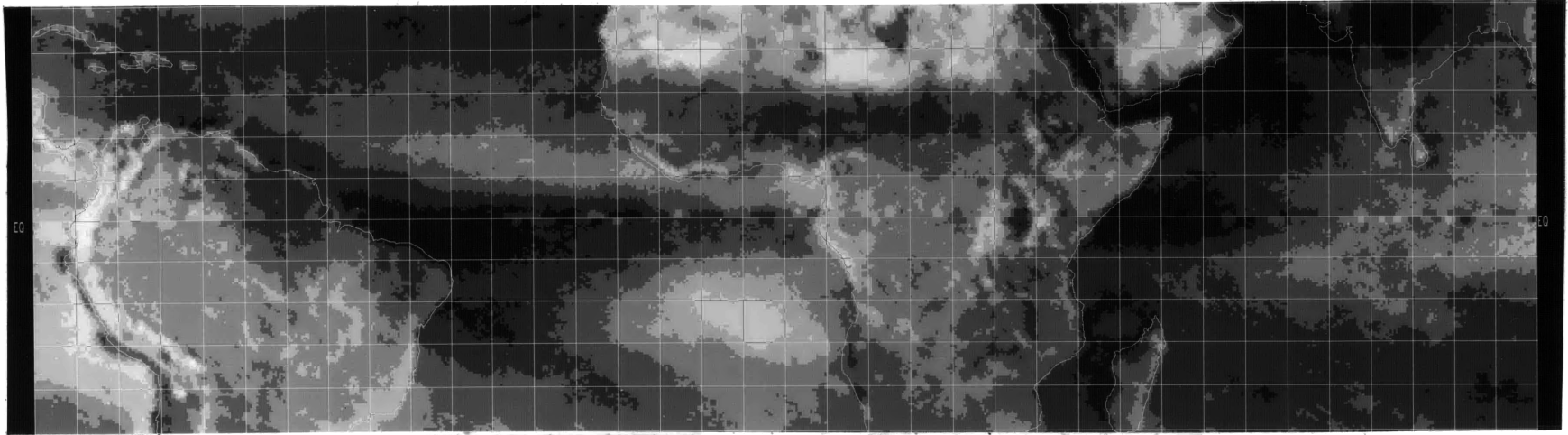


Fig. 3.14 same as Fig. 3.2, but for October

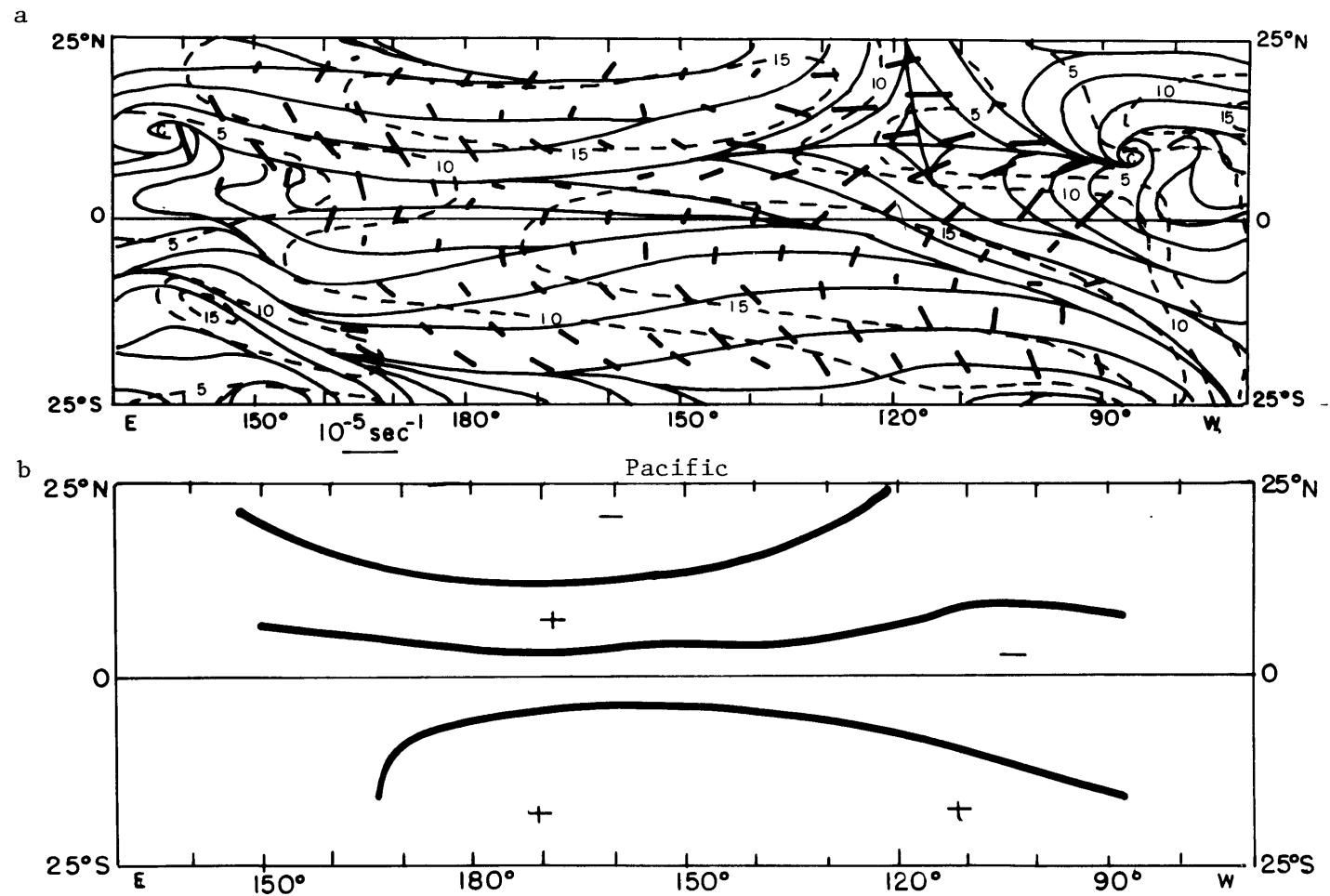


Fig. 3.15 Same as Fig. 3.1, but for October.

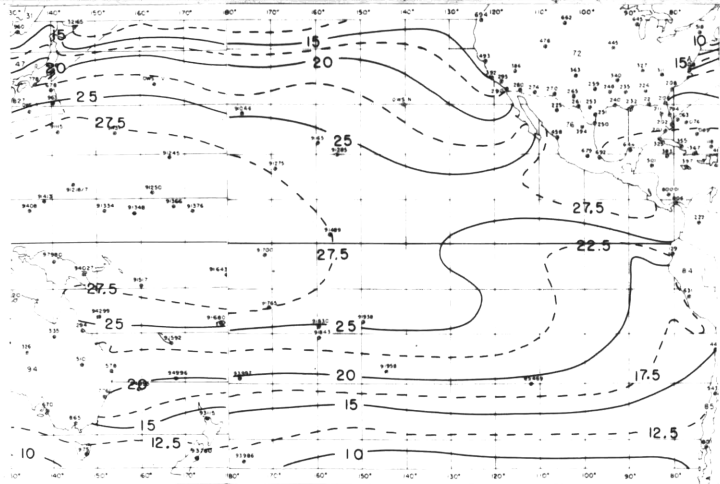
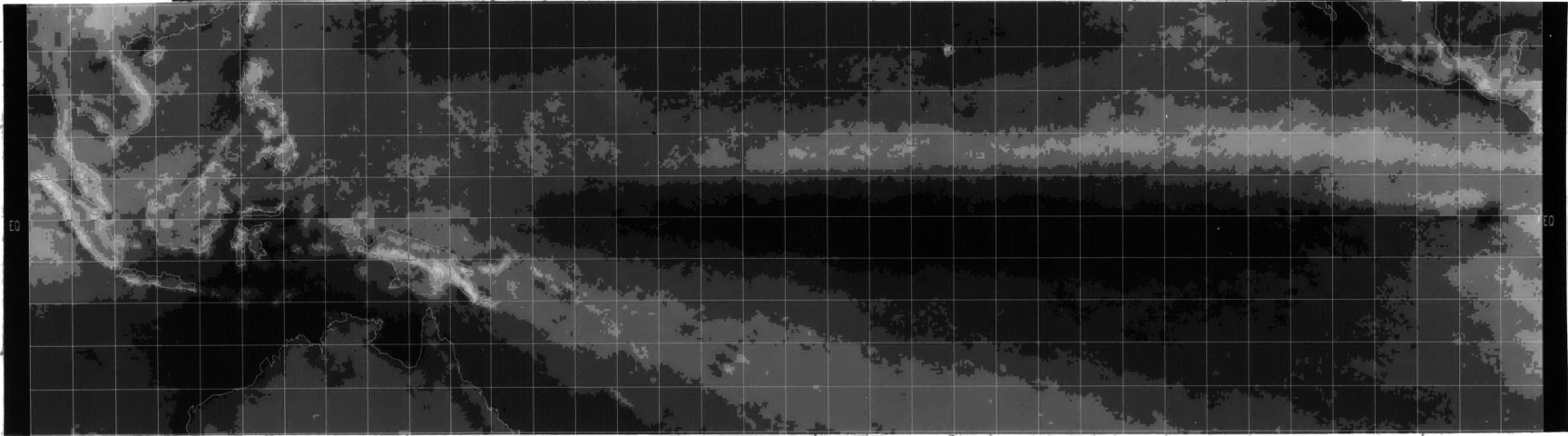


Fig. 3.16 same as Fig. 3.2, but for October

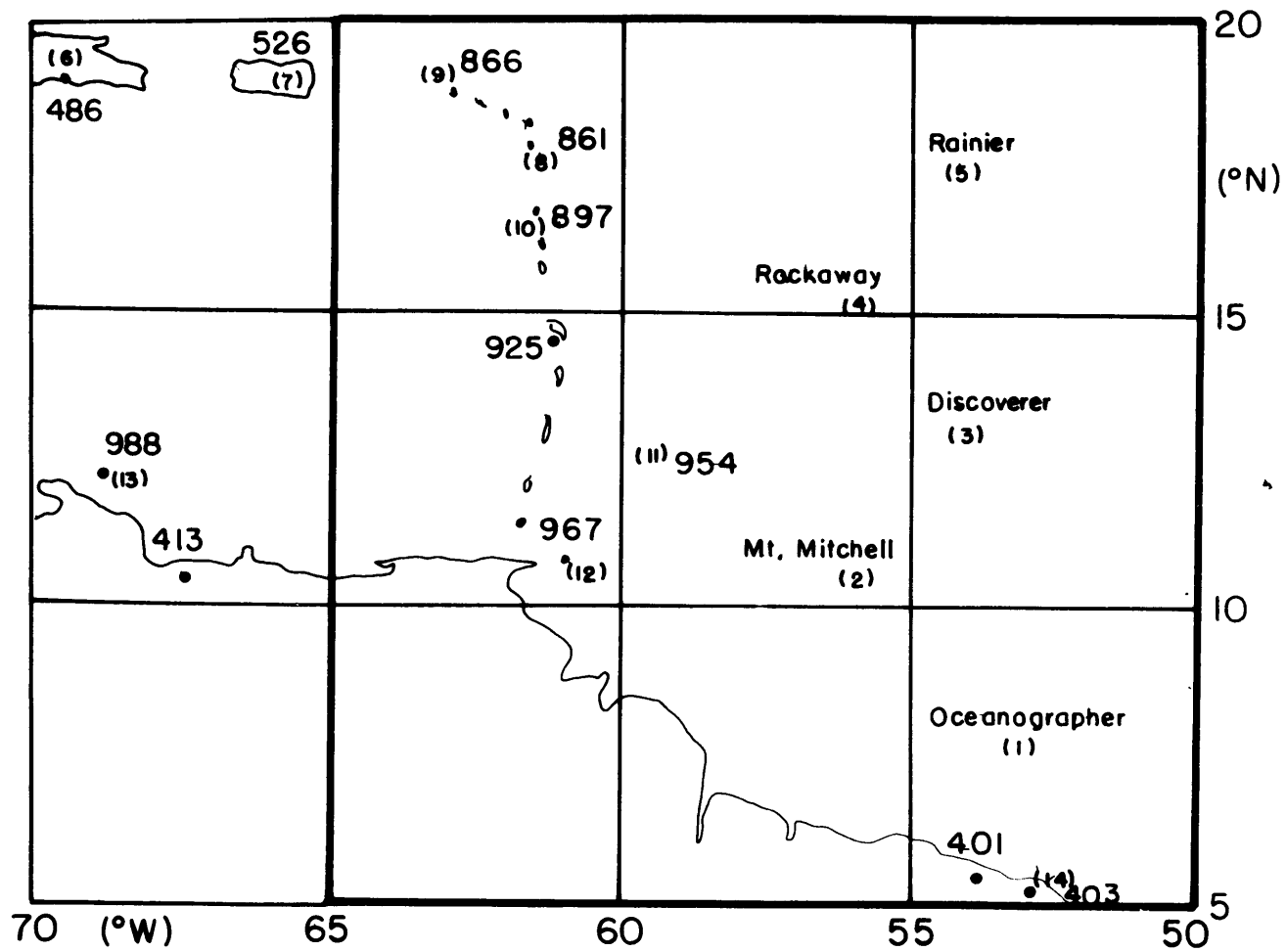
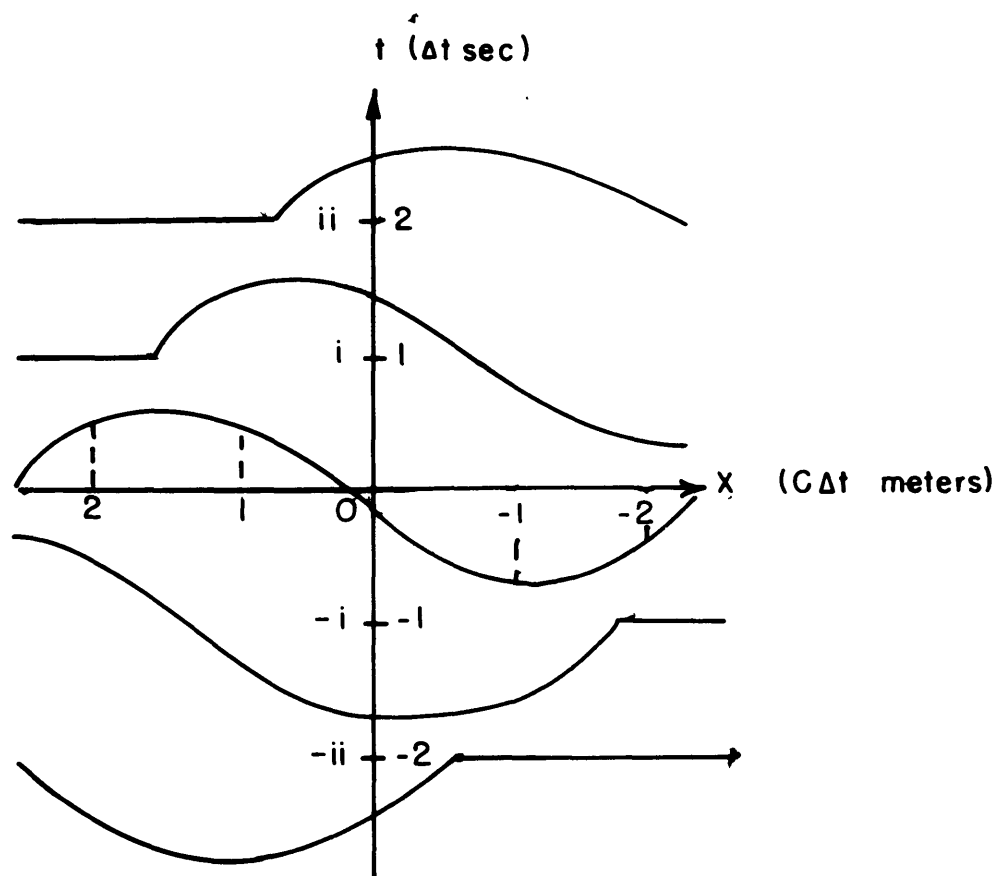
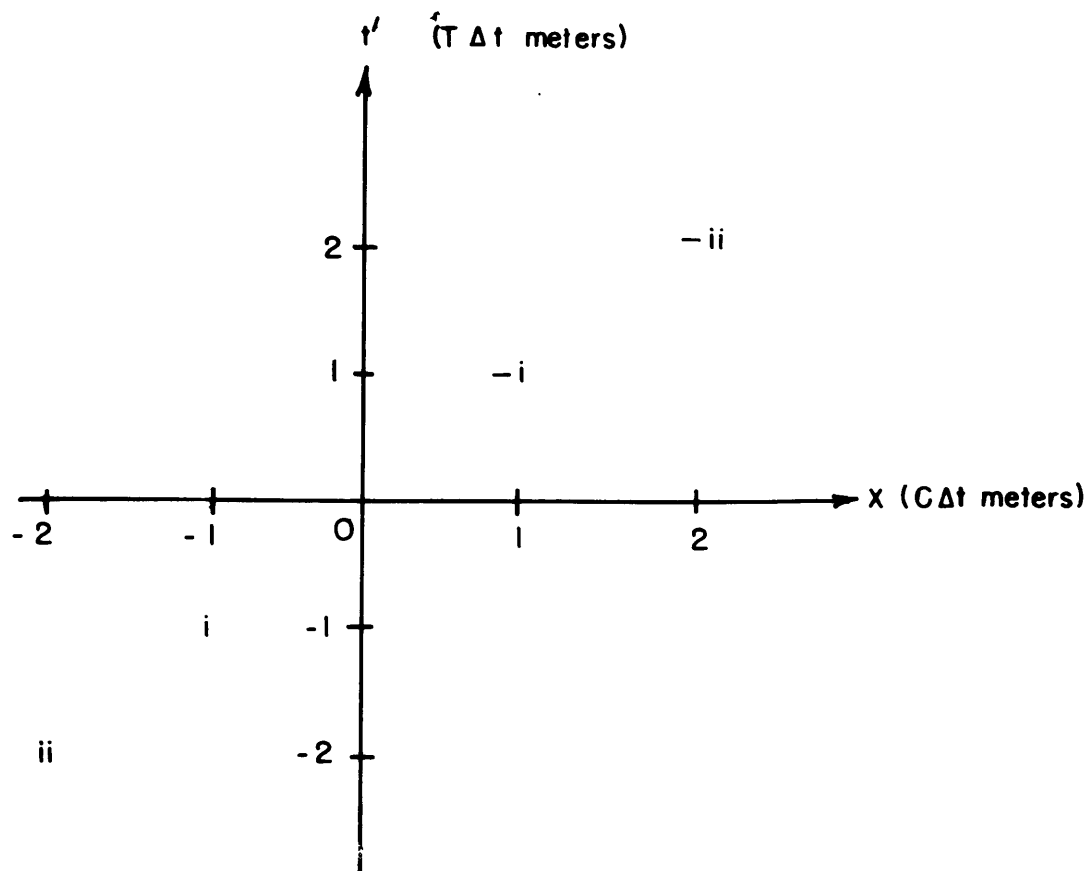


Fig. 4.1 The BOMEX Phase IV observation network: The area enclosed by the thick line was objectively analyzed. (See Table 4.1 for a description of the observation stations.)



A portion of an unchanging feature that propagates in the $+x$ -direction with constant speed $C \text{ m sec}^{-1}$ is sampled at $x = 0$ at intervals of Δt seconds. Then the observation (observations denoted by small Roman numerals) at $x=0$ at $\pm n\Delta t$ seconds is equivalent to one at $\mp nC\Delta t$ meters at $t = 0$.

Fig. 4.2 The time-compositing technique



They symbols used here are the same as those in Fig. 4.2. The locus of the composited asynchronous observations plotted in (x, t') -space represents the time-line of the sample of the event which passed through $x = 0$ at $t = 0$.

Fig 4.3 The time-compositing technique subject to Gandin's hypotheses in space and time.

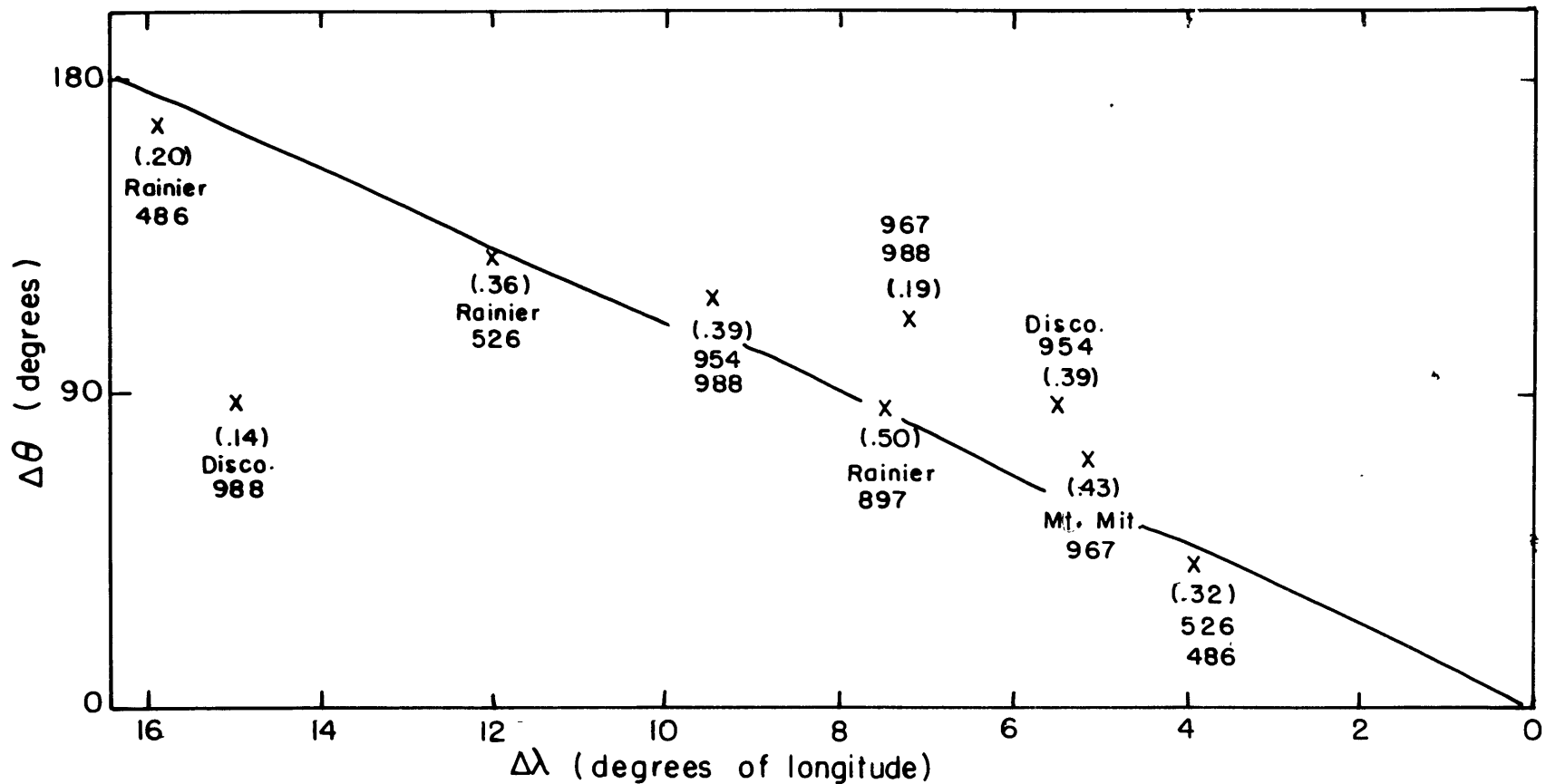


Fig. 4.4 Phase difference ($\Delta\theta$) versus longitudinal separation ($\Delta\lambda$) (shown by X) for the 950-mb meridional wind component of waves whose average period is $3 \frac{1}{3}$ days: A straight line was subjectively fit to obtain the estimated $\Delta\lambda$ at $\Delta\theta=180$ degrees. Also shown are the stations and the coherence squared (in parentheses) between the stations.

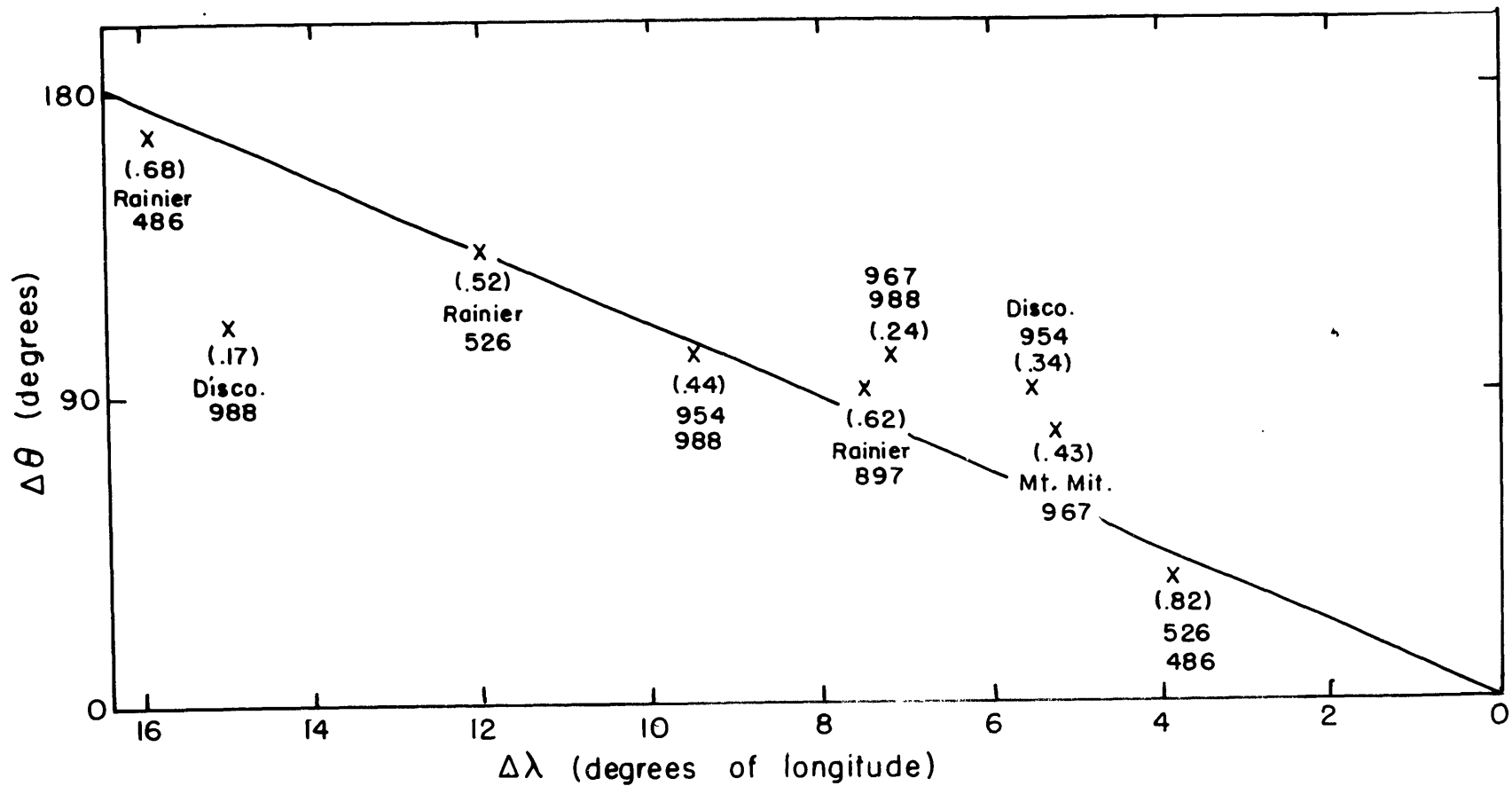


Fig. 4.5 Same as Fig. 4.4, but for 850 mb.

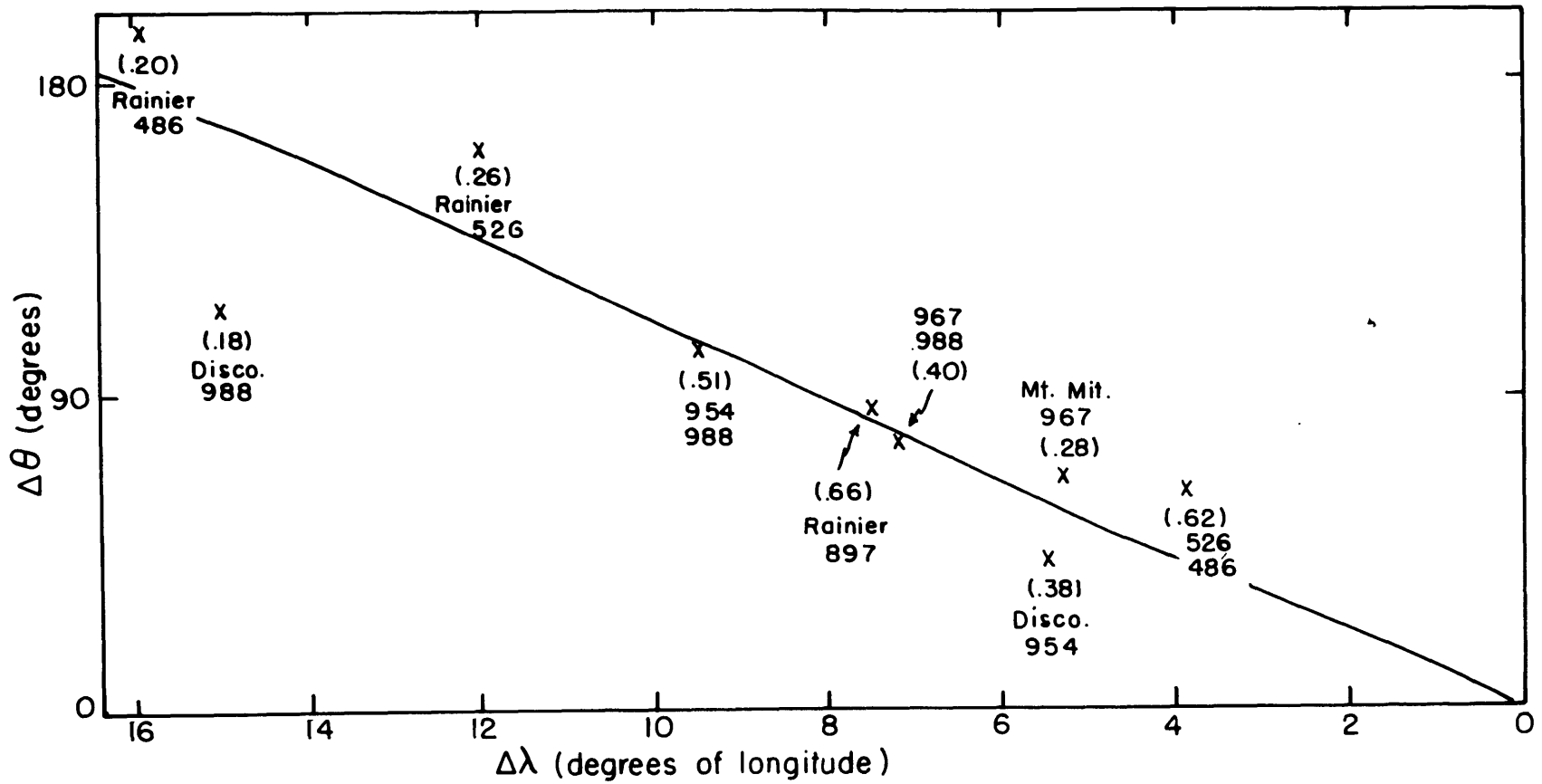


Fig. 4.6 Same as Fig. 4.4, but for 700 mb.

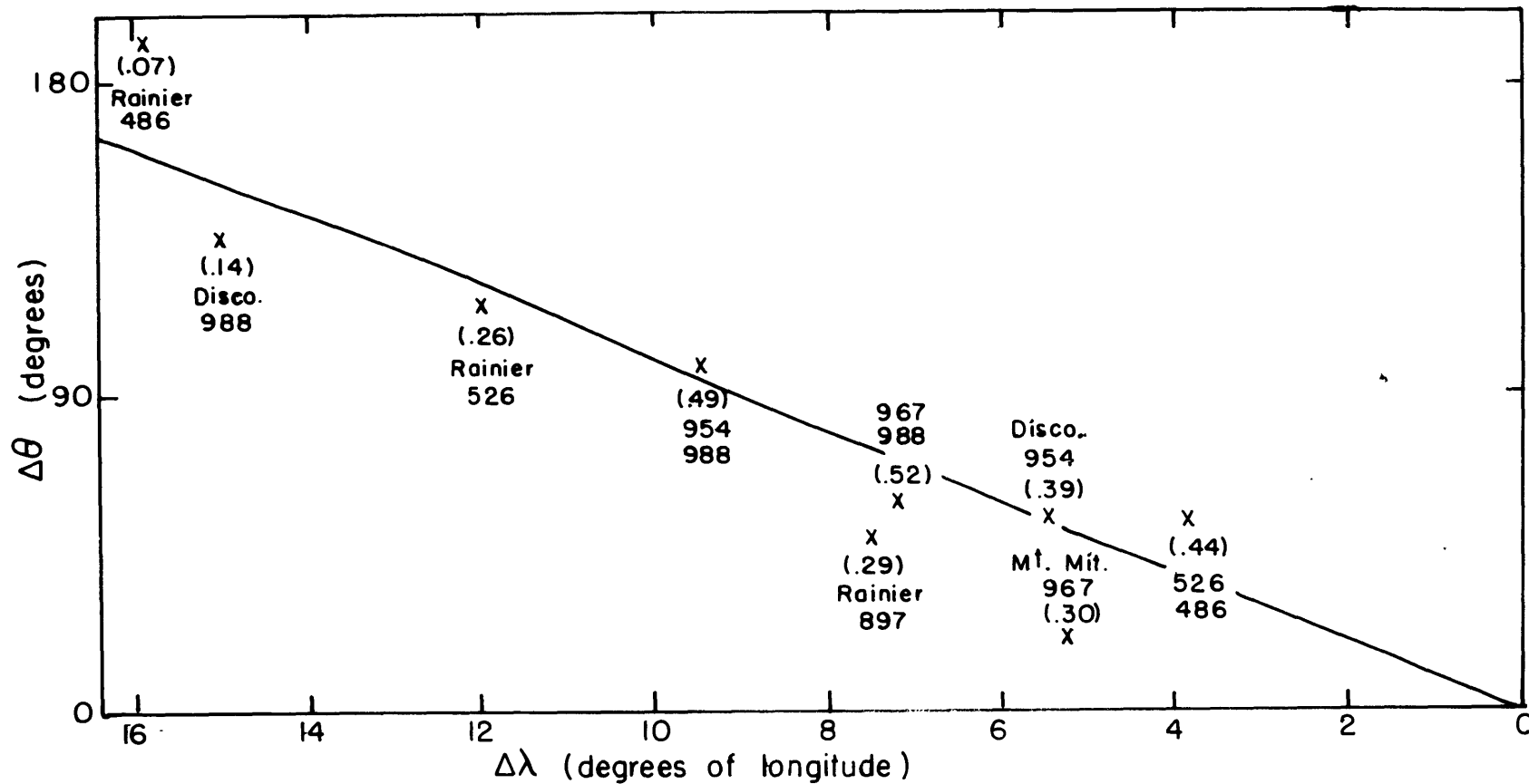


Fig. 4.7 Same as Fig. 4.4, but for 450 mb.

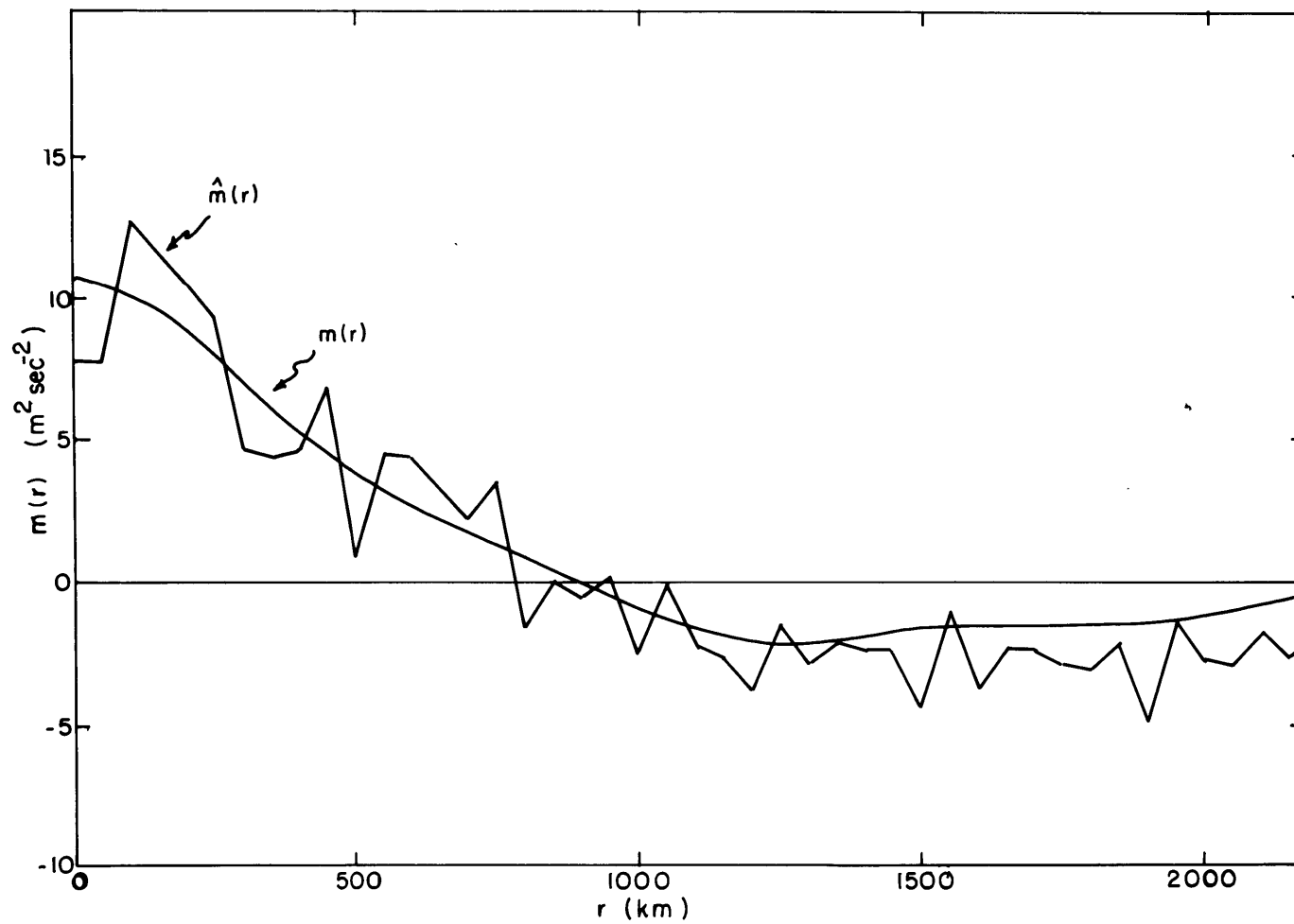


Fig. 4.8 The raw autocovariance curve ($\hat{m}(r)$) and the smoothed autocovariance curve ($m(r)$) of the meridional wind component for 25 July 1969 at 1200 GMT.

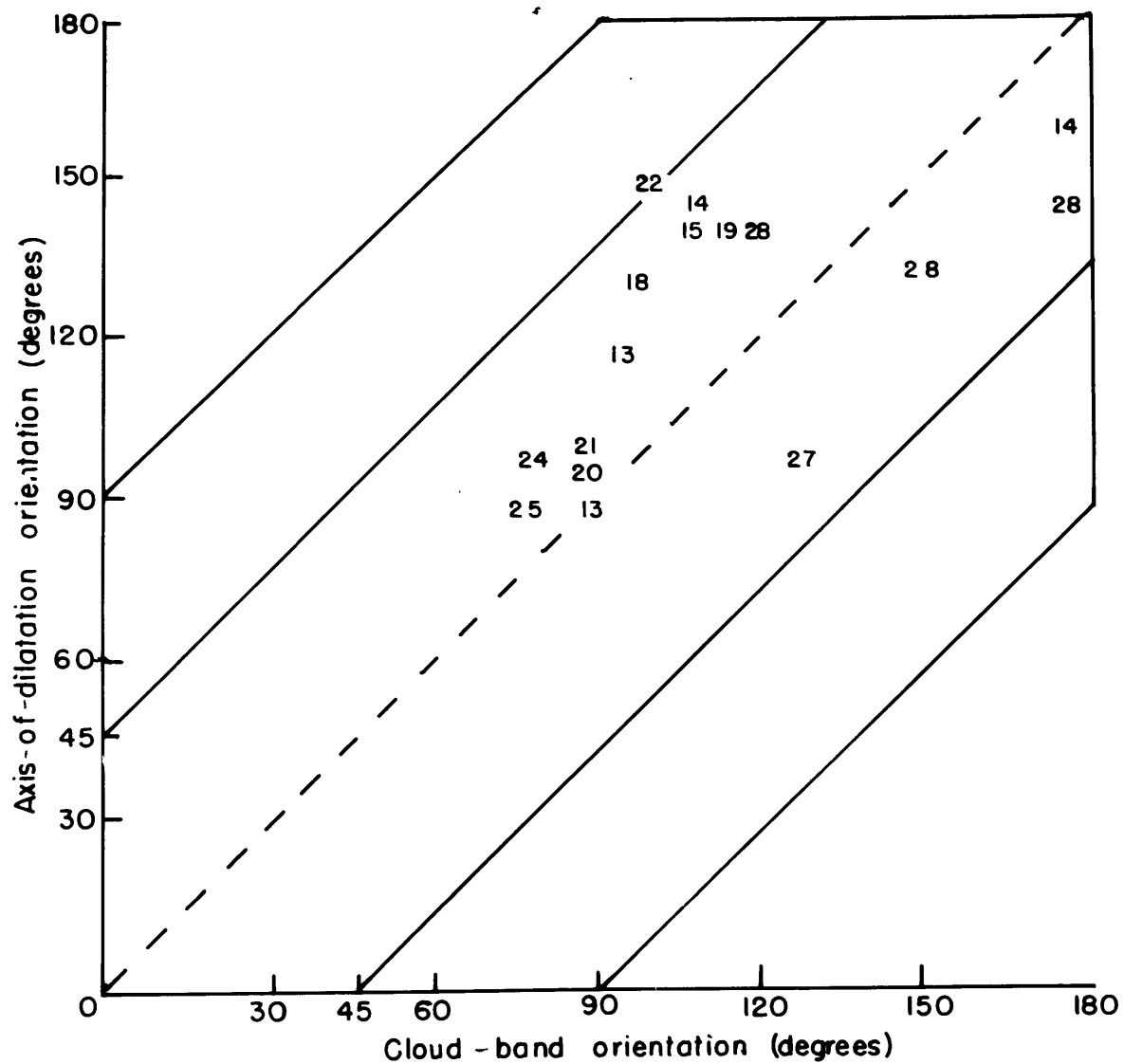


Fig. 4.9 Scatter diagram of 850-mb axis-of-dilatation orientation (measured clockwise from due north) versus cloud-band orientation. The numbers represent the days in July 1969 on which the cloud bands were observed.

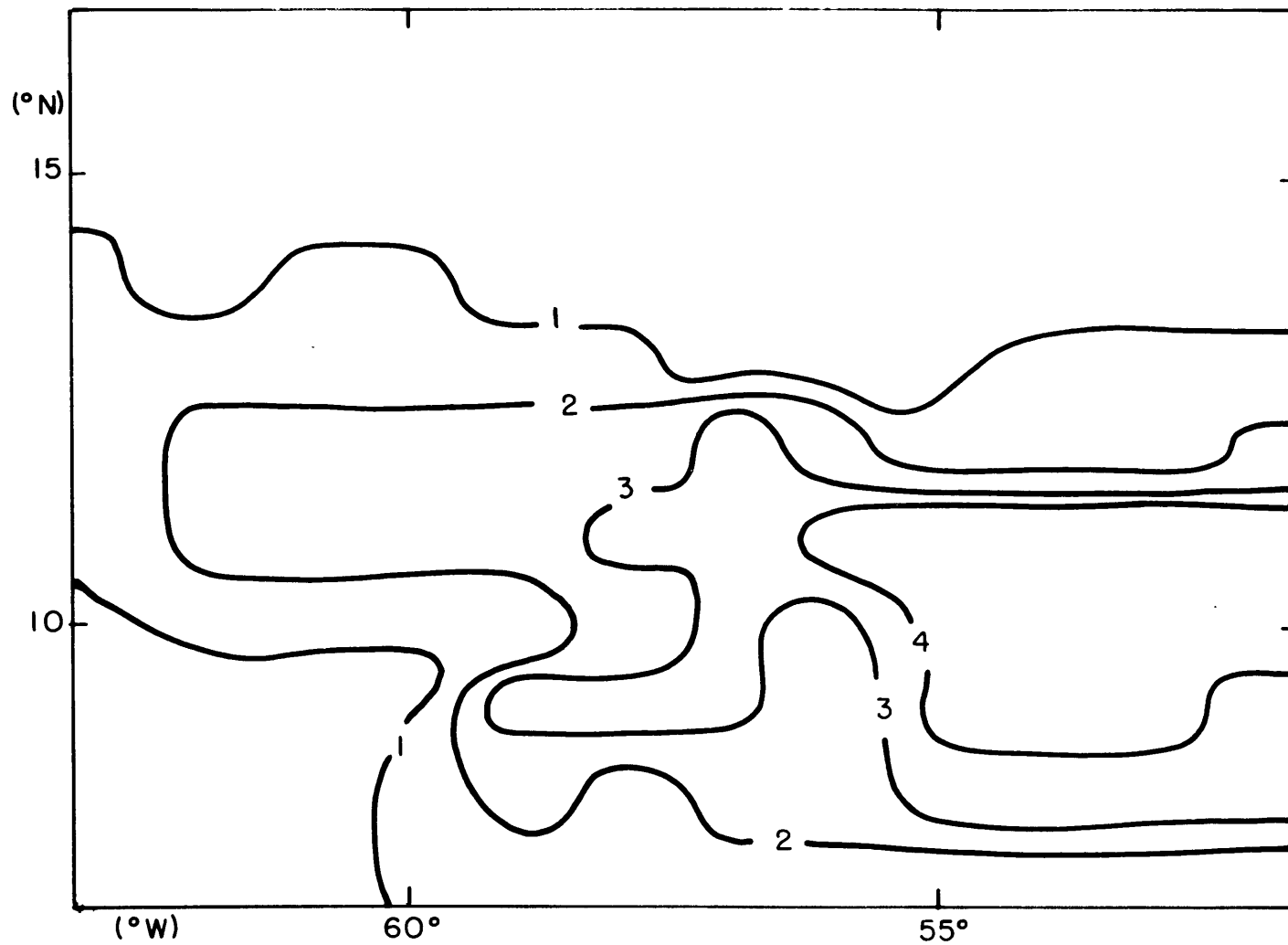


Fig. 4.10 Nephanalysis of the zonal cloud-band composite: The number of occurrences of cloud cover out of a possible 6 are given by the solid lines.

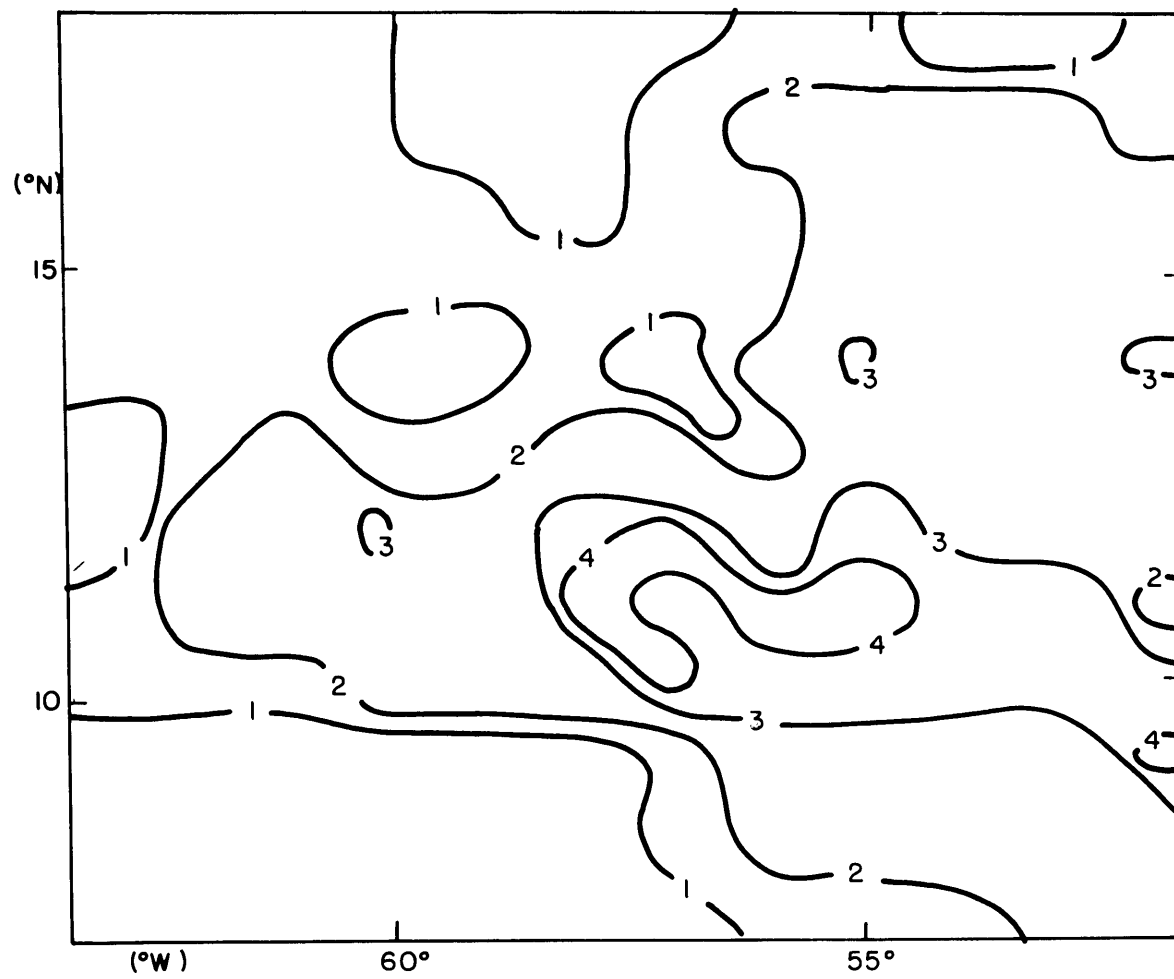


Fig. 4.11 Same as Fig. 4.10, but for the nonzonal cloud-band composite.

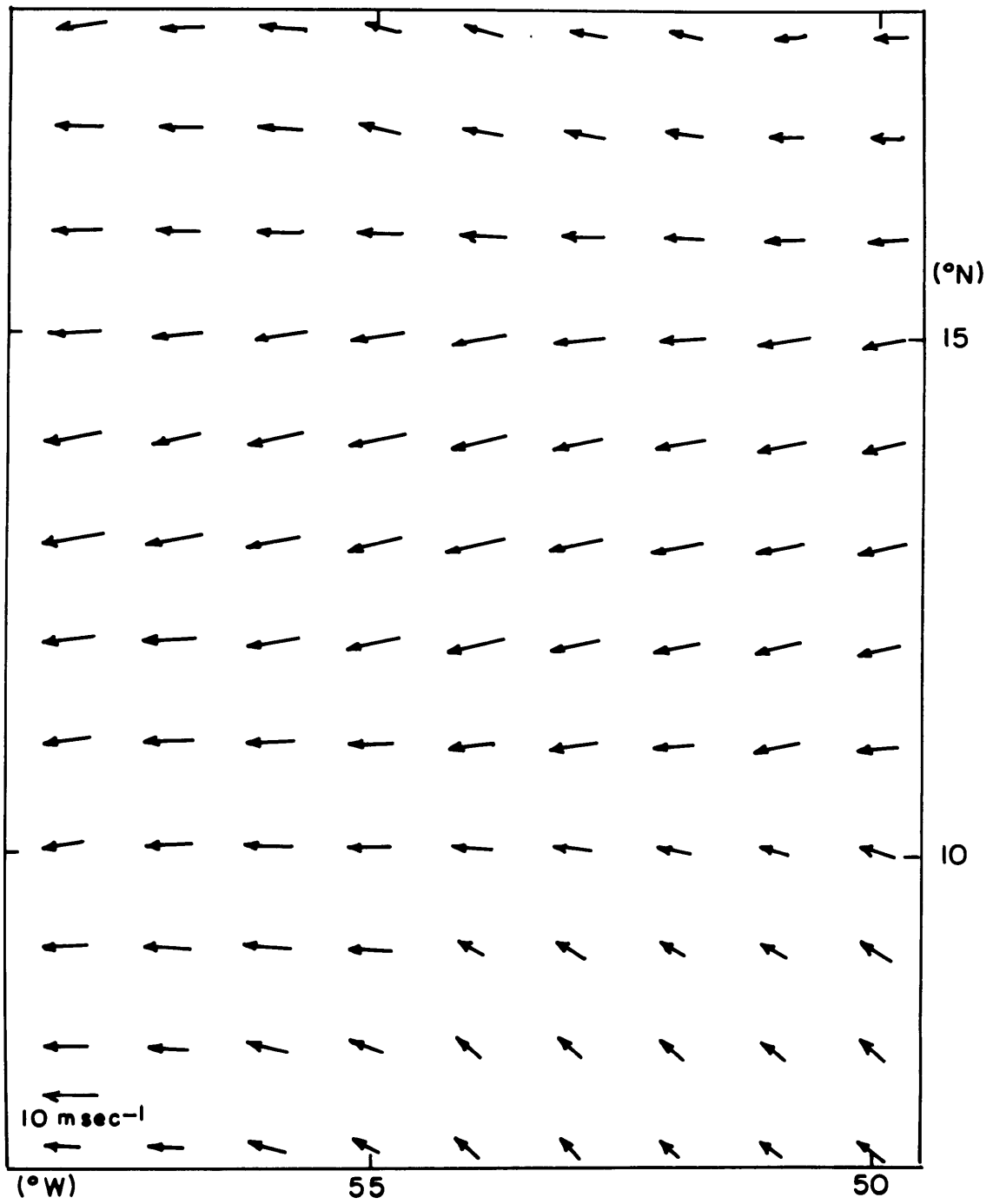


Fig. 4.12 The wind field (vectors) at 950 mb for the zonal cloud-band composite.

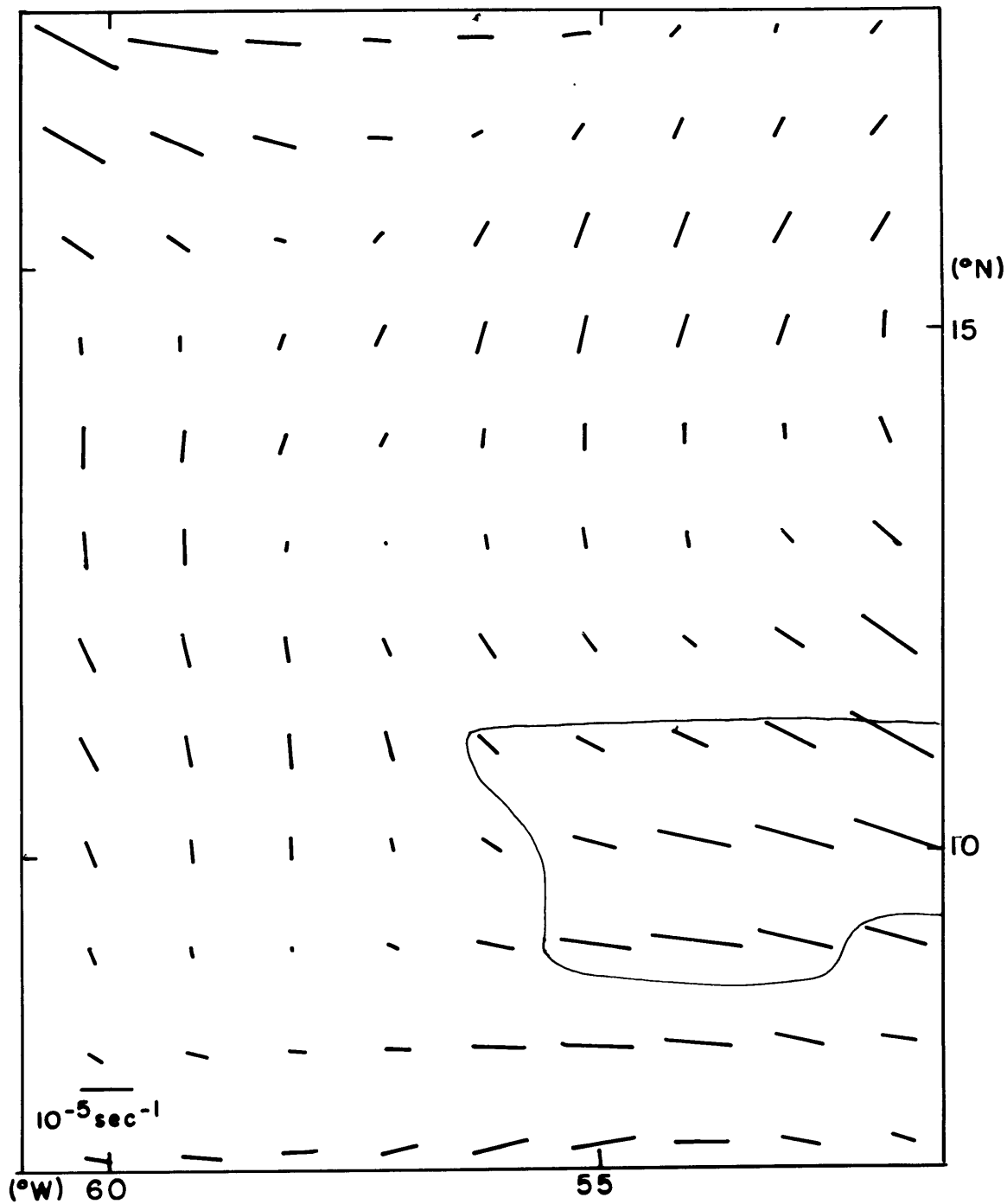


Fig. 4.13 The axes of dilatation of the 950-mb nondivergent wind for the zonal cloud-band composite: The orientations of the dashed lines represent the orientations of the axes of dilatation; the lengths of the dashed lines represent the magnitude of the resultant deformation. The area enclosed by thin solid line represents 67% or more frequency of cloudiness.

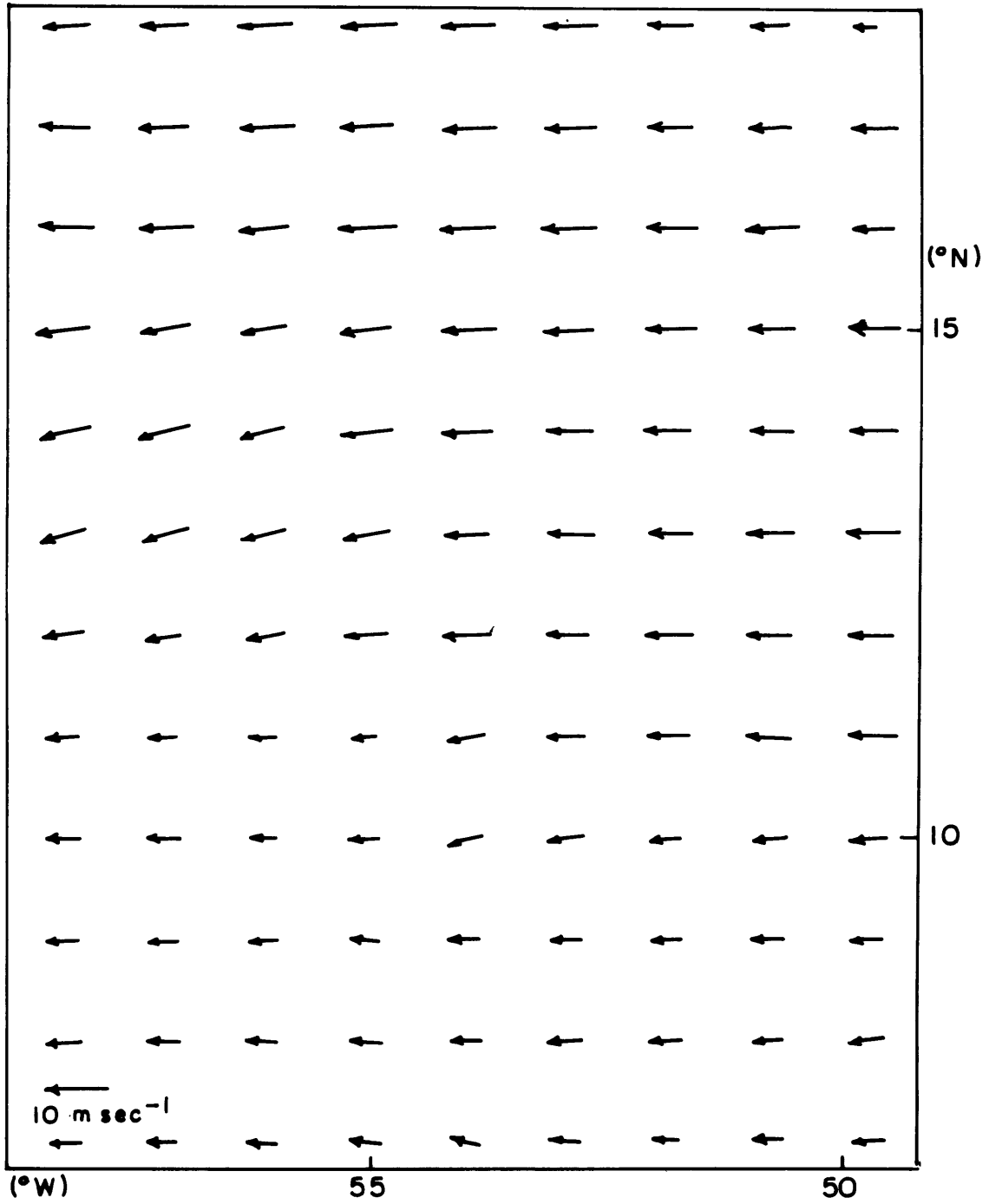


Fig. 4.14 Same as Fig. 4.12, but for the nonzonal cloud-band composite at 950 mb.

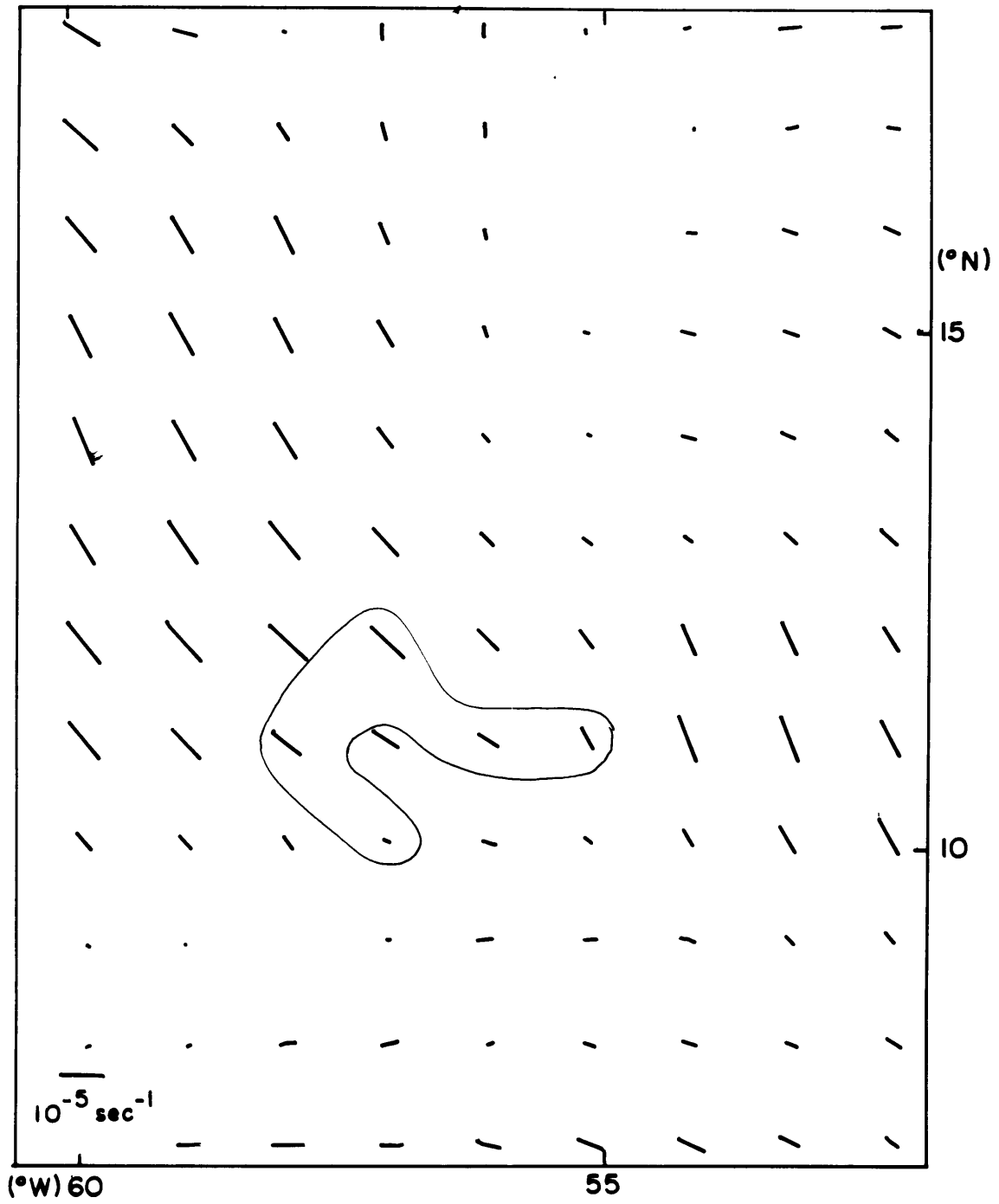


Fig. 4.15 Same as Fig. 4.13, but for the nonzonal cloud-band composite at 950 mb.

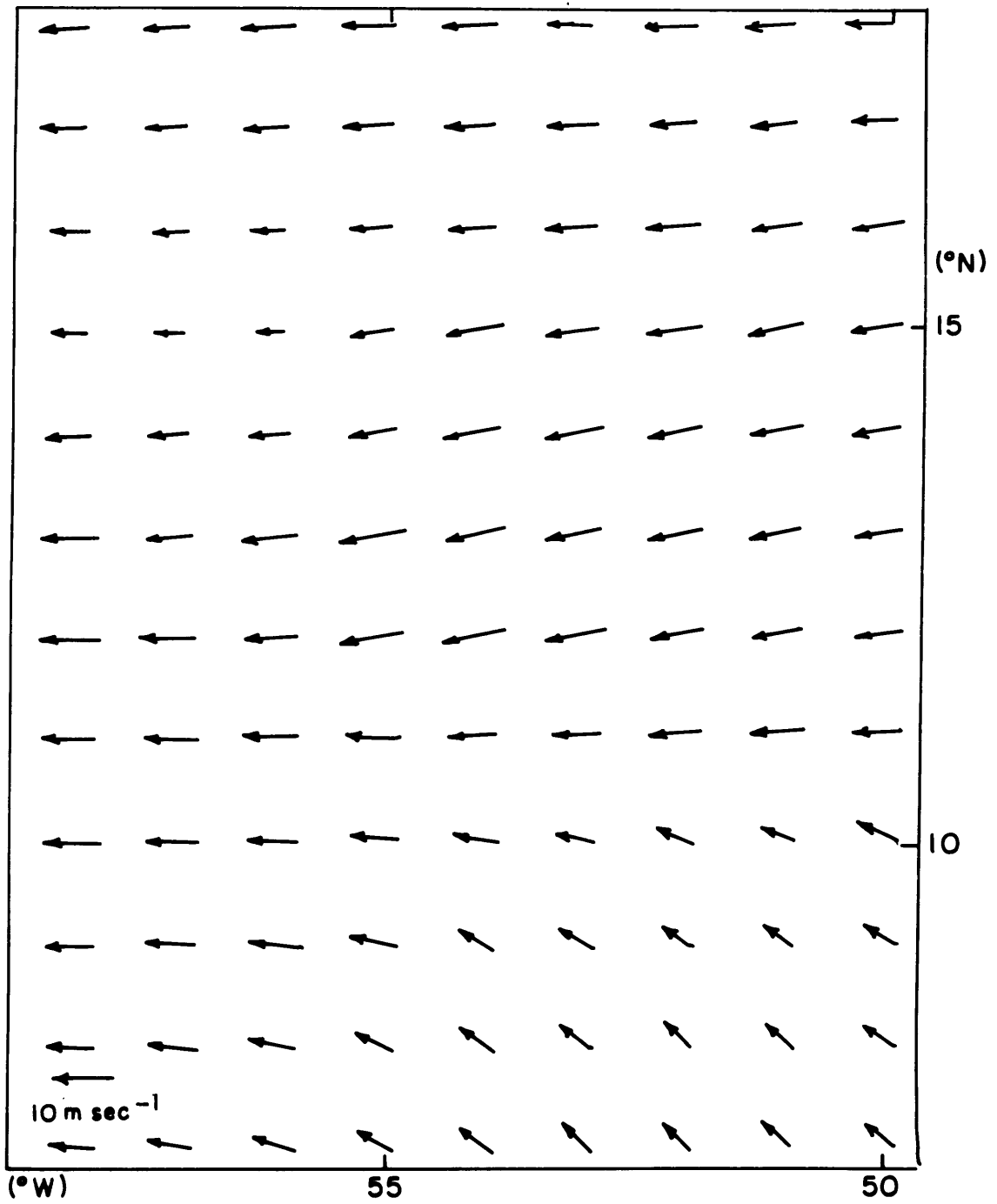


Fig. 4.16 Same as Fig. 4.12, but for the zonal cloud-band composite at 850 mb.

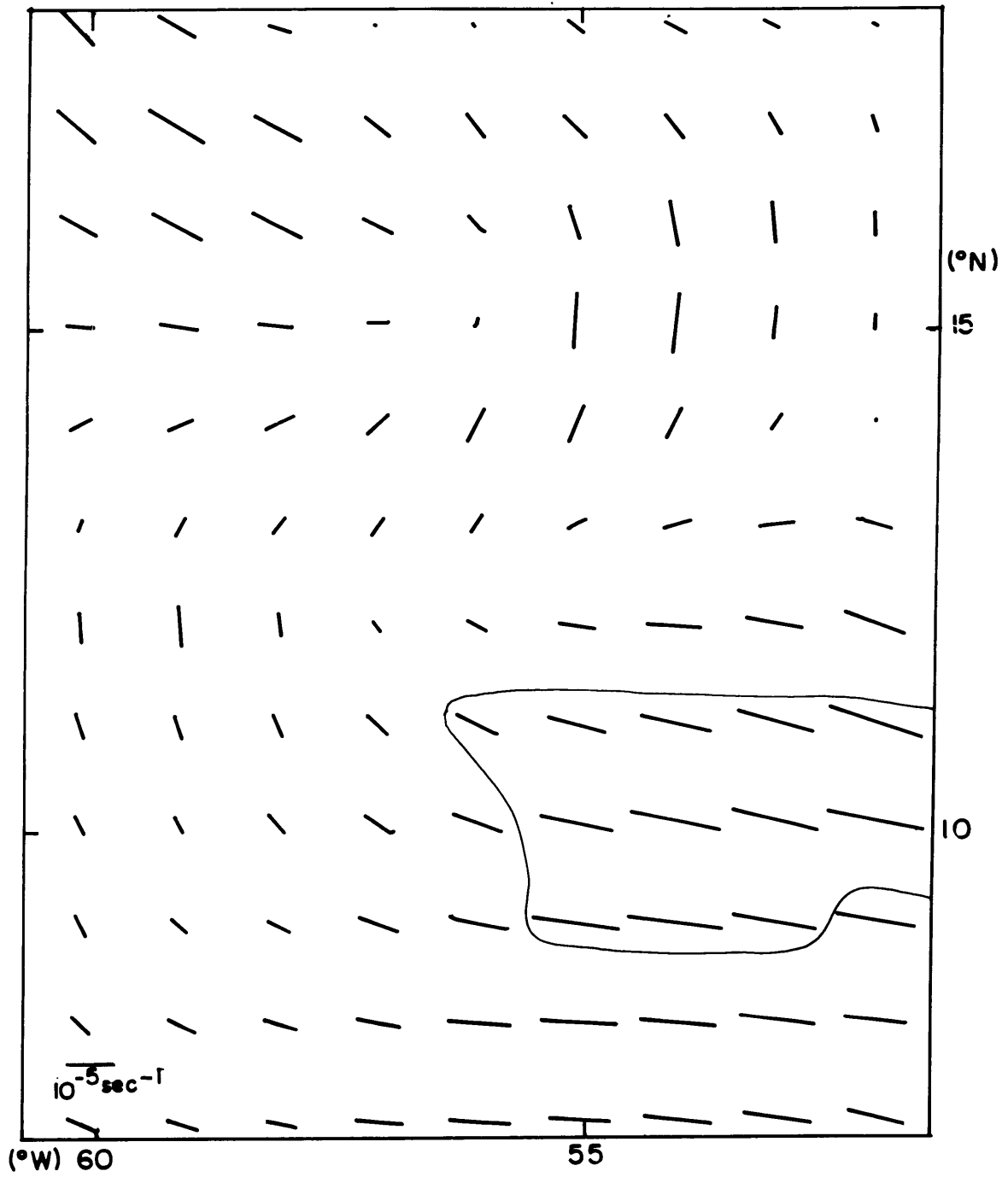


Fig. 4.17 Same as Fig. 4.13, but for the zonal cloud-band composite at 850 mb.

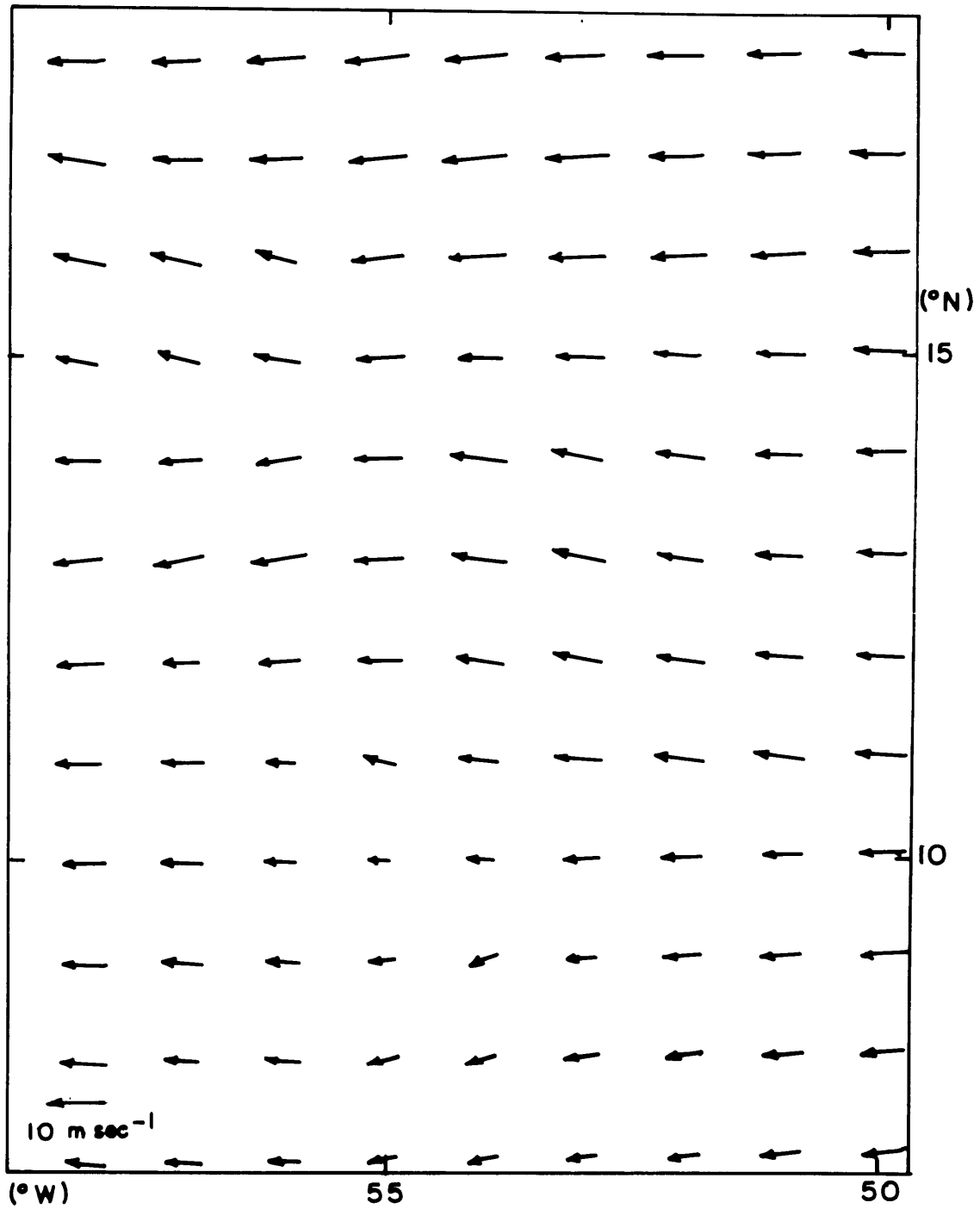


Fig. 4.18 Same as Fig. 4.12, but for the nonzonal cloud-band (and no-band) composite at 850 mb.

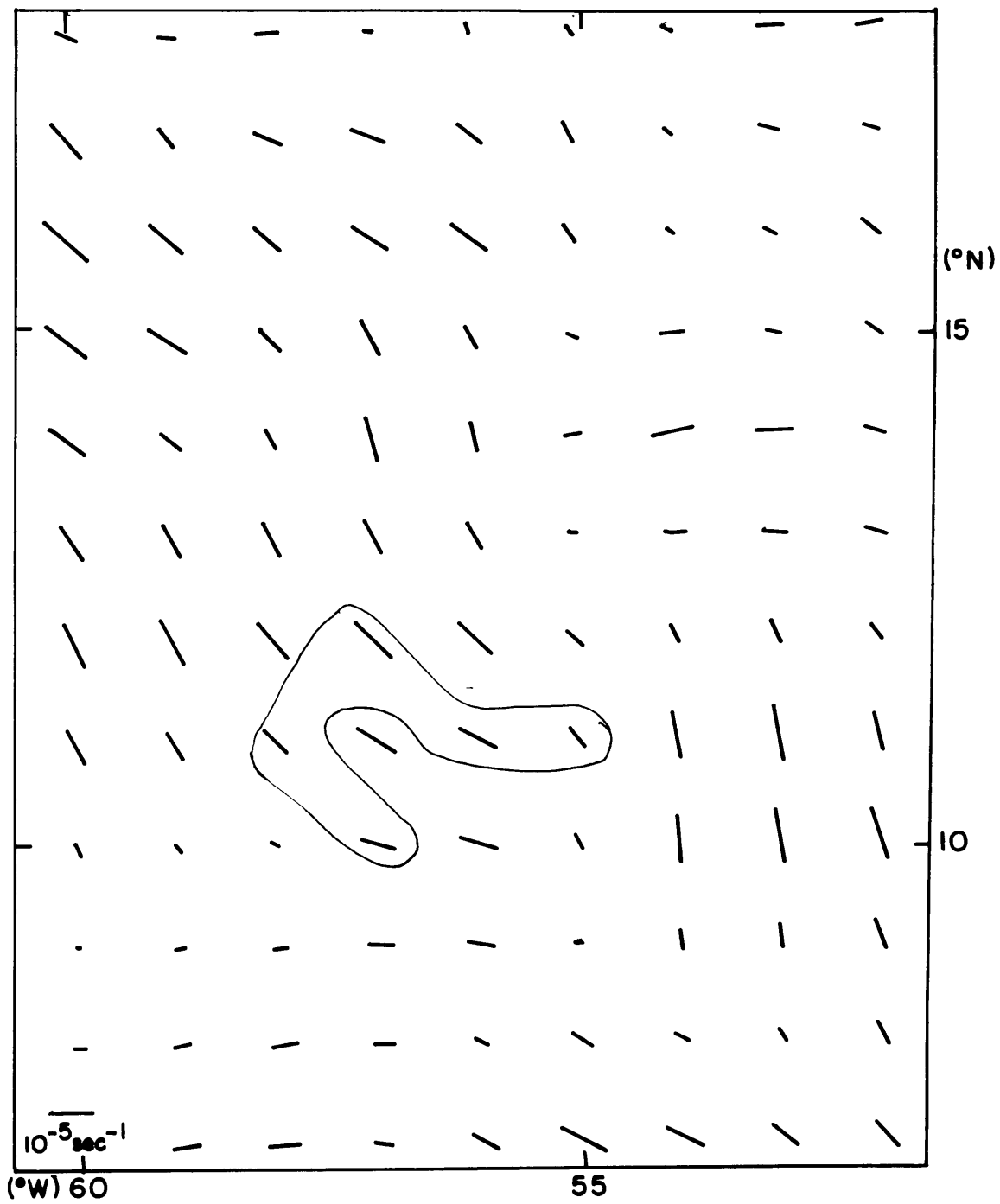


Fig. 4.19 Same as Fig. 4.13, but for the nonzonal cloud-band (or no-band) composite at 850 mb.

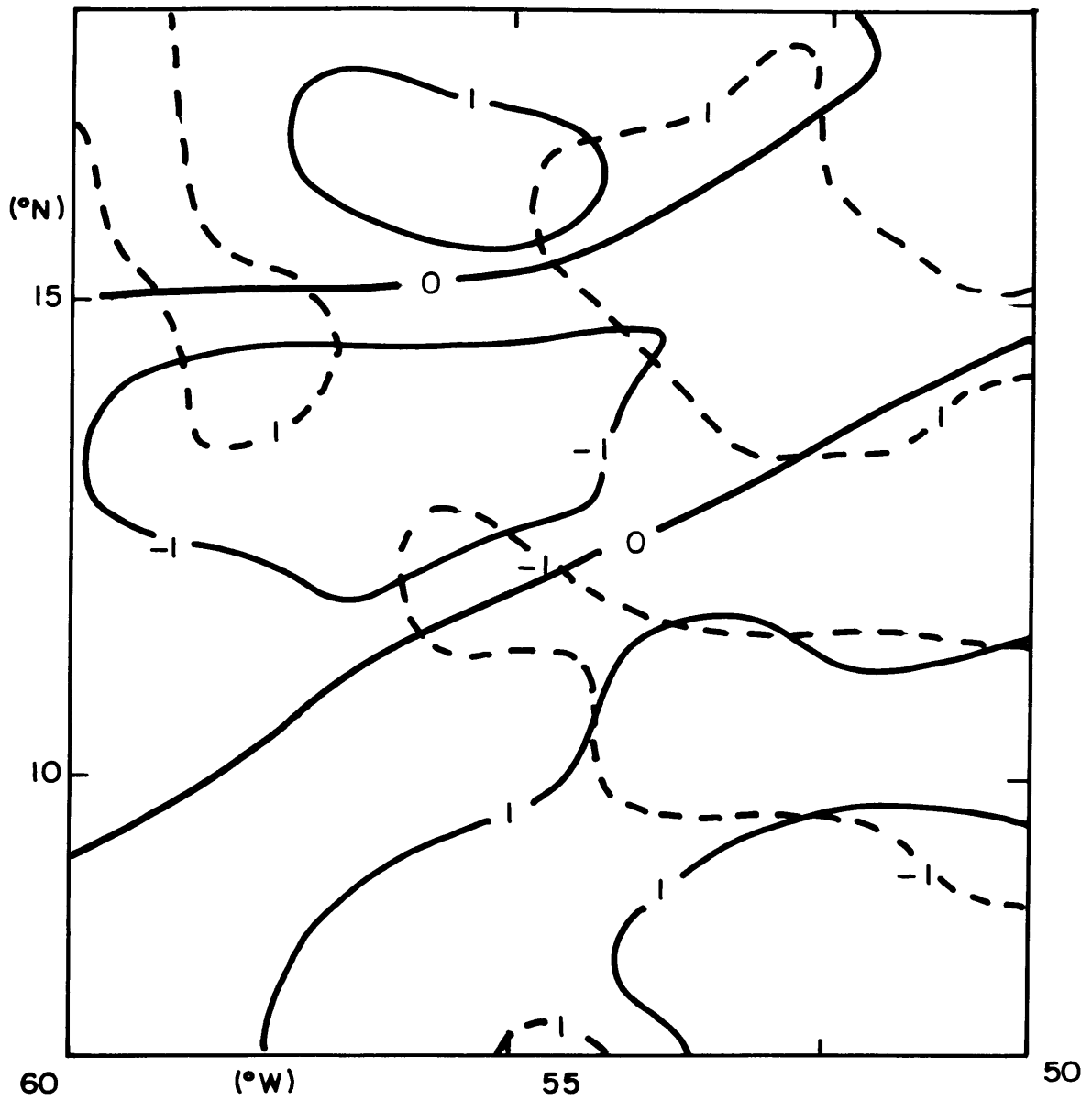


Fig. 4.20 Relative vorticity (ξ) (solid lines) in units of 10^{-5} sec^{-1} and vertical mass flux (ω) (dashed lines) in units of $\mu\text{b sec}^{-1}$ at 850 mb for the zonal cloud-band composite.

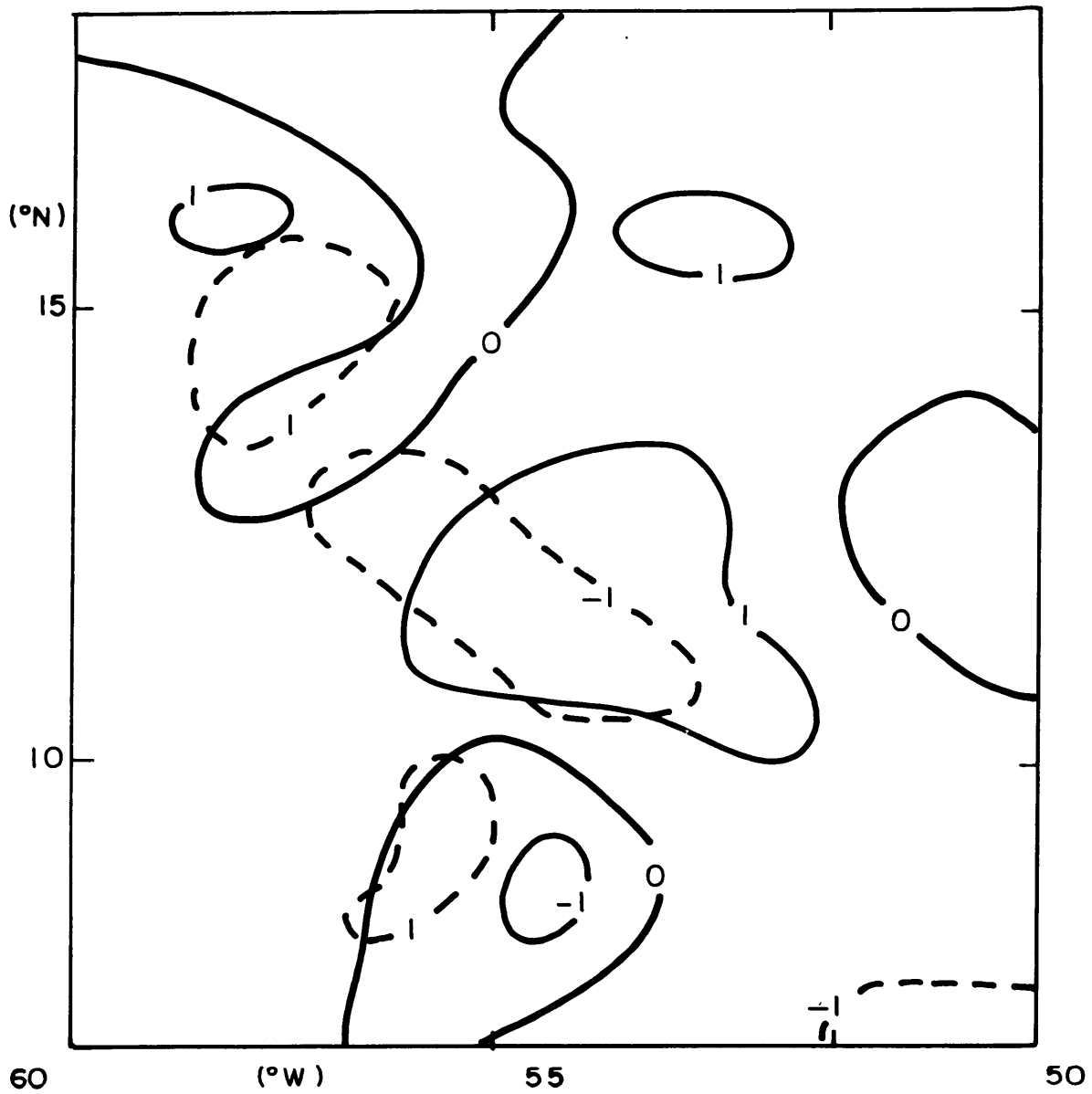


Fig. 4.21 Same as Fig. 4.20, but for the nonzonal cloud-band composite.

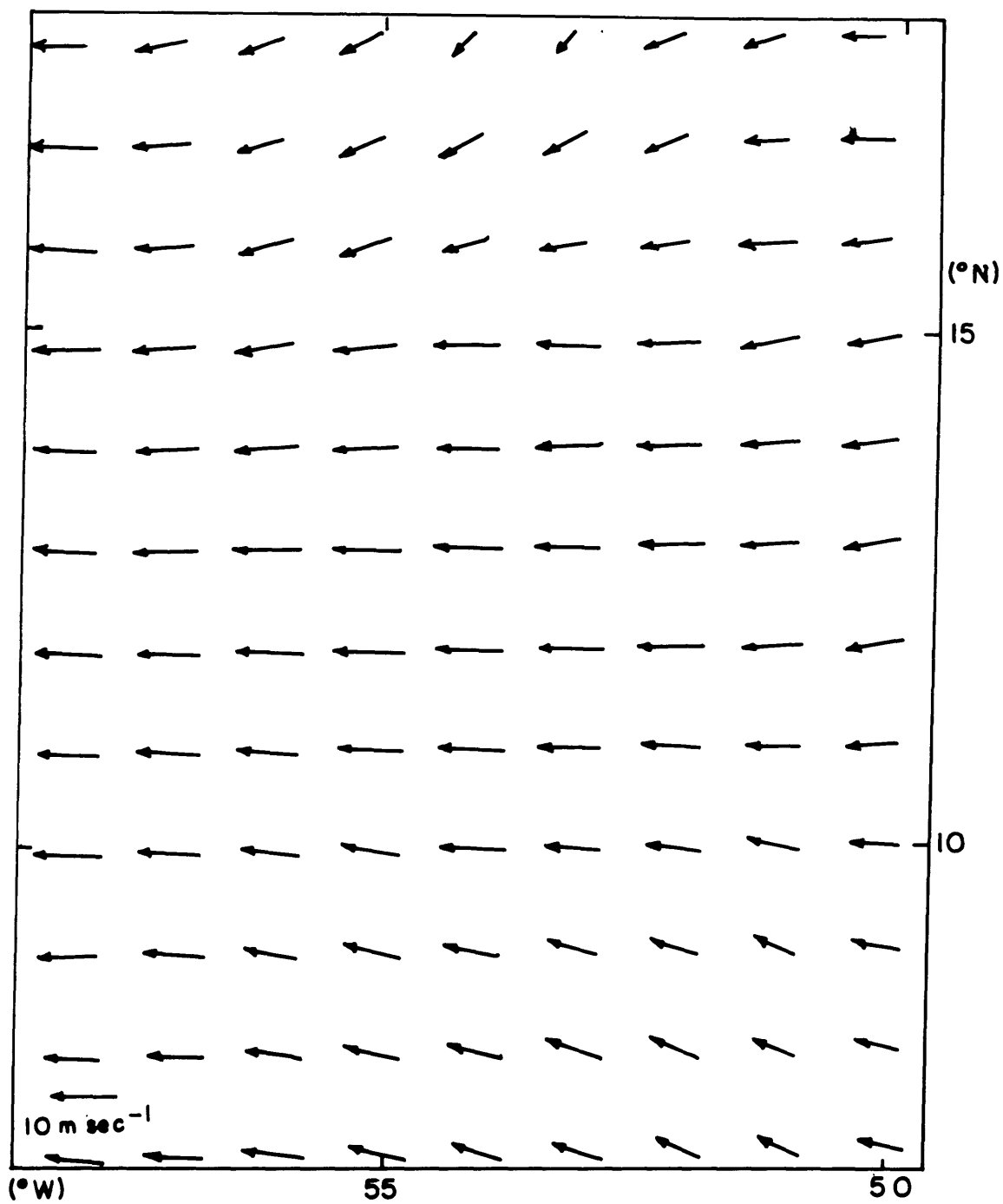


Fig. 4.22 Same as Fig. 4.12, but for the zonal cloud-band composite at 700 mb.

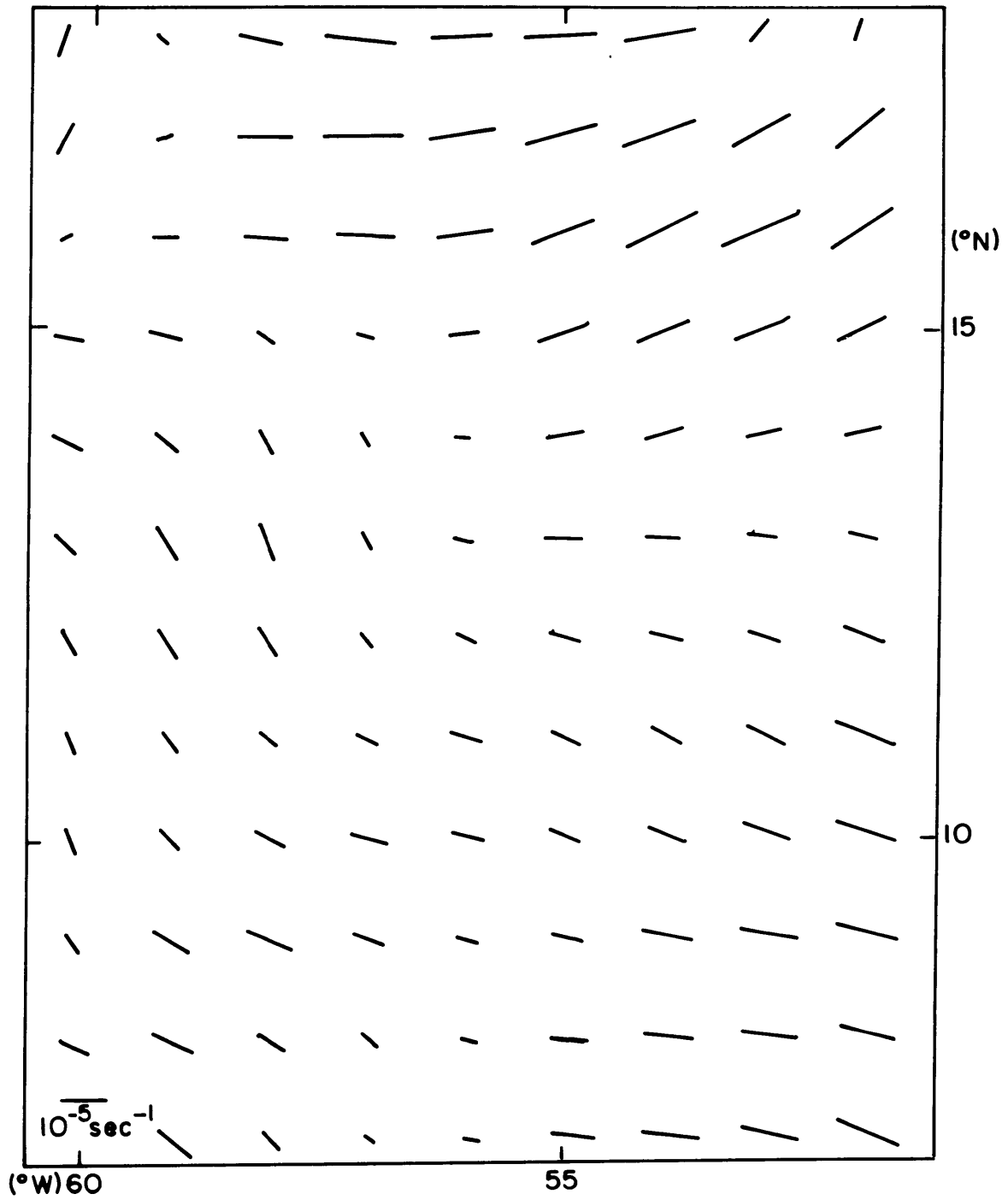


Fig. 4.23 Same as Fig. 4.13, but for the zonal cloud-band composite at 700 mb.

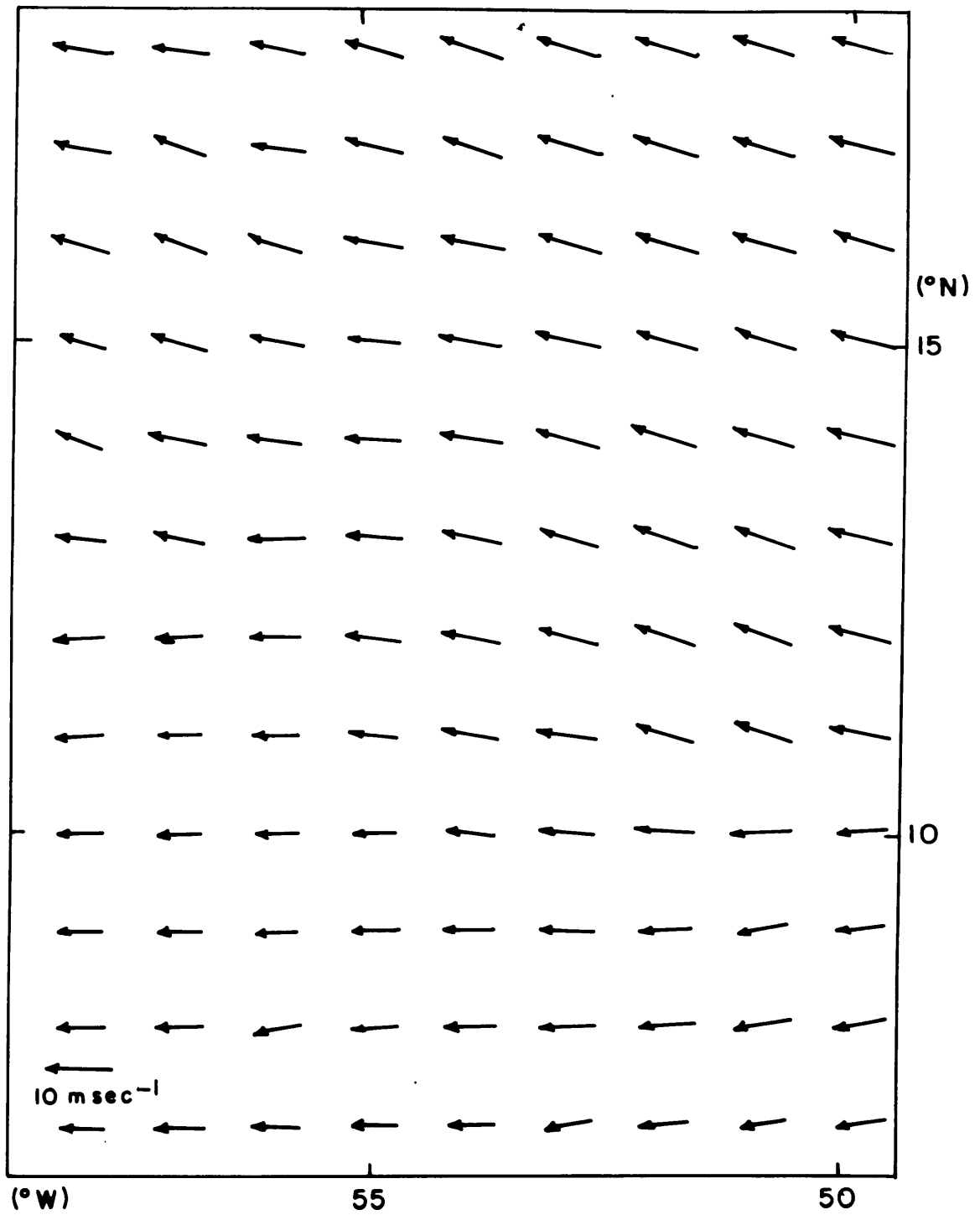


Fig. 4.24 Same as Fig. 4.12, but for the nonzonal cloud-band composite at 700 mb.

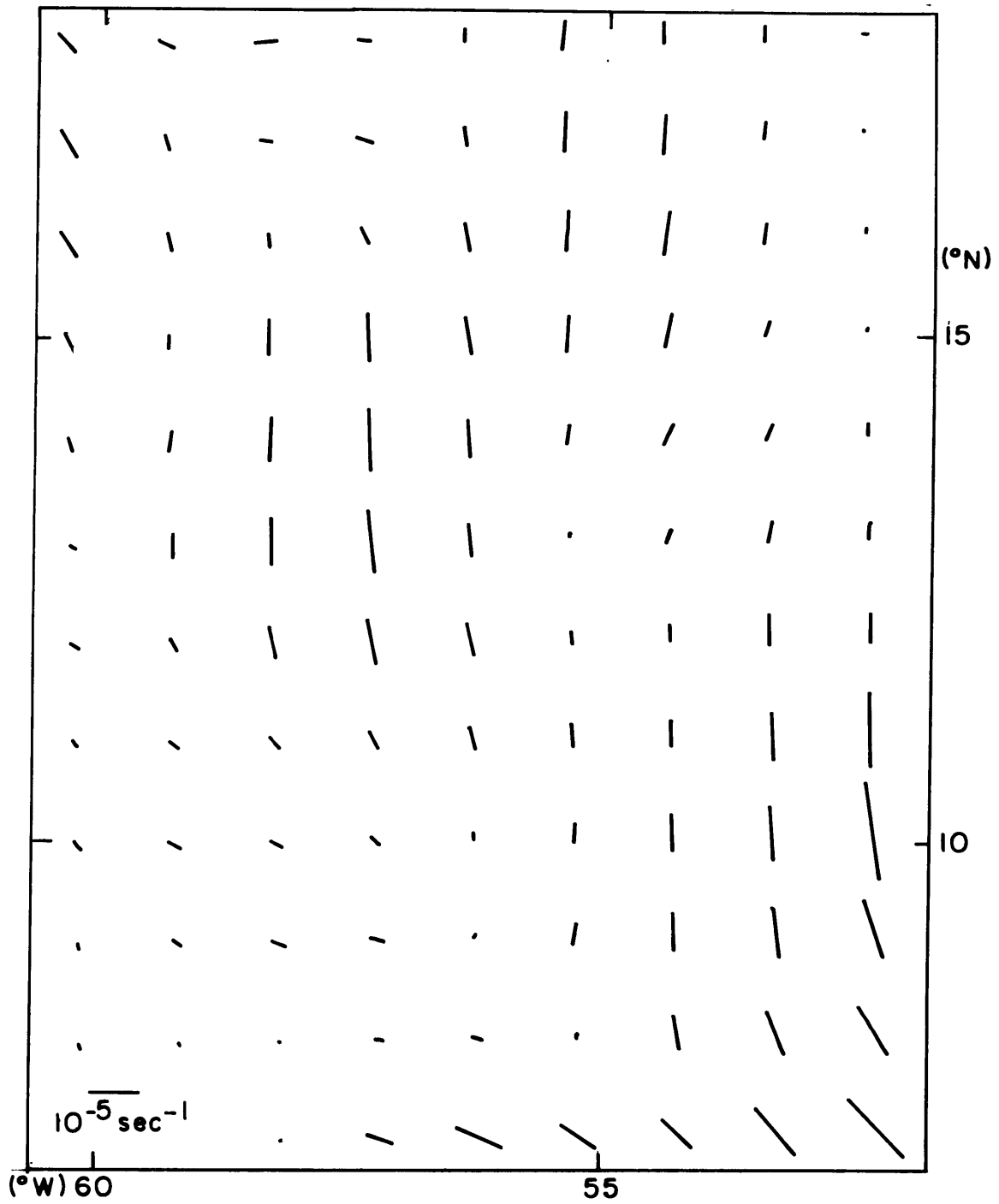


Fig. 4.25 Same as Fig. 4.13, but for the nonzonal cloud-band composite at 700 mb.

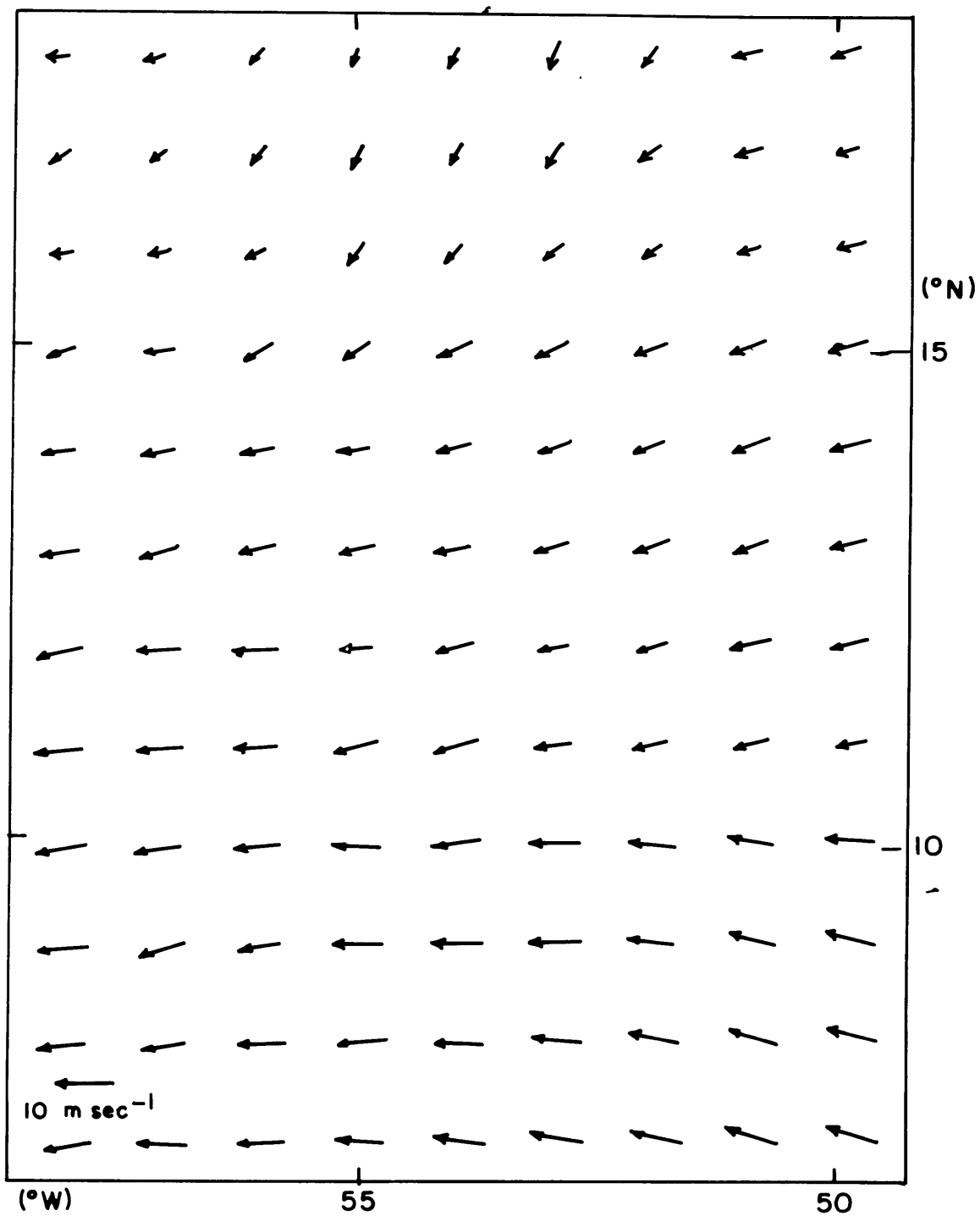


Fig. 4.26 Same as Fig. 4.12, but for the zonal cloud-band composite at 450 mb.

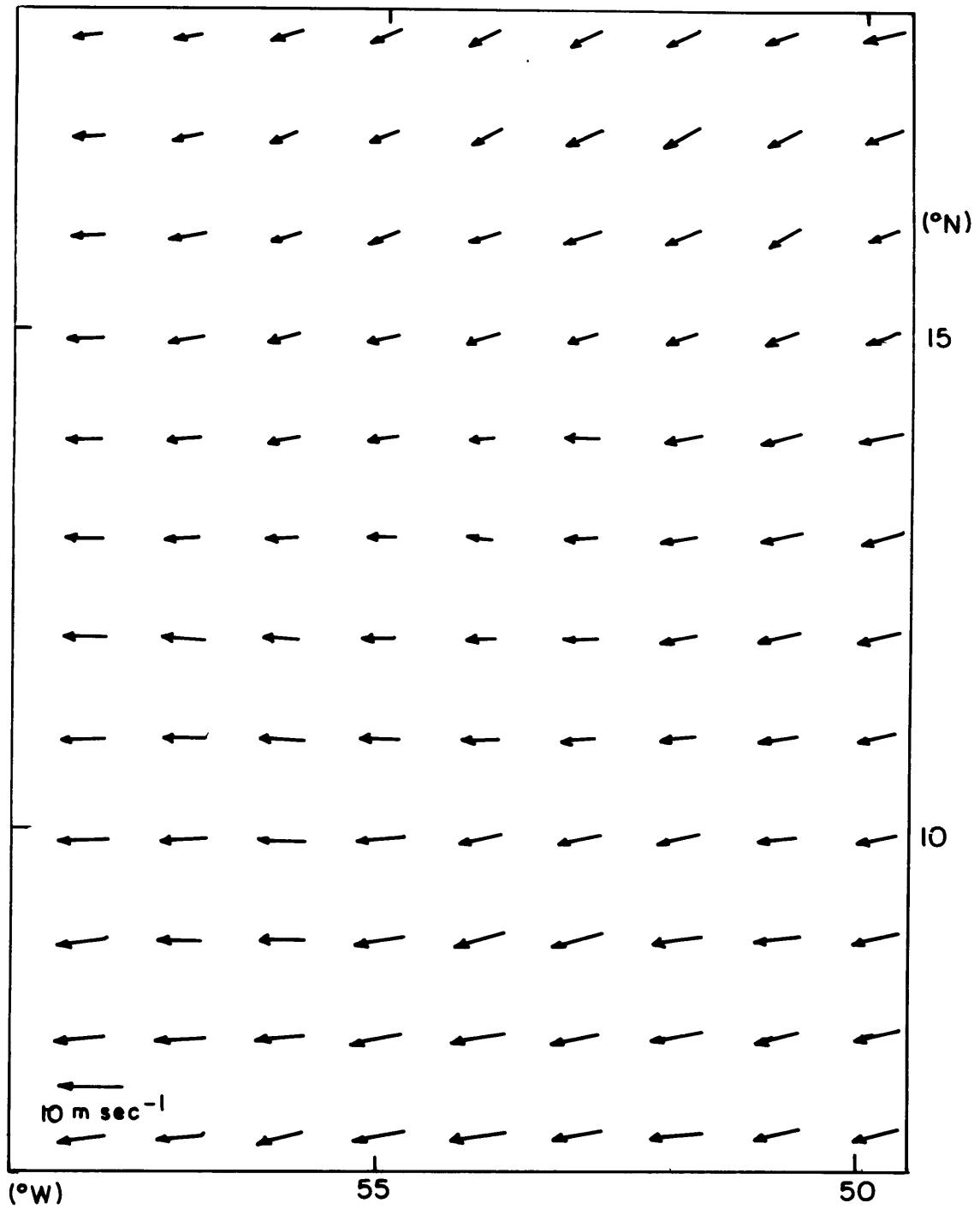


Fig. 4.27 Same as Fig. 4.12, but for the nonzonal cloud-band composite at 450 mb.

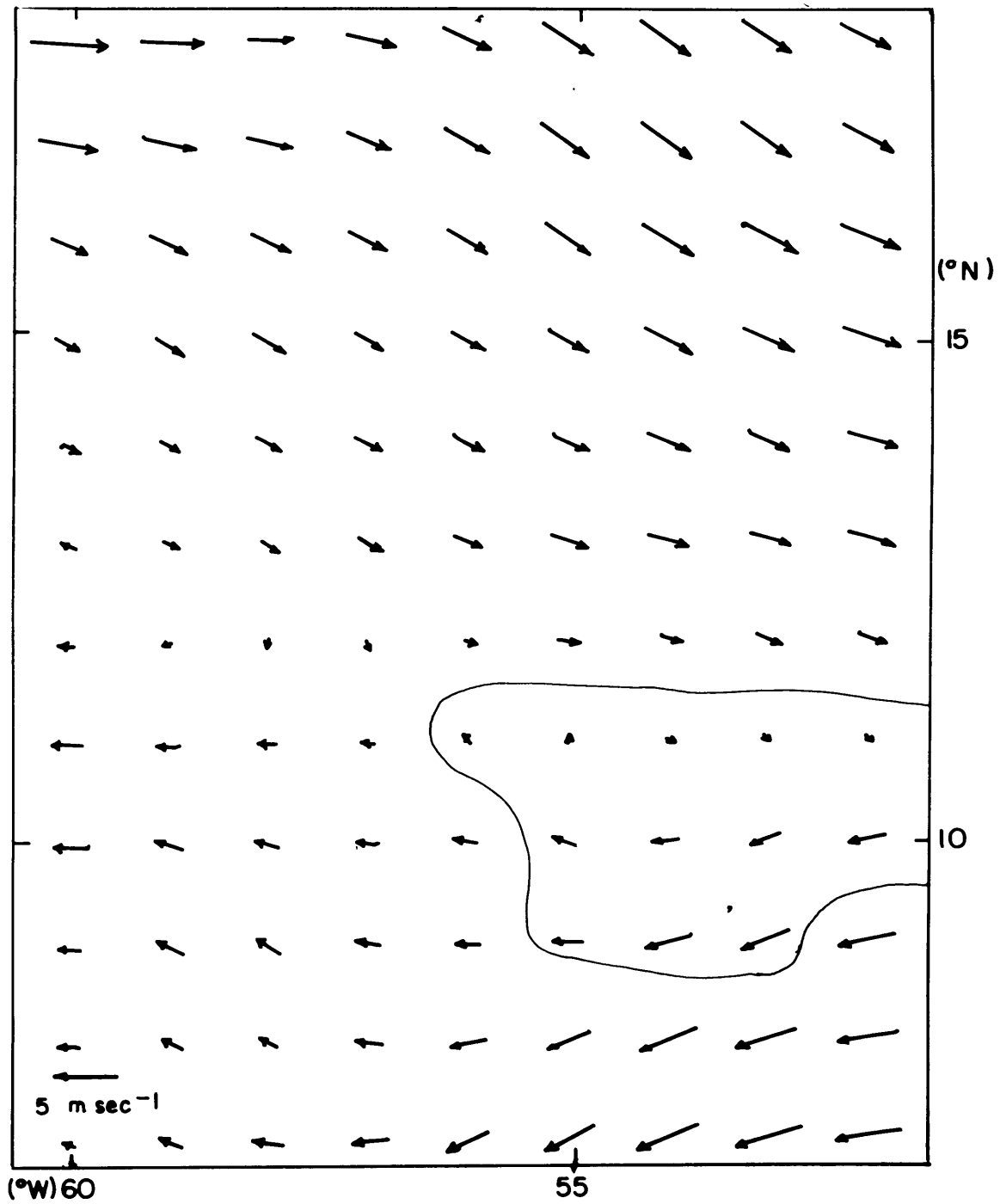


Fig. 4.28 The 950-450 mb nondivergent wind-shear (vectors) for the zonal cloud-band composite. The area enclosed by the solid line represents 67% or more frequency of cloudiness.

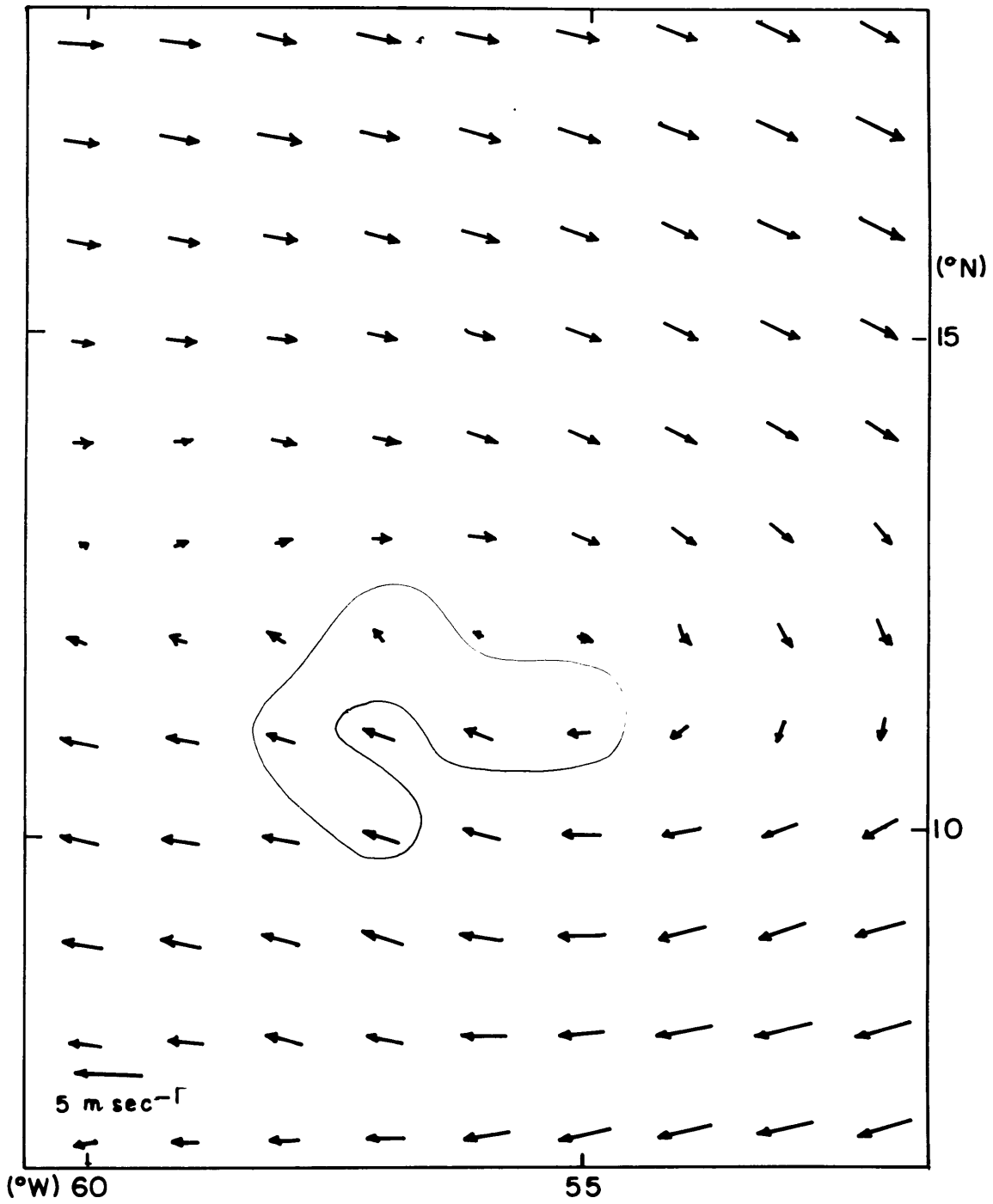


Fig. 4.29 Same as Fig. 4.28, but for the nonzonal cloud-band composite.

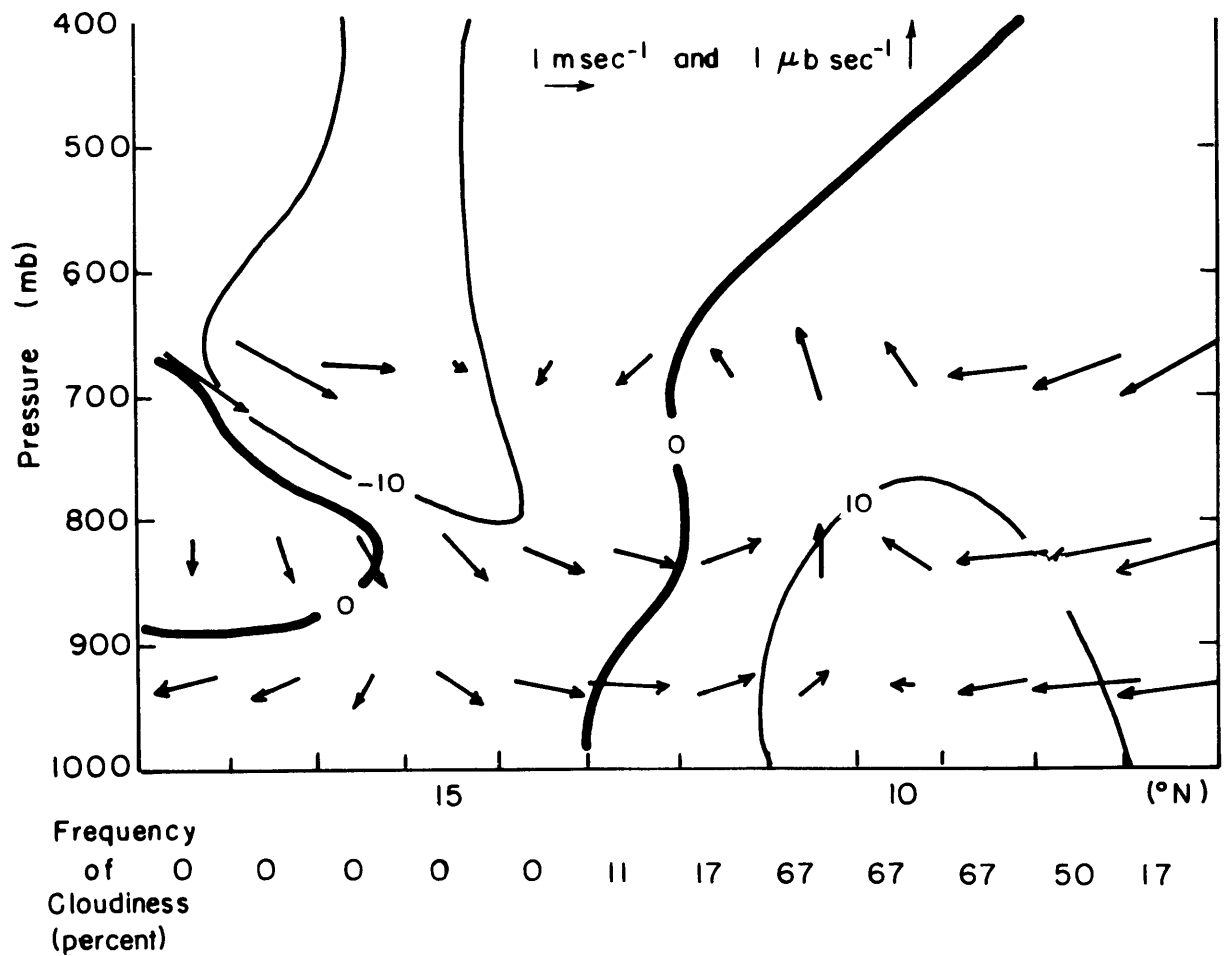


Fig. 4.30 The meridional flow pattern (vectors) and relative vorticity (ξ) (solid lines) in units of 10^{-6} sec^{-1} for the zonal cloud-band composite. The frequency of cloudiness is shown below.

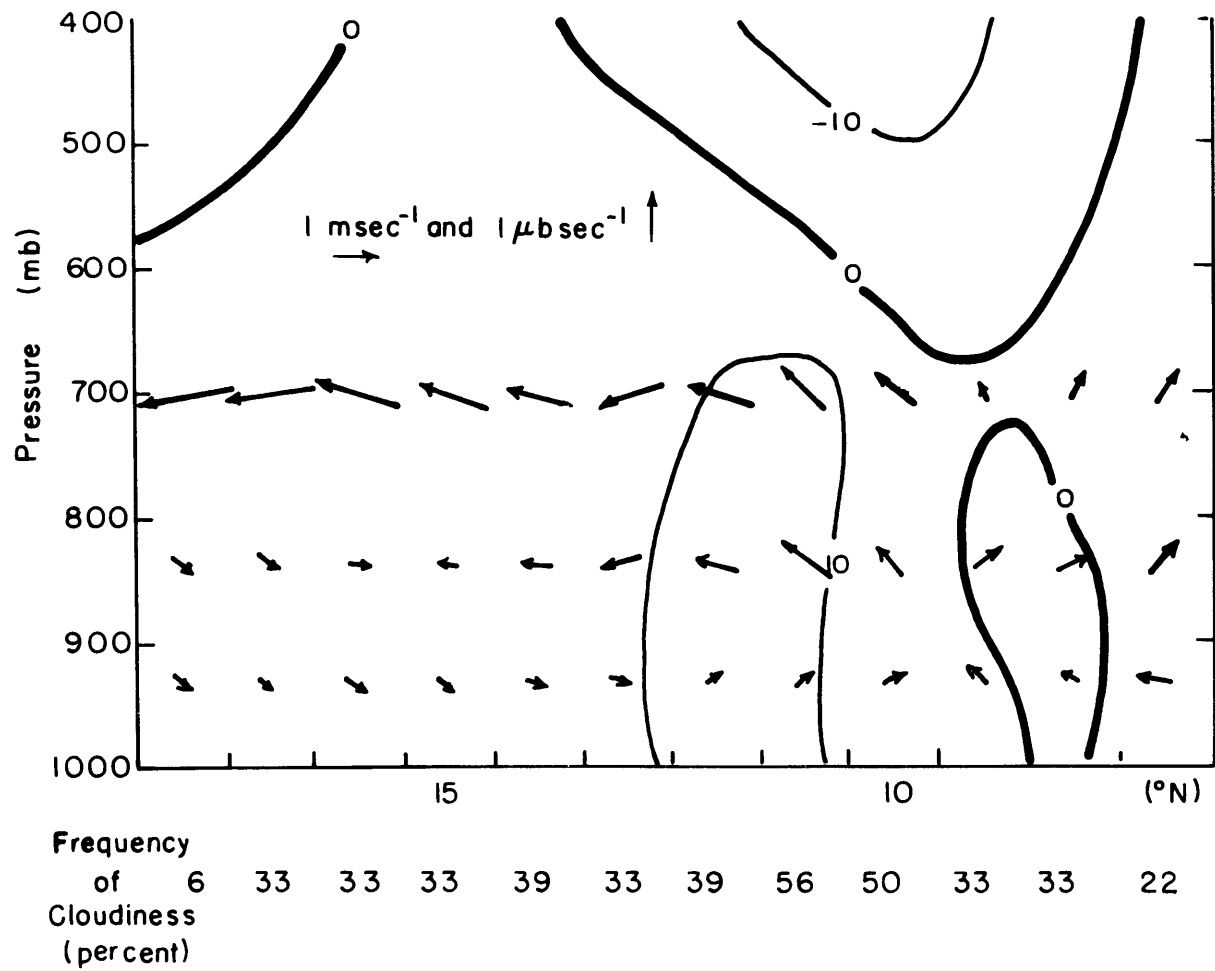


Fig. 4.31 Same as Fig. 4.30, but for the nonzonal cloud-band composite.

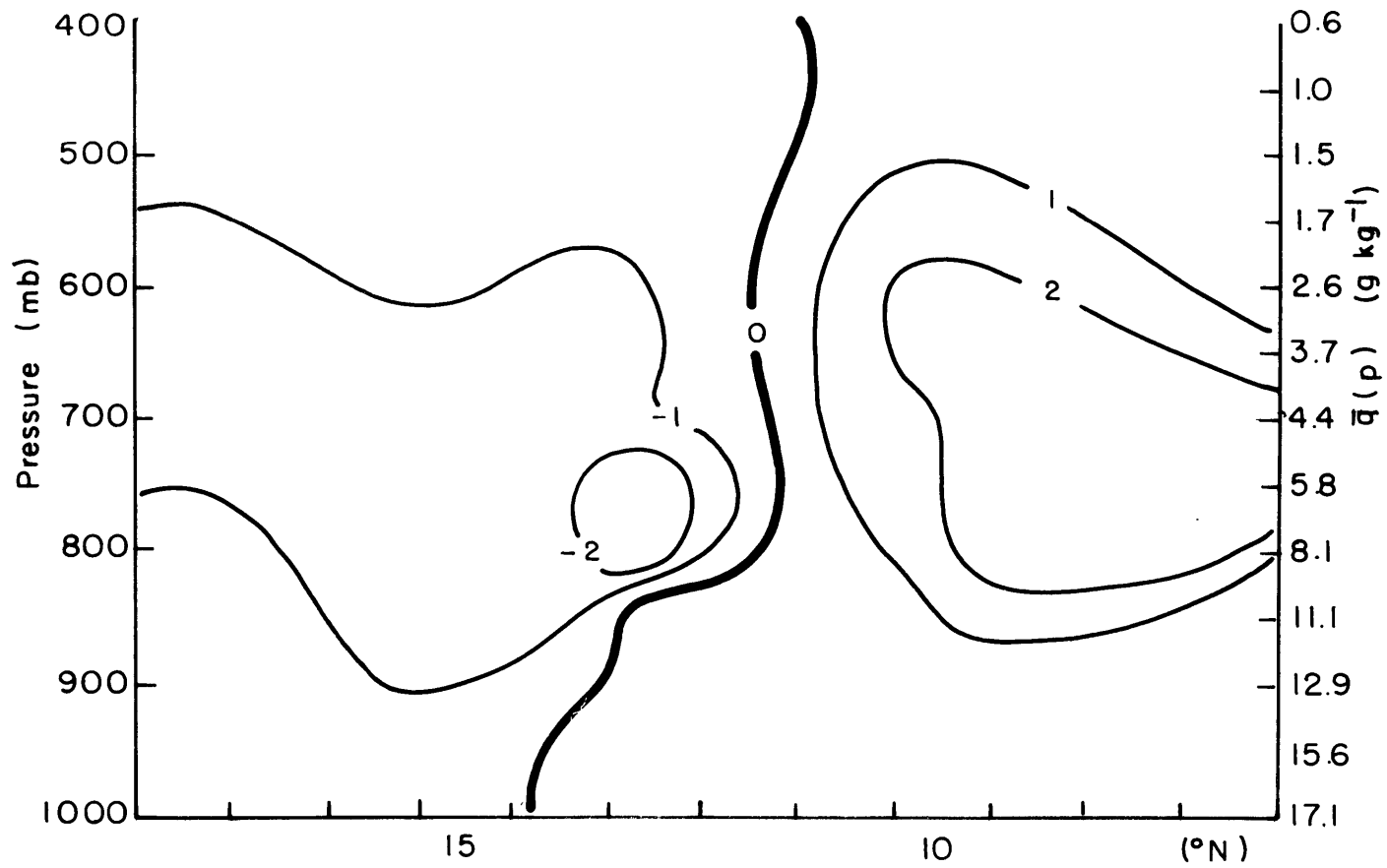


Fig. 4.32 The meridional distribution of water vapor mixing ratio (q) for the zonal cloud-band composite. The solid lines represent the deviation in g kg^{-1} of q from \bar{q} , shown at the right.

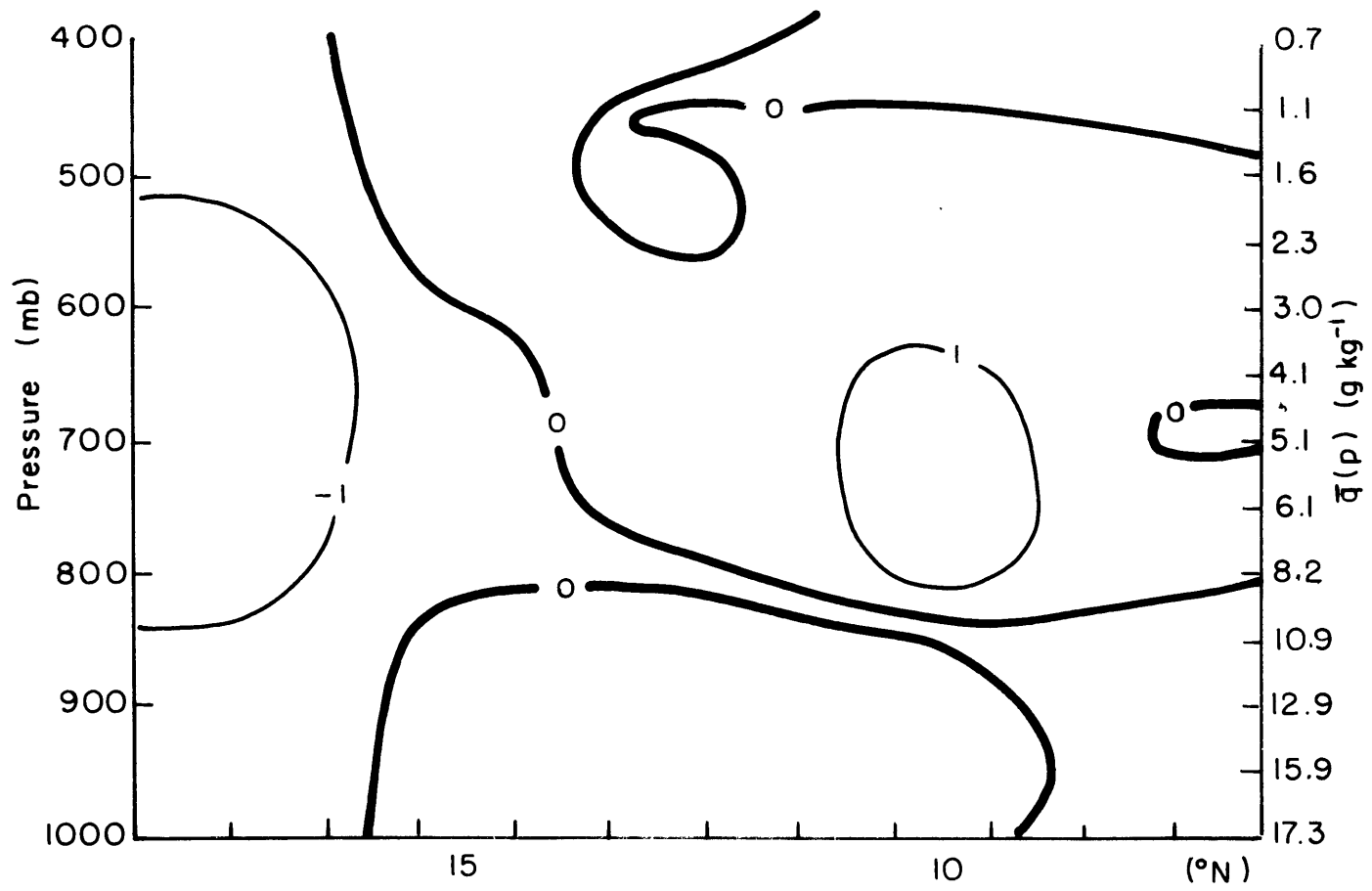


Fig. 4.33 Same as Fig. 4.32, but for the nonzonal cloud-band composite.

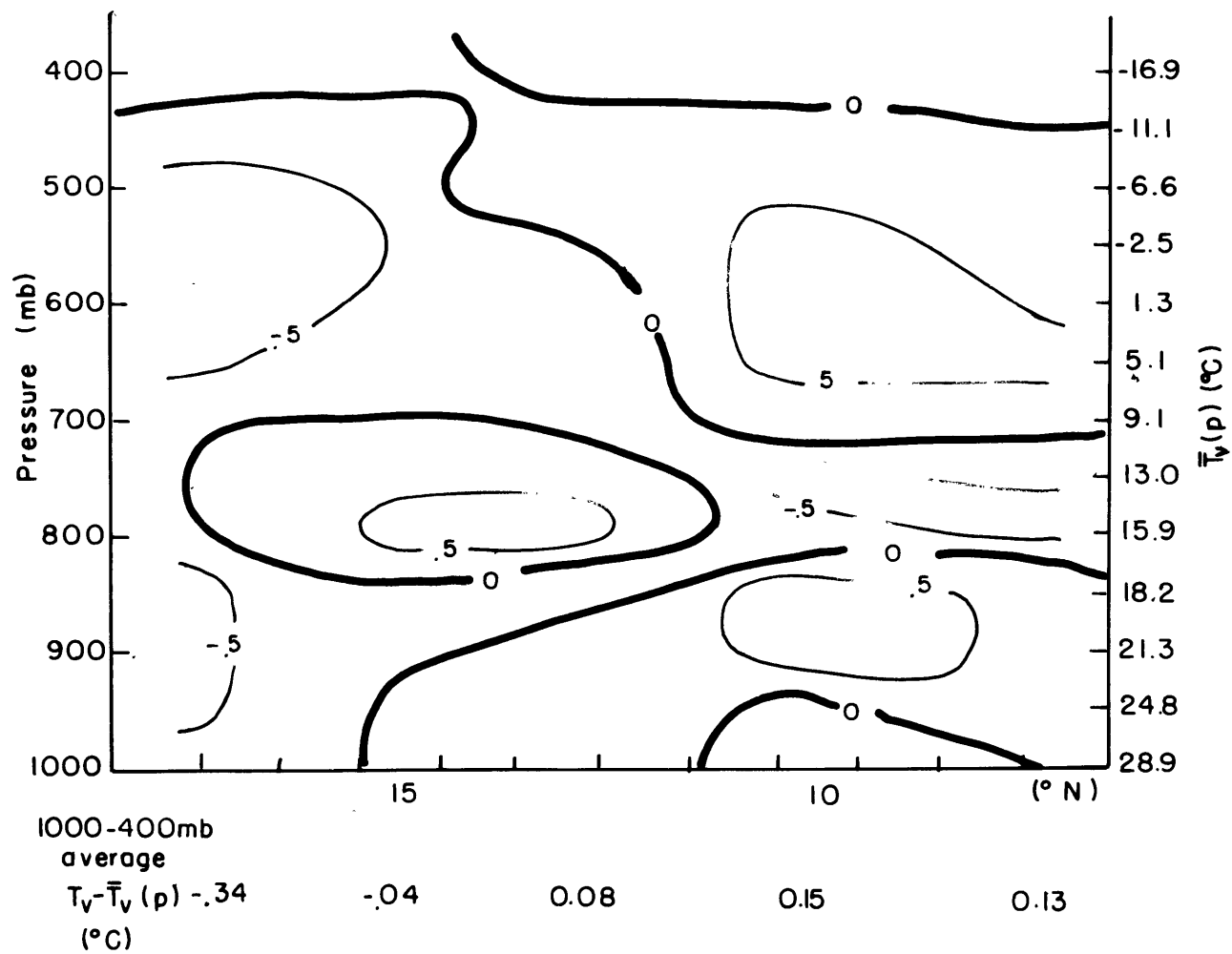


Fig. 4.34 The meridional distribution of virtual temperature (T_V) for the zonal cloud-band composite: The solid lines represent the deviation in $^{\circ}\text{C}$ of T_V from \bar{T}_V , shown at the right.

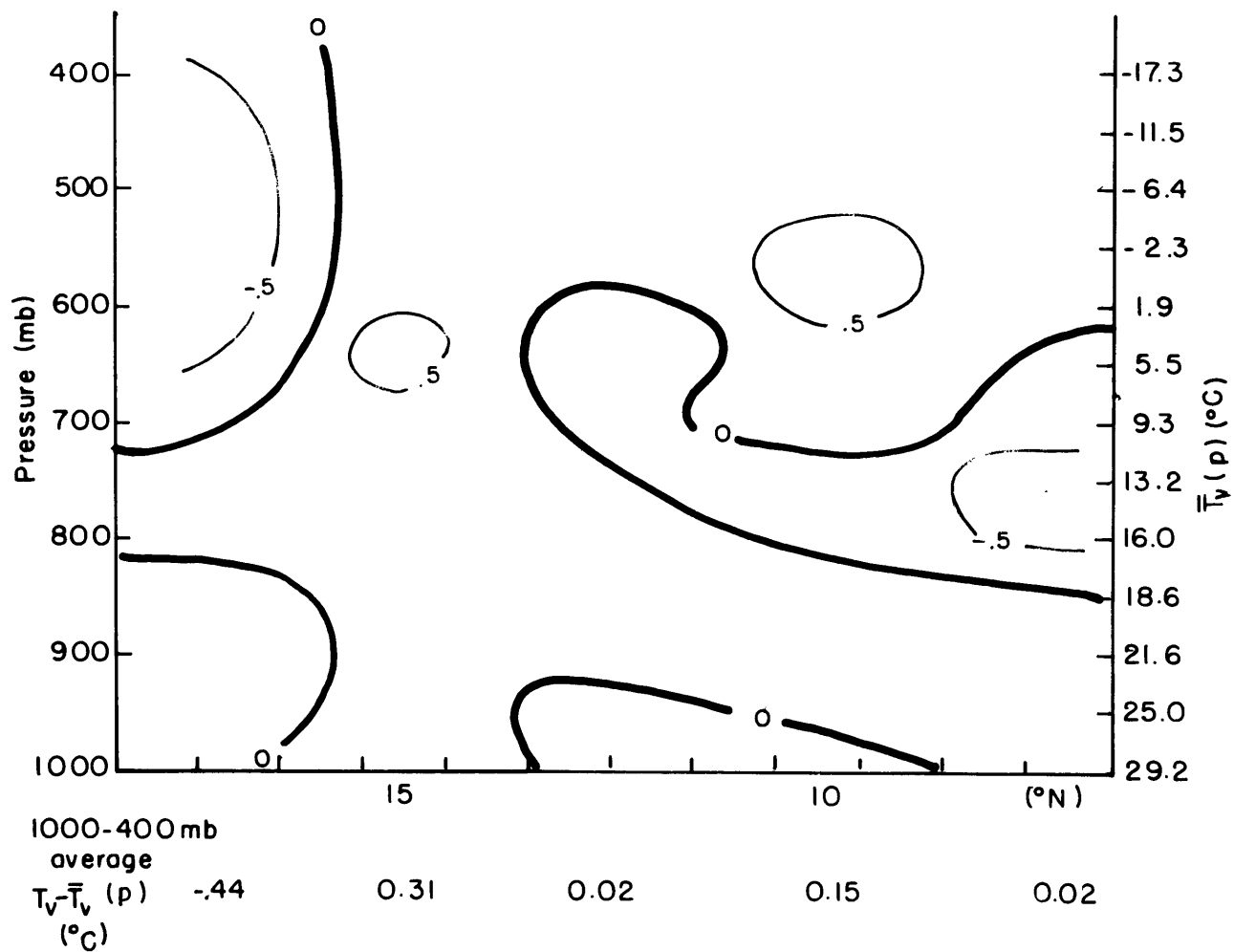


Fig. 4.35 Same as Fig. 4.34, but for the nonzonal cloud-band composite.

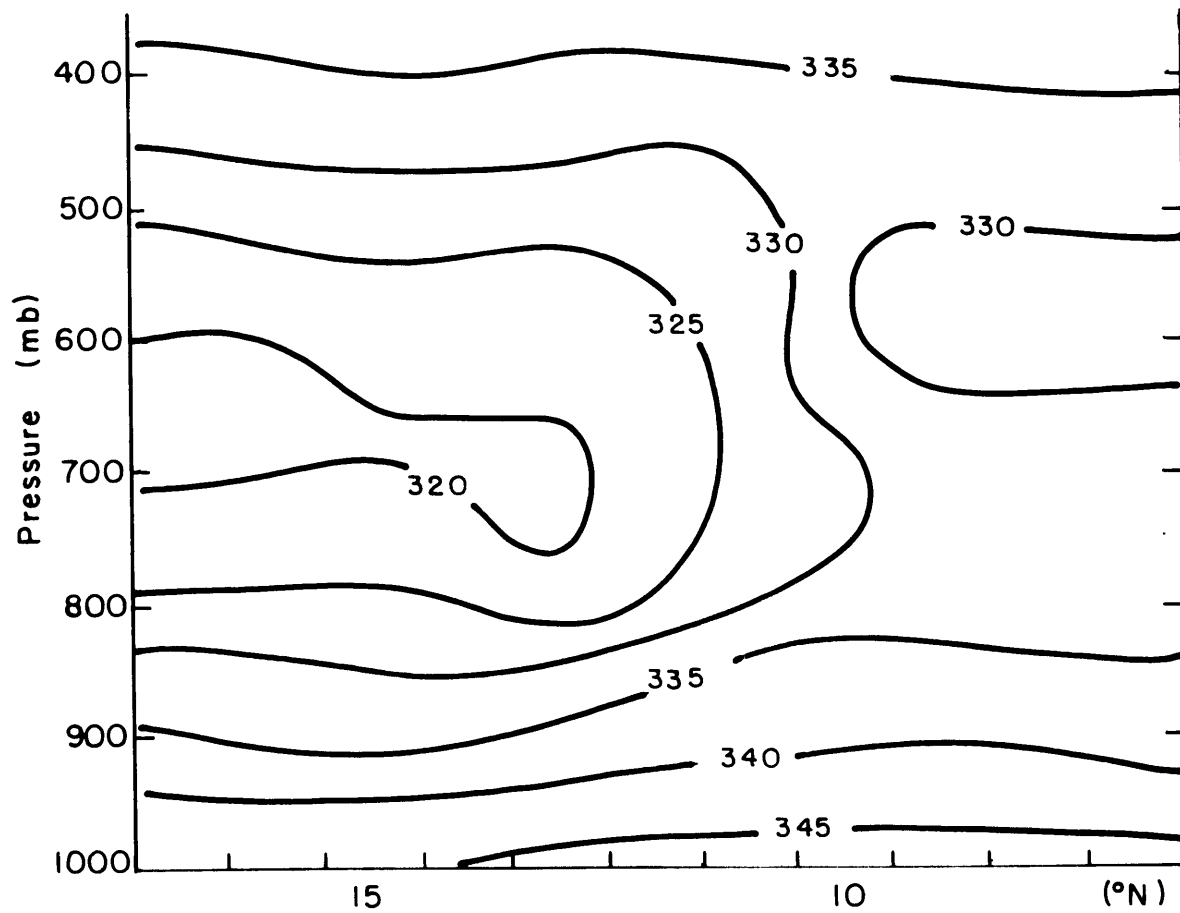


Fig. 4.36 The meridional distribution of equivalent-potential temperature (θ_e) in $^{\circ}$ K (solid lines) for the zonal cloud-band composite.

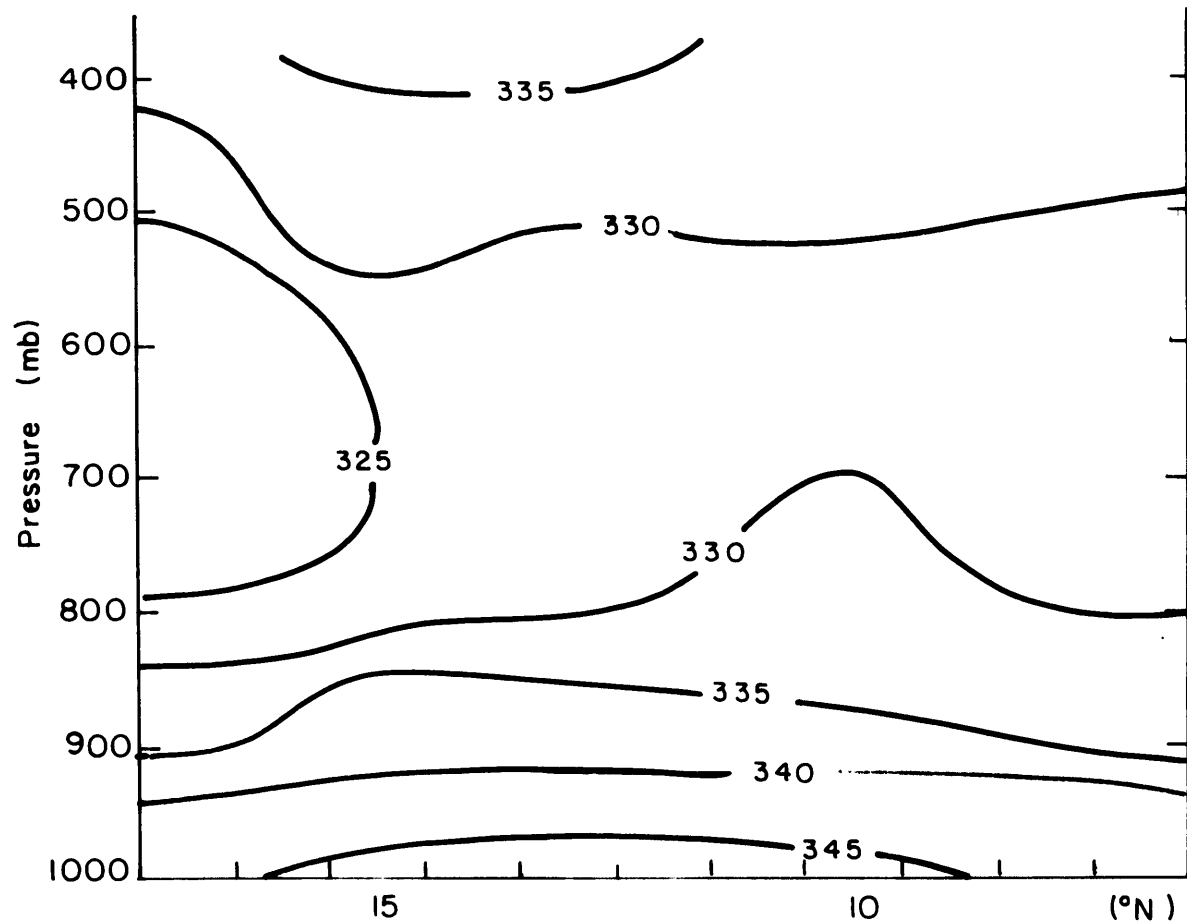


Fig. 4.37 Same as Fig. 4.36, but for the nonzonal cloud-band composite.

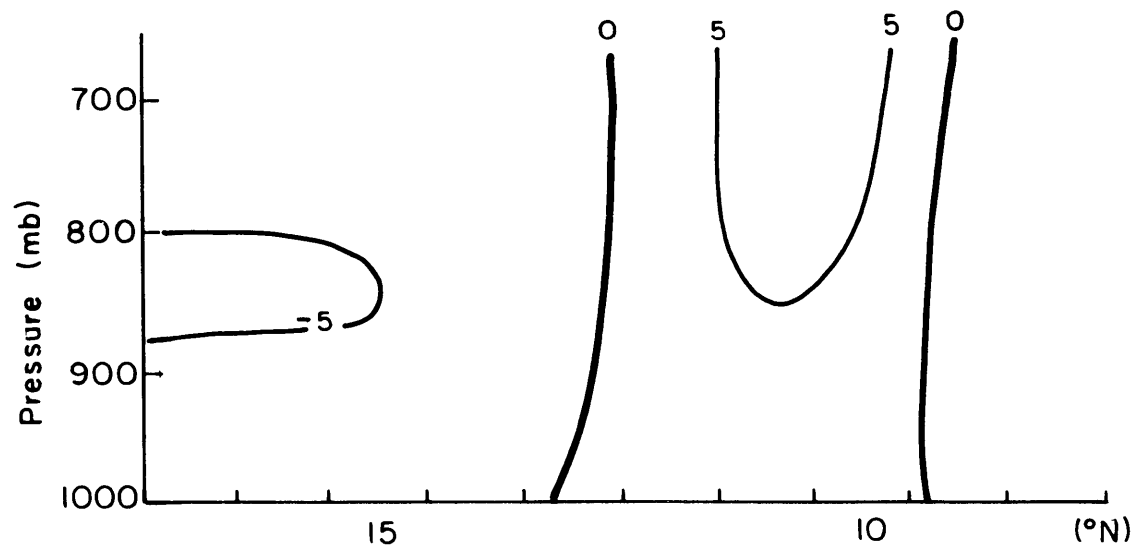
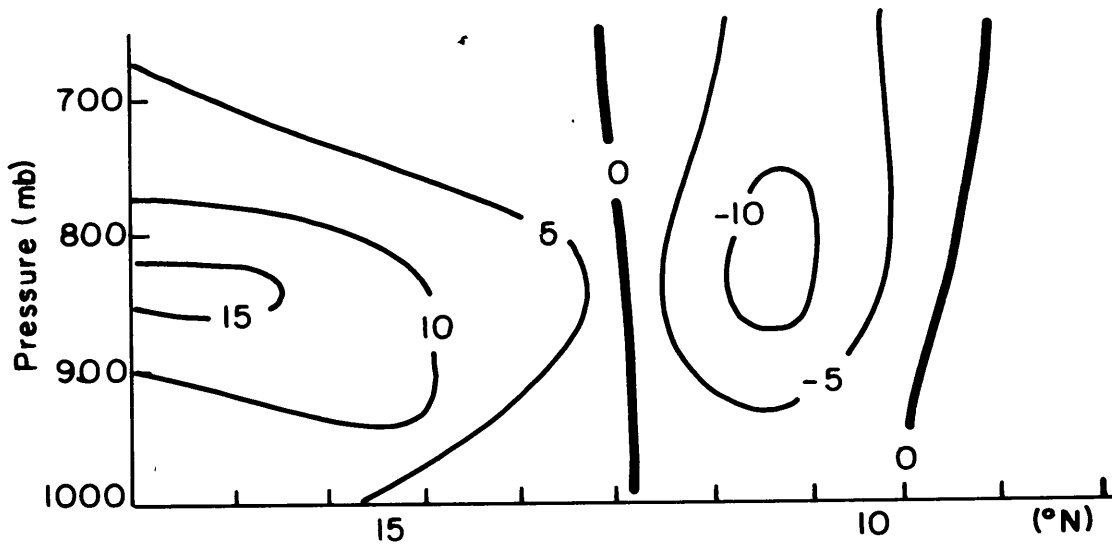


Fig. 4.38 The meridional distribution of the apparent heat source (Q_1) in $^{\circ}\text{C day}^{-1}$ for the zonal cloud-band composite.



$P_0 - E_0$ (cm day^{-1}) inferred	-1.8	-0.8	-0.6	-0.6	-0.9	0.7	2.5	2.2	0.2	-0.9
E_0 (cm day^{-1}) inferred	0.7	0.5	1.2	0.6	0.6	0.6	0.6	0.6	0.6	0.6
\hat{P}_0 (cm day^{-1}) inferred	-1.1	-0.1	0.3	2.9	-0.3	0.3	2.9	-0.3	-0.3	-0.3
P_0 (cm day^{-1}) measured	<0.2		0.9	1.1		0.9	1.1			
Sea-surface temp. ($^{\circ}\text{C}$)	T_0	27.8	28.0	27.8	28.2	27.8	28.2	28.2	28.3	28.3

Fig. 4.39 The meridional distribution of the apparent moisture source (Q_2) in $^{\circ}\text{C day}^{-1}$ for the zonal cloud-band composite. The inferred surface evaporation (E_0) and precipitation (P_0) rates, along with the measured precipitation rate (\hat{P}_0) and sea-surface temperature (T_0) are given below.

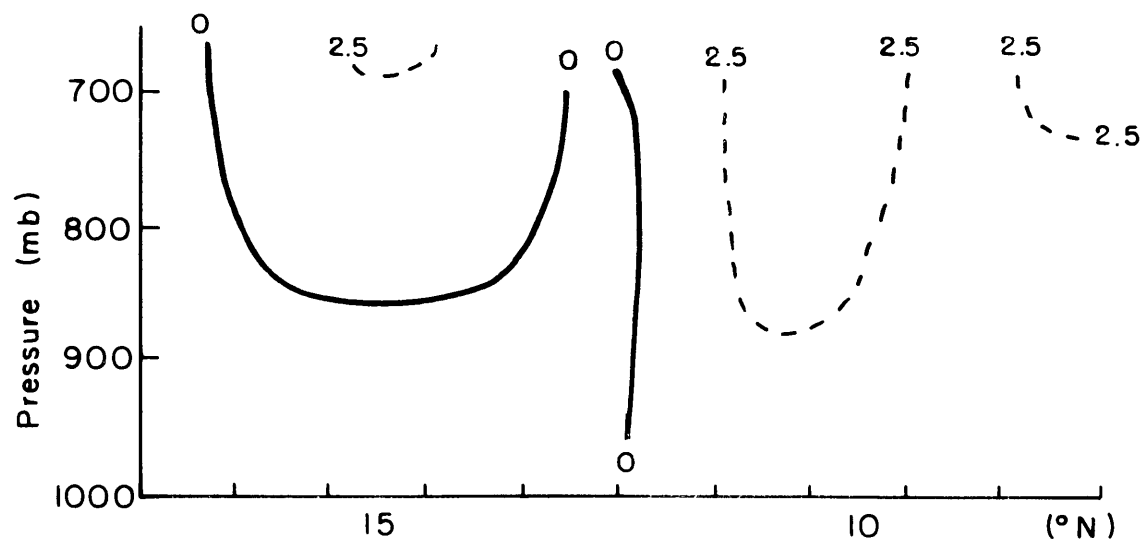
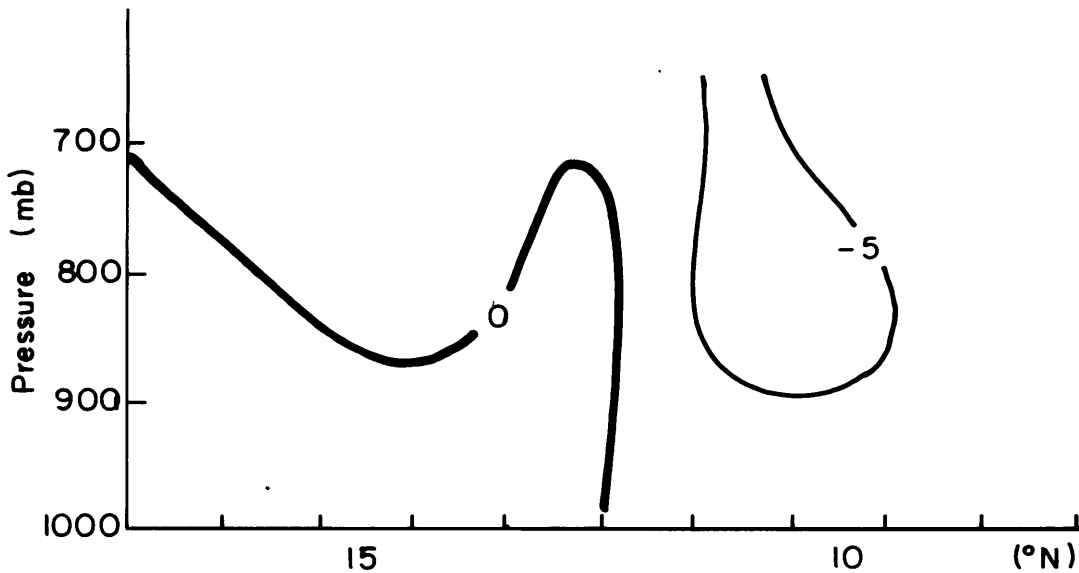
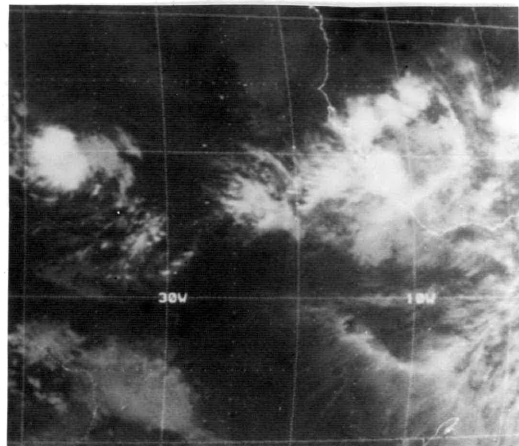


Fig. 4.40 Same as Fig. 4.38, but for the nonzonal cloud-band composite.

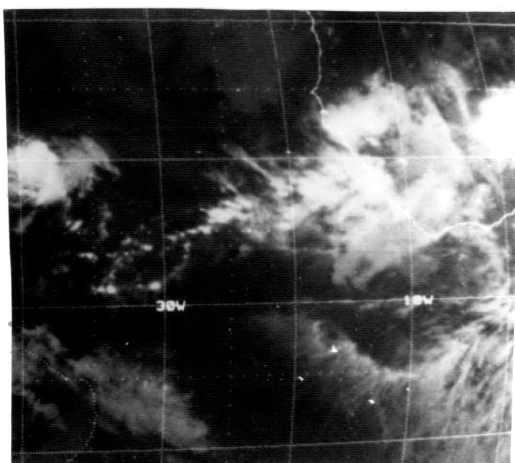


$P_0 - E_0$ (cm day^{-1}) inferred	-0.3	0.4	0.9	0.6	0	0.8	1.4	0.9	0.5	1.1
E_0 (cm day^{-1}) inferred	0.5		0.8		1.2		0.5			0.7
\hat{P}_0 (cm day^{-1}) inferred	0.2		1.7		1.2		1.7			1.8
P_0 (cm day^{-1}) measured	< 0.2				2.0		1.1			
T_0 Sea-surface temp ($^{\circ}\text{C}$)	27.9		28.2		27.9		28.5			28.6

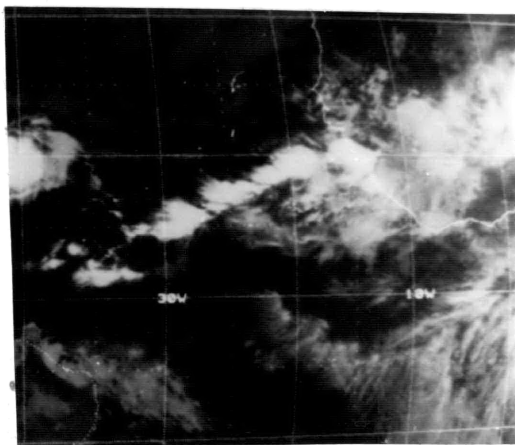
Fig. 4.41 Same as Fig. 4.39, but for the nonzonal cloud-band composite.



2100 GMT
11 August 1974

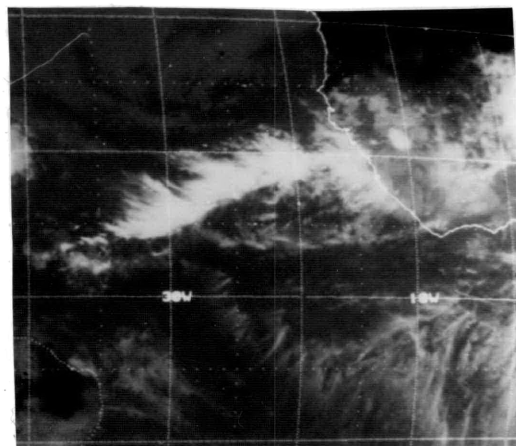


0000 GMT
12 August 1974

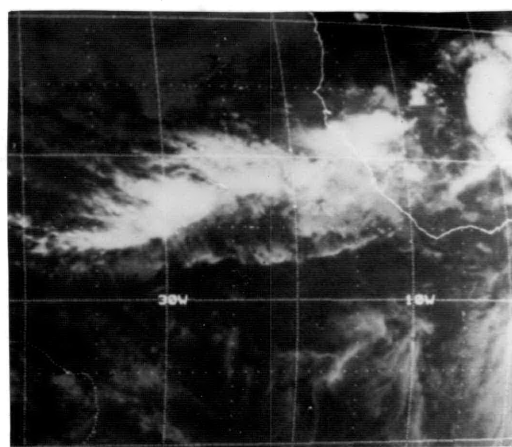


0600 GMT

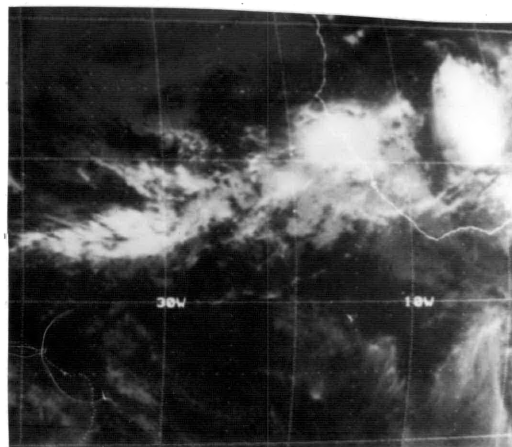
Fig. 5.1 SMS IR satellite photograph



1200 GMT
12 August 1974



1800 GMT



0000 GMT
13 August 1974

Fig. 5.2 SMS IR satellite photograph

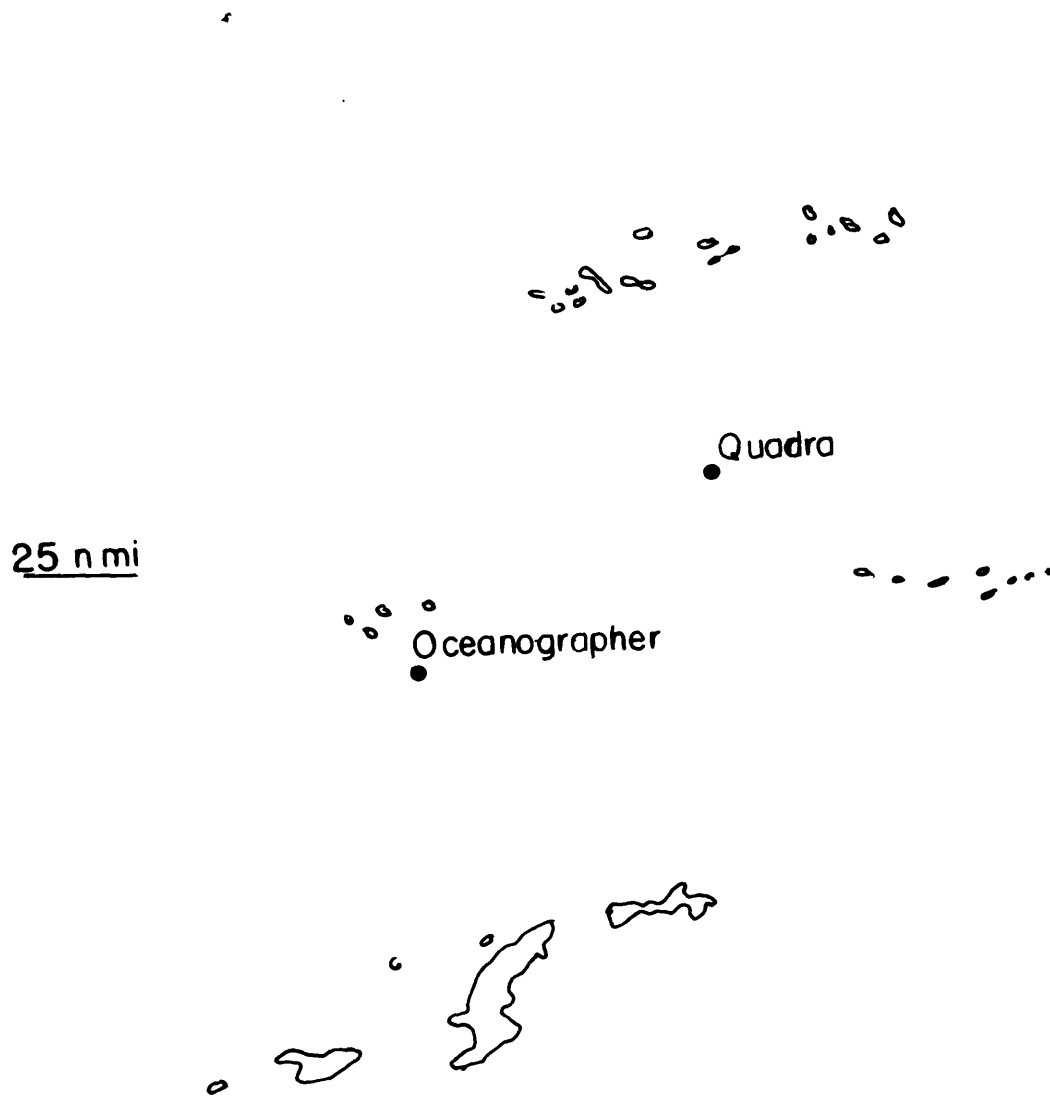


Fig. 5.3 Compositing low-level radar-echo distribution, 0000 GMT, 12 August, 1974.

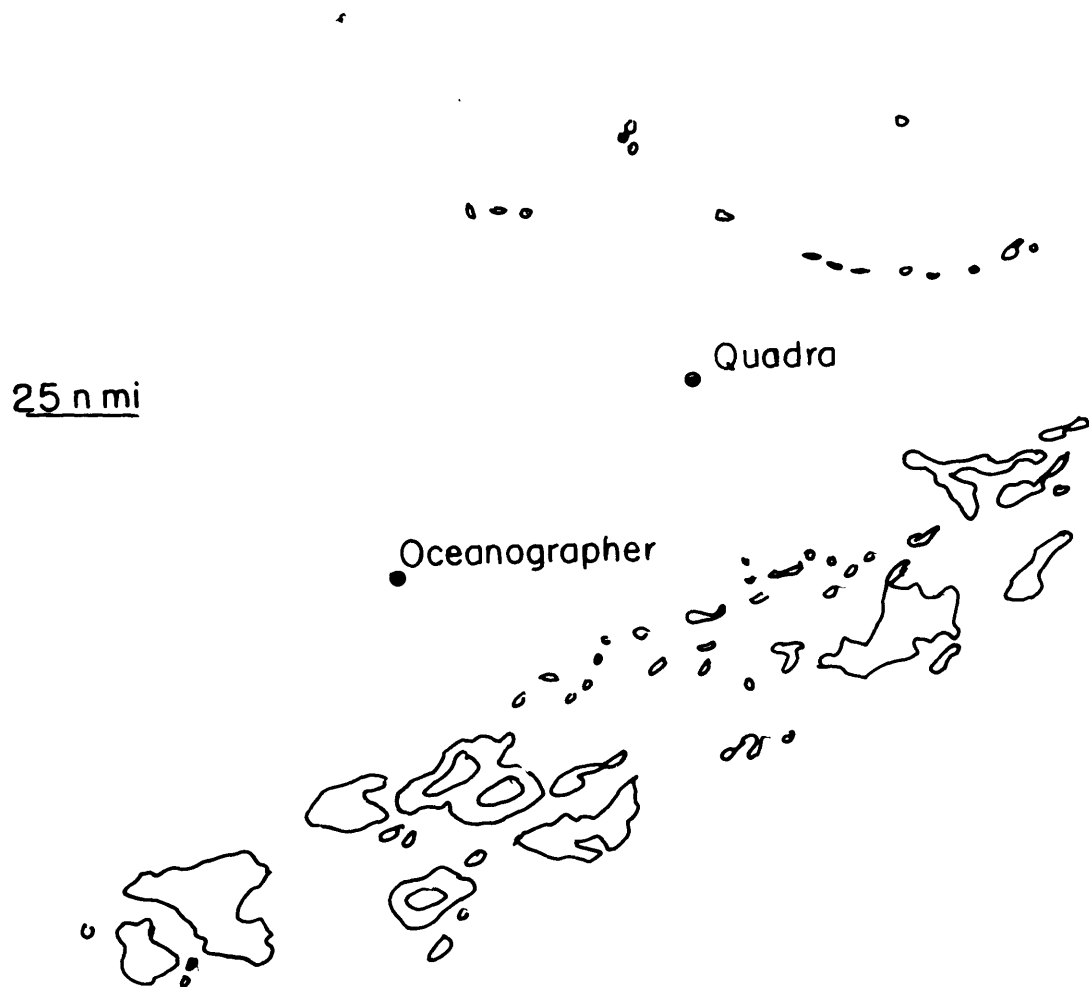


Fig. 5.4 Same as Fig. 5.3, but for 0600 GMT.

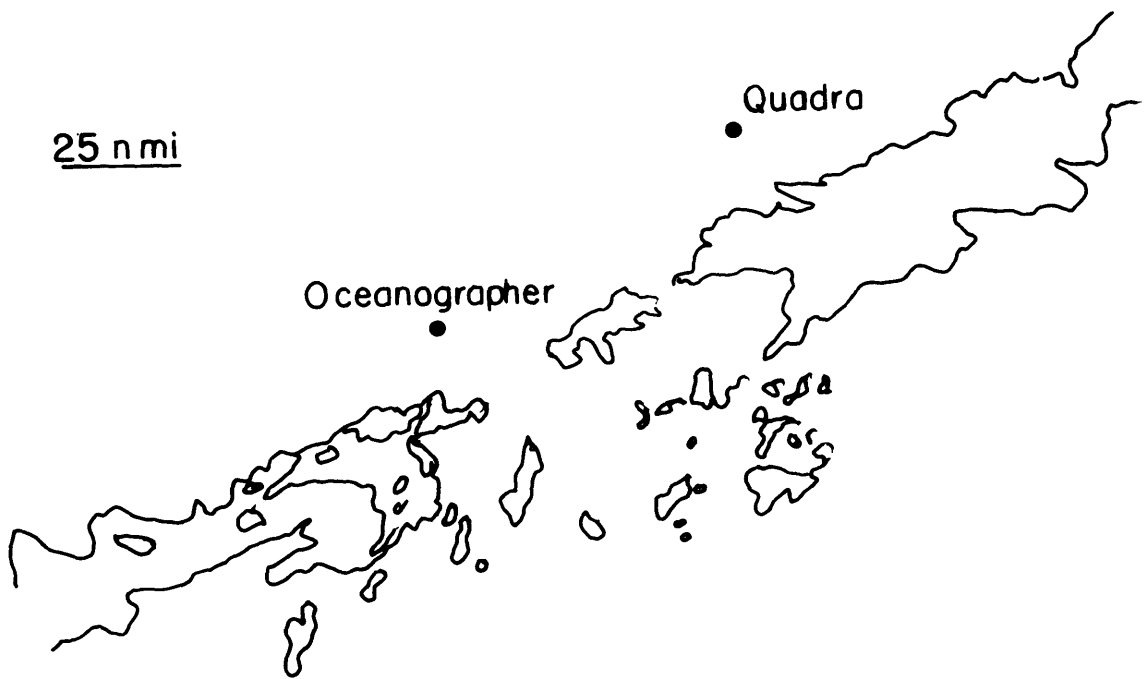


Fig. 5.5 Same as Fig. 5.3, but for 1200 GMT.

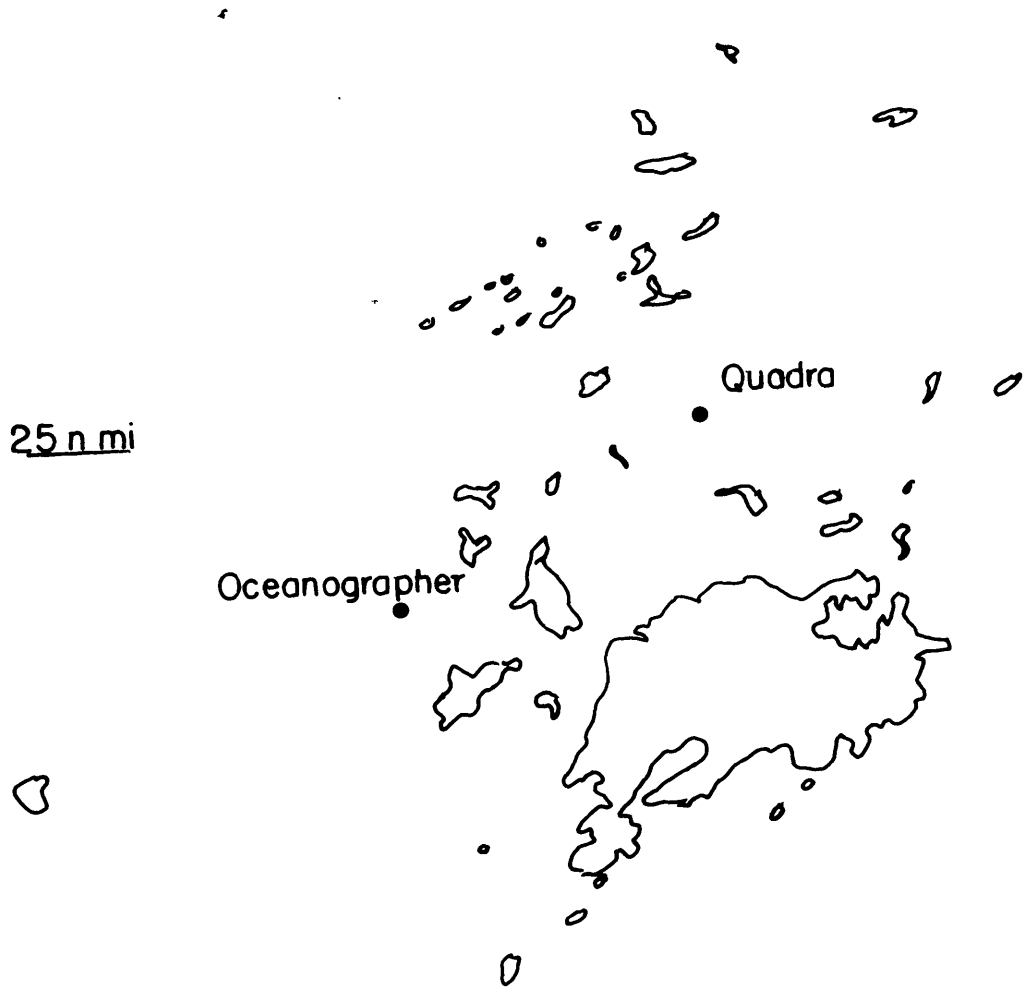


Fig. 5.6 Same as Fig. 5.3, but for 1800 GMT.

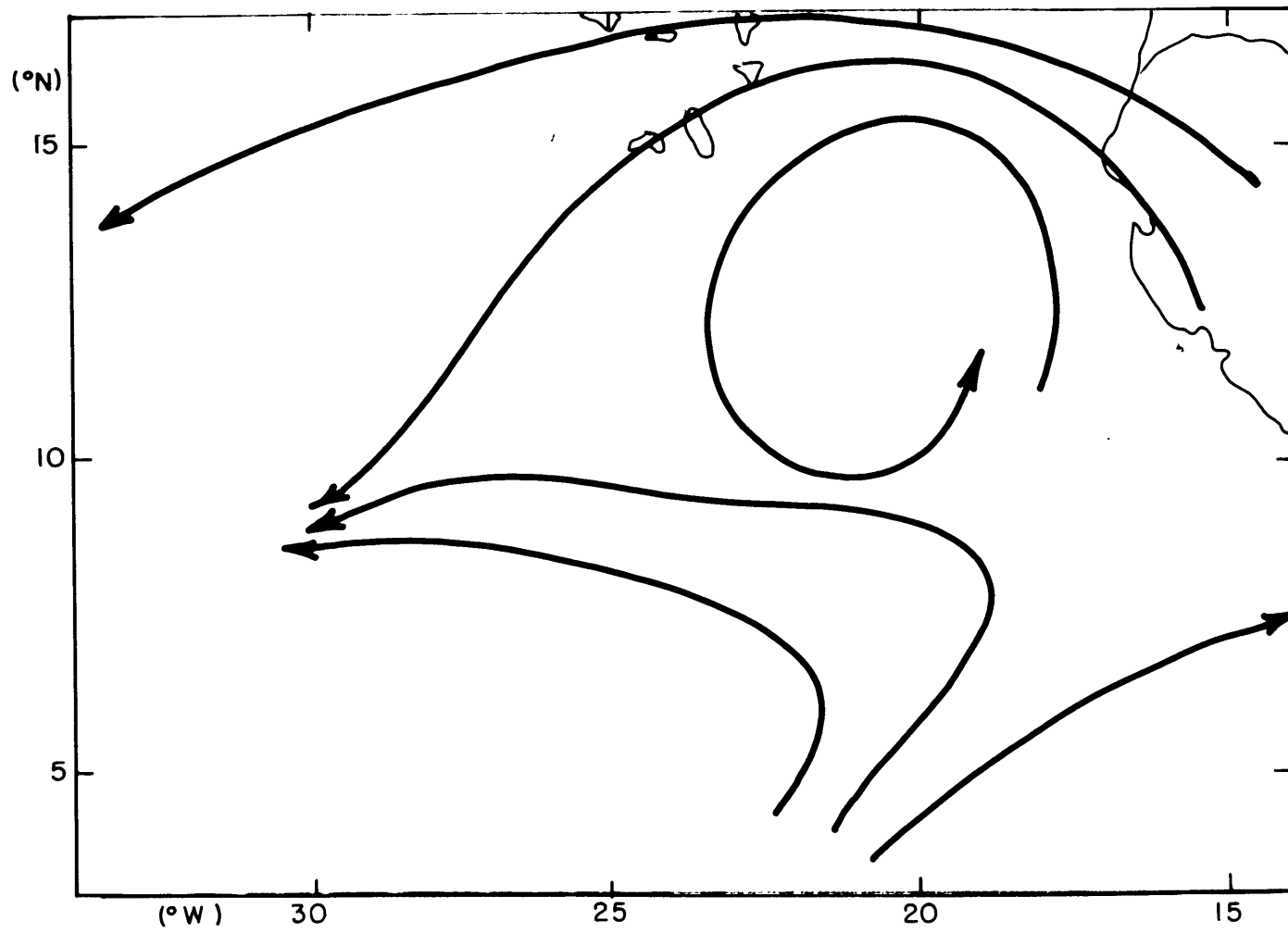


Fig. 5.7 850-mb streamlines (solid lines), 1800 GMT, 11 August, 1974.

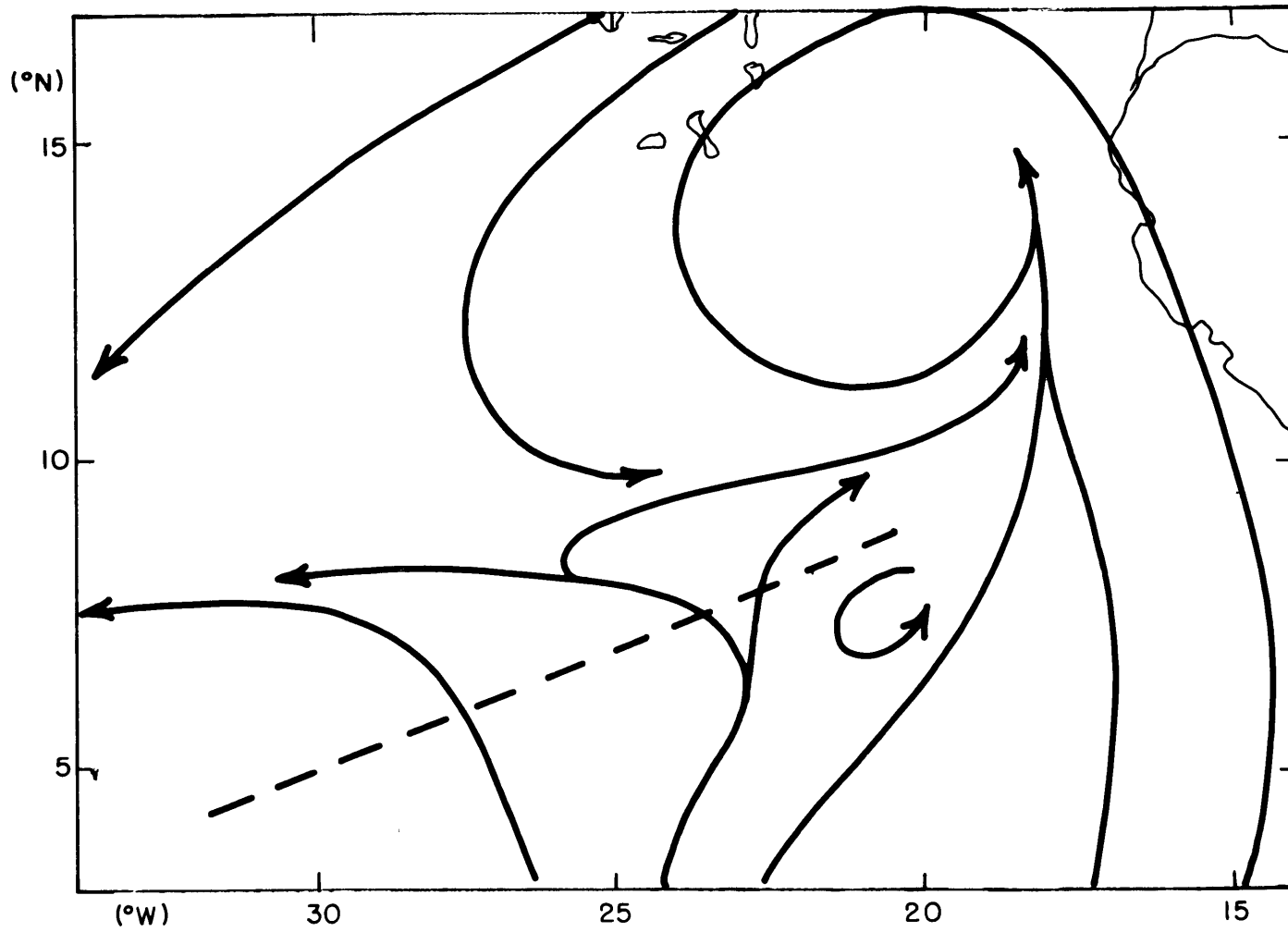


Fig. 5.8 Same as Fig. 5.7, but for 0000 GMT, 12 August, 1974.

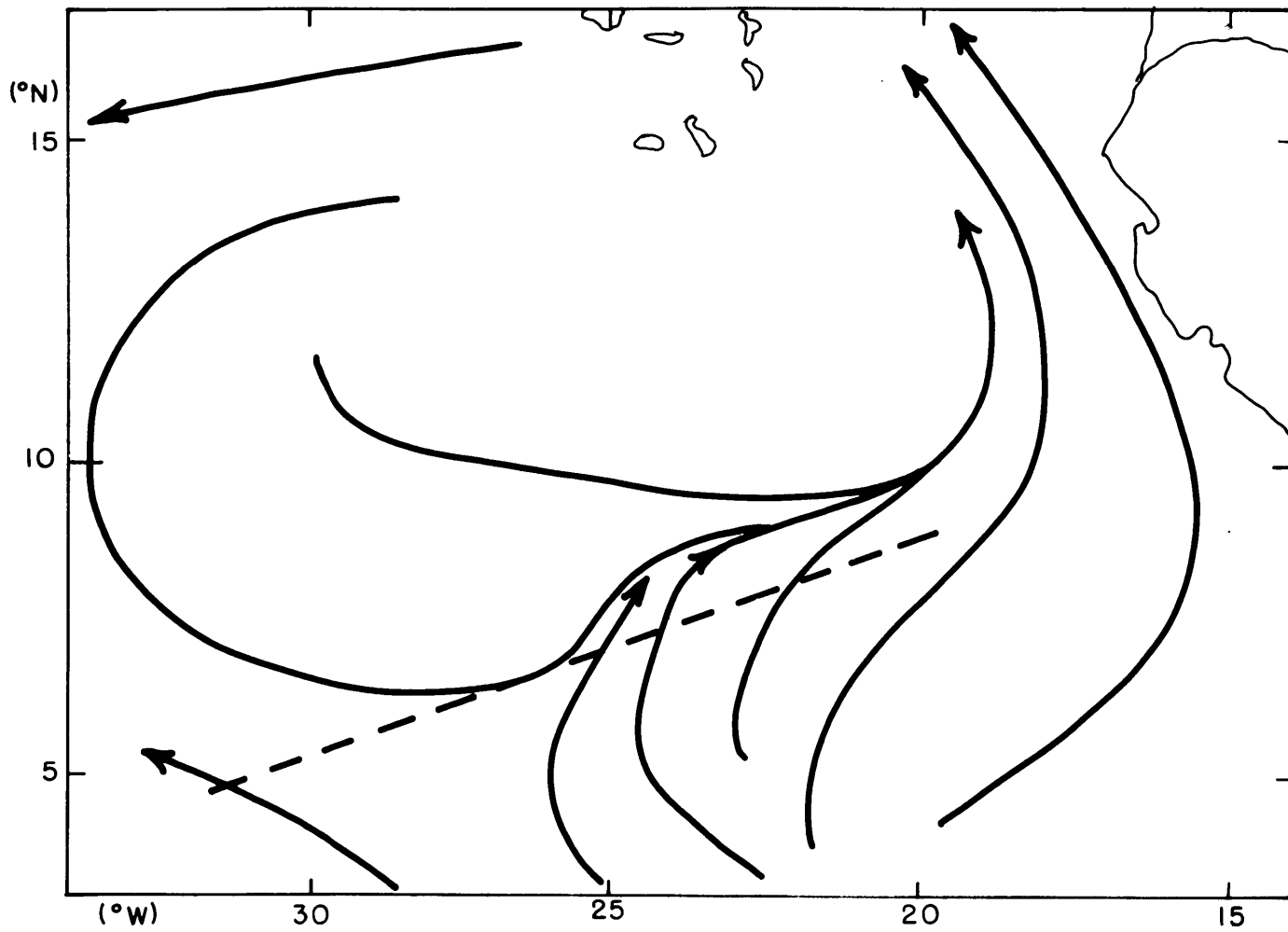


Fig. 5.9 Same as Fig. 5.8, but for 0600 GMT.

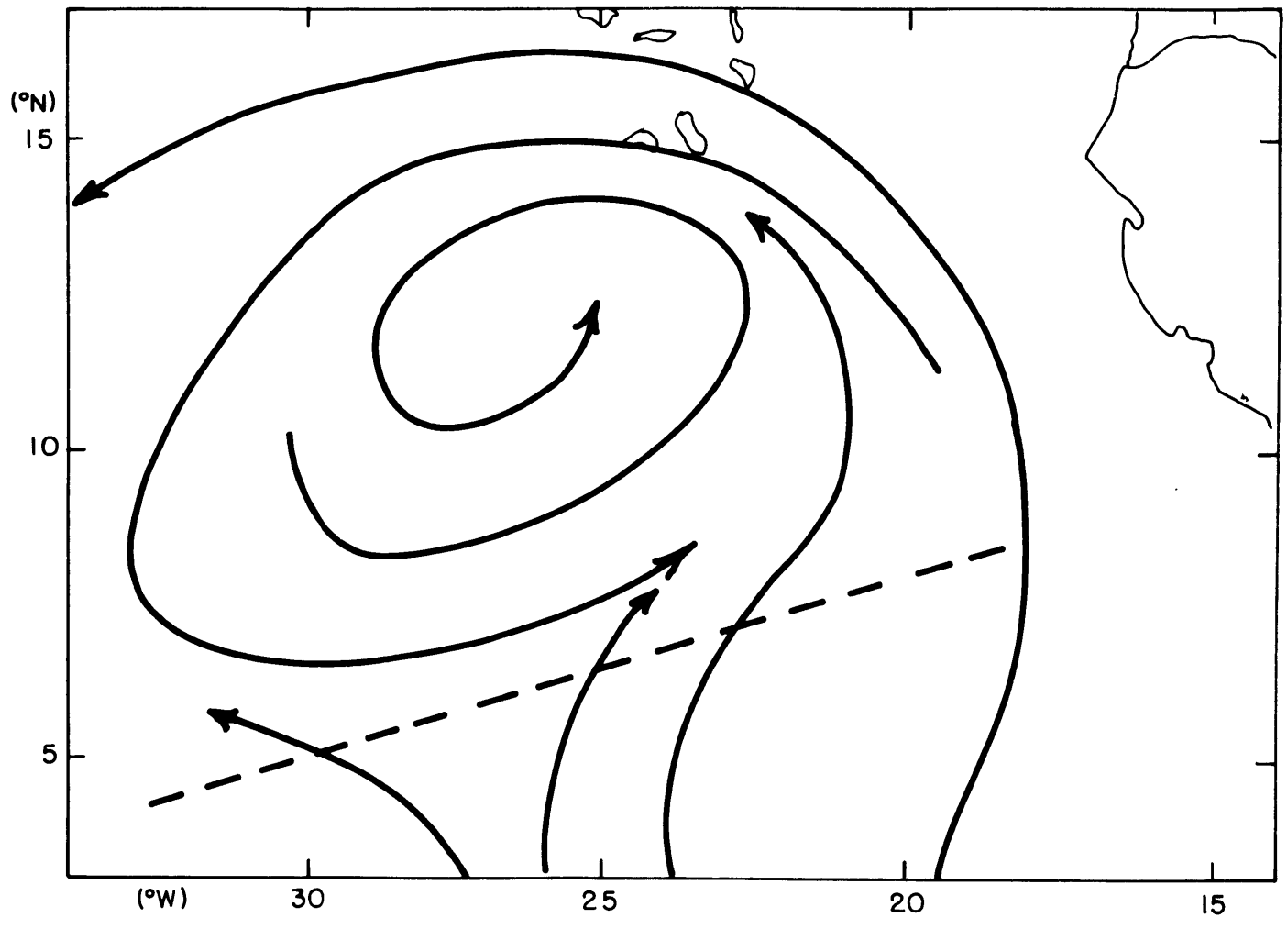


Fig. 5.10 Same as Fig. 5.8, but for 1200 GMT.

<u>pressure (mb)</u>	$\hat{T}(\text{°C})$			
	<u>0.5</u>	<u>1.0</u>	<u>1.0</u>	<u>4.0</u>
450	1.5	2.9	0.7	2.9
700	0.7	1.4	0.4	1.4
850	0.4	0.7	0.2	0.7
950	0.1	0.2	0.1	0.2
1000	0	0	0	0
$\overline{\frac{\partial T}{\partial y}}$ (°C/1000 km)	1.0	2.0	2.0	8.0
	L = 2000 km		L = 4000 km	
	warm core		baroclinic zone	

Table 2.1 $|\xi/f_0|$ for the quasigeostrophic analytic model

— indicates the maximum averaged over
a half-wavelength

<u>Station number</u>	Number of wind observations				<u>Name</u>	<u>Latitude° (N)</u>	<u>Longitude° (W)</u>	<u>Source</u>
	<u>950 mb</u>	<u>850 mb</u>	<u>700 mb</u>	<u>450 mb</u>				
1	83	80	80	76	<u>Oceanographer</u>	7.5	52.7	1,2,3
2	82	79	71	64	<u>Mt. Mitchell</u>	10.5	56.5	1,2
3	99	101	100	98	<u>Discoverer</u>	13.0	54.0	1,2,3
4	6	27	30	31	<u>Rockaway</u>	15.0	56.5	3
5	78	77	67	53	<u>Rainier</u>	17.5	54.0	1,2,3
6	37	37	37	37	Santo Domingo, D.R. (78486)	18.56	69.88	4
7	34	34	34	35	San Juan, P.R. (78526)	18.43	66.0	4
8	19	19	19	19	Antigua (78861)	17.2	61.8	4
9	19	19	19	19	St. Maarten (78866)	18.05	63.20	4
10	38	38	38	38	Raizet, Guadeloupe (78897)	16.27	61.52	4
11	34	35	35	35	Barbados (78954)	13.07	59.5	4
12	37	37	37	37	Trinidad (78967)	11.0	61.75	4
13	38	38	38	37	Curacao (78988)	12.2	68.96	4
14	17	18	18	18	Kourou, Fr. Guiana (81403)	5.2	52.7	5

<u>No.</u>	<u>Source</u>
1	Tape
2	Microfilm
3	Teletype
4	NHDT microfilm
5	ETAC teletype

Table 4.1 BOMEX Phase IV rawinsonde data

	Influence radius		r_{inf} (km)	
	<u>950 mb</u>	<u>850 mb</u>	<u>700 mb</u>	<u>450 mb</u>
zonal wind component (U)	980	1000	530	500
meridional wind component (V)	640	680	500	600

If $t_{inf} = 24$ hours ,

$$T(U) \sim 32 \text{ km hr}^{-1}$$

$$T(V) \sim 25 \text{ km hr}^{-1}$$

Table 4.2

Calculation of the scale factor of
the time-coordinate (T).

The data were from 14 fixed rawinsonde stations at 1200 GMT, 25 July 1969.
Only synchronous data were used.

	Westward Phase	speed	C (m sec ⁻¹)
Scale factor T (km hr ⁻¹)	0	8	16
20		26.7°	
25	33.8°	25.7°	27.7°
30		24.8°	

20 point average orientation of axis of dilatation (θ_d) is given in degrees measured counterclockwise from the x-axis.

1200 GMT, 24 July 1969

Table 4.3

Sensitivity of the estimated average axis-of-dilatation orientation (θ_d) to the scale factor (T) and phase speed (C).

<u>Date</u>	<u>Number of points in average</u>	$ \overline{\Delta\theta} $ (degrees)			
		<u>950 mb</u>	<u>850 mb</u>	<u>700 mb</u>	<u>450 mb</u>
7/13/69	46	34.1	18.6	40.5	38.0
14	38	32.9	35.5	31.6	59.8
15	14	54.5	43.4	54.7	49.8
18	28	26.3	35.3	55.0	38.8
19	40	34.0	33.5	33.1	53.8
20	13	21.5	12.2	17.8	43.0
21	17	31.0	25.9	32.3	58.9
22	33	38.2	43.4	46.6	51.8
24	20	23.9	25.7	26.4	23.4
25	37	35.1	22.1	27.1	29.1
27	22	30.9	41.3	34.6	24.1
28	44	25.8	33.2	31.9	39.8
Total number					
	$\leq 45^\circ$	11 (.003)	12 (.000)	9 (.073)	7 (.387)
	$\leq 40^\circ$	11 (.001)	9 (.033)	8 (.104)	6 (.457)
	$\leq 35^\circ$	9 (.012)	7 (.139)	8 (.049)	3 (>.306)
	$\leq 30^\circ$	4 (>.178)	5 (>.178)	3 (>.1777)	3 (>.178)
	$\leq 25^\circ$	2 large	3 large	1 large	2 (>.086)

The probability that random noise would have produced more than or equal to that number of samples is shown in parenthesis.

Table 4.4
Statistical analysis of $|\overline{\Delta\theta}|$

BIBLIOGRAPHY

- Albrecht, B. and S. K. Cox, 1975: The large-scale response of the tropical atmosphere to cloud-modulated infrared heating. J. Atmos. Sci., 32, 16-24.
- Allied Research Associates, 1969: The Nimbus III Data Catalog, Volume 3, July 1969. Goddard Space Flight Center, Greenbelt, MD.
- Anderson, R., J. Ashman, F. Bittner, G. Farr, E. Ferguson, V. Oliver, and A. Smith, 1969: Application of Meteorological Satellite Data in Analysis and Forecasting. ESSA Technical Report NESC 51, National Environmental Satellite Center, Suitland, MD.
- Atkinson, Gary and James C. Sadler, 1970: Mean-cloudiness and gradient-level wind charts over the tropics. Vol I and II, AWS Technical Report 215.
- Atkinson, Gary, 1975: Personal communication. Scott AFB, Ill.
- Bendat, J. S. and A. G. Piersol, 1966: Measurement and Analysis of Random Data, Wiley, New York.
- Bergeron, T., 1928: Uber die dreidimensional verknupfende Wetteranalyse. Geof. Publ. 5, No. 6.
- Betts, Alan K., 1974: Thermodynamic classification of tropical convective soundings. Mon. Wea. Rev., 102, 760-764.
- Blackman, R., and J. Tukey, 1958: The Measurements of Power Spectra from the Point of View of Communications Engineering. Dover.
- Blanchard, D. C., and A. H. Woodcock, 1957: Bubble formation and modification in the sea and its meteorological significance. Tellus, 9, 145-158.
- BOMAP, 1971: BOMEX Field Observations and Basic Data Inventory. NOAA, Rockville, MD
- Burpee, Robert W., 1971: The origin and structure of easterly waves in the lower troposphere of North Africa. Ph.D. thesis, Dept. of Meteorology, Cambridge, Mass.
- Carlson, T. N., 1969: Some remarks on African disturbances and their progress over the tropical Atlantic. Mon. Wea. Rev., 97, 716-726.
- CEDDA, 1975: BOMEX Permanent Archive: Description of Data. NOAA Technical Report EDS 12, NOAA, Washington, DC.

Charney, Jule G. and Arnt Eliassen, 1964: On the growth of the hurricane depression. J. Atmos. Sci., 21, 68-75.

Charney, Jule G. 1971: Tropical cyclogenesis and the formation of the Intertropical Convergence Zone. Mathematical Problems in the Geophysical Sciences; I. Geophysical Fluid Dynamics, 355-368. Lectures in Applied Mathematics, Vol. 13, American Math. Soc., Providence, RI.

Chernoff, Herman, 1975: Personal communication. MIT, Cambridge, MA.

Cho, H. and Y. Ogura, 1974: A relationship between cloud activity and the low-level convergence as observed in Reed-Recker's composite easterly waves. J. Atmos. Sci., 31, 2058-2065.

Cornelius, Clifford J., 1974: The Inclusion of Moisture in a Numerical Model of Steady-State Fronts. M.S. thesis, Dept. of Meteorology, Naval Postgraduate School, Monterey, Calif.

Cressman, George, 1957: An objective analysis study. Technical memorandum No. 12, Joint Numerical Weather Prediction Unit.

Cressman, George, 1959: An operational objective analysis system. Mon. Wea. Rev., 87, 367-374.

Dopplnick, T. G., 1970: Global radiative heating of the earth's atmosphere. Planetary Circulation Project Rept. No. 24, Dept. of Meteorology, MIT, Cambridge, MA.

Drake, Alvin W., 1967: Fundamentals of Applied Probability Theory, McGraw-Hill, New York.

Eddy, Amos, 1967: Two-dimensional statistical objective analysis of isotropic scalar data fields. University of Texas Atmos. Sci. Group Report 5, Univ. of Texas, Austin, Texas.

Eliassen, A., 1955: Lectures on physical weather prediction. Unpublished class notes. Dept. of Meteorology, MIT, Cambridge, MA.

Eliassen, Arnt, 1959: On the Formation of Fronts in the Atmosphere. The Atmosphere and the Sea in Motion; Scientific Contributions to the Rossby Memorial Volume, Rockefeller Institute Press, New York.

Eliassen, Arnt, 1966: Motions of intermediate scale: fronts and cyclones. Advances in Earth Science, MIT Press, Cambridge, MA, 111-138.

Faller, Alan J., 1956: A demonstration of fronts and frontal waves in atmospheric models. J. Met., 13, 1-4.

- Fett, Robert W., 1973: A quantitative description of weak tropical wave structure based on analysis of ATS cloud motion vectors. Paper presented at the Eighth Technical Conference on Hurricanes and Tropical Meteorology, Key Biscayne, Fla.
- Frank, Neil, L., 1969: The "inverted V" cloud pattern - an easterly wave? Mon. Wea. Rev., 97, 130-140.
- Gandin, L. S. 1963: "ob" ektivnyi analiz meteorologicheskikh polei. Translated by Israel Program for Scientific Translations, Jerusalem 1965, for U.S. Dept. of Commerce and NSF, Wash, D.C.
- Garstang, Michael, 1967: Sensible and latent heat exchange in low latitude synoptic scale systems. Tellus, 19, 592-508.
- Geotis, S., 1974: Personal communication, MIT, Cambridge, MA.
- Haltiner, George, 1971: Numerical Weather Prediction, John Wiley and Sons, Inc., New York.
- Hawkins, Harry F. and Daryl T. Rubsam, 1968: Hurricane Hilda, 1964, structure and budgets of the hurricane on October 1, 1964. Mon. Wea. Rev., 96, 617-636.
- Hoel, P. and S. Port, C. Stone, 1971: Introduction to Statistical Theory, Houghton Mifflin Co., Boston, MA.
- Hoskins, B. J., 1972: Discussions Q.J.R.M.S., 98, 862.
- Hoskins, B. J. and F. P. Bretherton, 1972: Atmospheric frontogenesis models: mathematical formulation and solution. J. Atmos. Sci., 29, 11-37.
- Hubert, Lester, 1975: Personal communication. NESS, Suitland, MD.
- Janota, Paul, 1971: An Empirical Study of the Planetary Boundary Layer in the Vicinity of the Intertropical Convergence Zone. Ph.D. thesis, Dept. of Meteorology, MIT, Cambridge, MA.
- Julian, Paul R., 1975: Comments on the determination of significance levels of the coherence statistic. J. Atmos. Sci., 32, 836-837.
- Leary, Colleen, 1972: Synoptic Case Study of a Warm Core Tropical Depression. S.M. thesis, Dept. of Meteorology, MIT, Cambridge, MA.
- Leese, John A., and C. Novak, V. Taylor, 1970: The determination of cloud pattern motions from geosynchronous satellite image data. Pattern Recognition, Pergamon Press, 279-292.

- Lindzen, Richard S., 1974: Wave-CISK in the tropics. J. Atmos. Sci., 31, 156-179.
- Mahrt, Larry J., 1972: A numerical study of the influence of advective accelerations in an idealized, low-latitude, planetary boundary layer. J. Atmos. Sci., 29, 1477-1484.
- Malkus, Joanne S. and Herbert Riehl, 1964: Cloud structure and distributions over the tropical Pacific Ocean. Tellus, 16, 275-287.
- Miller, Donald and Robert Feddes, 1971: Global atlas of relative cloud cover, 1967-70, based on data from meteorological satellites. NESS and ETAC.
- Mudrick, Stephen, 1973: A numerical study of frontogenesis. Ph.D. thesis, Dept. of Meteorology, MIT, Cambridge, MA.
- Namias, Jerome and Philip Clapp, 1949: Confluence theory of the high tropospheric jet stream. J. Met., 6, 330-336.
- Newell, Reginald, and J. Kidson, D. Vincent, G. Boer, 1972: The General Circulation of the Tropical Atmosphere and Interactions with Extratropical Latitudes, The MIT Press, Cambridge, MA.
- Nitta, Tsuyoshi and Stephen Esbensen, 1974: Heat and moisture budget analysis using BOMEX data. Mon. Wea. Rev., 102, 17-28.
- NOAA, 1971: Catalog of Meteorological Satellite Data - ESSA 9 Television Cloud Photography, July 1-Sept. 30, 1969. NOAA, Silver Spring, MD.
- Panofsky, H. and G. Brier, 1958: Some Applications of Statistics to Meteorology. Penn. State, University Park, PA.
- Pettersen, Sverre and James Austin, 1942: Fronts and frontogenesis in relation to vorticity. Papers in physical oceanography and meteorology, MIT and WHOI, Vol. VII, no. 2.
- Pettersen, Sverre, 1956: Weather Analysis and Forecasting, Vol. I. McGraw-Hill, New York.
- Phillips, Norman A., 1970: Unpublished class notes on dynamical meteorology, MIT, Cambridge, MA.
- Phillips, N. A., 1971: Unpublished class notes for course on numerical weather prediction, MIT, Cambridge, MA.

- Pielke, Roger, 1973: A three-dimensional numerical model of the sea breezes over South Florida. NOAA Technical Memorandum ERL WMPO-2, EML, Coral Gables, Fla.
- Pike, Arthur C., 1970: The inter-tropical convergence zone studied with an interacting atmosphere and ocean model. Scientific Report No. 2, AFCRL, Bedford, MA.
- Rasmussen, G., 1974: Personal communication, CEDDA, Rockville, MD.
- Rektorys, Karel, 1969: Survey of Applicable Mathematics, The MIT Press, Cambridge, MA.
- Riehl, Herbert, 1954: Tropical Meteorology. McGraw-Hill, New York.
- Ruttenberg, S., 1975: GATE Information Bulletin No. 6., NCAR, Boulder, Colorado.
- Sanders, Frederick and Jon Plotkin, 1966: Detailed analysis of an intense surface cold front. Paper delivered at meeting of the A.M.S., Denver, Colo.
- Sanders, Frederick, 1971: Analytic solutions of the nonlinear omega and vorticity equations for a structurally simple model of disturbances in the baroclinic westerlies. Mon. Wea. Rev., 99, 393-407.
- Sanders, F. and A. Pike, J. Gaertner, 1975: A baroclinic model for operational prediction of tracks of tropical storms. J. App. Met., 14, 265-280.
- Sanders, F., 1975a: Fronts and frontogenesis. Unpublished class notes, MIT, Cambridge, MA.
- Sanders, F., 1975b: Quantitative quasi-geostrophic theory: a readers' guide to "Analytic solutions...". Unpublished class notes, MIT, Cambridge, MA.
- Sanders, F., 1975c: Personal communication. MIT, Cambridge, MA.
- Sasaki, Y., 1970: Numerical variational analysis formulated under the constraints as determined by longwave equations and a low-pass filter. Mon. Wea. Rev. 98, 864-898.
- Sawyer, J. S., 1956: The vertical circulation at meteorological fronts and its relation to frontogenesis. Proc. Roy. Soc. A, 234, 346-362.
- Schaefer, Joseph T., 1973: The motion and morphology of the dryline. NOAA Technical Memorandum ERL NSSL-66, NSSL, Norman, Okla.

- Schaefer, Joseph T., 1975: Nonlinear biconstituent diffusion: A possible trigger of convection. J. Atmos. Sci., 32, 2278-2284.
- Shukla, J. and K. R. Saha, 1974: Computation of non-divergent stream-function and irrotational velocity potential from the observed winds. Mon. Wea. Rev., 102, 419-425.
- Smith, C. L., and E. Zipser, S. Daggupaty, and L. Sapp, 1975: An experiment in tropical mesoscale analysis: Part 2. Mon. Wea. Rev., 103, 893-902.
- Sommers, William T., 1967: Mesoscale analysis of complex cold front based on surface and tower data. S.M. thesis, Dept. of Meteorology, MIT, Cambridge, MA.
- Teweles, S., 1970: A spurious diurnal variation in radiosonde humidity reports. Bull. Amer. Met. Soc., 51, 836-840.
- Wallace, J. M., 1971: Spectral studies of tropospheric wave disturbances in the tropical western Pacific. Reviews of Geophysics and Space Physics, 9, 557-612.
- Williams, Knox T. and William Gray, 1973: Statistical analysis of satellite-observed trade wind cloud clusters in the western North Pacific. Tellus, 25, 313-336.
- Williams, Scott, 1973: Personal communication. BOMAR, Rockville, MD.
- Yanai, Michio, 1964: An experimental objective analysis in the tropics. Technical Paper No. 62, Dept. of Atmos. Sci., Colorado State University, Fort Collins, Colo.
- Yanai, Michio, and S. Esbensen, J. Chu, 1973: Determination of bulk properties of tropical cloud clusters from large-scale heat and moisture budgets. J. Atmos. Sci., 30, 611-627.
- Yanai, Michio, 1975: Concerning the determination of significance levels in spectrum and coherence analysis. Tropical Meteorology Paper No 11, Dept. of Meteorology, UCLA.
- Zipser, Edward J., 1969: The role of organized unsaturated convective downdrafts in the structure and rapid decay of an equatorial disturbance. J. App. Met., 8, 799-814.

BIOGRAPHICAL NOTE

Howie Bluestein (also known as Cb) was born October 8, 1948 in Chelsea, Mass. He attended public schools in Miami Beach, Fla. and in Boston, Mass. After having graduated from Hyde Park High School in 1966, he entered M.I.T., where he obtained the S.B. degree in electrical engineering in 1971, and the S.M. degrees in electrical engineering and in meteorology in 1972.

He is a member of Sigma Xi, the American Meteorological Society, Eta Kappa Nu, and the Institute of Electrical and Electronics Engineers. Photography, music, shell-collecting, and amateur radio are his main hobbies. He is a crazed lover of waterspouts, tornadoes, hurricanes, snowstorms, and other delectable meteorological exotica.